Theory and simulation of plasma-liquid interactions

Joshua Thomas Holgate

April 2018

Submitted in partial fulfilment of the requirements for the degree of
Doctor of Philosophy of Imperial College London

Department of Physics
Imperial College London
Prince Consort Road
London SW7 2BZ

Declaration

The content of this thesis is entirely my own unless indicated otherwise by a citation to the original work.

Joshua Holgate
April 2018

Copyright

Abstract

This thesis documents mathematical and computational studies of the hydrodynamic motion and stability of plasma-liquid interactions.

The thesis begins with a thorough review of the rapidly-emerging technological importance of plasma-liquid interactions in industry and nuclear fusion research. Deficiencies in current theories of plasma-liquid interactions are highlighted and used to identify those aspects which require significant improvements. The previously-unexplored effect of charge separation and sheath formation at a plasma-facing liquid surface is examined in detail. Two particular findings, which are supported by experimental observations, are the enhancement in droplet ejection rates from bursting bubbles at the surface of electrically-biased liquids and the pulsed emission of droplets from plasma-facing liquid surfaces which are deformed into Taylor cones by the electric field of the plasma sheath.

The behaviour of plasma-immersed droplets is also examined. Some commonly-used models of macroparticle charging are extended to include plasma flows, nonspherical particles or magnetic fields. The stability of droplets in plasmas is assessed and the rapid spinning of droplets in magnetised plasmas is shown to lead to their rotational breakup. This disruption mechanism is incorporated into simulations of droplet transport in tokamaks and results in forked trajectories which are strikingly-similar to those observed with fast cameras in tokamaks. The beneficial consequences of this rotational breakup process on the operation of next-generation fusion devices are emphasised.

Acknowledgements

I would like to thank my supervisor Michael Coppins for drawing my attention to the topic of droplets in plasmas and for providing me with the opportunity to study it. This thesis would not exist without his advice, support and generous supply of coffee over the past three-and-a-half years. A special thanks is also due to John Allen of the University of Oxford, a regular visitor to Imperial College, for inspiring a number of additional projects and collaborating with me to write them up.

I am indebted to Lloyd, Luke, Joe, Richard, Drew, Christos, Minas, Nikoleta and Nopparit for their camaraderie as fellow members of the dusty plasma team. Drew and Luke are each deserving of a special mention: Drew for bestowing me with his unusually-named plasma simulation software "pot"; and Luke for producing simulations of droplet trajectories in tokamaks which he has allowed me to show in this thesis.

I have also had the pleasure of spending time with many fantastic people in the wider plasma physics group at Imperial. I owe a huge thanks to everyone who I have shared an office with, eaten lunch with, played football with, done the crossword with, or gone to the pub with. You have all made the last few years immensely enjoyable and memorable.

Last, but certainly not least, I would like to thank my parents, my dog, my brother and my partner Rebecca for all of their love, support and encouragement.

Contents

List of Tables

List of Figures

1 Introduction

1.1 Plasmas, liquids and their interactions

The concept of four classical elements – earth, water, air and fire – was familiar to Greek cosmologists since their introduction by Empedocles in the fifth century BC. Indeed Empedocles was something of a scientific visionary and well worth taking seriously [1, p. 60–64]. His other achievements include the observation of the centrifugal force in a cup of water whirled on a length of string, a theory that the moon shines by reflected light (although he believed the same was true of the sun) and a proposal that light takes time to travel. He even developed a rudimentary theory of evolution, supposing that "countless tribes of mortal creatures were scattered abroad with all manner of forms, a wonder to behold" and that, eventually, only certain forms with advantageous features survived. However Empedocles' detractors might point to his self-regard as a god and eventual jump to his death in a volcano in order to prove it. The famous act is immortalised in the words of one anonymous poet: "Great Empedocles, that ardent soul, leapt into Etna, and was roasted whole."

Modern science has vindicated Empedocles' vision with the four states of matter – solid, liquid, gas and plasma – that abound in school physics textbooks. Fire can be identified as a plasma in which some of the gaseous particles are ionised by the removal of one, or more, electrons so that the resulting mix of charged and neutral particles moves under electromagnetic forces. The degree of ionisation need not be particularly large: only 0.1% gives the gas an electrical conductivity of half of the maximum possible [2, p. 1]. Tentative studies of ionised gases occurred during the 19th century, such as Faraday's discovery of "radiant matter" [3], but the modern field of plasma physics only truly began in the 1920s with the pioneering studies of Irving Langmuir; his introduction of the term "plasma" to describe a soup of charged particles is recalled in Lewi Tonk's entertaining anecdote [4].

The natural formation of plasmas is relatively rare on Earth. Fire, as mentioned above, is one example; lightning and the aurora are others. These limited examples are in contrast to the matter in the universe as a whole which, it is often claimed, is composed of over 99% plasma [5, p. 1]. However plasmas have rapidly assumed a crucial industrial and economic role over the latter half of the 20th century with applications not restricted to the fabrication of microelectronic chips, advanced material processing, fluorescent lighting and plasma displays. These artificially-produced plasmas inevitably come into contact with the materials which confine them. Traditionally these materials have been solid but, increasingly, devices and processes involving plasma-facing liquid surfaces are being developed. An overview of the ever-growing technological importance of plasma-liquid interactions is no small endeavour and several pages, indeed the entire next section, are required to do full justice to the subject. However it will soon become apparent to the reader that the ongoing development of these processes is an experimentally-led venture. This thesis details attempts to remedy this imbalance by introducing some new theoretical and computational models of plasma-liquid interfaces which, it is hoped, will accelerate the implementation of new plasma-liquid technologies.

1.2 Plasma-liquid interactions in the real world

The interactions between plasmas and liquids are exploited, or to be avoided, in a variety of industrial and fusion environments. Previous reviews of plasma-liquid interactions have been targeted at specific groups of applications [6, 7]. This thesis represents the first attempt to study the full spectrum of plasma-liquid interactions so it seems appropriate to review in detail their different and disparate occurrences.

1.2.1 Melt damage in tokamaks

Fusion is a sub-atomic process occurring in the cores of stars where hydrogen atoms are combined into helium and other heavier elements. The mass of the resulting elements is fractionally less than the combined mass of the original hydrogen atoms but this corresponds, *via* Einstein's famous formula $E = mc^2$, into a huge release of nuclear energy. The production of clean and abundant energy through controlled fusion reactions on Earth is a long-standing dream of physicists; it is nearly a century since Eddington's original hypothesis of nuclear fusion as the origin of stellar energy and his prediction of its terrestrial uses in the statement: "If, indeed, the sub-atomic energy in the stars is being freely used to maintain their great furnaces, it seems to bring a little nearer to fulfilment our dream of controlling this latent power for the well-being of the human race" [8].

The basic obstacle to fusion power generation is the need to confine the hydrogen fuel at sufficient densities and temperatures and for long enough to allow a significant number of fusion reactions to occur. The high-temperature fuel is ionised and hence forms a plasma which can be shaped and contained by applying magnetic fields. The leading device for such magnetic confinement of the plasma is the tokamak, invented in the USSR in 1950 [9], which contains the plasma using magnetic fields in a ring-doughnut-shaped configuration. However, despite this magnetic cage, some of the hot plasma can escape to the inner wall of the machine. This leakage of plasma is intrinsic to a successful fusion device, as the heavy fusion products must be removed from the core plasma to avoid diluting the hydrogen reactants, but it means that the vessel walls must be constructed of highly-resilient materials in order to resist erosion. Current- and next-generation tokamaks use tungsten in the so-called divertor region, where most of the escaping plasma is focussed, due to its high melting point and low chemical reactivity [10, 11].

Despite the high resistivity of the tungsten to erosion, it is inevitable that some tungsten impurities will make their way into the core plasma. The high atomic mass of these tungsten impurities cause strong bremsstrahlung radiation losses which inhibit the successful operation of a fusion device; the maximum tolerable concentration of tungsten impurities is on the order of 10^{-5} tungsten atoms per hydrogen atom [12, 13]. Excessive levels of tungsten impurities can cause to the loss of high-confinement modes of operation [14] or the complete loss of plasma stability and termination of the discharge in a violent event known as a disruption [15]. Disruptions are highly-damaging to the tokamak vessel and must be minimised in future devices; radiative collapse due to impurities is the leading cause of disruptions in current machines [15]. It is, therefore, imperative to keep tungsten impurities to an absolute minimum.

One method of reducing tungsten impurities is to restrict its use to the specific parts of the tokamak wall which are exposed to the highest fluxes of heat and plasma particles. Beryllium is often used for the remainder of the vessel wall due to its low atomic mass, which reduces the impact of its impurities on the plasma, but relatively-high melting point compared to other low mass metals [10]. Melt damage to beryllium surfaces must still be reduced in order to maximise the functionality and lifetime of these components.

Surface erosion in tokamaks occurs by two main mechanisms: sputtering, where individual atoms are removed from the surface [16], and melting. The latter process can be accompanied by the ejection of liquid metal drops into the plasma which are particularly detrimental because they introduce a high number of impurities in a small region; the local tungsten concentration can therefore exceed the critical level even if the total amount of tungsten released is relatively small on the full scale of the tokamak. The main melting processes are bulk melting due to high heat fluxes from the plasma [17] and local melting caused by unipolar arcs [18] and micro-exposed cracked surfaces [19]. The experimental observations of both processes are discussed in detail below.

1.2.1.1 Macroscopic melting

The past decade has seen several tokamaks fitted with metal walls in order to prepare for the next-generation ITER machine. The number of reports on melt damage in tokamaks has, correspondingly, seen a recent surge. A comprehensive review of the melt damage in JET, the largest current tokamak, is provided by Matthews *et al.* who identify three main types of bulk melting damage [17]. The first is the melting, splashing and flowing of exposed components during normal plasma operation. The resulting melt damage to the beryllium wall is illustrated in the top-left image of Fig. 1.1. The exposed beryllium is heated beyond its melting point and begins to flow along the surface against gravity due to the magnetic forces on the liquid; this effect is described in more detail in Ref. [20] which also describes the emission of beryllium drops from the melted layer. Further melting of exposed metal surfaces in JET has been seen in the case of a reciprocating probe which jammed while immersed in the plasma and sprayed a large number of

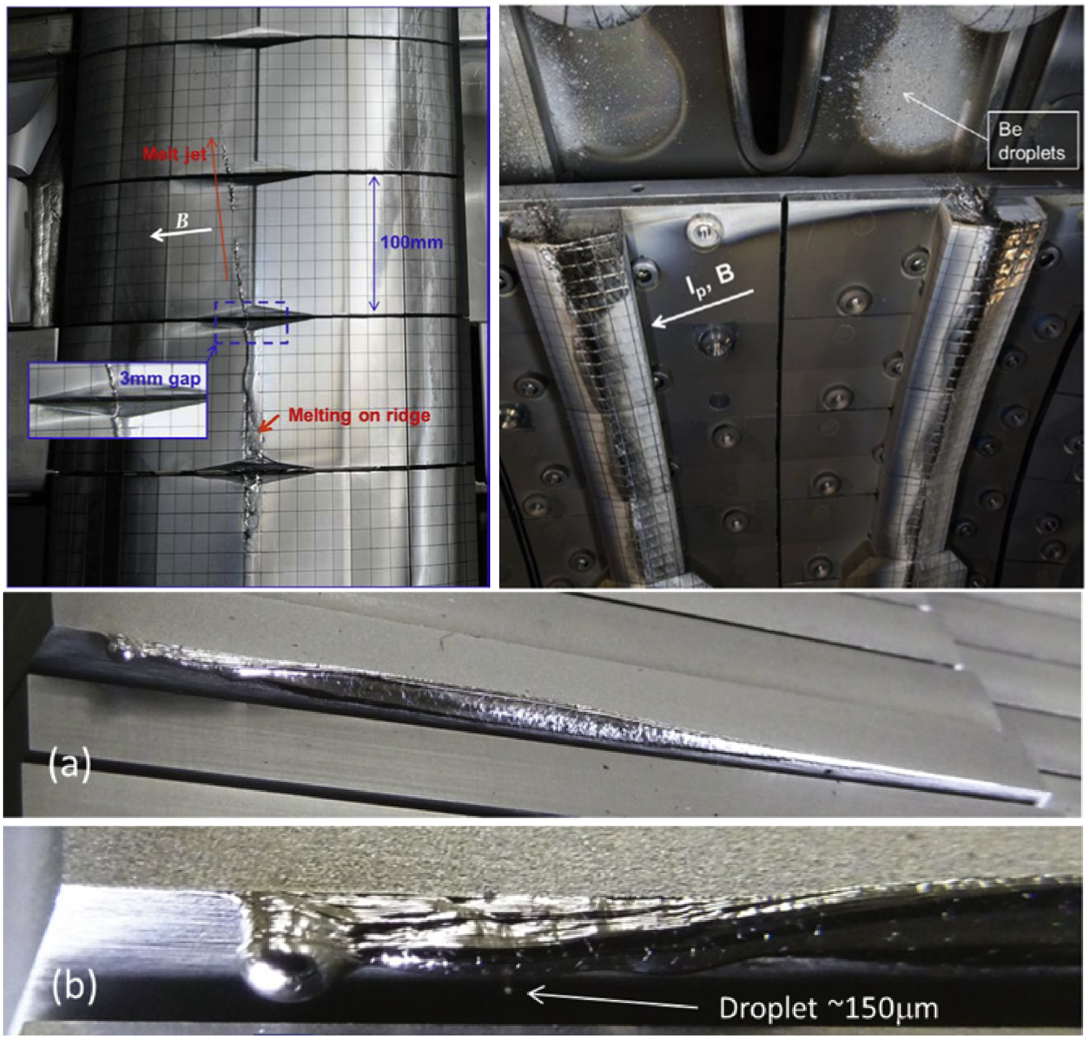

Figure 1.1: Examples of bulk-melted surfaces in the JET tokamak from Ref. [17]. Top-left: melting of a plasma-exposed beryllium surface leading to a stream of molten beryllium flowing up the wall. Top-right: bulk melting of beryllium and droplet formation due to disruptions impacting on the upper wall. Bottom: (a) image of the raised divertor tile, showing melting of the leading edge; (b) detail of the formation of a ~ 150 μm diameter tungsten droplet.

molten metal drops into the plasma [21].

Large-scale melting of beryllium is also observed after a disruption when all of the energy confined in the plasma is dumped onto a small region of the wall. These disruptions cause melting and formation of beryllium drops as shown in the top-right image of Fig. 1.1. Disruption events are mitigated by rapidly injecting neutral gases into the vessel at the onset of a disruption but nonetheless provide a significant source of damage to plasma-facing components [22]. Furthermore the beryllium drops which are released in these events are an operational concern due to their remobilisation during steady-state plasma operation [23].

The final bulk-melting mechanism is due to intermittent bursts of plasma onto the divertor due to edge-localised modes (ELMs) which are themselves caused by the need for the plasma to eject excess particles in order to remain in a steady high-confinement

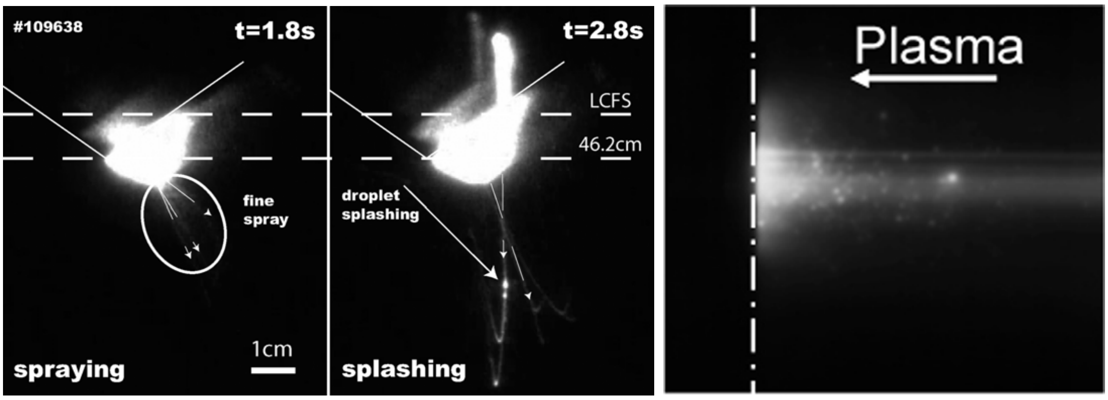

Figure 1.2: Examples of droplet emission during plasma exposure of tungsten surfaces in TEXTOR (left and centre, from Ref. [28]) and Pilot-PSI (right, from Ref. [31]).

mode of operation. The magnitude of these ELMs on ITER will be much greater than in JET; the somewhat artificial situation of raising a tungsten tile in the JET divertor allows the simulation of ELM-induced heat fluxes predicted in ITER [24]. These experiments result in melting of the leading edge of the tungsten tile as shown in the bottom image of Fig. 1.1. The melt layer flows under the magnetic force, in the same way as the melted beryllium surfaces discussed previously, and can lead to the production and ejection of large drops. It is hoped that the ELM-induced divertor melt damage on ITER will be moderated by applying magnetic perturbations to the plasma in order to reduce ELM intensity [25] and with active cooling by flowing a refrigerating liquid through the centres of the divertor tiles [26]. Still, it would be fairly surprising if some small-scale melting of ITER's tungsten divertor did not occur.

Experiments with deliberately-raised tungsten surfaces have also been performed on the TEXTOR [27, 28] and ASDEX-Upgrade [29] tokamaks. Melting and emission of molten drops was observed in both cases; Fig. 1.2 shows camera images of the ejection of drops from the exposed surface in TEXTOR. Similar experiments have been performed with tungsten surfaces in linear plasma devices which imitate the plasma conditions due to ELMs in ITER. Bazylev *et al.* reported on experiments at the QSPA-T device and attributed the emission of tungsten drops to Kelvin-Helmholtz instabilities of the molten metal surface [30] while de Temmerman *et al.* performed experiments at Pilot-PSI and ascribed their observations of droplet ejection to a bubble-bursting mechanism [31]. A final, but particularly intriguing, experiment involved the accidental exposure of a loose tungsten tile to the plasma in the Alcator C-Mod tokamak [32, 33]. The exposed surface suffered significant melt damage, as shown in Fig. 1.3, and produced copious numbers of tungsten drops which completely prevented the device from operating in high-confinement mode.

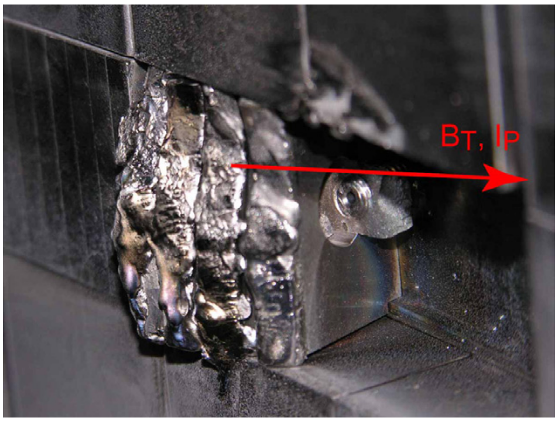

Figure 1.3: Severe melting and deformation of an accidentally-loosened tungsten tile in the wall of the Alcator C-Mod tokamak (from Ref. [32]).

1.2.1.2 Microscopic melting

Unipolar arcs are essentially electrical sparks between the plasma and the metal surface which can cause localised melting of the metal. They tend to form on irregular surfaces where the local enhancement of electric field causes an explosive emission of electrons which is often accompanied by melting and ejection of metal drops. The edge of the resulting crater provides a new raised point on the surface where a new arc spot can form. Arc spots therefore tend to move by repeatedly hopping across a surface which creates distinctive scratch-like marks. A very early observation of a unipolar arc spot, and ejection of drops, on the surface of a liquid mercury pool was reported by Allen and Magistrelli [34]. The physical mechanisms involved in unipolar arcs remain rather mysterious due to the difficulty in studying them under controlled and reproducible conditions although some progress is being made by inducing arcs with lasers [35, 36].

Observations of surface damage from unipolar arcs have been reported extensively on the DIII-D tokamak [37–39]. Arcing was identified as a major source of mobile dust and droplets in DIII-D since the total amount of arc-eroded metal could not be accounted for by the few micron-sized drops found in the immediate vicinity of the arc tracks [39]. Furthermore arcing was only observed during ELMs [39]. Other incidents of arcing have been recorded on the JT60-U tokamak and the LHD stellerator [40] and on the ASDEX-Upgrade [41, 42] and JET [43] tokamaks. Diagnostic mirrors are particularly sensitive to damage by arcing which can severely compromise their reflectivity; Garcia-Carrasco *et al.* have obtained some impressive micrographs of arc tracks on molybdenum mirrors in JET, as shown in Fig. 1.4, where the molten arc craters are clearly visible [43].

Another mechanism of localised melting is observed in tungsten samples which are repeatedly exposed to ITER-like transient heat fluxes. The constant thermal expansion-contraction cycles and recrystallisation of the tungsten can cause the formation of micron-scale cracks. The irregular heat flux on this uneven surface can cause highly-localised melting as illustrated in Fig. 1.4 which shows a micrograph of a tungsten sample after exposure to 10^5 ITER-like pulses on the JUDITH 2 electron beam facility

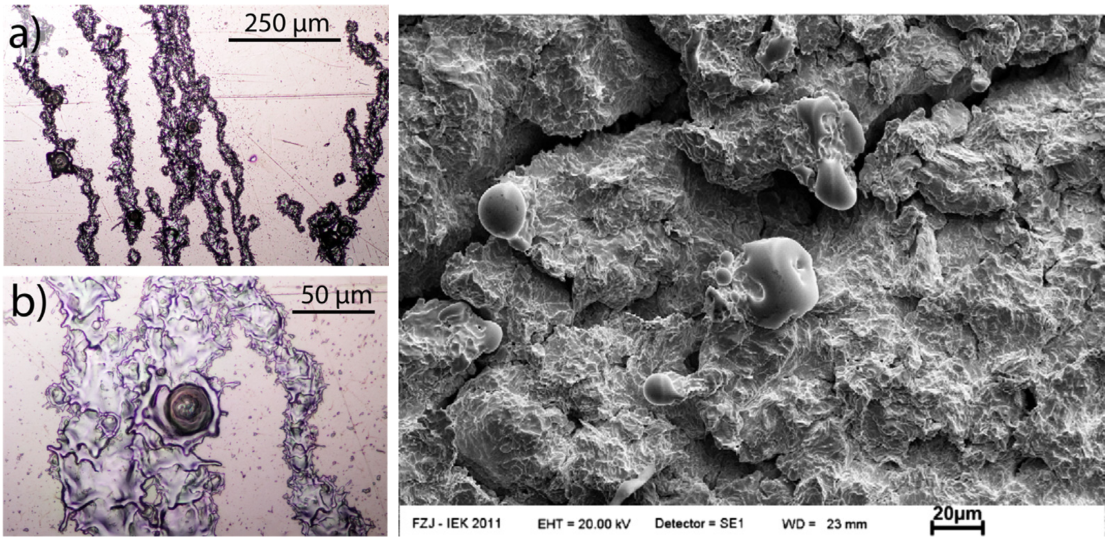

Figure 1.4: Examples of microscopic melting mechanisms. Left: (a) unipolar arc tracks on molybdenum diagnostic mirrors in JET; (b) detail of the arc tracks, showing microscopic melt damage and splashing (both from Ref. [43]). Right: localised melting of the exposed edges of microscopic cracks on a tungsten surface which is repeatedly exposed to ITER-like heat loads on the JUDITH 2 beam facility (from Ref. [19]).

[19]. Similar results have been reproduced on other neutral and plasma beam devices [44–47] but do not appear to have been observed yet on samples placed in tokamaks.

1.2.2 Liquid metal divertors in tokamaks

The operational challenges of solid tokamak walls have led to an alternative proposal to coat the walls with liquid metals. These liquid surfaces provide numerous advantages over traditional solid surfaces: in particular they are immune from melting, can be replenished *in situ*, have additional convective and evaporative cooling mechanisms [48, 49], are resistant to neutron damage, and, in the case of liquid lithium, can be used to breed tritium fuel and enhance plasma confinement [50, 51]. Their main drawback is their susceptibility to hydrodynamic instabilities and the resulting ejection of droplets into the plasma although, when metals with low atomic masses such as lithium are used, the resulting radiative losses due to impurities are less severe than for tungsten. Liquid metal divertor technology is currently underdeveloped compared to solid divertors and, despite its great promise, has not yet been incorporated into designs for future fusion power plants.

Some of the first tests of liquid lithium surfaces, and the emission of liquid drops from these surfaces, were reported from the CDX-U plasma device [52] and the DIII-D tokamak [53] in 2004. The lithium droplets formed in the DIII-D experiments caused degraded confinement and disruptions; the authors concluded that the hydrodynamic stability of the liquid surface is the most critical issue for liquid metal divertors. Recent experiments have attempted to stabilise the surface with small-scale capillary structures that maximise the surface tension force. One such example is the liquid-metal infused

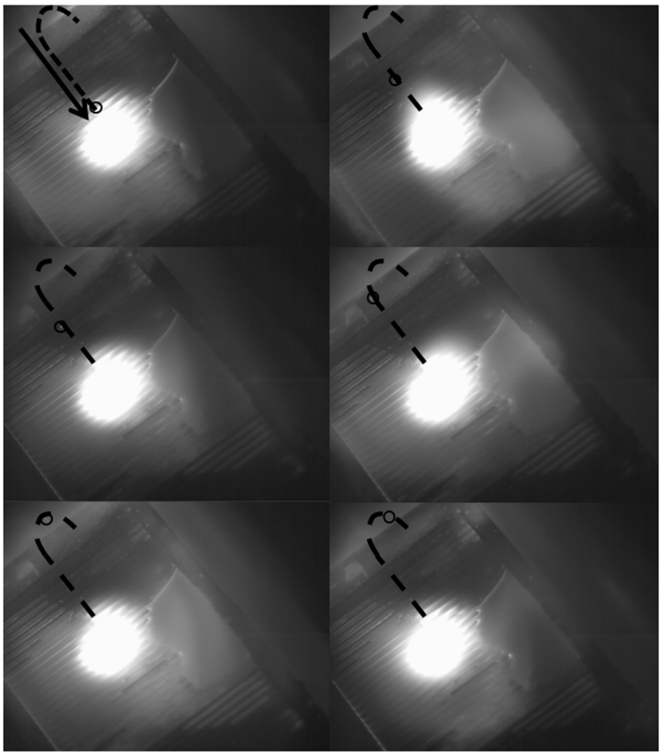

Figure 1.5: Lithium droplet emission from the LiMIT liquid divertor concept during testing on the Magnum-PSI facility (from Ref. [56]). The droplet is circled in each frame and its trajectory indicated by the dashed line while the incident plasma flow is in the direction of the arrow. The trenches, which confine the liquid lithium in the LiMIT design, are clearly visible along with the bright region where the plasma beam is focussed and where the ejected droplet originates.

trenches (LiMIT) concept [54] which has been deployed successfully on the HT-7 tokamak [55]. However experiments performed on the Magnum-PSI linear plasma device suggest that droplet ejection remains an issue for the successful operation of LiMIT divertors as indicated by Fig. 1.5 [56]. Numerous other capillary structures for stabilising the surface of a liquid divertor are in various stages of development [7] and liquid divertors remain an excellent long-term proposition for handling the immense heat fluxes of a fusion plasma.

1.2.3 Liquid metal drops in tokamaks

The various melting and erosion mechanisms in tokamaks lead to the formation of 1–100 μm-scale liquid drops which enter the plasma. If these drops penetrate into the core of the plasma then they can degrade the plasma performance and, in extreme cases, lead to disruptions. The presence of these drops can be inferred from the large quantities of resolidified spherical particles and splashes which have been collected from inside various tokamaks. A trio of papers, lead-authored by Fortuna-Zaleśna, provide particularly impressive micrographs of such spheres and splashes collected from ASDEX-Upgrade, TEXTOR and JET [57–59]. Some micrographs of resolidified tungsten spheres retrieved from ASDEX-Upgrade and of beryllium splashes collected in JET are reproduced in

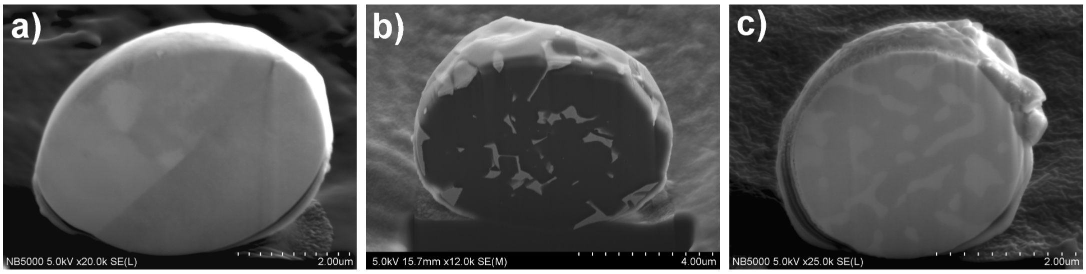

Figure 1.6: Micrographs of dissected tungsten spheres retrieved from inside ASDEX-Upgrade. The resolidified metal microstructure can be classified as (a) grained, (b) two-phased or (c) percolated (from Ref. [57]).

Figs. 1.6 and 1.7 respectively. Similar beryllium splashes have also been found on the surfaces of diagnostic mirrors and, as with the case of unipolar arcs, are detrimental to the functionality and lifetime of these components [43].

An understanding of the motion and lifetime of the drops once they enter the plasma is essential in order to determine the quantity and location of any impurities that they might release into the plasma or redeposit on sensitive surfaces such as diagnostic mirrors [60]. The motion of the drops in the plasma is linked intrinsically to their formation processes in the molten metal layer which determine their size and velocity upon entering the plasma. Understanding these droplet formation mechanisms has been identified as one of the key issues facing droplet transport models [61]. Another challenge is to explain the breakup of droplets which is observed by fast cameras on tokamaks. Figure 1.8 shows some characteristic forked trajectories for droplets which enter the plasma in JET from the lower divertor region as identified from a survey of camera images by Holgate *et al.* [62]; similar trajectories have been observed on DIII-D [37, Fig. 10]. This thesis aims to make some progress towards solving both of these challenges in modelling droplet transport in the plasma.

However not all droplets in tokamak plasmas are detrimental; the positive effect of lithium doping on the performance of the plasma has been known since it was used to dramatically improve the fusion performance on the TFTR tokamak over two decades ago [63]. The lithium binds to impurities and neutral hydrogen atoms and helps to maintain the purity of the plasma core [51]. The lithium may be coated onto the vessel walls, as in the liquid lithium divertor concepts, or injected as droplets directly into the plasma. The deliberate injection of liquid lithium droplets has recently improved the performance of both the DIII-D and EAST tokamaks [64, 65]. Note that the uncontrolled injection of large numbers of lithium drops from a liquid metal divertor remains detrimental to the plasma performance because too much lithium will excessively dilute the plasma.

1.2.4 Materials processing

Some of the earlier sections discussed the detrimental melting of metal surfaces in tokamaks. However the effectiveness of a plasma in melting metal surfaces is sometimes

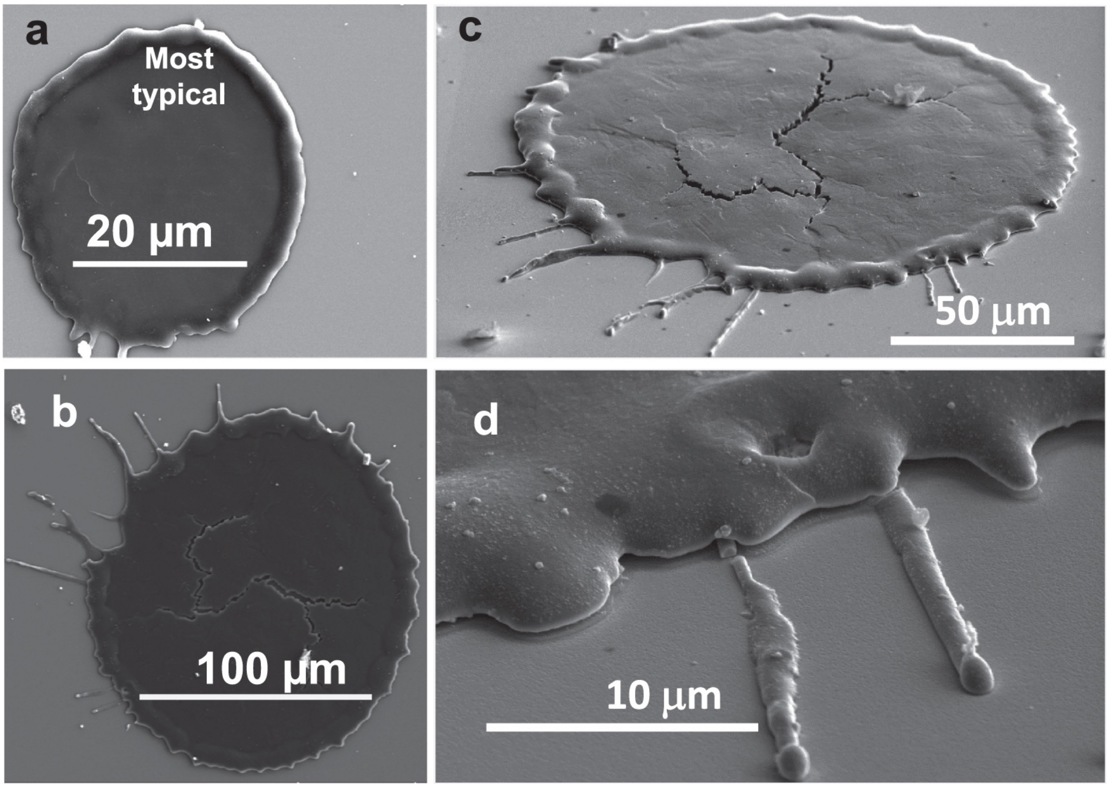

Figure 1.7: Examples of beryllium splashes collected from the inner wall of JET (from Ref. [58]). Images (b)-(d) show the same splash from different viewing angles and with differing magnifications.

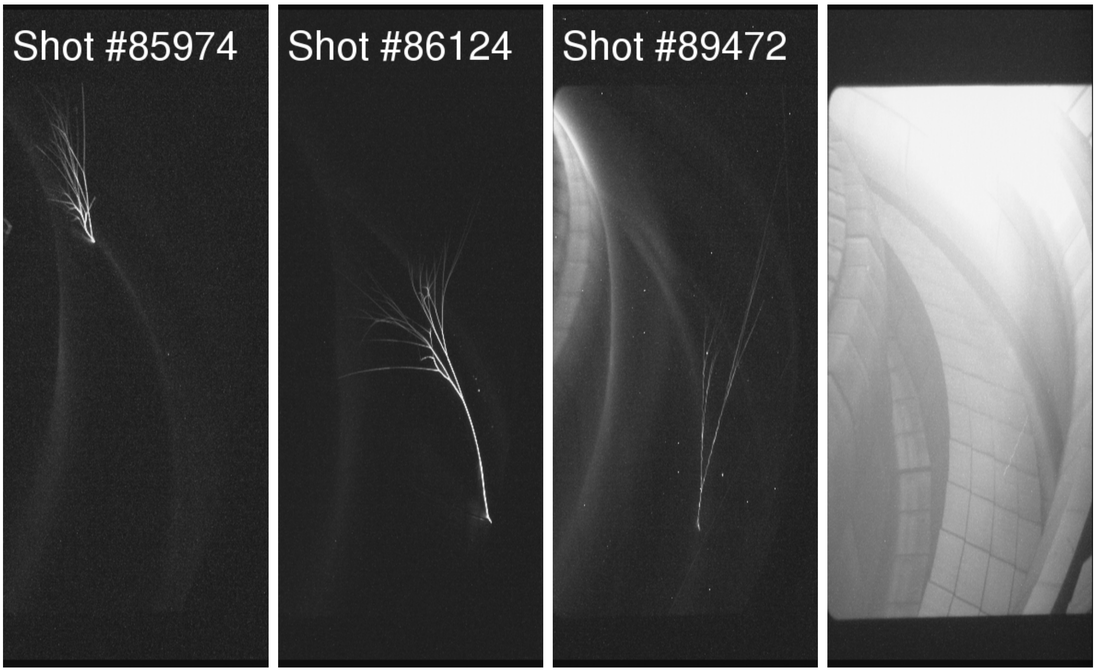

Figure 1.8: Examples of forked droplet trajectories observed with the divertor-view fast cameras on JET. Each image has a 250 ms camera exposure time except for the snapshot on the right which is taken immediately after a disruption has illuminated the divertor region in order to demonstrate the location of the divertor-view camera (adapted from Ref. [62]).

exploited in plasma cutting and welding devices. These operate by bringing an electrode into close proximity with the metal surface and injecting a gas in order to ignite an arc between the electrode and the surface [66]. These double-ended arcs, similar to the unipolar arcs observed in fusion devices, cause localised melting of the metal surface which facilitate cutting and welding processes. Plasma cutters allow quicker and lower cost operation compared to typical abrasive metal cutting methods [67] and are also effective on ceramics [68]. The removal rate of melted material in the efflux plasma is crucial for decreasing surface roughness and improving the quality of the cut and remains a topic of active research [69, 70]. The deliberate ignition of double-ended arcs has also been proposed as a method for melting and removing deposited layers to clean plasma-facing surfaces in tokamaks [71].

Plasma-liquid interactions also occur in plasma spraying processes where a fine powder is injected into a plasma jet so that it melts and deposits a layer on the surface of a material in a series of splashes [72]. Plasma spraying has become a leading technology for material coating, due to its fast deposition rates and thick layers of up to several millimetres wide, and is utilised across a range of industrial sectors including aeronautics, industrial gas turbines, automotive, materials mining and processing, biomedical and electronics [73]. Current research concerns plasma spraying of micro- and nanoparticles in liquid suspensions [74] and plasma spraying under very low pressures [75]. Plasma-enhanced vapour deposition is another technology for depositing very smooth material coatings, albeit at much lower rates than plasma spraying, where liquid drops are injected into the plasma and completely evaporate before being deposited on the material surface [76].

1.2.5 Electric propulsion of spacecraft

The operation of a conventional rocket engine involves burning a fuel to force it out of the combustion chamber and through a nozzle. The backwards acceleration of the exhaust gases provides a countering thrust on the rocket which propels it forwards with a force dependent on the quantity and velocity of the ejected gases. This ejection velocity is restricted to below 5000 m s^{-1} for conventional chemical rockets [77, p. 5]. Increasing the exit velocity of the spent fuel allows for a reduction in the mass and volume of fuel which needs to be carried by the spacecraft; this is the principal behind electric propulsion concepts which use electric fields to accelerate the exhaust to over 75000 m s^{-1} [77, p. 11]. However this improvement in efficiency comes at the cost of reduced mass ejection rates which limit the total thrust produced by these devices. Electric propulsion cannot perform the heavy lifting role required to launch a rocket into orbit but it is suitable for providing small amounts of thrust for the precision control of satellites or for the slow acceleration of spacecraft over prolonged periods of time. Two methods of electric propulsion involve plasma-liquid interactions: liquid-fed pulsed plasma thrusters and field-emission electric propulsion.

Pulsed plasma thrusters (PPTs) were the first electric propulsion method to be flown

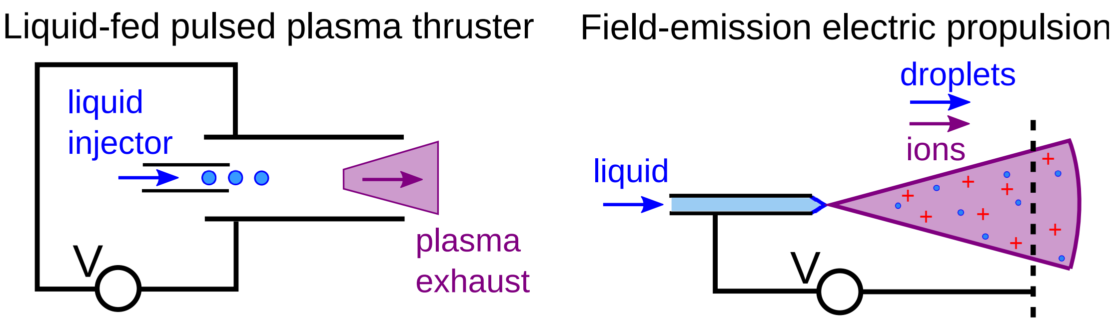

Figure 1.9: Operational designs of liquid-fed pulsed plasma thrusters (PPT, left) and field-emission electric propulsion devices (FEEP, right). A liquid propellant is injected into the PPT which is then ionised and accelerated with a pulsed applied voltage. FEEP draws liquid down a capillary and into a cone which emits ions and droplets due to a strong electric fields. These emitted particles are then accelerated towards a grid and out of the thruster.

in space, on the doomed Soviet Zond 2 probe in 1964 [78]. The basic design of a PPT is to apply a spark to a teflon block and create a small cloud of teflon plasma which is passed through two plates with a pulsed voltage applied across them. This voltage provides an electromagnetic force on the plasma which is ejected at a high velocity. Teflon is chosen as it is stable in a vacuum but it gives a low conversion efficiency from solid fuel into plasma propellant and each pulse produces an unpredictable quantity of ablated teflon plasma. These problems can be negated with a liquid, rather than solid, fuel [79]. Figure 1.9 shows a typical liquid-fed PPT where a controlled amount of liquid is injected between the electrodes [79]. Alternatively the liquid can be introduced passively with a porous flow system [80]. Research is ongoing into the best injection mechanism and choice of liquid; potential candidates include water, alcohols and liquid metals [81].

The second electric propulsion mechanism is field-emission electric propulsion (FEEP). This system, as illustrated in Fig. 1.9, involves the application of a voltage between a liquid anode and a metal grid. The liquid deforms under a strong electric field into a cone, the mathematical theory of which is discussed in Sec. 4.1.2, which emits ions, charged droplets or a mixture of the two from its apex. These particles are then accelerated towards the grid cathode and ejected at high velocities from the thruster. The thruster is often known as a colloid thruster when droplets are ejected [82]. Liquid metals or ionic liquids are used as the propellant; the high density of metals allows compact designs while the low surface tension of ionic liquids allows them to operated with low voltages [83]. The total thrust generated with FEEP can be increased with arrays of liquid cones [84]. Current research includes mitigation of grid erosion due to ion and droplet impacts [85], increasing the total amount of thrust generated [86] and miniaturisation of the thrusters [87]. Nevertheless FEEP has emerged as a leading concept for electric propulsion and is already used, for example, in the precision control of spacecraft positioning in the LISA Pathfinder mission which aims to detect gravitational waves [88].

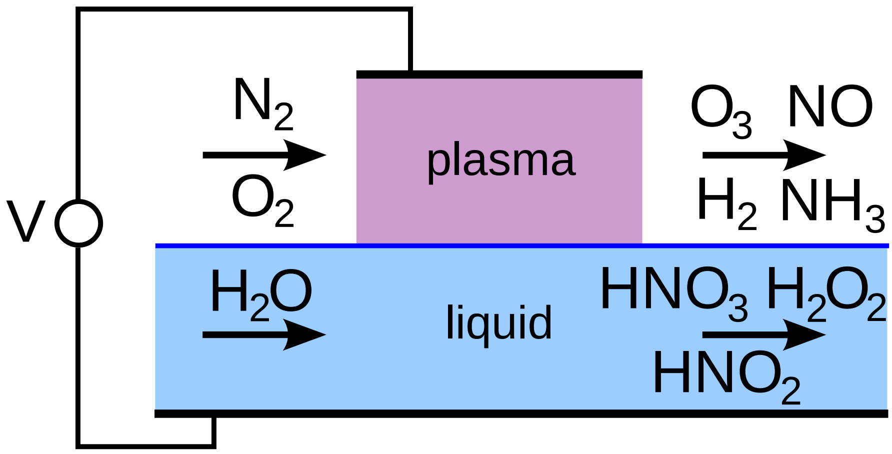

Figure 1.10: Schematic of plasma catalysis in an atmospheric pressure air-water reactor.

1.2.6 Chemical catalysis and nanoparticle synthesis

Another promising application currently driving innovation in plasma-liquid interactions is the catalysis of chemical reactions. Cavendish's "Experiments on air" [89], in which nitric acid was produced by passing a spark through a vessel containing water and air, is a very early example of plasma chemistry. The very first industrial plasma process, the synthesis of ozone in a dielectric barrier discharge, was later developed by Siemens in 1857 [90]. The celebrated Miller-Urey experiment [91] provides an additional famous example in which the production of amino acids, and hence the fundamental building materials for life, was demonstrated by imitating lightning strikes in Earth's primordial atmosphere. Surprisingly, given these historical precedents, it is only now that the widespread exploitation of plasmas and electrical discharges for chemical catalysis of liquid-phase reactions is starting to take place [92].

A typical plasma-catalysed reaction between air and water in an atmospheric DC discharge into useful chemicals such as ozone, nitric oxide and hydrogen peroxide is illustrated in Fig. 1.10 based upon figures in Refs. [93] and [94]. The nitrogen, oxygen and water molecules are extremely stable under standard atmospheric conditions. However the application of a plasma, or a high voltage to induce breakdown of the gases into a plasma, produces high-energy ions, electrons and radical species which can penetrate deep into the water and facilitate reactions into industrially-important products [95, 96]. Such products include peroxynitrate (ONOOH) which has excellent bactericidal properties [94]. Alternative techniques for applying the plasma to the liquid include plasma microjets at the liquid surface [97], direct production of the plasma in the liquid as bubbles or streamers [98], or injection of liquid drops into the plasma [99].

Different gases, liquids or solutions can be introduced to a plasma reactor in order to generate a range of chemical products; Table A2 of Ref. [6] summarises some common plasma-produced liquid phase species. Further examples include the electrolysis of a methanol solution into hydrogen and formaldehyde [100] and the breakdown of hazardous chemical pollutants in water [101].

The use of ionic solutions as the liquid phase allows the production of metallic nanoparticles. For example the application of a plasma microjet to an aqueous solution of silver nitrate leads to the formation of silver nanoparticles [102]; a similar setup using a gold chloride trihydrate solution yields gold nanoparticles [97]. The synthesis of other metallic nanoparticles in plasma-liquid systems are reviewed in Ref. [103]. Plasma microjets have also been administered to colloidal solutions of silicon nanocrystals in ethanol in order to improve the stability and lifetime of the silicon nanostructures for applications in photovoltaic cells [104].

As a slight aside it is noted that plasma-catalysed chemical reactions also occur in tokamak environments. Previous generations of tokamaks used carbon as a wall material due to its extremely high sublimation temperature which, at around 5800 K, far exceeds tungsten's melting temperature of around 3700 K. However the carbon surfaces reacted with the hydrogen plasma to form methane and other hydrocarbons [105]. These so-called chemical sputtering mechanisms cause rapid erosion of the carbon surfaces and render it unsuitable for future machines. Furthermore the catalysis of ammonia from nitrogen impurities has been observed in ASDEX-Upgrade [106] and lithium hydride salts have been generated in Magnum-PSI [107]. The strong ionic bonds of lithium hydride make it more resistant to erosion than pure lithium so this reaction might prove beneficial for the use of lithium surfaces in tokamaks.

1.2.7 Plasma medicine and decontamination of food

Several of the short-lived chemical species and radicals produced in plasma-liquid interactions have potent antimicrobial properties which make them ideal for the sterilisation of water and food products [108]. Of course, care must be taken not to cause any negative permanent chemical changes in the liquids undergoing treatment although the beneficial degradation of toxic compounds is of significant interest [109]. Plasmas are routinely used in the treatment of various liquids such as drinking and waste water [110], milk [111] and fruit juices [112, 113]. Many plasma-liquid treatment apparatuses are similar to Fig. 1.10 where the liquid simply has a plasma discharge applied to its surface with continuous liquid flow or a stirring mechanism to ensure treatment of the whole liquid volume [111, 113].

The bactericidal action of a plasma on a liquid surface is also of great benefit in medical applications which are reviewed in gruesome detail in Ref. [114]. Furthermore, despite their antimicrobial properties, plasmas have been shown to be non-damaging to living tissue provided that excessive dosages are avoided [115]. Plasma treatment of wounds can additionally accelerate the coagulation of blood by two mechanisms: activation of the platelets in the blood increases the rate at which they bind together while the rupturing of red blood cells releases haemoglobin and other proteins which coagulate into a membrane [116]. This second clotting mechanism is especially beneficial for patients with low platelet counts. Plasmas have also been found to assist in the treatment of ulcers [117] and cancers [118, 119].

1.2.8 Further examples

A few final examples of real-world plasma-liquid interactions do not fit into the categories above and are best suited to a miscellaneous section.

1.2.8.1 Natural occurrence of plasma-liquid interactions

A classic example of a naturally-occurring terrestrial plasma is a lightning bolt which, given that it originates in a thunderstorm cloud, could well interact with water droplets in the cloud. Early experiments, by Macky in 1931 [120] and English in 1948 [121], found that water droplets falling and disintegrating in electric fields exhibit a slight edge glow due to the local formation of a plasma. The rupture of water drops in thunderstorms subsequently attracted significant attention, notably that of Taylor [122], and is an important trigger for the onset of lightning strikes [123]. Lightning strikes on the primordial ocean are also hypothesised to have catalysed the creation of amino acids necessary for the development of life on Earth [91].

Plasmas also occur high in the Earth's atmosphere in the the ionosphere. The low temperatures of this region mean that most small objects, such as the ice particles in noctilucent clouds, are solid. However plasma-liquid interactions could occur due to the small molten meteorites known as spherules [124]. The atmospheres of other planetary bodies can contain clouds made of liquids with much lower melting points than on Earth such as the methane clouds in the upper atmosphere of Titan [125].

1.2.8.2 Laser-droplet interactions

Striking a droplet with a laser produces a controlled quantity of plasma. These mass-limited targets can be used as a source of extreme ultraviolet light [126] or as a target in high-intensity laser experiments to generate high-brightness X-ray or fast particle sources without undesirable effects such as target debris and electromagnetic pulses [127]. Lasers pulses have also been shown to generate filaments of plasmas which trigger the formation of water droplets in sub-saturated air [128]. It is claimed this process could allow the artificial production of laser-induced clouds with potential socio-economical benefits such as drought relief [128].

1.2.8.3 Plasma bubbles

Plasmas can form inside a liquid as bubbles or filaments but they tend to be transient due to the rapid quenching of the plasma by the liquid [129]. This thesis avoids making an attempt to describe these short-lived plasmas but they deserve to be mentioned for their uses in chemical catalysis [130] and decontamination of water [110]. The collapse of plasma bubbles appears to be much more forceful than for normal gas bubbles; for example laser-produced plasmas bubbles near an air-water interface can cause the ejection of water droplets into the air to heights of up to 50 cm [131]. Plasma bubbles in liquids also exhibit intriguing finger-like expansion mechanisms [132]. The application of ultrasound to a liquid causes the formation and collapse of plasma bubbles which can produce light, in a phenomenon called sonoluminescence [133], or catalyse chemical reactions in a process known as sonochemistry [134]. Acoustic cavitation of plasma bubbles is also notorious for the highly-dubious, and likely falsified [135], claim that they can produce fusion-relevant plasma conditions [136].

1.3 Previous studies of plasma-liquid surface instabilities

The many examples provided by the previous section illustrate the growing technological significance of plasma-liquid interactions but are primarily based on experimental observations. Complementary theoretical and numerical studies of plasma-liquid interactions are at an early stage but, nevertheless, there has been some prior work in this direction which is reviewed in this section.

1.3.1 Rayleigh-Taylor instabilities

The classic example of a Rayleigh-Taylor instability occurs when a heavier fluid is on top of a lighter fluid with gravity pulling the heavier fluid into the lighter fluid. If the interface between the two fluids is perfectly flat then the system is in equilibrium but even the slightest perturbation will grow exponentially and cause mixing of the fluids. This basic configuration is of limited direct applicability to plasma-liquid interactions since almost all of the real-world applications considered in Sec. 1.2 involve the heavier liquid being below the lighter plasma. One exception is the interaction of a tokamak plasma with molten metal on the roof of the vessel either due to liquid lithium wall coatings or beryllium melt damage. Both of these liquid metals have relatively low densities but high surface tensions which means that they often remain stable.

The Rayleigh-Taylor instability has been adapted to account for the magnetic fields involved in some plasma-liquid interactions by noting that the $\underline{j} \times \underline{B}$ Lorentz force is a body force like gravity. Jaworski *et al.* [137] supposed that a liquid lithium layer placed at the bottom of a tokamak could contain a constant magnetic field and current density so that the $\underline{j} \times \underline{B}$ force would point upwards against gravity; the gravitational strength ρg can then simply be replaced by $\rho g - jB$. The resulting instability is most severe for long-wavelength surface perturbations so Jaworski, Khodak and Kaita [138] argued that liquid metal divertors should attempt to avoid instabilities with small capillary structures such as those of the LiMIT concept described in Sec. 1.2.2. However their analysis takes the worst possible configuration of magnetic field and current; if either one of these points in the other direction then the direction of the Lorentz force reverses and the surface is always stable. Such magnetic stabilisation of flowing liquid metals is widely used in metallurgy and steel casting [139]. Alternatively the current might be directed out of the surface, for example due to electron emission from the interface, while the magnetic field remains in the plane of the surface so the Lorentz force pushes the molten metal sideways as observed in the beryllium jets on JET [17, 20]. Furthermore the $\underline{j} \times \underline{B}$

force applies equally to both the plasma and the liquid since $\underline{j}$ and $\underline{B}$ must be continuous across the interface. This force is not at all like gravity which acts predominantly on the liquid due to its much higher density. A final criticism is that the classic Rayleigh-Taylor theory applies to neutral fluids with no net electric charge. Plasmas can only be treated as quasineutral, where the electron and ion densities are nearly identical, over large distances much longer than their characteristic Debye length. Charge separation near the boundary of a plasma with a surface can generate strong electric fields which are particularly pronounced on short-wavelength scales. The inclusion of these electric fields in theories of the plasma-liquid interface is a key objective of this thesis.

1.3.2 Kelvin-Helmholtz instabilities

If one fluid flows quickly past another then the interface can become unstable and the fluids mix into each other; this is the Kelvin-Helmholtz instability. Such situations arise in plasma-liquid applications involving liquid flows, plasma jets or plasma exhaust at an oblique angle onto a tokamak divertor.

The role of Kelvin-Helmholtz instabilities on droplet emission from plasma-facing liquid metal surfaces in tokamaks has been considered extensively. The first mention of these instabilities in a tokamak environment appears to be that of Bazylev *et al.* [140] who referenced an earlier work on Kelvin-Helmholtz instabilities of a plasma-liquid interface in a pulsed laser experiment [141]. Bazylev later claimed that the size (20–40 μm) and velocity (4–6 m s^{-1}) of ejected tungsten droplets in a transient tungsten melting experiment with the QSPA-T plasma gun were consistent with a Kelvin-Helmholtz instability analysis [30]. Miloshevsky and Hassanein are also longstanding proponents of Kelvin-Helmholtz-induced emission of droplets from tungsten melt layers in tokamaks. They give the basic theory in Ref. [142] before extending it to viscous flows with heat transfer and concluding that viscosity destabilises the interface while heat transfer can stabilise the short-wavelength instabilities [143]. A further extension found the most unstable wavelength is ~ 30 μm and described how the application of a magnetic field perpendicular to the direction of melt-layer motion could enhance the instability and increase the tungsten erosion rate [144]. However the lengthscales of the instabilities in Bazylev's and Miloshevsky's works do not appear to justify the neglect of the electric field at the plasma boundary and application of neutral fluid models.

Fiflis *et al.* have recently performed some very interesting experiments on the stability of plasma-facing liquid lithium trenches due to Rayleigh-Taylor and Kelvin-Helmholtz instabilities [145]. They extended Jaworski's Lorentz-force-driven stability criterion [137] to include an oblique plasma flow and predicted that trenches with widths of 12 mm and above would be unstable. However their experiments found that lithium trenches remained stable beyond this value and placed the actual stability limit in the range 22–26 mm. The experiments also revealed that droplet ejection occurs primarily from the edges of trenches which the authors attributed to splashing of surface waves on the edges of the trenches. This splashing mechanism brings to mind the breaking

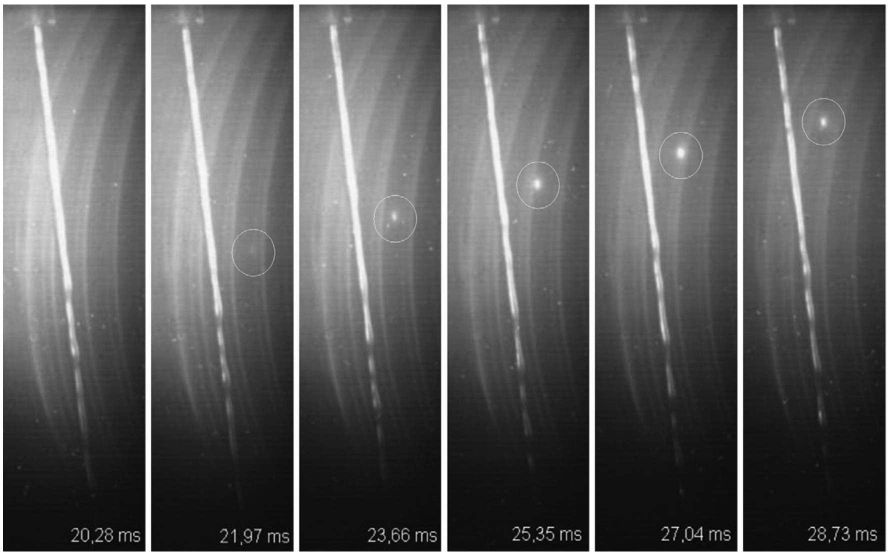

Figure 1.11: Interaction of a jet of liquid gallium with the plasma in the ISSTOK tokamak (from Ref. [146]). The onset of a Rayleigh-Plateau instability is clearly visible while the motion of a droplet, formed by the splashing of the jet off a collector, is indicated by the circled object.

of ocean waves on rocks; the unbroken ocean waves travel, without ejection of droplets, until they crash onto the rocks and produce a large spray of drops. Fiflis *et al.* also provided quantitative support for their wave-breaking explanation for droplet emission with nonlinear simulations of the liquid surface with a shallow-wave approximation in the absence of a plasma. However it is worth noting that their initial prediction of an upper limit on stable trench widths of 12 mm was based on Jaworski's worst-case situation of $\underline{j} \times \underline{B}$ being perfectly anti-aligned with gravity and that relaxing this assumption could give the transition from stable to Kelvin-Helmholtz-unstable surfaces at a wavelength in the same range as their experiments.

1.3.3 Rayleigh-Plateau instabilities

Rayleigh managed to attach his name to another instability, that of a cylindrical jet of liquid bursting into a chain of droplets in order to reduce the total surface area of the liquid, which has been termed the Rayleigh-Plateau instability. This instability has received some limited attention in studies of plasma-liquid interfaces. The earliest such study is that of Gomes *et al.* who introduced a jet of liquid gallium metal into the ISSTOK tokamak [146, 147]. The gallium has a lower melting point but a higher atomic mass than lithium which helps it radiate heat away from the divertor region of the tokamak. The onset of the Rayleigh-Plateau instability is evident in photos of the gallium jet in Fig. 1.11 but the jet reaches a collector before the formation of large gallium drops. However splashing off the collector produces additional droplets, one of which is highlighted in Fig. 1.11.

Another Rayleigh-Plateau instability is considered by Mesyats and Zubarev [148] who consider the molten metal rim of an arc spot crater as a liquid column bent into a loop.

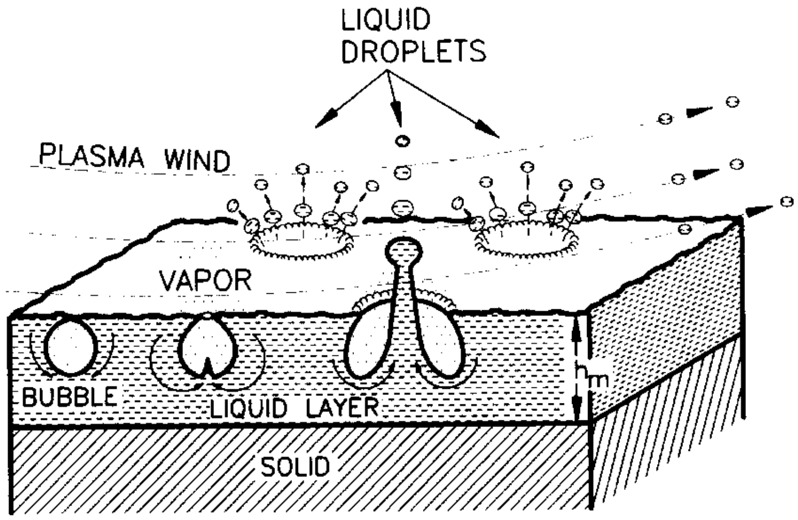

Figure 1.12: Illustration of the bubble-bursting mechanism for droplet ejection from liquid surfaces (from Ref. [150]). The bubble collapses, after its thin covering film has burst, and a jet of droplets emanates from the base of the bubble. Symmetry breaking Rayleigh-Plateau instabilities, as described in Sec. 1.3.3, are also depicted in the two distant bubble bursts.

They show that typical arc spot parameters cause the column of liquid metal to burst into a ring of droplets which are ejected from the arc spot. The micrographs of arc-damaged surfaces in JET, shown in Fig. 1.4, appear to be consistent with this proposed erosion mechanism. The previously-mentioned simulations of Fiflis *et al.* also used the Rayleigh-Plateau instability to provide a criterion for the formation of a droplet from the tips of waves [145] although, it must be said, their liquid configuration bears little resemblance to a column of liquid.

1.3.4 Bubble bursting

Hassanein and Konkashbaev first mentioned the bursting of bubbles on the surface of liquid metals as a mechanism for droplet ejection from melted surfaces in tokamaks [149] and restated their suggestion in Ref. [150]. These bubbles might originate from boiling of the liquid or the absorption of gases which can create blisters on the surface of plasma-facing metal components [151]. The basic mechanism is illustrated in Fig. 1.12: the film covering the surface of the bubble bursts, which can release some very fine droplets [152], and the subsequent collapse of the bubble forms a rising jet of liquid which pinches off, according to the Rayleigh-Plateau instability, to form a spray of droplets. This process is also observed, for instance, in the bursting bubbles at the surface of a glass of champagne; the ejected droplets are alleged to "complement the sensual experience of the taster" [153].

The comprehensive parametric study of Duchemin *et al.* [154] indicates that 10–100 μm bubbles at metallic surfaces eject droplets with velocities of 10–100 m s^{-1} and radii around one-tenth of initial bubble radius. Shi, Miloshevsky and Hassanein simu-

Table 1.1: The density, ρ, surface tension, γ, and viscosity, η, of typical liquids involved in plasma-liquid interactions. †The viscosity of beryllium has never been measured directly and is tentatively calculated from the formulae in Ref. [156].

	ρ /kg m^{-3}	γ /N m^{-1}	η /mPa s^{-1}
Water [157]	1000	0.072	0.89
Methanol [157]	790	0.022	0.54
Lithium [7]	570	0.4	0.25
Beryllium [20, 156]	1690	1.1	1.1†
Aluminium [155]	2380	1.02	0.8
Tungsten [155]	17600	2.5	7

lated the specific cases of tungsten and aluminium surface bubbles and found consistency with Duchemin's more general study [155]. The agreement between these predicted droplet velocities and those observed in de Temmerman's tungsten and aluminium melting experiments on Magnum-PSI [31] provides strong evidence that the bubble bursting mechanism is responsible for high-velocity droplet production in tokamaks.

1.4 Physical properties at the plasma-liquid interface

The real-world instances of plasma-liquid interactions, as described in the previous section, encompass a wide range of physical properties of both plasmas and liquids. The present section provides a brief overview of these properties. Table 1.1 gives the density, ρ, surface tension, γ, and dynamic viscosity, η, for water and methanol under standard atmospheric conditions and different liquid metals at their melting points. These values can change slightly due to variations in temperature, pressure and dissolved impurities. The interaction of a liquid with a plasma can also modify its physical properties due to chemical changes; for example it is likely that the strong inter-atomic bonds of lithium deuteride (LiD) compounds [107] could result in an enhanced surface tension of the molten mixture. The rough similarity in the physical properties of aluminium and beryllium means that aluminium is often used as a proxy for beryllium in surface erosion experiments [31].

The electron temperatures, T_e, and plasma number densities, n, which arise in various plasma-surface interactions are given in Tab. 1.2 along with the corresponding Debye lengths λ_D and the plasma species in each application. A tokamak contains a large variation in plasma parameters throughout the device, particularly when it is run in a high-confinement mode, so the MAST, JET and ITER values are provided for the so-called scrape-off layer which is the plasma which comes into contact with the walls. These values of electron temperatures increase by around a factor of four at the edge of the core region while the plasma densities roughly double at this point [158]. Any droplet which crosses into the core region will evaporate almost instantaneously due to the extreme plasma conditions [60].

A single plus sign has been affixed to all of the ion species in Tab. 1.2 to indicate that

Table 1.2: The number density, n, electron temperature, T_e, Debye length, λ_D, ion species and ion mass of typical plasmas involved in plasma-liquid interactions. Ion species are denoted by their standard chemical symbol except for deuterium which is given by D.

	n /m^{-3}	T_e /eV	λ_D /μm	Ion species	Ion mass
MAST [158]	$4.5{\times}10^{18}$	15	14	D^+	$2m_p$
JET [158]	$1.1{\times}10^{19}$	40	14	D^+	$2m_p$
ITER [158]	$1.6{\times}10^{19}$	50	13	D^+	$2m_p$
Magnum-PSI [31]	1×10^{20}	2	1	H^+/He^+	$m_p/4m_p$
Plasma arc torch [159]	1×10^{23}	2	0.032	N^+	$14m_p$
DC air discharge [6]	1×10^{19}	1	2.4	N^+	$14m_p$
RF low pressure discharge [76]	5×10^{16}	3	58	Ar^+	$40m_p$

the plasmas considered in this thesis are composed of singly-charged ions only. This is quite a reasonable assumption to make: the deuterium atoms in a tokamak have only a single electron so exclusively form singly-charged ions while the remaining examples have relatively low electron temperatures, and often high densities of background neutral particles, which give a predominance of singly-charged ions.

1.5 Focus of this work

This introduction has given some impression of the emerging technological importance of plasma-liquid interactions in diverse applications such as magnetic fusion devices, advanced materials processing, spacecraft propulsion, chemical catalysis, plasma medicine and water purification. It has also reviewed the present status of theoretical and computational research into plasma-liquid interactions which, in general, has been conducted on an *ad hoc* basis and usually treats the plasma as an uncharged liquid. Neglecting the fundamental electromagnetic properties of a plasma – its composition as a soup of charged particles and its characteristic motion under electric and magnetic fields – calls the conclusions of these studies into question.

This thesis aims to incorporate basic plasma-surface processes, particularly the separation of charge and resulting electric fields, into theoretical models of plasma-liquid interactions. These models are applied to problems involving the stability of plasma-facing liquid surfaces in Chapter 4 with a focus on the implications of electric fields in the plasma on the formation and ejection of droplets. Chapter 5 then describes the shape and stability of liquid droplets in plasmas due to charging, spinning and translations of these droplets. Both of these chapters depend on the fundamental interactions of a plasma with a surface, either solid or liquid, which are examined in Chapter 3. However, before all of this can begin, it is necessary to elucidate the basic mathematical description of plasmas, liquids, and their interactions.

2 Fluid descriptions of plasmas, liquids, and their interactions

The importance of studying plasma-liquid interactions by theoretical and computational means has been motivated in the preceding chapter. Accordingly, the present chapter sets out to state clearly the equations describing the motion of plasma-liquid interfaces. Proceeding from these equations to various solutions for the motion and instability of plasma-liquid interfaces is then relatively straightforward; Einstein, after all, is alleged to have proclaimed “if I only had one hour to save the world I would spend fifty-five minutes defining the problem and only five minutes finding the solution” (although the original source of this aphorism is suspiciously absent from a collection of his quotes [160]). A clear mathematical representation of plasma-liquid interactions is essential if progress is to be made.

Both plasmas and liquids can be represented using fluid equations which makes the fluid description a natural choice for modelling plasma-liquid interactions. The suitability of fluid models for problems involving plasma-surface interactions is assessed before diving into the full fluid equations for plasmas, liquids, and their interactions.

2.1 What is a fluid?

The precise definition of a fluid varies amongst authors. Landau and Lifshitz simply define a fluid as a liquid or gas [161, p. 1]; Lamb states that a fluid’s fundamental property is that it cannot be in equilibrium under an “oblique” stress between adjacent parts of the fluid [162, p. 1]; Faber argues that a fluid is “a material with no rigidity” [163, p. 3]; and Acheson, perhaps wisely, avoids making any statement whatsoever [164]. However two essential properties of fluids appear to be at least implicit in all of these texts.

Firstly a fluid is any material which deforms under the application of a shear stress *i.e.* a force, per unit area, applied parallel to a cross-sectional area of the fluid as illustrated in Fig. 2.1. Consider, for example, the spreading of a cold knob of butter, taken directly from the fridge, over a freshly-toasted slice of bread. The immediate application of a knife to the butter yields disappointing results: the shear stress is transferred through the butter into the toast and, to the consternation of the hungry butter-spreader, a hole is ripped through the middle of the toast. The experienced toast-preparer will instead wait for the the butter to melt slightly and become a fluid; the shear stress exerted by the knife now causes a steady flow of butter across the surface of the toast.

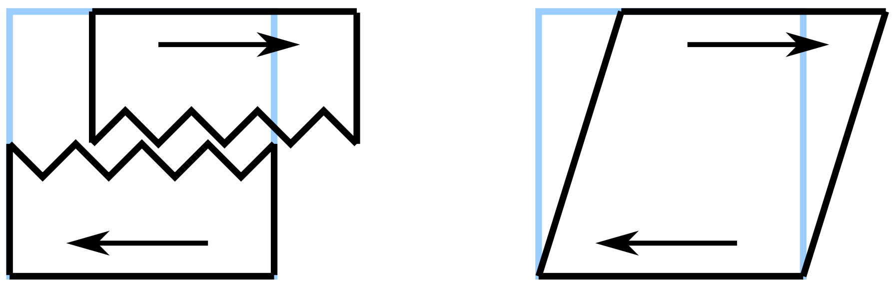

Figure 2.1: Illustration of the reaction of solids and fluids to shear stresses. Solids resist deformation and will fracture under the application of excessive shear stresses. Fluids, on the other hand, can deform and flow smoothly when shear stresses are applied.

The second important property of a fluid is that it is continuous in a mathematical sense: it can be arbitrarily subdivided into small portions with the same properties as the bulk fluid. This property is sometimes referred to as the continuum assumption. It means that fluid properties such as density, pressure and velocity can be defined everywhere and at infinitesimally-small points in space. Fluids which satisfy the continuum assumption are purely mathematical constructions since real-world liquids, gases and plasmas are formed of individual particles on the atomic scale. However it is often sufficient to take a local average of the properties of these particles in order to determine the equivalent fluid property at this point and hence construct a fluid which accurately reproduces the real-world motion of the material. The process of moving from the kinetic model of a plasma, which uses the full distribution function of the particles' velocities at each point, to the fluid model is treated by several authors [2, Sec. 12.5; 165, Sec. 8.2; 166, Sec. 2.5] and is not considered in this thesis which favours a purely fluid-mechanical approach.

Both plasmas and liquids can be described using fluid models: they deform under shear stresses and, on the macroscopic lengthscales of real-world plasma-liquid interactions, their discrete atomic nature can be disregarded. Fluid models for both liquids and plasmas are well-established and are introduced in the next two sections. However the boundary conditions on the interface between these fluids has not previously been considered in detail; this is remedied in Sec. 2.4.

2.2 Two-fluid description of a plasma

A plasma, as previously discussed, is composed of electrons and ions which can each be described as a fluid. These coexisting and mutually-interacting fluids give rise to the two-fluid model of a plasma. The motion of each fluid is determined by three equations describing the flows of material, momentum and energy; these are referred to as the continuity equation, the momentum equation and the energy equation respectively and each is considered in turn below.

2.2.1 Continuity equations

The change in the number of particles within any closed volume of fluid must be accounted for by particles leaving and entering through the surface of the volume and the rate of production or annihilation of particles within the volume. This balance leads to the continuity equations for electrons and ions,

$$\frac{\partial n_e}{\partial t} + \nabla \cdot (n_e \underline{u}_e) = n_e s, \tag{2.1}$$

$$\frac{\partial n_i}{\partial t} + \nabla \cdot (n_i \underline{u}_i) = n_e s, \tag{2.2}$$

where $\underline{u}_e$ and $\underline{u}_i$ are the velocities of the electron and ion fluids and n_e and n_i are their number densities *i.e.* the number of electrons or ions per unit volume. The terms on the left-hand side give the rate of change of density and the particle flux at a point in the fluid while the right-hand side is the rate of creation of particles. The ions are assumed to be singly-charged, as discussed in Sec. 1.4, so that electrons and ions are created at equal rates. The main mechanism of electron and ion production is through the ionisation of neutral gas particles by collisions with electrons which, due to their small mass, tend to be zipping around much more quickly than the ions. The source term is therefore given by the number density of electrons multiplied by an ionisation frequency s.

2.2.2 Momentum equations

Newton's second law, that the rate of change of momentum of an object is equal to the force exerted on it, provides one of the foundations of classical mechanics and can be applied to an infinitesimally-small volume of the ion or electron fluids to give the momentum equations [165, p. 202]

$$m_e n_e \frac{\partial \underline{u}_e}{\partial t} + m_e n_e (\underline{u}_e \cdot \nabla)\underline{u}_e + m_e n_e s \underline{u}_e = -e n_e (\underline{E} + \underline{u}_e \times \underline{B}) - \nabla p_e - \nu_{ei} n_e m_e (\underline{u}_e - \underline{u}_i), \tag{2.3}$$

$$m_i n_i \frac{\partial \underline{u}_i}{\partial t} + m_i n_i (\underline{u}_i \cdot \nabla)\underline{u}_i + m_i n_e s \underline{u}_i = e n_i (\underline{E} + \underline{u}_i \times \underline{B}) - \nabla p_i - \nu_{ie} n_i m_i (\underline{u}_i - \underline{u}_e). \tag{2.4}$$

The left-hand sides of these equations describe the rate of change of momentum of each fluid while the right hand sides give the forces acting on the fluids.

The first two terms give the change in fluid momentum due the variation of the fluid velocity in an infinitesimally-small volume. The convective derivative $(\underline{u} \cdot \nabla)\underline{u}$ accounts for the momentum carried by fluid moving in and out of this volume. The third term on the left-hand side gives the change in momentum due to any newly-created electrons or ions which are initially stationary but must be accelerated up to the velocity of the bulk fluid. This technique of ensuring that the momentum equations are satisfied in the presence of ionisation was originally introduced by Woods [167].

The first term on the right-hand side gives the electromagnetic Lorentz force due to the electric field $\underline{E}$ and magnetic field $\underline{B}$ acting on singly-charged electrons and ions of charge $-e$ and e respectively. The second term is due to variations in the isotropic electron and ion pressures, p_e and p_i, which are themselves caused by the random thermal motion of the electrons and ions. The final term accounts for the transfer of momentum between electrons and ions due to collisions with each other. The collision frequency of electrons with ions is ν_{ei} and of ions with electrons is ν_{ie}. The total momentum between the fluids must be conserved in these collisions which leads the simple relation $\nu_{ei} n_e m_e = \nu_{ie} n_i m_i$ [165, p. 203].

2.2.3 Energy equations and equations of state

The principle of the conservation of energy can also be applied to the infinitesimally-small volume of fluid in order to calculate the variation in temperature, and hence the thermal pressure, throughout the fluid. However the plasmas described by this particular two-fluid model are assumed to have separate isothermal electron and ion temperatures given by T_e and T_i respectively. The energy equations are redundant in this description of the plasma but the pressures in the momentum equations remain to be specified. If the electrons and ions are taken to behave like ideal gases then these pressures are given in terms of Boltzmann's constant k_B by the equations of state

$$p_e = n_e k_B T_e, \tag{2.5}$$

$$p_i = n_i k_B T_i. \tag{2.6}$$

2.2.4 Maxwell's equations

The electrons and ions move under the action of electric and magnetic fields which are themselves determined by Maxwell's equations. These equations form a staple of any undergraduate physics degree and are merely stated here as

$$\nabla \cdot \underline{E} = \frac{\rho_q}{\epsilon_0} = \frac{e}{\epsilon_0}(n_i - n_e), \tag{2.7}$$

$$\nabla \cdot \underline{B} = 0, \tag{2.8}$$

$$\nabla \times \underline{E} = -\frac{\partial \underline{B}}{\partial t}, \tag{2.9}$$

$$\nabla \times \underline{B} = \mu_0 \underline{j} + \frac{1}{c^2}\frac{\partial \underline{E}}{\partial t} = \mu_0 e(n_i \underline{u}_i - n_e \underline{u}_e) + \frac{1}{c^2}\frac{\partial \underline{E}}{\partial t}, \tag{2.10}$$

where $\rho_q = e(n_i - n_e)$ gives the local charge density of the plasma and $\underline{j} = e(n_i \underline{u}_i - n_e \underline{u}_e)$ is the electrical current at a point in the plasma. The constants ϵ_0, μ_0 and c are, unsurprisingly, the permittivity and permeability of free space and the speed of light which can be mutually expressed as $\epsilon_0 \mu_0 = 1/c^2$. The time-dependent part of Eq. 2.10, known as the displacement current, can be neglected when the electric field varies on timescales of typical plasma flows because of its very small $1/c^2$ factor. If the magnetic field is time invariant then the electric field can be written in terms of the electrostatic potential as $\underline{E} = -\nabla\phi$ which ensures that Eq. 2.9 is always satisfied; Eq. 2.7 then becomes the Poisson equation

$$\nabla^2\phi = \frac{e}{\epsilon_0}(n_e - n_i). \tag{2.11}$$

2.2.5 Maxwell's tensor and Poynting's vector

The plasma stress tensor is introduced in the next subsection in order to describe the forces in a plasma. An intrinsic part of this tensor is Maxwell's stress tensor which describes the electromagnetic forces on a collection of charges. Maxwell's tensor is briefly reviewed here, paraphrasing the arguments of Griffiths [168, p. 351-353], before moving on to the full plasma stress tensor.

The Lorentz force per unit volume on a collection of electrons and ions is given by

$$\underline{f}_L = \rho_q\underline{E} + \underline{j} \times \underline{B} = e\left(n_i - n_e\right)\underline{E} + e\left(n_i\underline{u}_i - n_e\underline{u}_e\right) \times \underline{B} \tag{2.12}$$

which can be expressed in terms of the fields alone by inserting Eqs. 2.7 and 2.10 to give

$$\underline{f}_L = \epsilon_0\left(\nabla\cdot\underline{E}\right)\underline{E} + \frac{1}{\mu_0}\left(\nabla\times\underline{B}\right)\times\underline{B} - \frac{1}{\mu_0 c^2}\frac{\partial\underline{E}}{\partial t}\times\underline{B}. \tag{2.13}$$

The next steps require a few algebraic tricks. The product rule is applied to the time derivative of $\underline{E}\times\underline{B}$ to give

$$\frac{\partial}{\partial t}\left(\underline{E}\times\underline{B}\right) = \frac{\partial\underline{E}}{\partial t}\times\underline{B} + \underline{E}\times\frac{\partial\underline{B}}{\partial t} \tag{2.14}$$

which can be combined with Eq. 2.9 and rearranged into the form

$$\frac{\partial\underline{E}}{\partial t}\times\underline{B} = \frac{\partial}{\partial t}\left(\underline{E}\times\underline{B}\right) + \underline{E}\times\left(\nabla\times\underline{E}\right) \tag{2.15}$$

in order to replace the last term of Eq. 2.13. The divergence-free property of the magnetic field also allows the introduction of the additional term $(\nabla\cdot\underline{B})\underline{B}$ to Eq. 2.13 and the force density follows as

$$\underline{f}_L = \epsilon_0\left[\left(\nabla\cdot\underline{E}\right)\underline{E} - \underline{E}\times\left(\nabla\times\underline{E}\right)\right] + \frac{1}{\mu_0}\left[\left(\nabla\cdot\underline{B}\right)\underline{B} - \underline{B}\times\left(\nabla\times\underline{B}\right)\right] - \frac{1}{c^2}\frac{\partial}{\partial t}\left(\frac{\underline{E}\times\underline{B}}{\mu_0}\right). \tag{2.16}$$

Next a vector calculus identity,

$$\underline{E}\times\left(\nabla\times\underline{E}\right) = \frac{1}{2}\nabla\left(E^2\right) - \left(\underline{E}\cdot\nabla\right)\underline{E} \tag{2.17}$$

together with the equivalent identity for the magnetic fields, can be used to remove the terms containing a curl. The product rule for a tensor divergence, $\nabla\cdot(\underline{\underline{EE}}) =$

$(\nabla \cdot \underline{E})\,\underline{E} + (\underline{E} \cdot \nabla)\,\underline{E}$, then allows the force density to be written in the form

$$\begin{aligned}\underline{f}_L &= \nabla \cdot \left[\epsilon_0 \left(\underline{E}\underline{E} - \frac{E^2}{2}\underline{\underline{I}}\right) + \frac{1}{\mu_0}\left(\underline{B}\underline{B} - \frac{B^2}{2}\underline{\underline{I}}\right)\right] - \frac{1}{c^2}\frac{\partial}{\partial t}\left(\frac{\underline{E} \times \underline{B}}{\mu_0}\right) \\ &= \nabla \cdot \underline{\underline{M}} - \frac{1}{c^2}\frac{\partial \underline{S}}{\partial t}. \end{aligned} \tag{2.18}$$

where $\underline{\underline{I}}$ is the identity matrix and the tensor product of, for example, the electric field vectors, $\underline{E} = (E_x, E_y, E_z)$, is

$$\underline{E}\underline{E} = \begin{pmatrix} E_x^2 & E_xE_y & E_xE_z \\ E_xE_y & E_y^2 & E_yE_z \\ E_xE_z & E_yE_z & E_z^2 \end{pmatrix}. \tag{2.19}$$

The right-hand side of Eq. 2.18 reveals two parts of the electromagnetic force on the collection of charges. The second term describes the momentum flux of any time-varying electromagnetic fields in terms of the Poynting vector $\underline{S} = (\underline{E} \times \underline{B})/\mu_0$; the presence of the $1/c^2$ factor often allows this term to be neglected on the timescales associated with the plasma motion. The first term gives the electromagnetic forces due to the instantaneous arrangement of the collection of charges together with any externally-applied fields. This is the divergence of Maxwell's stress tensor $\underline{\underline{M}}$.

2.2.6 The plasma stress tensor

The full form of the plasma stress tensor can now be derived. A similar derivation is provided by Landau and Lifshitz for what they call the "momentum flux density tensor" of a neutral and inviscid fluid [161, p. 11]. The plasma stress tensor, which is simply the sum of Maxwell's tensor for the electromagnetic stresses and Landau and Lifshitz's tensor for the stresses in the electron and ion fluids, is derived as follows.

The left-hand side of the electron momentum equation, Eq. 2.3, is rewritten using the result

$$\begin{aligned}\frac{\partial}{\partial t}\left(m_e n_e \underline{u}_e\right) + \nabla \cdot \left(m_e n_e \underline{u}_e \underline{u}_e\right) &= m_e n_e \frac{\partial \underline{u}_e}{\partial t} + m_e \underline{u}_e \left[\frac{\partial n_e}{\partial t} + \nabla \cdot \left(n_e \underline{u}_e\right)\right] + m_e n_e \left(\underline{u}_e \cdot \nabla\right) \underline{u}_e \\ &= m_e n_e \frac{\partial \underline{u}_e}{\partial t} + m_e n_e s \underline{u}_e + m_e n_e (\underline{u}_e \cdot \nabla)\underline{u}_e \end{aligned} \tag{2.20}$$

which is easily obtained by using the product rule followed by a substitution of the electron continuity equation for the term in square brackets. The same relation also applies to the left-hand side of the ion momentum equation. The electron and ion momentum equations are then summed to produce

$$\begin{aligned}&\frac{\partial}{\partial t}\left(m_e n_e \underline{u}_e + m_i n_i \underline{u}_i\right) + \nabla \cdot \left(m_e n_e \underline{u}_e \underline{u}_e + m_i n_i \underline{u}_i \underline{u}_i\right) \\ &\qquad = e\left(n_i - n_e\right)\underline{E} + e\left(n_i \underline{u}_i - n_e \underline{u}_e\right) \times \underline{B} - \nabla\left(p_e + p_i\right). \end{aligned} \tag{2.21}$$

The elimination of the electron-ion collision terms is unsurprising given that momentum must be conserved in these collisions. The first two terms on the right-hand side of this expression can be identified immediately as the sum of the divergence of the Maxwell stress tensor and the Poynting momentum flux described by Eq. 2.18. The Poynting flux can often be neglected as noted in Sec. 2.2.5. Furthermore, the pressure terms can be replaced by the divergence of a diagonal tensor and a rearrangement of the resulting expression yields an equation for the conservation of momentum of the entire plasma as

$$\frac{\partial}{\partial t}\left(m_e n_e \underline{u}_e + m_i n_i \underline{u}_i\right) = \nabla \cdot \left[\underline{\underline{M}} - m_e n_e \underline{u}_e \underline{u}_e - m_i n_i \underline{u}_i \underline{u}_i - \left(p_e + p_i\right) \underline{\underline{I}}\right]. \tag{2.22}$$

This equation is essentially an embellished form of Newton's second law for the two-fluid description of a plasma. The term on the left-hand side represents the rate of change of momentum per unit volume of the plasma [161, p. 11] so the right-hand side is identified as the force per unit volume, *i.e.* force density $\underline{f}_p$, on the plasma. The term in the square brackets is the plasma stress tensor which has the full form

$$\underline{\underline{\sigma}} = \epsilon_0 \left(\underline{E}\underline{E} - \frac{E^2}{2}\underline{\underline{I}}\right) + \frac{1}{\mu_0}\left(\underline{B}\underline{B} - \frac{B^2}{2}\underline{\underline{I}}\right) - m_e n_e \underline{u}_e \underline{u}_e - m_i n_i \underline{u}_i \underline{u}_i - \left(p_e + p_i\right) \underline{\underline{I}}. \tag{2.23}$$

This stress contains three main parts: the electromagnetic Maxwell stresses, the ram pressures due to the bulk flows of electron and ions, and the thermal pressures caused by random motion of the electrons and ions. The simple expression of the forces in a plasma in terms of the divergence of the plasma stress tensor makes it vital for calculating the forces on surfaces, both solid and liquid, in contact with plasmas. Furthermore the left-hand side of Eq. 2.22 is zero for a steadily-flowing plasma and the resulting conservation equation for the stress tensor, $\underline{f}_p = \nabla \cdot \underline{\underline{\sigma}} = \underline{0}$, can be useful for calculating the profiles of these time-invariant plasma flows. The diagonal symmetry of the stress tensor also allows a conservation equation for angular momentum, $\underline{r} \times \underline{f}_p = \nabla \cdot (\underline{r} \times \underline{\underline{\sigma}})$, to be derived.

2.2.7 Electron Boltzmann relation

A few simple assumptions allow a significant simplification of the electron momentum equation to be made. The negligible mass of the electron allows the inertia, source and collision terms to be ignored and if the fields are purely electrostatic then $\underline{E} = -\nabla\phi$. Inserting these approximations, together with the electron equation of state Eq. 2.5, into the electron momentum equation gives $k_B T_e \nabla n_e = e n_e \nabla \phi$ which is easily integrated to find the electron Boltzmann relation

$$n_e = n_0 \exp\left(\frac{e\phi}{k_B T_e}\right) \tag{2.24}$$

where n_0 is the electron density at $\phi = 0$. The assumptions which lead to this expression are clearly not applicable to a number of cases and care must be taken in its use [169]. The inclusions of the magnetic field and the electron ram pressure terms in the plasma stress tensor are clearly incompatible with the the Boltzmann relation approximation.

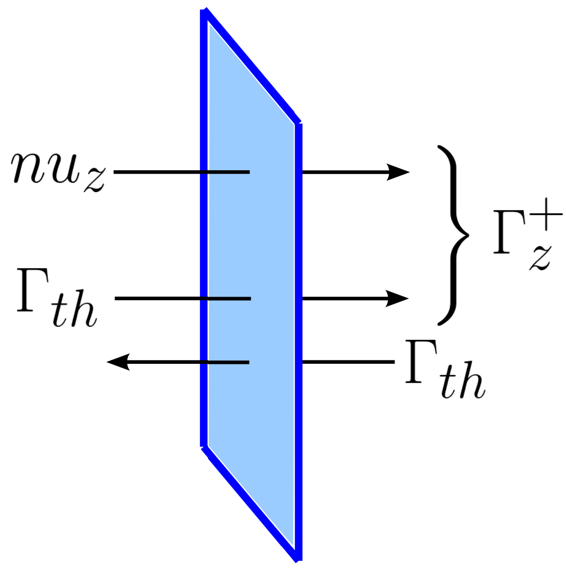

Figure 2.2: Illustration of the one-way flux of particles across a surface. The thermal flux, Γ_{th}, is due to the random motion of particles and is balanced by an equal thermal flux in the opposite direction when the plasma is in equilibrium. However the thermal flux, together with the bulk flow, must both be included in the total one-way flux.

2.2.8 One-way thermal fluxes

A surface in contact with a plasma provides a sink for the electrons and ions in the plasma. The strength of the sink is determined by the total number of particles flowing into it so a calculation of the one-way particle flux, *i.e.* the number of particles crossing a surface in one direction per unit area of that surface, is required when modelling plasma-surface interactions. This one-way flux must include the thermal flux of particles across the surface, as illustrated by Fig. 2.2, which would be balanced by an equal thermal flux in the opposite direction if no absorbing surface were present. Information about the distributions of electron and ion velocities $f_e(\underline{x}, \underline{v})$ and $f_i(\underline{x}, \underline{v})$, which have thus far been neglected in the fluid equations, must therefore be included.

The following derivation of the one-way flux is given for electrons but can be applied to ions by swapping the e subscripts for i. The surface is taken, without loss of generality, to have its normal in the z-direction so that the incremental flux of electrons crossing the surface with velocities in the element $d^3\underline{v}$ is $d\Gamma_{ez} = v_z f_e(\underline{x}, \underline{v}) d^3\underline{v}$. An integration over all velocities with positive z-components then gives the one-way flux as

$$\Gamma_{ez}^+ = \int_{-\infty}^{\infty} dv_x \int_{-\infty}^{\infty} dv_y \int_0^{\infty} \left[v_z f_e(\underline{x}, \underline{v})\right] dv_z. \tag{2.25}$$

If the electron distribution function is assumed to be a drifting Maxwellian with average velocity $\underline{u}_e$,

$$f_{Me}(\underline{x}, \underline{v}) = n_e\left(\underline{x}\right) \left(\frac{m_e}{2\pi k_B T_e}\right)^{3/2} \exp\left[-\frac{k_B T_e (\underline{v} - \underline{u}_e)^2}{2m_e}\right], \tag{2.26}$$

then the one-way flux is evaluated as [170]

$$\Gamma_{ez}^{+} = n_e \left\{ \left(\frac{k_B T_e}{2\pi m_e} \right)^{1/2} \exp\left(-\frac{m u_{ez}^2}{2k_B T_e} \right) + \frac{u_{ez}}{2} + \frac{u_{ez}}{2} \operatorname{erf}\left[u_{ez} \left(\frac{m_e}{2k_B T_e} \right)^{1/2} \right] \right\}. \quad (2.27)$$

where $\operatorname{erf}(x)$ denotes the error function.

Two limiting cases of this expression for the one-way particle fluxes are particularly prevalent in this thesis. Boltzmann electrons are described by a stationary Maxwellian particle distribution where the thermal motion of the particles far exceeds their average bulk motion and hence $u_{ez} \ll (k_B T_e/m_e)^{1/2}$. The first term of Eq. 2.27 becomes dominant in this limit so the one-way flux of Boltzmann electrons is

$$\Gamma_{e,Boltz} = n_e \left(\frac{k_B T_e}{2\pi m_e} \right)^{1/2} = n_0 \left(\frac{k_B T_e}{2\pi m_e} \right)^{1/2} \exp\left(\frac{e\phi}{k_B T_e} \right) \quad (2.28)$$

where Eq. 2.24 has been used to express n_e in terms of the exponential Boltzmann factor. On the other hand cold ions are described by a distribution where the thermal motion of ions is negligible compared to their bulk motion so that the distribution tends towards a delta-function. This limit is given by $u_{iz} \gg (k_B T_i/m_i)^{1/2}$ so the one-way cold-ion flux follows from the last two terms of Eq. 2.27 as $n_i u_{iz}$.

2.2.9 Dimensionless summary of two-fluid plasma equations

The fluid equations and plasma stress tensor can be expressed in dimensionless form in order to reduce the number of free parameters in the equations and to assist in finding their solutions. This procedure also provides a convenient place to summarise the two-fluid plasma equations. The variable conversions are summarised in Table 2.1 in terms of the electron Debye length

$$\lambda_D = \left(\frac{\epsilon_0 k_B T_e}{n_0 e^2} \right)^{1/2} \quad (2.29)$$

and the cold-ion sound speed

$$c_s = \left(\frac{k_B T_e}{m_i} \right)^{1/2}. \quad (2.30)$$

The continuity equations, Eqs. 2.1 and 2.2, become

$$\frac{\partial N_e}{\partial \tau} + \nabla \cdot (N_e \underline{U}_e) = N_e S, \quad (2.31)$$

$$\frac{\partial N_i}{\partial \tau} + \nabla \cdot (N_i \underline{U}_i) = N_e S, \quad (2.32)$$

Table 2.1: Summary of the dimensional and dimensionless variables used in the two-fluid plasma model.

Variable name	Dimensional symbol	Dimensionless symbol	Relation
Position	$\underline{x}$	$\underline{X}$	$\underline{x} = \lambda_D \underline{X}$
Time	t	τ	$t = \frac{\lambda_D}{c_s}\tau$
Electron/ion velocity	$\underline{u}_{e,i}$	$\underline{U}_{e,i}$	$\underline{u}_{e,i} = c_s \underline{U}_{e,i}$
Electron/ion number density	$n_{e,i}$	$N_{e,i}$	$n_{e,i} = n_0 N_{e,i}$
Electrostatic potential	ϕ	Φ	$\phi = \frac{k_B T_e}{e}\Phi$
Electric field	$\underline{E}$	$\underline{F}$	$\underline{E} = \frac{k_B T_e}{e\lambda_D}\underline{F}$
Magnetic field	$\underline{B}$	$\underline{\beta}$	$\underline{B} = \frac{m_i c_s}{\lambda_D e}\underline{\beta}$
Ionisation frequency	s	S	$s = \frac{c_s}{\lambda_D} S$
Electron-ion collision frequency	ν_{ei}	$\mathcal{N}_{ei}$	$\nu_{ei} = \frac{c_s}{\lambda_D}\mathcal{N}_{ei}$
Plasma stress tensor	$\underline{\underline{\sigma}}$	$\underline{\underline{\Sigma}}$	$\underline{\underline{\sigma}} = n_0 k_B T_e \underline{\underline{\Sigma}}$
Ion-to-electron mass ratio	$\frac{m_i}{m_e}$	μ	$\mu = \frac{m_i}{m_e}$
Ion-to-electron temperature ratio	$\frac{T_i}{T_e}$	Θ	$\Theta = \frac{T_i}{T_e}$
One-way electron/ion flux	$\Gamma^+_{e,i}$	$\gamma^+_{e,i}$	$\Gamma^+_{e,i} = n_0 c_s \gamma^+_{e,i}$

where ∇ now indicates differentiation with respect to the dimensionless spatial coordinates. The momentum equations, Eqs. 2.3 and 2.4, become

$$N_e \frac{\partial \underline{U}_e}{\partial \tau} + N_e(\underline{U}_e \cdot \nabla)\underline{U}_e + N_e S \underline{U}_e = -\mu N_e(\underline{F} + \underline{U}_e \times \underline{\beta}) - \mu \nabla N_e - \mathcal{N}_{ei} N_e(\underline{U}_e - \underline{U}_i), \tag{2.33}$$

$$N_i \frac{\partial \underline{U}_i}{\partial \tau} + N_i(\underline{U}_i \cdot \nabla)\underline{U}_i + N_e S \underline{U}_i = N_i(\underline{F} + \underline{U}_i \times \underline{\beta}) - \Theta \nabla N_i - \frac{\mathcal{N}_{ei}}{\mu} N_e(\underline{U}_i - \underline{U}_e). \tag{2.34}$$

where the ideal gas equations of state have been used to rewrite the pressure terms and the ion-electron collision frequency has been replaced by using $\nu_{ei} n_e m_e = \nu_{ie} n_i m_i$. The dimensionless form of the electron Boltzmann relation is

$$N_e = \exp(\Phi). \tag{2.35}$$

Gauss's law, Eq. 2.7, and Ampère's law without the displacement current, Eq. 2.10

without the second term, also become

$$\nabla \cdot \underline{F} = (N_i - N_e), \tag{2.36}$$

$$\nabla \times \underline{\beta} = \frac{c_s^2}{c^2}(N_i\underline{U}_i - N_e\underline{U}_e) \tag{2.37}$$

respectively where $\underline{F} = -\nabla\Phi$. The rate of change of momentum of the plasma, Eq. 2.22, is given by

$$\frac{\partial}{\partial\tau}\left(\frac{N_e\underline{U}_e}{\mu} + N_i\underline{U}_i\right) = \nabla \cdot \underline{\underline{\Sigma}} \tag{2.38}$$

where the dimensionless plasma stress tensor, Eq. 2.23, is

$$\underline{\underline{\Sigma}} = \underline{F}\underline{F} - \frac{F^2}{2}\underline{\underline{I}} + \frac{c^2}{c_s^2}\left(\underline{\beta}\underline{\beta} - \frac{\beta^2}{2}\underline{\underline{I}}\right) - \frac{N_e\underline{U}_e\underline{U}_e}{\mu} - N_i\underline{U}_i\underline{U}_i - (N_e + N_i)\,\underline{\underline{I}} \tag{2.39}$$

and where the pressures have once again been expressed in terms of densities according to the ideal gas equations of state. The condition $\nabla\cdot\underline{\underline{\Sigma}} = \underline{0}$ for time-invariant plasmas is referred to as the stress continuity condition. Finally the dimensionless one-way fluxes of electrons and ions in the positive z-direction are given by

$$\gamma_{ez}^{+} = N_e\left\{\left(\frac{\mu}{2\pi}\right)^{1/2}\exp\left(-\frac{U_{ez}^2}{2\mu}\right) + \frac{U_{ez}}{2} + \frac{U_{ez}}{2}\,\mathrm{erf}\left[\frac{U_{ez}}{(2\mu)^{1/2}}\right]\right\}, \tag{2.40}$$

$$\gamma_{iz}^{+} = N_i\left\{\frac{1}{(2\pi)^{1/2}}\exp\left(-\frac{U_{iz}^2}{2\Theta}\right) + \frac{U_{iz}}{2} + \frac{U_{iz}}{2}\,\mathrm{erf}\left[\frac{U_{iz}}{(2\Theta)^{1/2}}\right]\right\}. \tag{2.41}$$

These expressions can be replaced by

$$\gamma_{e,Boltz}^{+} = \left(\frac{\mu}{2\pi}\right)^{1/2}\exp\left(\Phi\right), \tag{2.42}$$

$$\gamma_{i,T_i=0}^{+} = N_iU_{iz} \tag{2.43}$$

for Boltzmann electrons and cold ions respectively.

2.3 Fluid description of a liquid

The previous sections has reviewed a two-fluid description of a plasma based on coexisting and mutually interacting electron and ion fluids. A liquid, unsurprisingly, can also be described as a fluid. This fluid is much simpler than the plasma fluids especially when the liquid is taken to be conducting and incompressible. A slight complication is the inclusion of viscous forces and this is handled after introducing the incompressibility condition.

2.3.1 Incompressible liquids

The continuity equation of a liquid, by analogy with Eq. 2.1, is

$$\frac{\partial \rho}{\partial t} + \nabla \cdot (\rho \underline{v}) = 0 \tag{2.44}$$

where ρ and $\underline{v}$ are the density and velocity of the liquid and where dimensional units are used. The zero on the right-hand side indicates that there are no sources or sinks of liquid. All of the liquids considered in this thesis are incompressible so that ρ is a constant; this allows a reduction of the continuity equation to

$$\nabla \cdot \underline{v} = 0 \tag{2.45}$$

which is named the incompressibility condition.

2.3.2 Viscous stresses

The momentum equation of a liquid, by analogy with Eq. 2.3, is

$$\rho \frac{\partial \underline{v}}{\partial t} + \rho \left(\underline{v} \cdot \nabla \right) \underline{v} = -\nabla p + \nabla \cdot \underline{\underline{\tau}} + \rho \underline{g} + \underline{j} \times \underline{B} \tag{2.46}$$

where p is the pressure, $\underline{\underline{\tau}}$ is the viscous stress tensor, $\underline{g}$ is the acceleration due to gravity and $\underline{j} \times \underline{B}$ is the Lorentz force due to any current density $\underline{j}$ flowing in the conducting liquid. This momentum equation differs from the plasma case due to the absence of sources and sinks of liquid and of electric forces which are expelled from the conducting liquid. However it includes a gravitational term, due to the relatively high mass density of liquids compared to plasmas, and viscous forces which are given by the divergence of the viscous stress tensor.

The viscous components of the stress tensor were first deduced by Stokes based upon three assumptions:

1. The viscous stress is a linear function of the velocity gradients such as $\partial v_x/\partial y$, $\partial v_y/\partial x$ and so on. This is the defining property of Newtonian fluids.

2. The viscous stresses vanish if there is no deformation of the fluid.

3. The stress tensor is isotropic since the fluid properties have no preferred direction.

An appropriate combination of velocity gradients is given by $\partial v_x/\partial y + \partial v_y/\partial x$ as demonstrated by Acheson with the following example [164, p. 209-210]. Consider a steadily-rotating flow around the z-axis with angular velocity $\underline{\omega} = \omega \underline{\hat{z}}$ such that $\underline{v} = \omega \underline{\hat{z}} \times \underline{x}$ and hence $v_x = -\omega y$ and $v_y = \omega x$. The velocity gradients are simply $\partial v_x/\partial y = -\omega$ and $\partial v_y/\partial x = \omega$. There is no stretching or shrinking involved in this liquid flow; therefore Stokes' second assumption states that the viscous stresses much vanish and hence $\partial v_x/\partial y + \partial v_y/\partial x = 0$ is identified as a suitable linear combination of velocity gradients.

Note that this expression is invariant under $x \leftrightarrow y$ so that Stokes' third assumption is also satisfied. The full stress tensor follows as

$$\tau_{ij} = \eta \left(\frac{\partial v_i}{\partial x_j} + \frac{\partial v_j}{\partial x_i} \right) \tag{2.47}$$

where the constant of proportionality η is the viscosity of the liquid.

2.3.3 Momentum equations

Taking the divergence of the viscous stress tensor, in combination with the incompressibility condition Eq. 2.45, yields the simple result $\nabla \cdot \underline{\underline{\tau}} = \eta \nabla^2 \underline{u}$. Inserting this into Eq. 2.47 produces the Navier-Stokes momentum equation

$$\rho \frac{\partial \underline{v}}{\partial t} + \rho \left(\underline{v} \cdot \nabla \right) \underline{v} = -\nabla p + \eta \nabla^2 \underline{u} + \rho \underline{g} + \underline{j} \times \underline{B}. \tag{2.48}$$

The momentum equation may alternatively be expressed in a conservative form, by analogy with Eq. 2.22, as

$$\frac{\partial}{\partial t} \left(\rho \underline{v} \right) = \nabla \cdot \underline{\underline{\tau}}' + \rho \underline{g} = \underline{f}_l. \tag{2.49}$$

The tensor $\underline{\underline{\tau}}'$ includes the ram and thermal pressures and the viscous and magnetic stresses in the liquid and takes the form

$$\underline{\underline{\tau}}' = -\rho \underline{v}\underline{v} - p \underline{\underline{I}} + \underline{\underline{\tau}} + \frac{1}{\mu_0} \left(\underline{B}\underline{B} - \frac{B^2}{2} \underline{\underline{I}} \right). \tag{2.50}$$

This version of the momentum equation is particularly useful for considering the continuity of stress across a plasma-liquid interface which is the focus of the final section of this chapter. Note that the gravitational force is a body force which cannot be written in terms of a divergence[1].

2.4 Boundary conditions at the plasma-liquid interface

So far this chapter has introduced fluid equations which describe the motion of plasmas and liquids but has provided little additional material compared to standard textbooks on these topics. However the coupling of these two sets of fluid equations is an entirely new subject and is the focus of the final section of this chapter. Some simple boundary conditions for electrically-conducting liquids are discussed before moving on to the more interesting stress continuity condition across the interface.

2.4.1 Parameterisation and motion of the interface

The z-coordinates of the interface which separates the plasma and liquid regions is given by a time-varying height function as $z = \xi(x, y, t)$ with the plasma assumed to occupy

[1] Actually the forces in a self-gravitating mass of fluid can be expressed in terms of a stress tensor but this is of no use for laboratory-based fluids where gravity is imposed externally by the Earth's mass.

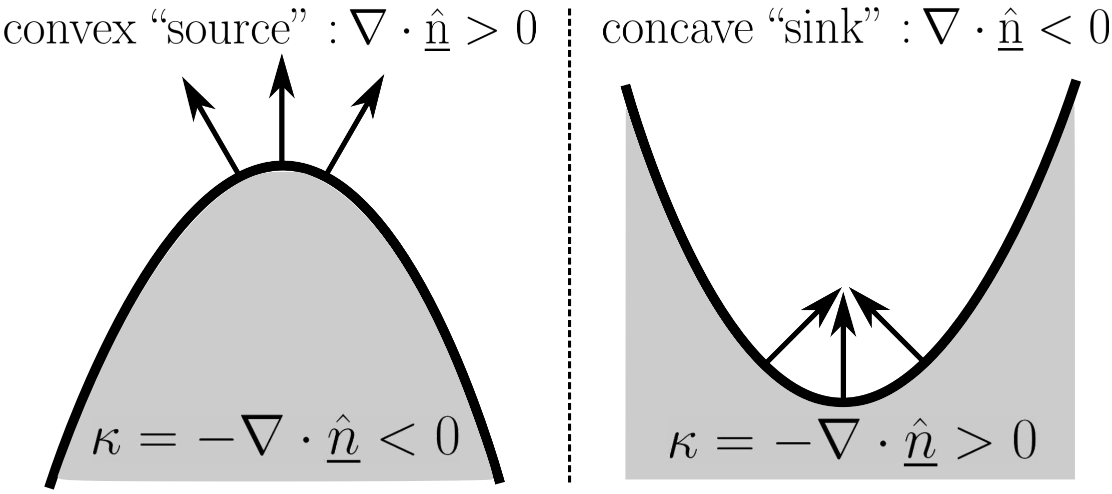

Figure 2.3: An illustration of the curvature of convex and concave surfaces. Convex surfaces are, effectively, sources of normal vectors so that $\nabla \cdot \underline{\hat{n}} > 0$ and hence $\kappa < 0$. The surface tension force, $\underline{f}_s = \gamma\kappa\underline{\hat{n}}$, therefore acts in the reverse direction to $\underline{\hat{n}}$ so that it tends to pull the surface flat. The opposite is true for concave surfaces: $\underline{f}_s$ aligns with $\underline{\hat{n}}$ so, once again, the surface is pulled flat.

the region $z > \xi$ while the liquid occupies $z < \xi$. The unit normal to this interface, which points towards the plasma, is calculated using

$$\underline{\hat{n}} = \left[\underline{\hat{z}} - \frac{\partial \xi}{\partial x}\underline{\hat{x}} - \frac{\partial \xi}{\partial y}\underline{\hat{y}}\right]\left[1 + \left(\frac{\partial \xi}{\partial x}\right)^2 + \left(\frac{\partial \xi}{\partial y}\right)^2\right]^{-\frac{1}{2}}. \tag{2.51}$$

The curvature of the surface is essential for calculating the surface tension force and is given by $\kappa = -\nabla \cdot \underline{\hat{n}}$ which is negative for convex surfaces and positive for concave surfaces as illustrated by Fig. 2.3.

The height function, ξ, is coupled to the motion of the liquid region by the surface convection condition [162, p. 7]

$$\frac{\partial \xi}{\partial t} + v_{x,z=\xi}\frac{\partial \xi}{\partial x} + v_{y,z=\xi}\frac{\partial \xi}{\partial y} = v_{z,z=\xi}. \tag{2.52}$$

The surface provides a sink for the plasma so no equivalent boundary condition exists in terms of the plasma fluid velocities.

2.4.2 Electromagnetic boundary conditions

If the surface is assumed to be a perfect conductor then its surface forms an equipotential surface. The electric field in the plasma region must by perpendicular to this surface so that

$$\underline{\hat{n}} \times \underline{E}_{z=\xi^+} = \underline{0} \tag{2.53}$$

where ξ^+ indicates that the boundary condition applies to the plasma side of the surface. The electric field inside the conducting liquid is, of course, zero.

If a magnetic field is present then its boundary conditions are found by integrating the Maxwell equations $\nabla \cdot \underline{B} = 0$ and $\nabla \times \underline{B} = \mu_0 \underline{j}$ across the surface using the divergence theorem and Stokes' theorem respectively. This process yields the conditions

$$\hat{\underline{n}} \cdot \left[\underline{B}_{z=\xi^+} - \underline{B}_{z=\xi^-}\right] = 0, \tag{2.54}$$

$$\hat{\underline{n}} \times \left[\underline{B}_{z=\xi^+} - \underline{B}_{z=\xi^-}\right] = \mu_0 \underline{j}_{surf}, \tag{2.55}$$

where $\underline{j}_{surf}$ is the current flowing in a microscopic layer on the surface of the liquid. Plasma-liquid interactions in magnetic fields are considered only briefly in this thesis and these boundary conditions are stated here principally for the sake of completeness.

2.4.3 Pressure jump condition

The well-known Young-Laplace equation gives a pressure jump, *i.e.* a jump in the force per unit area in the normal direction, of $\gamma\kappa$ where γ is the surface tension coefficient. This is converted to a body force per unit volume with the use of a δ-function as [171]

$$\underline{f}_s = \gamma\kappa\delta(z - \xi)\hat{\underline{n}} \tag{2.56}$$

where $\delta(z-\xi)$ is zero everywhere except for at the plasma-liquid interface. The definition of curvature as $\kappa = -\nabla \cdot \hat{\underline{n}}$ ensures that the surface tension force tends to pull the surface flat as indicated by Fig. 2.3. The body force per unit volume of plasma has already been derived in Sec. 2.2.6 as $\underline{f}_p = \nabla \cdot \underline{\underline{\sigma}}$ in terms of dimensional units; the equivalent force density in the liquid region is given by $\underline{f}_l = \nabla \cdot \underline{\underline{\tau}}' + \rho\underline{g}$ with $\underline{\underline{\tau}}'$ defined by Eq. 2.50.

Consider the balance of forces on a small surface element of the plasma-liquid interface. A very small control volume can be constructed which encloses the interface, as depicted in Fig. 2.4, and the conservation of momentum in this volume gives

$$\int_{V\to 0} \frac{\partial}{\partial t}\left(\rho\underline{v} + m_e n_e \underline{u}_e + m_i n_i \underline{u}_e\right) dV = \int_{V\to 0} \left(\underline{f}_p + \underline{f}_l + \underline{f}_s\right) dV \tag{2.57}$$

and inserting the expressions for each of the force densities produces

$$\begin{aligned}\int_{V\to 0} \left[\frac{\partial}{\partial t}\left(\rho\underline{v} + m_e n_e \underline{u}_e + m_i n_i \underline{u}_e\right) - \rho\underline{g}\right] dV &= \int_{V\to 0} \left[\nabla \cdot \underline{\underline{\sigma}} + \nabla \cdot \underline{\underline{\tau}}' + \gamma\kappa\delta(z - \xi)\hat{\underline{n}}\right] dV \\ &= \int_{\xi^+} \underline{\underline{\sigma}} \cdot \hat{\underline{n}} dS - \int_{\xi^-} \underline{\underline{\tau}}' \cdot \hat{\underline{n}} dS + \int_{\xi} \gamma\kappa\hat{\underline{n}} dS.\end{aligned} \tag{2.58}$$

The first two terms in the final expression have been converted into surface integrals using the divergence theorem while the third term used an integration over the δ function. The surface integral on the liquid side of the interface, as denoted by ξ^-, is negative because the surface normal of the control volume is anti-aligned with the normal to the plasma-surface interface. Note that the plasma stress tensor is not present in the liquid region and, likewise, the liquid pressure vanishes in the plasma region.

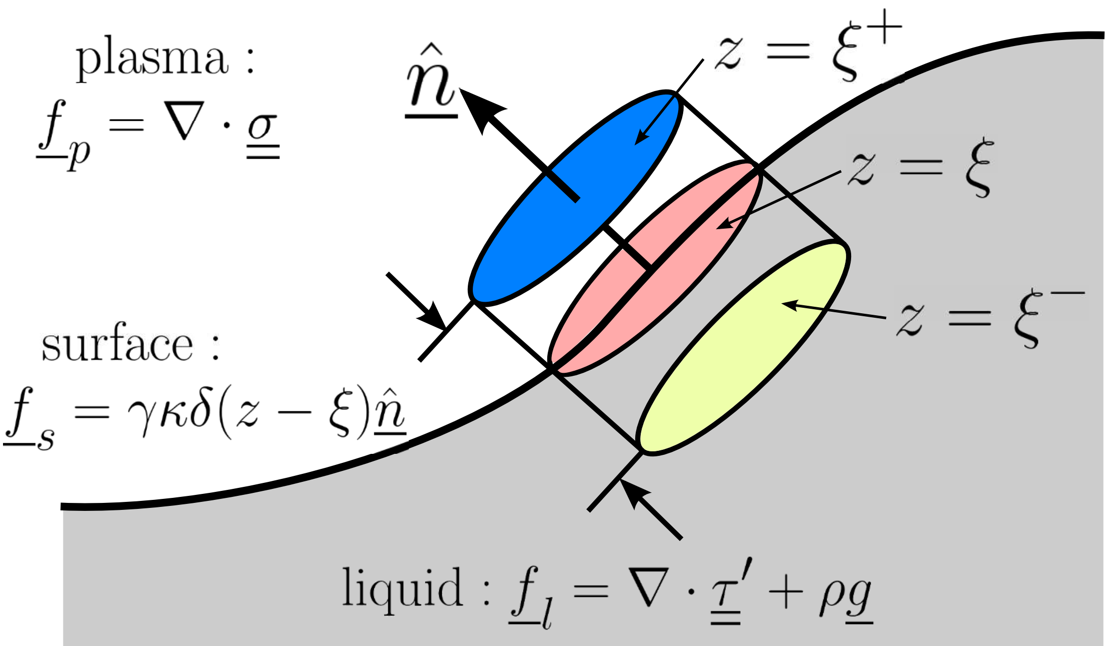

Figure 2.4: An illustration of the control surface for calculating the pressure jump across a plasma-liquid interface. The control surface is shrunk in the direction perpendicular to the surface so that its volume tends to zero while its surface area remains finite. In this limit the surfaces at ξ, ξ^+ and ξ^- become identical and stresses must be continuous across them.

The control volume is now shrunk in the direction perpendicular to the surface so that its volume tends to zero and, accordingly, the volume integral on the left-hand side of Eq. 2.58 disappears. However the surface remains of finite, but very small, extent so the surface integrals do not vanish. Instead the surfaces at ξ, ξ^+ and ξ^- become identical so that the three individual integrands must sum to zero and hence

$$\hat{\underline{n}} \cdot \left[\underline{\underline{\sigma}} - \underline{\underline{\tau}}'\right]_{z=\xi} + \gamma\kappa\hat{\underline{n}} = \underline{0}. \tag{2.59}$$

Finally the scalar product of this expression can be taken with the normal vector in order to produce the pressure jump condition (*cf.* [161, p. 241])

$$\hat{\underline{n}} \cdot \left[\underline{\underline{\sigma}} - \underline{\underline{\tau}}'\right]_{z=\xi} \cdot \hat{\underline{n}} + \gamma\kappa = 0 \tag{2.60}$$

although the pressure terms are, for now, hidden away inside the stress tensors. A shear stress balance across the interface can also be obtained by taking the scalar product of Eq. 2.59 with a unit vector in a tangential direction to the surface.

The pressure jump condition can be expanded in terms of the explicit fluid variables of the plasma and liquid. Making the simplifications of no magnetic fields or viscosity gives the pressure jump condition as

$$\left[\frac{\epsilon_0 E^2}{2} - m_e n_e \left(\underline{u}_e \cdot \hat{\underline{n}}\right)^2 - m_i n_i \left(\underline{u}_i \cdot \hat{\underline{n}}\right)^2 - p_e - p_i + \rho \left(\underline{v} \cdot \hat{\underline{n}}\right)^2 + p\right]_{z=\xi} + \gamma\kappa = 0. \tag{2.61}$$

The ram pressure of the electrons is much smaller than the ions, because $m_e \ll m_i$, so this term can be ignored. Furthermore the ram pressure of the liquid can be shown to be negligible, under typical conditions, by making a Galilean (non-relativistic) transform into a frame moving with the interface at velocity $(\underline{v} \cdot \hat{\underline{n}})\hat{\underline{n}}$. Most of the terms in the pressure jump equation are unchanged except for the liquid ram pressure, which vanishes in this frame of reference, and the ion ram pressure which becomes $-m_i n_i[(\underline{u}_i - \underline{v}) \cdot \hat{\underline{n}}]^2$. Characteristic velocities of the ions and liquid are given by their sound speeds which are on the order of 10 km s^{-1} and 1 km s^{-1} respectively. In fact the ions are accelerated towards the surface in a layer known as the electrostatic sheath, which is discussed in the next chapter, and hence move significantly faster than their sound speed; meanwhile the deformation rate of the liquid surface is unlikely to approach its sound speed without causing shocks and breakup of the surface. The approximation $|\underline{u}_i| \gg |\underline{v}|$ is therefore valid and the liquid velocity is ignored. In the unlikely circumstance that the plasma-liquid interface moves at speeds approaching the plasma sound speed then the ram pressure of the liquid must be included. After these considerations the liquid pressure at its interface with the plasma becomes

$$p_{z=\xi} = \left[m_i n_i \left(\underline{u}_i \cdot \hat{\underline{n}} \right)^2 + p_e + p_i - \frac{\epsilon_0 E^2}{2} \right]_{z=\xi} - \gamma \kappa \tag{2.62}$$

or, in dimensionless plasma units,

$$p_{z=\xi} = n_0 k_B T_e \left[N_i \left(\hat{\underline{n}} \cdot \underline{U}_i \right)^2 + N_e + \Theta N_i - \frac{F^2}{2} \right]_{z=\xi} - \gamma \kappa. \tag{2.63}$$

2.5 Concluding remarks

This chapter has reviewed the basic fluid theory of plasmas and liquids and has established some boundary conditions which apply at plasma-liquid interfaces. The remainder of this thesis simply takes the fundamental equations given in this chapter and solves them in various different geometries: Chapter 4 focusses on the behaviour of initially-flat liquid surfaces while Chapter 5 examines the deformation and breakup of droplets in plasmas. However, before calculating the dynamic motion of these plasma-liquid interfaces, it is useful to begin by tackling some simpler problems involving plasma interactions with non-deformable objects. The subject of plasma interactions with surfaces of fixed shape is itself a diverse and evolving subject which the next chapter examines in detail.

3 Plasma behaviour near surfaces and objects

Langmuir's observation of a highly-charged region at a plasma-surface boundary was one of the earliest discoveries in plasma science [172]. He named this region the sheath. The sheath contains a large electric field which draws ions out of the plasma in order to give an equal flux of ions and electrons, which move much faster than the ions, to the plasma-facing surface. Any credible theory of plasma-liquid interactions must account for the large electric fields and particle fluxes of sheath region; yet previous studies of plasma-liquid interactions have, broadly, neglected their role. The purpose of this chapter is to remedy this oversight by examining the behaviour of a plasma in the vicinity of a surface or droplet. The significance of sheath formation and charge accumulation, and their implications for plasma-liquid interactions, is highlighted.

3.1 Sheaths

3.1.1 The Bohm (planar) sheath

Possibly the simplest example of a plasma-surface interaction involves a perfectly-flat surface with the electrons described by the Boltzmann relation and the ion fluid having zero temperature. The plasma flow is taken to be time-independent and there are no sources of, or collisions between, electrons and ions. This model yields simple but powerful results such as the Bohm criterion for the formation of a charged sheath region between the surface and the quasineutral bulk plasma. As such this model provides a firm foundation for studying plasmas in the vicinity of surfaces with complex geometries which arise in plasma-liquid interactions. The relevant two-fluid plasma equations are

$$\frac{d\Phi}{dZ} = -F_z, \tag{3.1}$$

$$\frac{d}{dZ}\left(N_i U_{iz}\right) = 0, \tag{3.2}$$

$$N_i U_{iz} \frac{dU_{iz}}{dZ} - N_i F_z = 0, \tag{3.3}$$

$$\frac{d}{dZ}\left[\frac{F_z^2}{2} - N_i U_{iz}^2 - \exp\left(-\Phi\right)\right] = 0, \tag{3.4}$$

which are the electrostatic gradient condition, the ion continuity equation, Eq. 2.32, the ion momentum equation, 2.34, and the one-dimensional stress conservation equation, $d\Sigma_{zz}/dZ = 0$ with Σ_{zz} given by Eq. 2.39, respectively. The planar geometry of the problem means that the vector quantities contain z-components only and all of the parameters vary with respect to Z only. A surface is placed in the $Z = 0$ plane which absorbs electrons and ions from the plasma which occupies the $Z > 0$ region. The rapid motion of the electrons, being of both smaller mass and higher thermal energy than the ions, causes an accumulation of negative charge on the surface. The upstream boundary conditions are given by a quasineutral plasma far away from the surface where $\Phi = 0$, $F_z = 0$, $N_i = 1$ and $U_{iz} = U_0$. These boundary conditions ensure that $N_i = N_e$ in the quasineutral bulk plasma.

3.1.1.1 The Bohm criterion

The equations are solved as follows: the ion continuity equation integrates to $N_i U_{iz} = U_0$ while the ion momentum equation, together with the electrostatic gradient condition, integrates to $U_{iz}^2/2 + \Phi = U_0^2/2$. Inserting these expressions into the stress continuity equation then yields

$$\frac{F_z^2}{2} - U_0^2 \left(1 - \frac{2\Phi}{U_0^2}\right)^{1/2} - \exp\left(\Phi\right) = -U_0^2 - 1. \tag{3.5}$$

This equation was first described as a "stress balance" by Allen [173]. The potential profile is calculated by numerically integrating F_z with respect to Z. However a much more profound result can be obtained analytically with a power-series expansion in terms of Φ at $\Phi \approx 0$ which gives

$$\frac{F_z^2}{2} - U_0^2 \left(1 - \frac{\Phi}{U_0^2} - \frac{\Phi^2}{2U_0^4}\right) - 1 - \Phi - \frac{\Phi^2}{2} + \mathcal{O}\left(\Phi^3\right) = -U_0^2 - 1 \tag{3.6}$$

and hence

$$\frac{F_z^2}{2} \approx \left(1 - \frac{1}{U_0^2}\right)\frac{\Phi^2}{2}. \tag{3.7}$$

This equation can only be satisfied when the term in brackets is positive. The speed of the plasma, at a large distance from the surface, is therefore given by $U_0^2 \geq 1$ or, in dimensional terms by reference to Table 2.1,

$$|u_i|_{\phi=0} \geq c_s = \left(\frac{k_B T_e}{m_i}\right)^{1/2}. \tag{3.8}$$

This is the renowned **Bohm criterion** [174] for the formation of a charged sheath region between the quasineutral bulk plasma and the surface. In physical terms it means that the ions must enter the sheath region with enough speed to maintain a surplus of positive charge in the sheath. If ions entered the sheath at less than the ion sound speed then Eq. 3.7 would give an imaginary, *i.e.* oscillatory, solution for the electrostatic potential which is incompatible with the quasineutral upstream boundary conditions [175].

3.1.1.2 The presheath and equality Bohm condition

The calculation of a Bohm sheath assumes that the electrostatic potential is measured from $\Phi = 0$ at the boundary between the quasineutral plasma and the sheath. The ions must enter the sheath at the Bohm speed; hence they must be accelerated before they enter the sheath through an additional potential drop. This quasineutral ion-accelerating region is known as the presheath [175].

It can be shown that the quasineutrality of a presheath can only be maintained while $U_{iz}^2 < 1$ as per the following example. Consider a one-dimensional, quasineutral, cold-ion, Boltzmann-electron plasma with ionisation. Quasineutrality means that the ion density satisfies the electron Boltzmann relation, $N_i = N_e = \exp(\Phi)$ so the electric force on the ions can be rewritten using $dN_i/dZ = N_i d\Phi/dZ$. The ion momentum equation, Eq. 2.34, therefore becomes

$$N_i U_{iz} \frac{dU_{iz}}{dZ} + N_i S U_{iz} = -\frac{dN_i}{dZ}. \tag{3.9}$$

Combining this with the continuity equation, $d(N_i U_{iz})/dZ = N_i S$, yields an equation for the ion velocity,

$$\frac{dU_{iz}}{dZ} = \frac{1 + U_{iz}^2}{1 - U_{iz}^2} S, \tag{3.10}$$

which is singular at $U_{iz}^2 = 1$. The assumption of quasineutrality breaks down if the ions exceeds the ion sound speed. Matching the Bohm condition with the presheath quasineutrality condition gives the equality form of the Bohm criterion, $U_0^2 = 1$, at the plasma-sheath edge. This result is unaffected by the addition of inter-particle collisions and magnetic fields [176].

The width of the ionising presheath can be found by solving Eq. 3.10 with the initial condition $U_{iz} = 0$ at $Z = 0$. This yields the implicit solution

$$Z = \frac{2 \tan^{-1}(U_{iz}) - U_{iz}}{S} \tag{3.11}$$

and the presheath-sheath boundary is identified from $U_{iz} = 1$ as

$$Z = \frac{\pi - 2}{2S} \approx \frac{0.571}{S}. \tag{3.12}$$

Therefore the presheath width is inversely proportional to the ionisation rate.

The acceleration of ions in the presheath can occur due to alternative processes such as geometric focussing of ions onto spherical surfaces or collisions between electrons and ions [175]. The geometric presheath is considered in more detail in Sec. 3.2.1.

3.1.1.3 The floating wall condition

Thus far the surface has been asserted to be negatively-charged. This is easily shown for an electrically-isolated surface by equating the one-way fluxes of Boltzmann electrons and cold ions, given by Eqs. 2.42 and 2.43, into the surface at $z = 0$ to give the floating wall condition

$$[-N_i U_{iz}]_{z=0} = \left(\frac{\mu}{2\pi}\right)^{1/2} \exp(\Phi_{Z=0}) \tag{3.13}$$

with $\mu = m_i/m_e$ as specified in Table 2.1. The ion flux is constant throughout the sheath, according to the continuity equation, and is evaluated as $N_i U_{iz} = -1$ by using the equality form of the Bohm criterion. The floating wall condition rearranges to give the floating wall potential as

$$\Phi_{Z=0} = \frac{1}{2} \ln\left(\frac{2\pi}{\mu}\right). \tag{3.14}$$

The electron mass is always much smaller than the ion mass so $\mu \gg 2\pi$ and the logarithm always produces negative surface potentials. For example hydrogen has $m_i = m_p$, where m_p is the mass of a single proton, and hence $\Phi_{Z=0} = -2.839$. The floating wall potentials for other commonly used plasma ions are indicated on Fig. 3.1.

3.1.1.4 One-dimensional sheath profiles

The potential profile in the Bohm sheath must be calculated numerically despite the simplicity of the model. This calculation is easily performed by applying a shooting method to the stress balance equation, Eq. 3.5, which is rearranged after application of the equality form the the Bohm criterion, $U_0^2 = 1$, to give

$$\frac{d\Phi}{dZ} = -F_z = \left[2\left(1 - 2\Phi\right)^{1/2} + 2\exp\left(\Phi\right) - 4\right]^{1/2} \tag{3.15}$$

where F_z is taken to be so that ions are accelerated towards the wall. The integration starts with a specified potential at the wall and shoots outwards into the plasma region. The resulting potential profiles are plotted in Fig. 3.1 for the floating wall potentials of hydrogen, helium, nitrogen, argon and xenon plasmas. These profiles are all identical except for a shift to the left or right which ensures that the floating wall condition is satisfied. The potentials approach zero asymptotically as $Z \to \infty$ so, in theory at least, the plasma-sheath transition is located an infinite distance from the surface. However almost all of the potential drop occurs within $10\lambda_D$ of the surface.

3.1.2 Two-dimensional sheath profiles

The planar geometry of the Bohm sheath is a mathematical luxury which is often inapplicable to real-world situations. Plasma-liquid interactions, in particular, lead to highly-deformed surfaces with complex geometries. The numerical calculation of the sheath profile around a nonplanar surface protrusion is considered briefly in preparation for the later sections on modelling plasma-liquid interactions. The plasma is still taken to be composed of cold ions and Boltzmann electrons but the surface is no longer perfectly flat. However the sheath profile adjacent to a nearly-planar surface still appears to be one-dimensional at a large distance from the surface; the Bohm criterion therefore remains applicable in the asymptotic limit $Z \to \infty$ which corresponds to the plasma-sheath edge. A simple power-series expansion of Eq. 3.15 at the sheath edge allows the

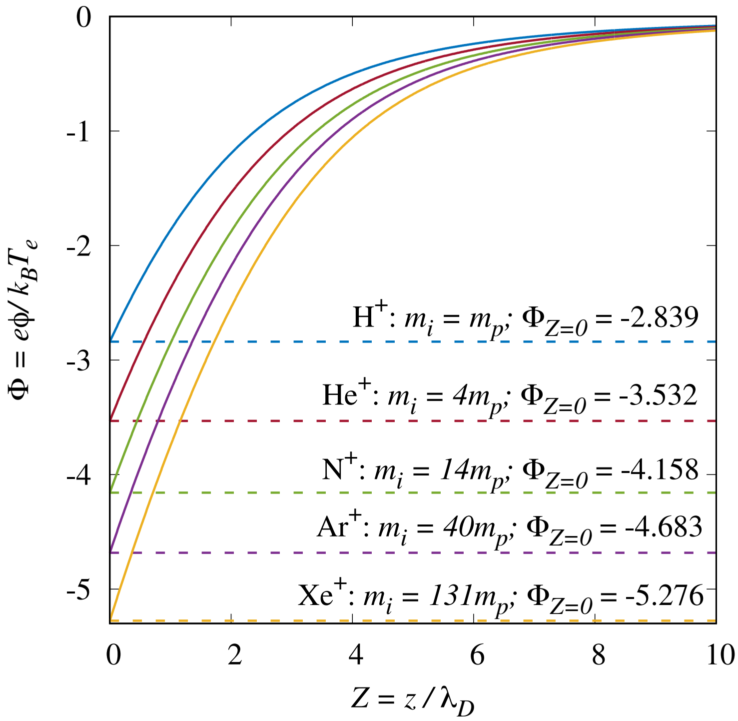

Figure 3.1: Variation of the electrostatic potential through a one-dimensional Bohm sheath. The solutions are identical except for a transposition to the left or right to ensure that the floating wall potential is satisfied at $Z = 0$.

asymptotic boundary conditions to be applied at a finite distance from the surface and thereby facilitates numerical simulations of the sheath.

The series expansion of Eq. 3.15 at $\Phi = 0$ yields

$$\frac{d\Phi}{dZ} \approx \left(\frac{2}{3}\right)^{1/2} (-\Phi)^{3/2} \tag{3.16}$$

which may be integrated and rearranged to give

$$(-\Phi)^{1/2} \approx \frac{2}{(2/3)^{1/2} Z + C} \tag{3.17}$$

where C is the constant of integration. The Bohm condition gives $\Phi = 0$ when $Z \to \infty$ so the constant of integration is zero. The approximate potential at the sheath edge follows as

$$\Phi \approx -\frac{6}{Z^2} \tag{3.18}$$

which is valid provided that $-\Phi \ll 1$. The sheath-edge boundary conditions for the ion

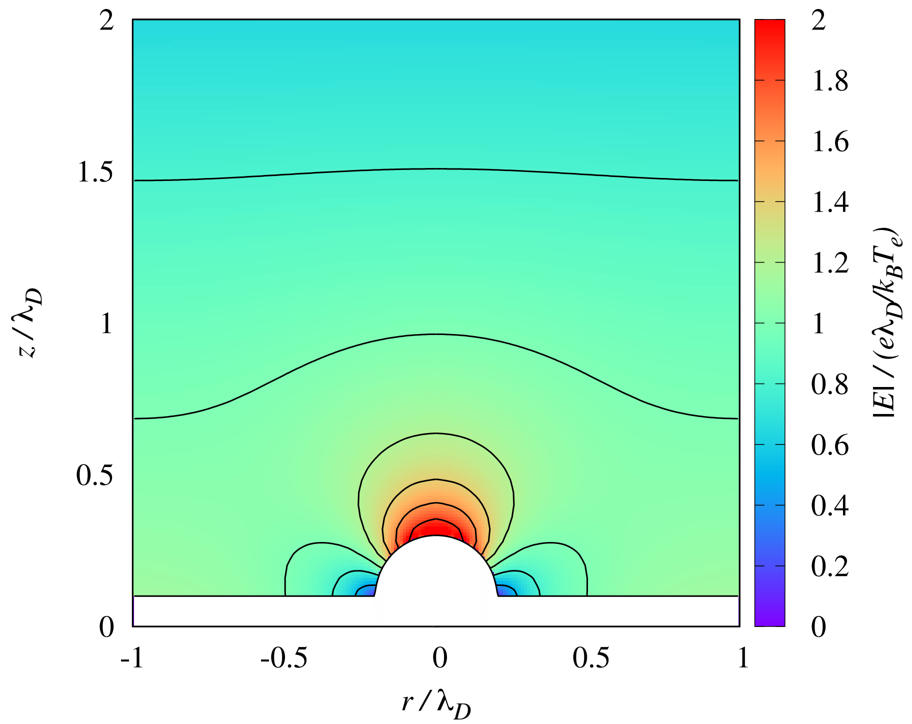

Figure 3.2: Variation in electric field strength through a two-dimensional sheath near a hemispherical protrusion (from Ref. [177]). The simulation is enabled by a power-series expansion of the stress balance equation which provides the upstream sheath-edge boundary conditions.

velocity and density are given by conservation of energy and particle number as

$$U_{iz} = -\left(1-2\Phi\right)^{1/2} \approx -1+\Phi \approx -1-\frac{6}{Z^2}, \tag{3.19}$$

$$N_i = -\frac{1}{U_{iz}} \approx 1+\Phi \approx 1-\frac{6}{Z^2}. \tag{3.20}$$

The numerical calculation of a nonplanar sheath profile can now be performed on a computational domain of finite extent. Equations 3.18-3.20 provide upstream boundary conditions for the cold-ion, Boltzmann-electron fluid equations

$$\frac{\partial N_i}{\partial \tau} + \nabla\cdot(N_i\underline{U}_i) = 0, \tag{3.21}$$

$$\frac{\partial \underline{U}_i}{\partial \tau} + (\underline{U}_i\cdot\nabla)\underline{U}_i = -\nabla\Phi, \tag{3.22}$$

$$\nabla^2\Phi = \exp\left(\Phi\right) - N_i. \tag{3.23}$$

which originate from Eqs. 2.32, 2.34 and 2.36 respectively. Time derivatives are retained in these equations as a numerical device which allows the system to relax to its equilibrium steady state. A code which solves Eqs. 3.21–3.23 in cylidrical (r-z) coordinates is described in full detail in Ref. [177]; a brief overview of the workings of this code is provided as follows for all but the most inquisitive readers.

The values taken by the continuous fluid variables in Eqs. 3.21–3.23 can only be stored at a finite number of points by the computer. Values of the fluid variables are stored on a regular grid, with uniform spacings in the r and z directions, using a staggered arrangement with N_i and Φ specified at the centres of cells and the components of $\underline{U}_i$ given at the edges of cells. This arrangement suppresses non-physical grid-scale oscillations [178, p. 26–27]. Spatial derivatives can be calculated straightforwardly from the differences in values between neighbouring cells; this code uses a second-order upwind scheme for these spatial derivatives. Boundary conditions along the $r = 0$ axis are imposed by cylindrical symmetry as $\partial/\partial r = 0$ and $U_{ir} = 0$. Simulations of the sheath region use the asymptotic conditions, Eqs. 3.18-3.20, for the sheath edge but only the electric potential needs to be specified at the plasma-facing surface due to the upwind discretisation of N_i and $\underline{U}_i$. If the surface is nearly-planar and the outer edge is far away from any nonplanar features then the conditions $\partial/\partial r = 0$ and $U_{ir} = 0$ also apply at the outer radial edge of the simulation.

Time must also be treated in a discrete manner. Equations 3.21 and 3.22 provide values of $\partial N_i/\partial \tau$ and $\partial N_i/\partial \tau$ which are used to calculate new values of the fluid variables on the grid after a short interval of time has passed. This time-stepping is performed using the forward Euler method and the size of the time step is altered dynamically to ensure that the Courant-Friedrichs-Lewy (CFL) condition is satisfied [177]. Finally, at each moment in time, the instantaneous electric potential must be calculated from Eq. 3.21 which is solved using a simple overrelaxation method. The new fluid variables can then be used to perform another short step into the future, which provides further new values to make an additional step, and so on until each variable reaches a steady value.

An example of the electric field profile in a sheath near a hemispherical protrusion, as obtained using the numerical method as described above, is displayed in Fig. 3.2. The upstream sheath-edge boundary conditions, Eqs. 3.18-3.20, are applied at $Z = 20$. The electric field strength is, unsurprisingly, enhanced near the apex of the sphere by a factor of 1.91; the equivalent enhancement factor for a protrusion in a vacuum field is exactly 3 [179]. In real-world plasma-surface interactions this enhancement in electric field can cause field-induced emission of electrons from the surface [180] which, in turn, could lead to the formation of damaging arcs or hotspots on the plasma-facing surface. Alternatively, when the surface is a liquid, the enhancement of the electric field near small perturbations can drive electrohydrodynamic instabilities of the liquid surface; these instabilities are discussed in detail later in this thesis.

3.2 Dust and droplets in unmagnetised plasmas

The sheaths considered so far have been restricted to near-planar geometries and must be extended to spherical geometry in order to properly describe droplets in plasmas. This section considers two models of plasma interactions with spherical objects: the first applies the cold-ion model of the previous section to objects in plasmas while the second accounts for non-zero ion temperatures in a collisionless plasma model.

3.2.1 Spherical sheaths: Allen-Boyd-Reynolds theory

The solution of the cold-ion, Boltzmann-electron model in the vicinity of a spherical absorbing object was first presented by Allen, Boyd and Reynolds (ABR) [181] but the following description follows the methodical treatment of Kennedy and Allen [182]. This non-planar case allows the formation of a quasineutral presheath of finite width even in the absence of ionisation. The original ABR model considered individual ions rather than a continuous ion fluid but the streamlines of a cold-ion fluid are identical to the ion trajectories; these two alternative concepts therefore reduce to the same mathematical formulation.

If the surface of the sphere is located, in dimensionless units, at $R = A = a/\lambda_D$ then the floating condition $\gamma_{ir}^{-}|_A = \gamma_{er}^{-}|_A$, using the one-way fluxes in Eqs. 2.42 and 2.43, gives the balance of particle fluxes as

$$(N_i U_{ir})_A = \left(\frac{\mu}{2\pi}\right)^{1/2} \exp\left(\Phi_A\right) \tag{3.24}$$

where the subscript A indicates that the quantities are evaluated at the surface of the sphere. Integration of the time-independent, source-free ion continuity equation in spherical coordinates, $\nabla \cdot (N_i \underline{U_i}) = 0$, reveals that $N_i U_i R^2$ is a conserved quantity which, by comparison with the floating condition, gives

$$N_i U_{ir} = \frac{A^2}{R^2}\left(\frac{\mu}{2\pi}\right)^{1/2} \exp\left(\Phi_A\right). \tag{3.25}$$

Integration of the ion momentum equation implies that the quantity $U_{ir}^2/2 + \Phi$, *i.e.* the ion energy, is also conserved. The ions are assumed to be at rest where $\Phi = 0$ so that $U_{ir} = (-2\Phi)^{1/2}$. Inserting the expressions for the ion density and velocity and the Boltzmann electron density into Gauss's law produces the differential equation

$$\frac{1}{R^2}\frac{d}{dR}\left(R^2 F_r\right) = \frac{A^2}{R^2}\left[\frac{\mu}{4\pi(-\Phi)}\right]^{1/2} \exp\left(\Phi_A\right) - \exp\left(\Phi\right). \tag{3.26}$$

The numerical solution of this equation, together with $d\Phi/dR = -F_r$, requires two boundary conditions. These are provided by the assumption of quasineutrality far from the sphere where the left-hand side of Eq. 3.26 is far smaller than either of the terms on the right and hence

$$\frac{A^2}{R^2}\left[\frac{\mu}{4\pi(-\Phi)}\right]^{1/2} \exp\left(\Phi_A\right) \approx \exp\left(\Phi\right). \tag{3.27}$$

A recent revisitation of the ABR theory by Thomas [183] showed that the quasineutrality condition can be expressed explicitly in terms of R as

$$\Phi \approx \frac{1}{2} W_0 \left[-\frac{\mu A^4 \exp\left(2\Phi_A\right)}{2\pi R^4}\right] \tag{3.28}$$

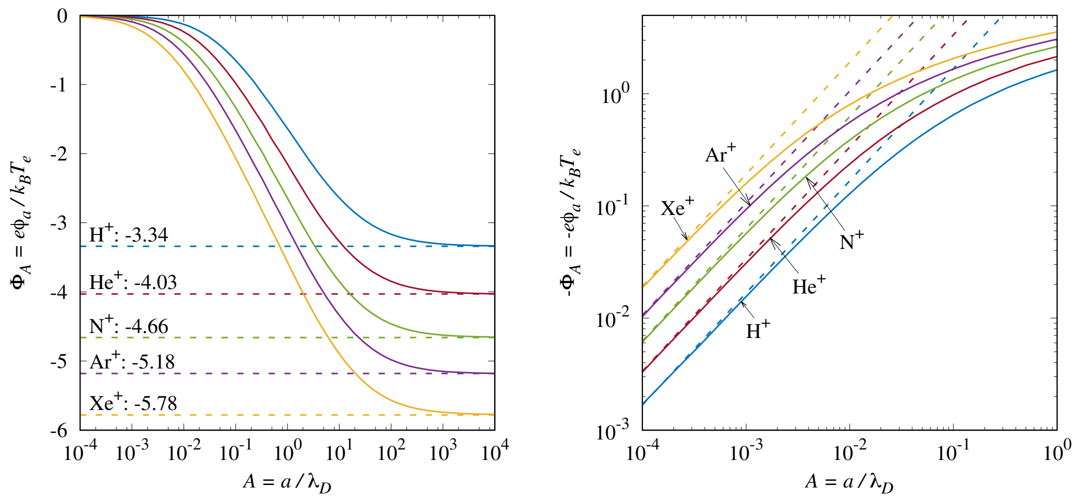

Figure 3.3: The floating potentials of various spherical surfaces as calculated by the Allen-Boyd-Reynolds theory on log-linear axes (left) and log-log axes (right). The floating potentials of very large spheres are given by the combined potential drop across a planar sheath and collisionless presheath according Eq. 3.31 while the small-sphere potentials are given by the asymptotic limit in Eq. 3.32.

where $W_0(z')$ is the principal branch of the Lambert W function of z' [184]. The second boundary condition can be found by differentiation[1] as

$$F_r = -\frac{d\Phi}{dR} \approx \frac{4\Phi}{R(1+2\Phi)}. \tag{3.29}$$

These boundary conditions present two minor difficulties: the outer radius at which they should be applied has not yet been specified and they are dependent on the potential of the sphere Φ_A which is *a priori* unknown. The first issue is resolved by comparing Eq. 3.26 with the quasineutrality condition $|n_i - n_e| \ll n_e \approx n_i$ which shows that an appropriate outer radius is [183]

$$R_{out} = \max\left[\left(\frac{4\mu A^4}{\pi}\right)^{1/4} \exp\left(\frac{1}{32} + \frac{\Phi_A}{2}\right), 2\right]. \tag{3.30}$$

The second issue is negated by constructing an iterative numerical scheme which seeks out the unique value of Φ_A which exists for each combination of μ and A. An initial trial value of Φ_A is used to provide boundary conditions for Poisson's equation, Eq. 3.26, which is integrated towards the surface of the sphere using a shooting method. If the integration finds that the potential at the sphere's surface is different to the trial value Φ_A then this trial value is modified. This procedure is repeated for the new trial value in order to determine whether this, too, requires updating and so on until a self-consistent value of Φ_A is obtained.

[1] By using the formula for differentiating $W_0(z')$: $\dfrac{dW_0(z')}{dz'} = \dfrac{W_0(z')}{z'[1+W_0(z')]}$.

The results of the calculation of Φ_A are displayed in Fig. 3.3 for various values of μ and A. These results reproduce those of Kennedy and Allen [182] and Thomas [183]. The potentials of the spheres tends to the total potential drop across a planar plasma sheath and collisionless presheath,

$$\Phi_A = \frac{1}{2} \ln \left(\frac{2\pi}{\mu} \right) - \frac{1}{2}, \tag{3.31}$$

as given by Eq. 3.14 with the additional $\Delta\Phi = 0.5$ which is required to accelerate the ions to the Bohm speed in the presheath. This large-sphere limit is exactly as expected since very large spheres ($a \gg \lambda_D$) appear, from the perspective of the nearby plasma, to be planar in much the same way that the surface of the Earth appears to be flat when viewed from close to ground level. The opposite limit was tackled by Arinaminpathy, Allen and Ockendon who used a method of matched asymptotic expansions to obtain small-sphere limit [185]

$$\Phi_A \approx -0.98 \frac{a}{\lambda_D} \left(\frac{m_i}{2\pi m_e} \right)^{1/2} = -0.98 A \left(\frac{\mu}{2\pi} \right)^{1/2} \tag{3.32}$$

where credit is due to Thomas for unpacking their nested doll of normalisations [186]. This limit is indicated by the dashed lines in the log plot in the right panel of Fig. 3.3 and is in excellent agreement with the numerical solutions as $A \to 0$. The numerical solutions for these small spheres are slightly tricky to obtain because the quasineutrality of the plasma at the outer radius where the integration is started from is almost *too* good and the differences between the ion and electron densities becomes comparable to the floating-point computational error. Thomas describes some improved boundary conditions which allow the calculation of these small-sphere surface potentials [183] while the solutions obtained here used a third-order total variation diminishing integration scheme, as specified in Ref. [187], in order to ensure smooth potential profiles.

3.2.2 Drag force on an object in a plasma

The ABR theory describes a stationary object in a plasma but the cold-ion, Boltzmann-electron equations, Eqs. 3.21-3.23, can be applied to a two-fluid plasma flowing around a sphere and solved numerically, for the first time, using the method described in Sec. 3.1.2. The boundary conditions are provided by a small-Φ perturbation to the cold-ion, Boltzmann-electron equations for a steadily-flowing quasineutral plasma with speed $-U_f$ in the z-direction. The numerically-determined plasma flow pattern can then be used, together with the plasma stress tensor, to determine the net force on a spherical object in a plasma; this drag force is crucial for determining the motion and transport of dust grains and droplets in, for example, tokamak [60] and interstellar [188] plasmas.

The electrostatic potential profile around a sphere of radius λ_D at its floating potential in a supersonic plasma flow of velocity $\underline{u}_f = -2c_s\hat{\underline{z}}$ is shown in Fig. 3.4. The panel on the left shows the potential throughout the full computational domain while the image

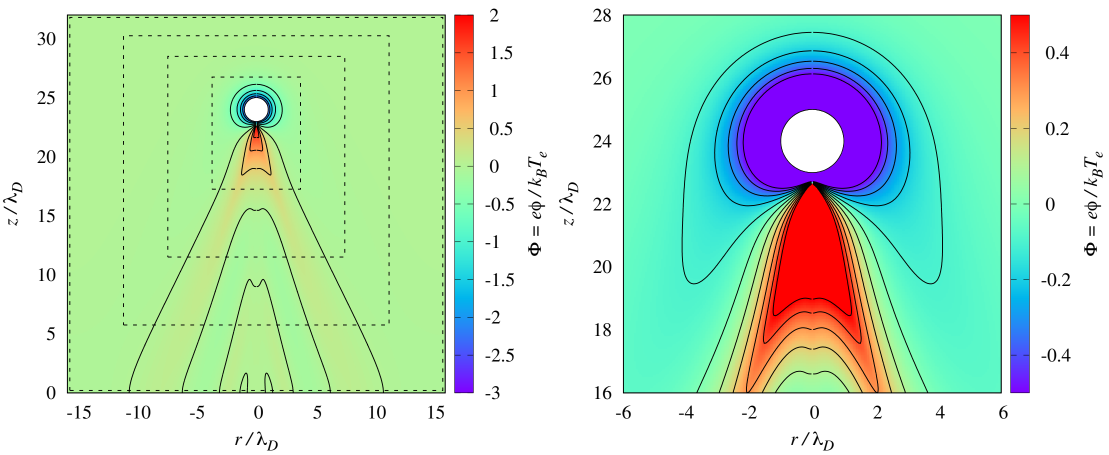

Figure 3.4: The electrostatic potential distribution around a sphere of radius λ_D at floating potential and in a hydrogen plasma flowing at a supersonic velocity of $\underline{u}_f = -2c_s\hat{\underline{z}}$ far away from the sphere.

on the right focusses on the region close to the sphere. The most striking feature of these images is the appearance of a series of nested cones downstream from the object. The ions are initially focussed towards a region immediately behind the sphere by the negative charge on the sphere; this positively-charged region then repels ions and attracts electrons and therefore induces a negatively-charged region downstream which subsequently induces another positively-charged region and so on. This oscillatory wake behaviour behind dust grains, including the nested-cone structure, has been observed before in PIC simulations of Debye-scale dust grains [189, 190]. The apex of the cones is also positioned immediately behind the dust grain in accordance with these PIC simulations. The qualitative reproduction of kinetic PIC results by the two-fluid model is quite reassuring, considering the coarse assumptions of cold ions and Boltzmann electrons, and vindicates its use in modelling plasma-surface interactions. The fluid model has several advantages over PIC and kinetic methods such as smooth solutions and relatively short computational runtimes [177].

The image on the left of Fig. 3.4 also features a number of dashed rectangles which correspond, in the cylindrical coordinates of the simulation, to cylinders which enclose the spherical object. These cylinders are "control surfaces" [191] on which the drag force on the sphere, and the ion current to the sphere, can be calculated. The total ion current through a surface which encloses the sphere is

$$I_i = en_0c_s\lambda_D^2 \oint N_i\underline{U}_i \cdot d\underline{S} \tag{3.33}$$

where the surface element is normalised to a squared Debye length. Application of the divergence theorem to this surface integral gives a volume integral over $\nabla \cdot (N_i\underline{U}_i)$ which is zero in the plasma region due to the ion continuity equation; the integral therefore reduces to the current through the surface of the sphere for any control surface which encloses the sphere. The electron current at the surface of the sphere is given by the one-way flux of Boltzmann electrons, Eq. 2.42, as

$$I_e = -4\pi e n_0 c_s \lambda_D^2 A^2 \left(\frac{\mu}{2\pi}\right)^{1/2} \exp\left(\Phi_A\right) \tag{3.34}$$

where A and Φ_A are the normalised radius and potential of the sphere.

The floating potential of the sphere is obtained when $I_i + I_e = 0$ which is determined within the simulation by evolving the charging equation $dQ_A/dt = I_i + I_e$, where Q_A is the charge of the sphere, to its equilibrium value. The equivalent equation for the dimensionless potential of the sphere is obtained by making the slightly dubious assumption that the sphere has a vacuum capacitance. The resulting equation is

$$\begin{aligned} \frac{d\Phi_A}{d\tau} &= \frac{1}{4\pi\epsilon_0 A\lambda_D}\frac{e}{k_B T_e}\frac{\lambda_D}{c_s}\frac{dQ_A}{dt} \\ &= \frac{1}{2A}\int R\left(N_i U_{ir}\underline{\hat{r}} + N_i U_{iz}\underline{\hat{z}}\right)\cdot d\underline{L} - A\left(\frac{\mu}{2\pi}\right)^{1/2}\exp\left(\Phi_A\right), \end{aligned} \tag{3.35}$$

where $\underline{L}$ is a line in R-Z space which begins and ends on axis at $Z = 0$ and encloses the sphere. The potential of the sphere is updated using this equation at each time step of the simulation so that, after a long simulation time, the sphere settles at its floating potential. The assumption that the sphere has a vacuum capacitance does not affect the final value of the floating potential but only the time taken to reach this value.

The drag force on a sphere can be calculated from the volume integral of the divergence of the plasma stress tensor as

$$\frac{\underline{D}}{n_0 k_B T_e \lambda_D^2} = -\int \left(\nabla\cdot\underline{\underline{\Sigma}}\right) dV = -\oint \underline{\underline{\Sigma}}\cdot d\underline{S} \tag{3.36}$$

where the drag force $\underline{D}$ retains its dimensions of $n_0 k_B T_e \lambda_D^2$. The minus sign arises because it is the force on the sphere, rather than the plasma, that is being considered. The z-component of the drag force is therefore given by

$$\frac{D_z}{n_0 k_B T_e \lambda_D^2} = -\left(\oint \underline{\underline{\Sigma}}\cdot d\underline{S}\right)\cdot\underline{\hat{z}} = -2\pi\int R\left(\Sigma_{rz}\underline{\hat{r}} + \Sigma_{zz}\underline{\hat{z}}\right)\cdot d\underline{L} \tag{3.37}$$

where the final expression follows from the cylindrical symmetry of the system and the stress tensor components, from Eq. 2.39, are

$$\Sigma_{zz} = \frac{F_z^2 - F_r^2}{2} - N_i U_{iz}^2 - \exp\left(\Phi\right), \tag{3.38}$$

$$\Sigma_{rz} = F_r F_z - N_i U_{ir} U_{iz}. \tag{3.39}$$

The stress continuity equation $\nabla\cdot\underline{\underline{\Sigma}} = \underline{0}$ means that the calculation of the drag force should yield exactly the same result for any surface enclosing the grain when the plasma is flowing steadily. This result is entirely analogous to the ion current as discussed above and was exploited in Allen's control surface approach to calculating the ion drag force on

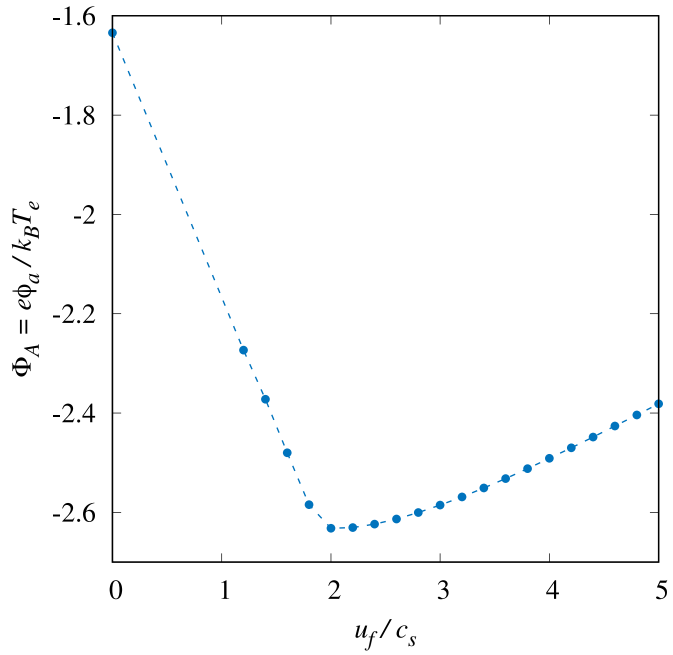

Figure 3.5: Floating potentials of Debye-radius spheres in flowing hydrogen plasmas. The supersonic values are calculated using the control surface approach while the stationary value is from the Allen-Boyd-Reynolds theory.

a sphere in a quasineutral plasma flow [191]. The control surface approach is particularly valuable for calculating the charging and drag of highly-deformed objects such as liquid drops in strong plasma flows; however the simpler example of spheres is presented here.

The ion current and drag force have been calculated for the sphere in the plasma flow of $\underline{u}_f = -2c_s\hat{\underline{z}}$ shown in Fig. 3.4. The four control surfaces are chosen as cylinders which align with the computational grid thereby eliminating the need for interpolation between cells. The values of the total dimensionless ion current, $I_i/en_0c_s\lambda_D^2$, are calculated as 15.38, 15.45, 15.48 and 15.55 for each surface moving from the inner to the outer surface respectively. The ion current is therefore conserved to around one-hundredth of a percent which is solely due to the numerical error of the simulation. The dimensionless drag forces, $D_z/n_0k_BT_e\lambda_D^2$, are 35.44, 35.37 and 35.42 on the outer three surfaces, with mutual error of only 0.2%. However the innermost surface has a dimensionless drag of 36.05, just under 2% larger than the other values. The main contribution to this numerical error appears to be due to the discretisation of the electric field in the wake behind the grain.

The floating potentials of spheres with Debye-length radii have been determined for various plasma flow speeds and are displayed in Fig. 3.5. The second closest control surface to the sphere, as shown in Fig. 3.4, is used in the calculation of the ion current. The boundary conditions used here are only valid for fast-flowing plasmas, where any velocity perturbations at the edge of the simulation domain are small and satisfy $U_1 \ll U_f$, but an additional point has been added for a stationary sphere according to the

Allen-Boyd-Reynolds theory. A smooth, albeit generously interpolated, transition from the floating potentials of stationary to supersonic spheres is observed.

The ion current and drag force are dependent on both the plasma flow speed and the floating potential of the sphere; the latter quantity is itself also dependent on the flow speed. It is therefore informative to isolate the dependence of the ion current and drag force on the flow speed by fixing the potential of the sphere. This calculation has direct practical applications to electrically-biased spherical probes rather than isolated dust grains and droplets. Figure 3.6 shows the dimensionless ion current to the sphere, as calculated on the second-innermost control surface in Fig. 3.4, for spheres with Debye-length radii and various surface potentials and plasma flow speeds. The solid lines indicate the expected ion current in the high-velocity regime according to Nitter[2] [192, Eq. 27]

$$\frac{I_i}{en_0 c_s \lambda_D^2} = \pi A^2 U_f \left(1 - \frac{2\Phi_A}{U_f^2}\right) \qquad \text{for} \qquad U_f^2 \geq -2\Phi_A. \tag{3.40}$$

This formula was obtained with a grazing orbit calculation which used the conservation of ion energy and angular momentum in a spherically-symmetric potential in order to determine which ions are collected on the sphere. The control surface calculations are in good qualitative agreement with Nitter's formula with both predicting a minimum in the ion current at around $U_f \sim 2$. However Eq. 3.40 quantitatively underestimates the ion currents to charged spheres and hence will predict more negatively charged floating potentials than the control surface approach. There are two contributing factors to this discrepancy. Firstly it is clear, from Fig. 3.4, that the electric potential around a sphere in a quickly-flowing plasma is not spherically-symmetric which renders this assumption void. Secondly the electric potential possesses steep gradients, particularly behind the sphere, which means that ions which initially overshoot the sphere can bend back onto to sphere and be collected. This effect has been termed the absorption radius effect [193].

The control surface method can also be used to calculate the drag forces on the same spheres as for the ion currents. The second-innermost cylinder of Fig. 3.4 is once again used and the results are plotted as points in Fig. 3.7. Nitter gives the formula [192, Eq. 45]

$$\frac{D_z}{n_0 k_B T_e \lambda_D^2} = -\pi A^2 \left(U_f^2 - 2\Phi_A\right) \tag{3.41}$$

for the drag force due to ions collected on these spheres which is plotted as the solid lines in Fig. 3.7. Equation 3.41 gives good qualitative agreement with the control surface calculations but slightly underestimates the total drag forces on charged spheres. The reasons for this discrepancy are the same as for the ion currents: the derivation of Eq. 3.41 makes bold assumptions about both spherical symmetry and the absence of absorption radii which are not fully applicable to Debye-length-sized spheres in flowing plasmas. Furthermore Eq. 3.41 includes only the forces due to ions which hit the sphere,

[2] Nitter's expression actually omits the prefactor of U_f since he considers a sphere in a plasma sheath where the flux of ions is given by the Bohm criterion and hence is independent of the local ion speed.

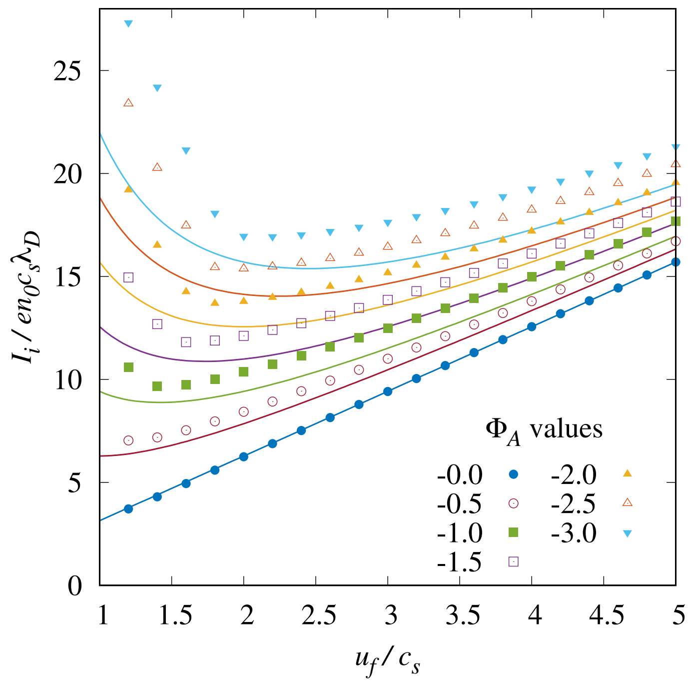

Figure 3.6: The dimensionless ion currents collected on spheres of Debye-length radii with varying surface potentials and plasma flow speeds. The points indicate the results of control surface calculations using the two-fluid plasma model while the solid lines correspond to Eq. 3.40.

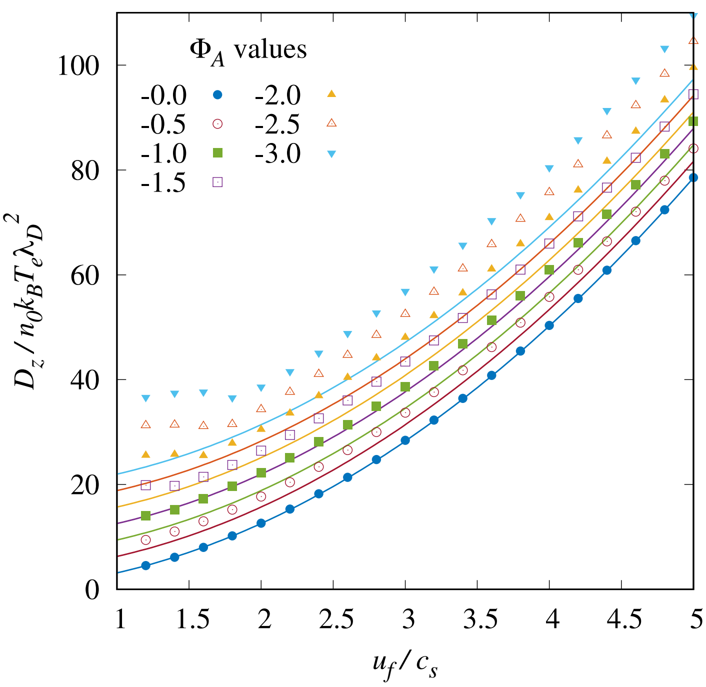

Figure 3.7: The drag forces on spheres with Debye-length radii and varying surface potentials and plasma flow speeds. Simulation results using the control surface approach are shown as points while the drag force due to ion collection, Eq. 3.41, is shown by solid lines.

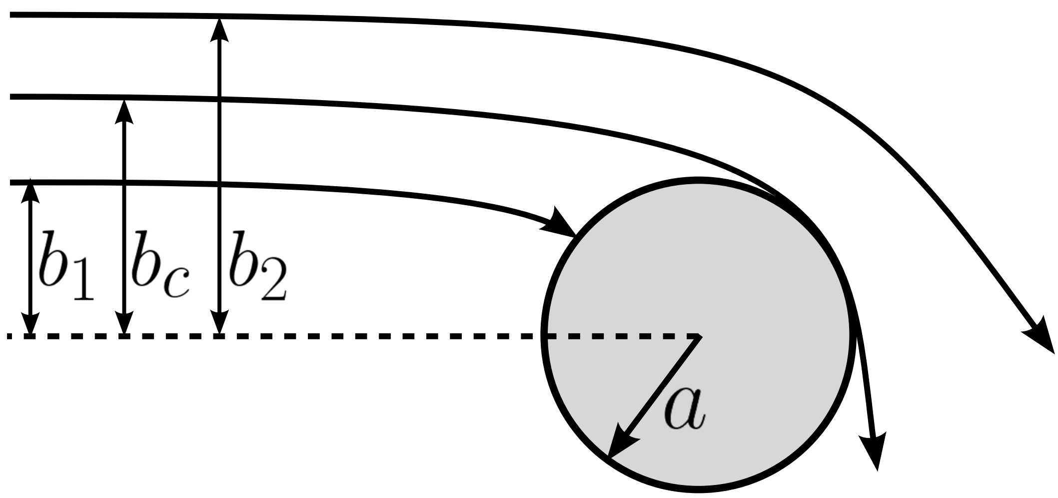

Figure 3.8: Illustration of the critical impact parameter b_c which corresponds to a grazing orbit in the OML theory. Ions with $b_1 < b_c$ are collected on the sphere, and contribute to the ion current, while those with $b_2 > b_c$ bypass the sphere and make no contribution to the current. Based on [183, Fig. 2.3].

i.e. the ion ram pressure, whereas integrating the plasma stress tensor over a control surface straightforwardly handles the electrostatic forces as well.

3.2.3 Orbit-motion limited (OML) charging theory

The cold-ion ABR theory of Sec. 3.2.1 finds that the charge carried by a stationary droplet in a plasma tends to zero as $a/\lambda_D \to 0$. These small liquid drops have vanishing charge and must be electrohydrodynamically stable. An alternative charging theory using warm ions, the orbit-motion limited (OML) theory [194, 195], predicts that small droplets have a finite amount of charge and offers the hypothesis that very small droplets might be susceptible to electrostatic breakup. The cold-ion theories treated the ions as a fluid where all of the ions travel with the same velocity whereas OML accounts for a distribution of ion velocities and hence is a kinetic theory.

Ions with non-zero temperature are not constrained to radial motion. Their non-radial motion can be accounted for by conserving their angular momentum as they move towards, and are collected on, a sphere of radius a and potential ϕ_a. An ion which has an initial velocity of u_∞ and an impact parameter of b_c, as defined in Fig. 3.8, will only just reach the surface of the grain if its radial velocity is zero at $r = a$. All of its velocity is in the angular direction at this point and the magnitude of this velocity, u_a, is given, by conservation of angular momentum, as $m_i u_a a = m_i u_\infty b_c$. If the electrostatic potential at the initial position of the ion is taken to be zero then conservation of energy gives the magnitude of this velocity as $u_a^2 = u_\infty^2 - 2e\phi_a/m_e$. These two conservation laws can be combined to give the collision cross-section for ions with initial velocity u_∞ as

$$\sigma_{coll}\left(u_\infty\right) = \pi b_c^2 = \frac{u_a^2 a^2}{u_\infty^2} = \pi a^2 \left(1 - \frac{2e\phi_a}{m_i u_\infty^2}\right) \tag{3.42}$$

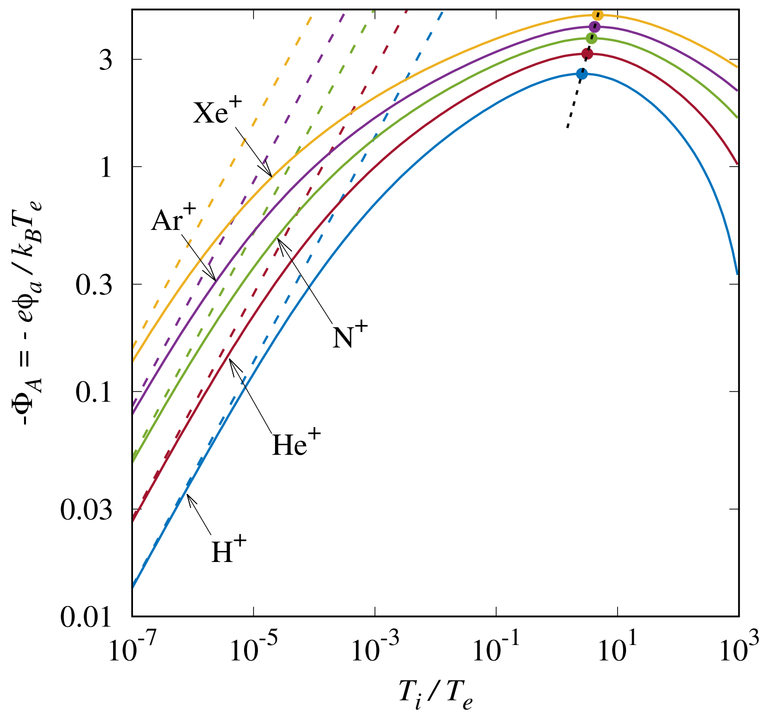

Figure 3.9: The floating potentials of spheres in plasmas according to the OML theory expression in Eq. 3.48. The asymptotic behaviour for $T_i/T_e \to 0$, as given in Eq. 3.50, is shown by the dashed lines. The maximum floating potential for each species of ion is given by Eq. 3.49 and lies on the line $-e\phi_a/k_BT_e = T_i/T_e$.

The total current to the sphere due to the collection of ions is then given by

$$I_i = e \int_0^\infty u_\infty f_{Mi}\left(u_\infty\right) \sigma_{coll}\left(u_\infty\right) du_\infty \tag{3.43}$$

which is evaluated, for the stationary Maxwellian distribution in Eq. 2.26, as

$$I_i = 4\pi^2 a^2 n_0 e \left(\frac{m_i}{2\pi k_B T_i}\right)^{3/2} \int_0^\infty u_\infty^3 \left(1 - \frac{2e\phi_a}{m_i u_\infty^2}\right) \exp\left(\frac{-m_i u_\infty^2}{2k_B T_i}\right) du_\infty \tag{3.44}$$

$$= 4\pi a^2 n_0 e \left(\frac{k_B T_i}{2\pi m_i}\right)^{1/2} \left(1 - \frac{e\phi_a}{k_B T_i}\right). \tag{3.45}$$

The sphere charges negatively under floating conditions, due to the high thermal velocity of the electrons, so the electrons are mostly repelled from the surface and their density satisfies the Boltzmann relation as described in 2.2.7. The one-way flux of Boltzmann electrons, Eq. 2.28, gives the electron current to the sphere as

$$I_e = -4\pi a^2 e \Gamma_{e,Boltz} = -4\pi a^2 n_0 e \left(\frac{k_B T_e}{2\pi m_e}\right)^{1/2} \exp\left(\frac{e\phi_a}{k_B T_e}\right). \tag{3.46}$$

The floating potential is found from the condition $I_i + I_e = 0$ as the solution to

$$\left(\frac{T_i}{T_e} - \frac{e\phi_a}{k_B T_e}\right) = \left(\frac{T_i m_i}{T_e m_e}\right)^{1/2} \exp\left(\frac{e\phi_a}{k_B T_e}\right) \tag{3.47}$$

which has a closed-form solution in terms of the Lambert W function [183] as

$$\frac{e\phi_a}{k_B T_e} = -W_0\left[\left(\frac{T_i m_i}{T_e m_e}\right)^{1/2} \exp\left(\frac{T_i}{T_e}\right)\right] + \frac{T_i}{T_e} \tag{3.48}$$

which is plotted in Fig. 3.9. Note that the grain radius does not appear as a factor in the OML floating potential of a sphere due to the cancellation of the a^2 factors in Eqs. 3.45 and 3.46.

The maximum floating potential for a given species of ions can be found by maximising Eq. 3.48 with respect to T_i/T_e. The resulting maximum floating potential, and the corresponding value of T_i/T_e, have the identical expressions

$$\left(-\frac{e\phi_a}{k_B T_e}\right)_{max} = \left(\frac{T_i}{T_e}\right)_{max} = \frac{1}{2} W_0\left(\frac{m_i}{2m_e}\right). \tag{3.49}$$

This equality is displayed by all of the maxima in Fig. 3.9 sitting on a line of unit gradient with the values 2.59, 3.18, 3.73, 4.19 and 4.73 for singly-charged hydrogen, helium, nitrogen, argon and xenon plasmas respectively.

3.2.4 The transition from ABR to OML

The results of the ABR fluid theory and OML kinetic theory are clearly incompatible: ABR predicts that ϕ_a vanishes for $a \ll \lambda_D$ while OML specifies a finite value of ϕ_a which is independent of a. The limitations of ABR are evident given that it was developed from a cold-ion model so it is only valid for $T_i \ll T_e$. The shortcomings of OML are slightly more subtle and are related to the grazing-orbit assumption that the impact parameter b_c, for ions which only just reach the sphere's surface, separates ion orbits which are collected on or bypass the sphere. In fact all collecting spheres in plasmas possess an absorption radius at $r > a$ which separates these collected and non-collected ion trajectories so the actual ion current is larger than the OML prediction and the resulting floating potential is less negative [193]. However the difference between the absorption radius and the surface of the sphere becomes negligible when $a \ll \lambda_D$ and the OML theory becomes an excellent approximation [194]. Lampe found that the absorption radius effect only needs to accounted for when $0.03(a/\lambda_D)(T_e/T_i) \gg 1$ [196].

The agreement of OML with ABR's vanishing-ϕ_a prediction is observed in the limit $T_i \ll T_e$ where a series expansion of Eq. 3.48 gives

$$\frac{e\phi_a}{k_B T_e} \approx -\left(\frac{T_i m_i}{T_e m_e}\right)^{1/2}. \tag{3.50}$$

The fact that OML and ABR are compatible when $T_i \ll T_e$ and $a \ll \lambda_D$ offers the

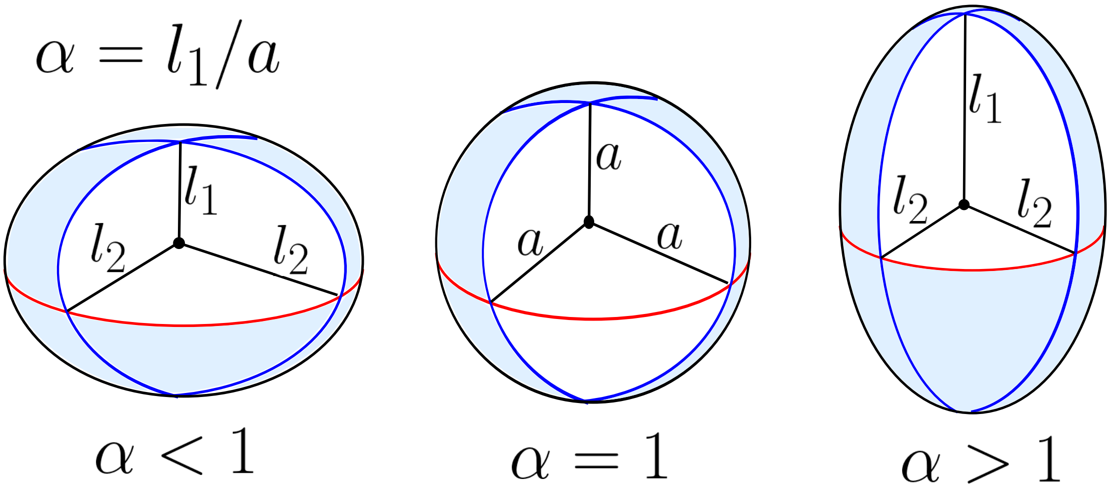

Figure 3.10: Illustration of oblate and prolate spheroids: oblate spheroids (left) have elongations $\alpha = l_1/a < 1$ while prolate spheroids (right) have $\alpha = l_1/a > 1$. The volumes of the spheroids is the same as as a sphere of radius a such that $a^3 = l_1 l_2^2$.

tantalising possibility of a unified theory of sphere charging in a plasma which reproduces OML or ABR in the appropriate regime. One contender for this unified theory is the orbital motion calculation of Kennedy and Allen which accounts for the absorption radius effect and is compatible with both OML and ABR [194, Fig. 10]. However this generality is obtained at the cost of intractable algebra which necessitates numerical solutions and no general closed-form expression for ϕ_a has yet been discovered.

The development of the OML and ABR charging theories would be a wasted endeavour without experimental verifications. Fortunately there are many. Measurements from Langmuir probes with $a \sim \lambda_D$ in low-pressure argon and neon RF plasmas are in excellent agreement with the ABR theory [197, 198] for temperature ratios at least as high as $T_e/T_i = 0.3$ [198]. However a low-pressure helium plasma begins to exhibit OML-like behaviour for these elevated temperature ratios due to the enhanced thermal velocity of the light helium ions which causes non-negligible angular motion [198]. Chen found the OML theory to be appropriate for a small probe with $a \ll \lambda_D$ in an argon RF plasma [199]. OML provides such a good description of the collected currents, even under conditions where high collisionality should render the assumption of unimpeded orbital motion invalid, that Chen describes the remarkable accuracy of OML as both “surprising” and “fortuitous” [199].

3.2.5 Charging of non-spherical plasma-immersed objects

The ABR and OML charging theories have been developed for spherical objects in a plasma but liquid droplets are not constrained to spherical shapes. The application of OML to spheroids was first studied by Laframboise and Parker [200]. The deformation of a spheroid can be characterised by the ratio of lengths of its polar axis to the radius of a sphere with the same volume as illustrated in Fig. 3.10; this ratio is referred to as the elongation α. Rice-grain-shaped prolate spheroids have $\alpha > 1$ while flattened lentil-like oblate spheroids have $\alpha < 1$. Laframboise and Parker found that the spherical OML theory applies to spheroids with $0.537 < \alpha < 1.398$. Further work on spheroid charging was performed by Zahed, Mahmoodi and Sobhanian [201] who derived vacuum capacitances for conducting spheroids and applied them to Laframboise and Parkers results; as such their work was also limited to moderately deformed spheroids. Holgate and Coppins have noted that Zahed's results for the vacuum capacitances of spheroids differ from those given by Landau and Lifshitz [202, p. 24]. Landau and Lifshitz's expressions are provided in terms of the principal radii of the spheroid, l_1 and l_2 in the notation of Fig. 3.10, but some algebraic manipulation allows tham to be expressed in terms of the elongation α as [203]

$$C(\alpha) = \begin{cases} 4\pi\epsilon_0 a \dfrac{(1-\alpha^3)^{1/2}}{\alpha^{1/2}\cos^{-1}\left(\alpha^{3/2}\right)} & \text{for} \quad \alpha < 1 \\ 4\pi\epsilon_0 a & \text{for} \quad \alpha = 1 \\ 4\pi\epsilon_0 a \dfrac{(\alpha^3-1)^{1/2}}{\alpha^{1/2}\cosh^{-1}\left(\alpha^{3/2}\right)} & \text{for} \quad \alpha > 1. \end{cases} \tag{3.51}$$

Holgate and Coppins found additionally that ϕ_a changes by less than 1% from the OML value for spheroids with $0.06 < \alpha < 3.7$ in hydrogen and deuterium plasmas and those with $0.2 < \alpha < 2.1$ in argon plasmas [203]. These limits were the result of a modified OML-type calculation which is briefly described and extended here in order to determine the floating potentials of plasma-immersed spheroids in flowing Maxwellian plasmas.

The crux of Holgate and Coppins' method is to integrate a distant Maxwellian distribution over all paths which end on the spheroid, as in a typical OML derivation, but with collected orbits identified by numerical integration of ion orbits in the electric field of a conducting spheroid in a vacuum rather than by the conservation of angular momentum. Each orbit starts on a distant spherical surface which fully encloses the spheroid. The calculation is performed several times but with the electric potential of the spheroid's surface changed each time; in this way the variation of I_i and I_e with ϕ_a can be determined. The functions $I_i(\phi_a)$ and $I_e(\phi_a)$, which are analogous to Eqs. 3.45 and 3.46, are then found by linear interpolation and the floating potential of the spheroid is determined by the solution of floating condition $I_i(\phi_a) + I_e(\phi_a) = 0$. Full details of the method, including expressions for the integrals and equations of motion used to determine the electron and ion currents, are provided in the original paper [203]. This method can be applied to a range of spheroid shapes and for Maxwellian distributions with different drift velocities.

Fig. 3.11 shows the floating potentials of oblate and prolate spheroids with a hydrogen plasma flowing along either the l_1 or l_2 axes and at velocities up to $u_f = 5c_s$. These results are given in terms of the aspect ratio, l_1/l_2, rather than the elongation but the two quantities are simply related by $\alpha = (l_1/l_2)^{2/3}$. The small deviation of floating potentials from the spherical values is clear for the $u_f = 0$ cases although this deviation

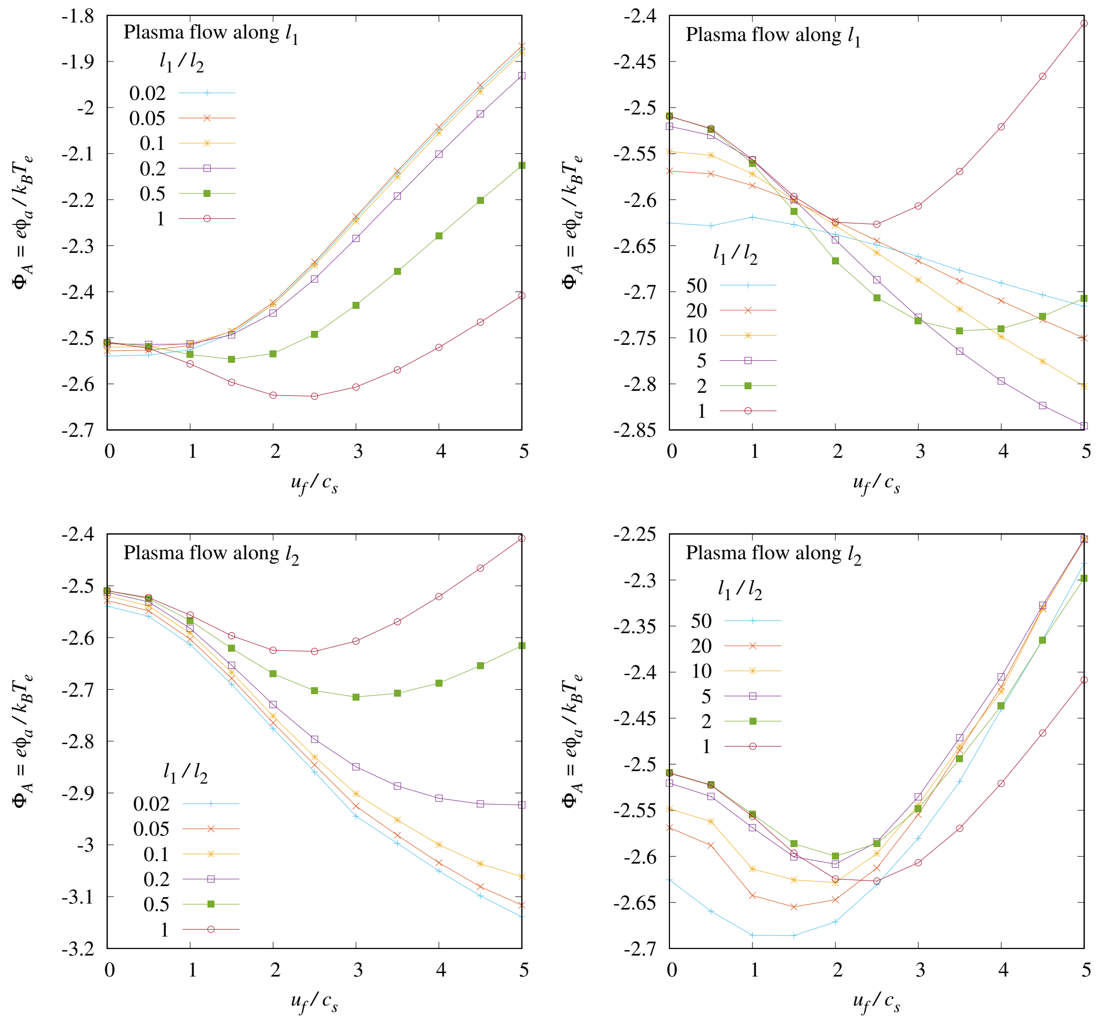

Figure 3.11: The floating potentials of spheroids in flowing hydrogen plasmas according to a modified OML-type calculation. The left and right columns show oblate and prolate spheroids respectively; the top and bottom rows distinguish between flow along the l_1 or l_2 axes as illustrated in Fig. 3.10.

grows significantly as the plasma velocity increases. The change in floating potential with increasing plasma flow speeds is qualitatively similar to the cold-ion, Boltzmann-electron model for flow past a sphere given in Fig. 3.5; the floating potential initially becomes more negative until a turning point, typically around $u_f \sim 2c_s$, after which it becomes gradually less negative.

It would be interesting to compare the results of Fig. 3.11 to the idealised limiting cases of thin discs or cylinders for the prolate and oblate spheroids respectively. Furthermore the spherical ABR theory might be extensible to spheroids either by solving the cold-ion, Boltzmann-electron equations in spheroidal coordinates or by a numerical calculation using the scheme described in Secs. 3.1.2 and 3.2.2. For now these efforts are left as a future study.

3.3 Dust and droplets in magnetised plasmas

All of the theories of plasma-surface interactions described so far have made no consideration of magnetic fields. The modification of the plasma behaviour in the presence of magnetic fields is a very active area of research with obvious applications in magnetic confinement fusion devices. The extension of sphere-charging models to magnetic fields is considered in this section along with a novel mechanism for droplet spinning in a magnetised plasma.

3.3.1 Floating potential of spheres in magnetised plasmas

The collection of electron and ion currents on objects placed into plasmas remains an open research problem as testified to by the biannual "International Workshop on Electric Probes in Magnetized Plasmas" which has now passed its 12th edition [204]. The effect of dust charging in magnetised plasmas is of vital importance, for instance, in studies of dust transport in magnetic fusion devices [60] and alignment of dust grains in the interstellar medium [205]. Current-collecting probes are ubiquitous in magnetic fusion devices such as the recently-completed MAST-Upgrade tokamak in Oxfordshire which features a suite of over 600 Langmuir probes [206]; interpreting the data from these probes presents a concerning issue.

The first comprehensive calculation of charge collection on a spherical object in a plasma is due to Sonmor and Laframboise (SL) who numerically integrated the motion of electrons and ions in a Coulomb potential around the sphere and under the application of a uniform, constant magnetic field [207]. The use of a Coulomb potential restricts the results to small spheres with $a \ll \lambda_D$. The electrons and ions are assumed to be drawn from a distant Maxwellian plasma and the currents are determined by integrating those parts of the Maxwellian distributions which correspond to particle trajectories hitting the sphere. The numerical results for the attracted species, which are ions for the usual case of a negative sphere, are presented in a handy tabulated form and are plotted in Fig. 3.12. The current is normalised to the thermal ion current to an uncharged sphere

$$I_0 = 4\pi a^2 e n_0 \left(\frac{k_B T_i}{2\pi m_i}\right)^{1/2}, \tag{3.52}$$

which follows from Eq. 2.28, and the magnetic field is parameterised by the ratio of the sphere's radius to the mean ion gyroradius which is denoted as

$$\beta_i = aeB \left(\frac{2}{\pi m_i k_B T_i}\right)^{1/2}. \tag{3.53}$$

The unmagnetised OML case and the limit of infinite magnetic field have been added to Fig. 3.12. The OML limit $I_i = I_0(1 - \Phi_A)$ follows from Eq. 3.45 while, in the highly-magnetised case, ions are effectively bound to the magnetic field lines and are collected over the cross-sectional circular area of the sphere which faces the magnetic field. Ions

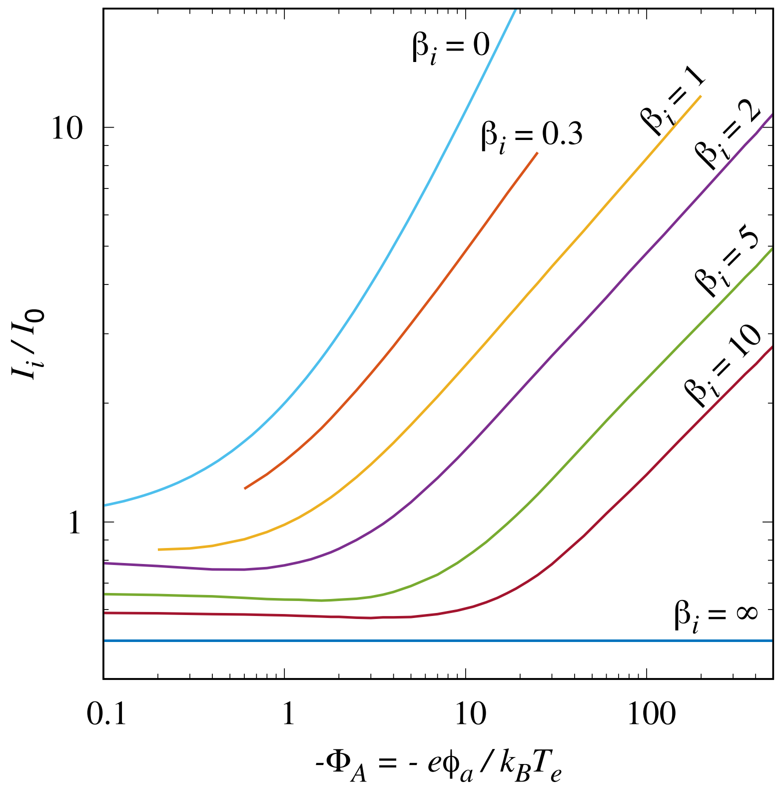

Figure 3.12: The normalised ion current to small spheres ($a \ll \lambda_D$) in magnetised plasmas as tabulated by Sonmor and Laframboise [207]. A gradual transition is evident from the unmagnetised OML ion current to the highly-magnetised case which is independent of the potential of the sphere.

can be collected on both sides of the sphere, *i.e.* over an area of $2\pi a^2$, which gives an ion current of $I_0/2$ which is independent of the charge on the sphere. The electrons behave similarly but are still repelled from the sphere; their current is accordingly given as half of the OML value in Eq. 3.46. Solving the floating condition $I_i + I_e = 0$ in the high-field limit therefore yields

$$\left.\frac{e\phi_a}{k_B T_e}\right|_{\beta_i \to \infty} = \frac{1}{2} \ln\left(\frac{T_i m_e}{T_e m_i}\right) \tag{3.54}$$

which is -3.758 for a hydrogen plasma with $T_e = T_i$.

SL's results are sufficient to calculate the floating potential of small spheres in magnetised plasmas but, given that they were concerned with biased probes, they declined to do so. It was not until the work of Patacchini, Hutchinson and Lapenta (PHL) that these floating potentials were explicitly calculated and compared with a PIC code simulation [208]. This PIC code used the Boltzmann relation for electrons which, as discussed in Sec. 2.2.7, is not valid in a magnetic field. PHL attempted to circumvent this issue by using an empirical fit to SL's results in order to calculate the electron current to the sphere; nevertheless the assumption of Boltzmann electrons around the sphere calls into question the validity of their results.

Two recently-published simulations of spheres in magnetised plasmas dispense with the electron Boltzmann relation. The first, by Lange [209], is a PIC code where both the electrons and ions are simulated. The results appear to follow SL's $a \ll \lambda_D$ data but with around 10% more negative charge accumulating on the sphere. The second is a treecode simulation by Thomas and Holgate [183, 210] which calculates the interparticle interactions of every single electron and ion using the Barnes-Hut algorithm [211]. This algorithm approximates the electric force experienced by a single particle due to a group of distant particles by treating the distant particles as a single particle with the same net charge as the group. This approximation reduces the runtime of the N-body simulation from $\mathcal{O}(N^2)$ to a more manageable $\mathcal{O}(N \log N)$. The clustering process involves halving the size of the 3-dimensional computational domain along each axis, resulting in an 8-fold split, and repeating this process until each subdomain contains only a single electron or ion. This repeated splitting results in a tree-like data structure which motivates the "treecode" name. No overcharging of the sphere is observed in the treecode; however great care was taken to implement boundary conditions according to a Maxwellian plasma infinitely-far from the sphere rather than a Maxwellian plasma at the immediate edge of the simulation domain by using a particle reinjection algorithm developed by Hutchinson [212]. As such, it appears likely that the systematic discrepancy in Lange's simulations are due to oversimplistic boundary conditions.

The original treecode results used relatively low electron and ion temperatures of 220 K which cause around 100 electron charges to collect on the spheres [210]. Random fluctuations of a few extra electrons or ions therefore amount to a significant proportion of the sphere's total charge. Ongoing simulations are resolving this issue by considering warmer plasmas, with $T_e = T_i = 1$ eV, and half a million simulated electrons and ions. The preliminary, and quite limited, results are shown in Fig. 3.13 along with the the floating potential according to SL's calculations. Good agreement between these calculations is observed for $a \ll \lambda_D$. Both sets of results reproduce the OML ($\beta_i \to 0$, Eq. 3.48) and highly-magnetised ($\beta_i \to \infty$, Eq. 3.54) limits. It would be interesting to see whether the charging behaviour of the treecode could be replicated by repeating SL's calculations with a Debye-shielded potential; work towards this objective is currently underway in the Imperial College Dusty Plasma Group. It is also worth mentioning that this treecode has also been used to verify the spheroidal OML-type calculations described in Sec. 3.2.5 for stationary unmagnetised plasmas [210].

3.3.2 Spinning of spheres in magnetised plasmas

There are many processes which can lead to the spinning up of droplets in a plasma; these include the shear of plasma flow [213], asymmetry of radiation to the grain [214], rocket forces from dust grain ablation [215], and interaction between electric fields and a dipole induced on an electrically insulating grain by plasma flows [216]. The latter process occurs in the plasma sheath, and has been predicted to cause droplets to spin

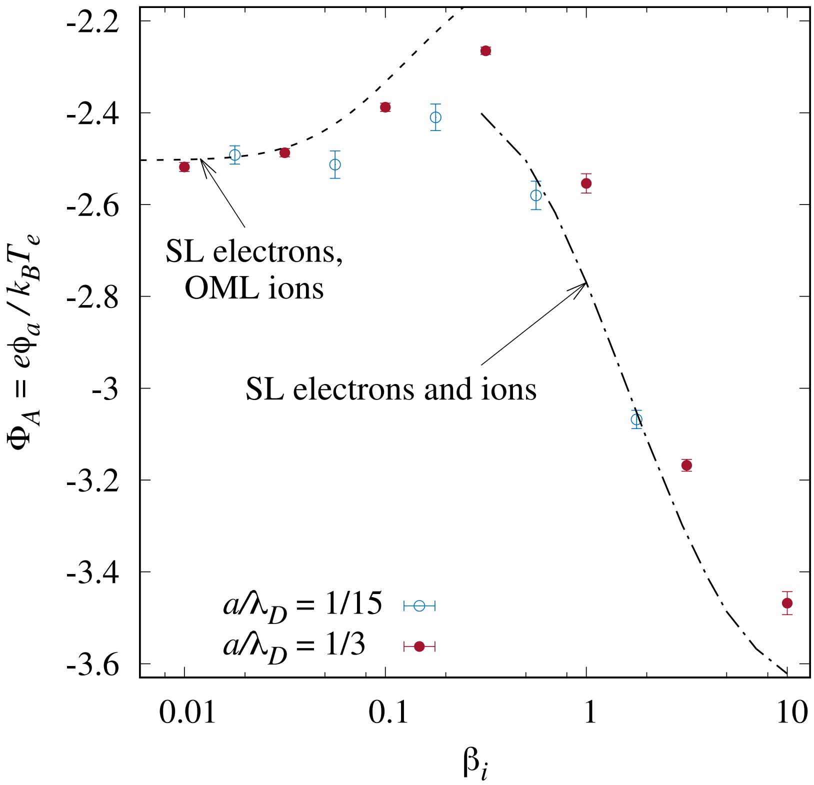

Figure 3.13: Floating potentials of spheres in magnetised hydrogen plasmas as computed by treecode simulations. These are compared with the floating potentials calculated using Sonmor and Laframboise's (SL's) electron currents, from a direct-orbit integration method [207], and the OML ion currents or both of SL's electron and ions currents.

at up to 6×10^5 s^{-1} in a low-temperature argon plasma [216].

In a magnetised plasma there are additional spinning mechanisms due to $\underline{E}\times\underline{B}$ plasma flows [217], ion gyromotion [218], and a $\underline{J} \times \underline{B}$ torque from currents flowing through the grain which can lead to dust grains spinning at $\sim 10^6$ s^{-1} in tokamak conditions [218]. The $\underline{J} \times \underline{B}$ mechanism has been verified by PIC simulations [219] and will be taken as the dominant contribution to dust grain spinning in a tokamak edge plasma.

The $\underline{J} \times \underline{B}$ spinning mechanism occurs when the ion gyroradius is larger than a dust grain radius while the electron gyroradius is smaller than it; such conditions are provided by a typical tokamak edge plasma[3]. Under these conditions the electrons follow the magnetic field, and are preferentially collected on the surfaces of the grain which are normal to the field lines, while the ions are collected uniformly over the whole surface of the grain. These electron and ion currents are illustrated in Fig. 3.14. The unequal distributions of electron and ion current densities on the surface of the droplet causes a recombination current to flow inside the droplet in a direction perpendicular to the magnetic field which is responsible for the $\underline{J} \times \underline{B}$ torque. Krasheninnikov has outlined

[3]The gyroradius $r_g = mv/eB$ is 300 μm for ions moving at the sound speed and 5 μm for electrons in a JET-like edge plasma with $T_e = 40$ eV and $B = 3$ T; typical droplet radii are 10-100 μm.

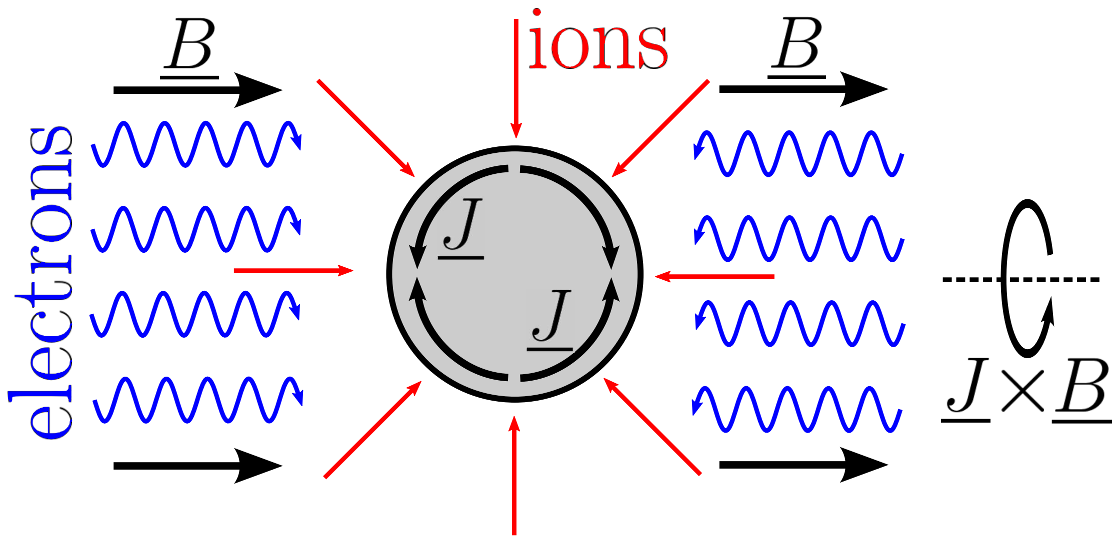

Figure 3.14: Illustration of the nonuniform collection of electrons on a droplet in a magnetised plasma which gives rise to a recombination current $\underline{J}$ inside the droplet and hence a $\underline{J} \times \underline{B}$ torque.

an estimate of the magnitude of this torque [218], and the resulting angular velocity of the droplet, which is worth reviewing to fill in any gaps for future readers.

The recombination current density inside the drop is given, roughly, by $J = e\Gamma_i \sim en_0 c_s$ from which the magnitude of the torque can be estimated as

$$\tau_{\underline{J}\times\underline{B}} = \int_a \underline{r} \times (\underline{J} \times \underline{B})\, dV \sim en_0 c_s a^4 B. \tag{3.55}$$

The droplet would spin up indefinitely if this were the only torque on it. However there is a second torque, due to the collection of randomly-moving ions from the plasma, which tends to slow down the rotation. Each of these ions, when viewed in a frame which is co-rotating with the droplet with angular velocity ω_d, has an average angular momentum of $L_i \sim m_i a^2 \omega_d$ at the moment of impact with the droplet. The net slow-down torque due to the flux of these ions is estimated as

$$\tau_{sd} = 4\pi a^2 \Gamma_i L_i \sim n_0 c_s a^4 m_i \omega_d. \tag{3.56}$$

The difference between the $\underline{J} \times \underline{B}$ torque and the slow-down torque gives the change in angular momentum of the droplet so, by estimating the moment of inertia of a drop of density ρ_d as $\sim \rho_d a^5$, the rate of change of droplet angular velocity is found as

$$\frac{d\omega_d}{dt} \sim \frac{n_0 c_s m_i}{\rho_d a} \left(\frac{eB}{m_i} - \omega_d \right). \tag{3.57}$$

This equation suggests that the droplets will ultimately attain the same angular velocity as the ion gyrofrequency, $\omega_{gi} = eB/m_i$, which is over 10^8 s^{-1} for a JET-like magnetic field of $B = 3$ T. However it would take a characteristic spin-up time on the order of $t_{spin} \sim \rho_d a / n_0 c_s m_i$ for the droplet to reach such high values; this works out at roughly

100 s for 10 μm tungsten droplets or 3 s for 10 μm lithium droplets under JET-like plasma conditions. The survival times of droplets in tokamaks is often quoted as 0.01 s [218, 220] although this is significantly shorter than droplet lifetimes observed on the JET cameras; nevertheless droplets are unlikely to survive for timescales approaching t_{spin}. Solving Eq. 3.57 for an initially-stationary droplet, and linearising for $t \ll t_{spin}$, gives an estimate of the angular velocity of a droplet as

$$\omega_d \sim \frac{eB}{m_i}\left[1 - \exp\left(-\frac{n_0 c_s m_i t}{\rho_d a}\right)\right] \sim \frac{eBn_0c_s}{\rho_d a}t. \tag{3.58}$$

This estimate has been verified by PIC simulations [219] but no direct observations of such spinning have yet been recorded. The breakup of rotating droplets in tokamaks might provide the first such observations but this requires a quantitative comparison with the stability limits of spinning droplets as developed in Sec. 5.3.

3.4 Implications for plasma-liquid interactions

The results contained in this section might appear to be a digression from the main discourse on plasma-liquid interactions. Nothing could be further from the truth. The accumulation of charge on plasma-facing surfaces or plasma-immersed droplets is crucial in determining their motion, equilibrium shapes and stability particularly on small lengthscales where the plasma offers no shielding of the electric field. Even on large lengthscales, where the sheath becomes effectively invisible, the electric field at the plasma-liquid interface extends deep into the plasma where it accelerates ions towards the liquid surface in accordance with the Bohm criterion. However the effects of electrical charge and fields on plasma-liquid interactions have been almost completely ignored in the previous studies described in Sec. 1.3. The following chapters integrate the effects of charging and sheath formation into hydrodynamic studies of these interfaces beginning with plasma-facing surfaces in Chapter 4 and moving to plasma-immersed droplets in Chapter 5.

4 Plasma-facing liquid surfaces

The most frequently-encountered form of plasma-liquid interaction in Chapter 1 involves the direct contact of a plasma with a liquid surface; examples occur at the walls of magnetic fusion devices, in plasma welding and cutting, plasma catalysis of liquid-phase chemical reactions, nanoparticle synthesis, decontamination of water and food products, and plasma treatment of wounds. The dynamics and stability of these interfaces depends on the electric field in the sheath region which has been described in detail in Sec. 3.1. This chapter begins by considering the electric field due to just the accumulated free charge on the liquid surface, with a discussion of its implications for droplet ejection from bursting bubbles, before moving on to include fully the thermal pressures and inertial forces of the electron and ion fluids. Both linear stability analyses and non-linear numerical simulations are utilised throughout.

4.1 Ideal electrohydrodynamic limit

If the lengthscale of surface deformations is much smaller than the Debye length then the electric field close to a conducting surface is almost entirely dominated by the free charges on the surface. The charge density of electrons and ions in the plasma is insufficient to modify the electric field significantly over these short, sub-Debye distances so the electric field close to the surface can be well approximated as a vacuum field. Furthermore the curvature of these highly-deformed surfaces gives strong enhancement of the electric field so the electric stress becomes the dominant term in the pressure jump condition. The plasma-liquid fluid equations therefore reduce to those of a charged liquid in a vacuum; this thesis refers to these as the ideal electrohydrodynamic equations which are considerably easier to solve than the full system of plasma-liquid fluid equations.

4.1.1 The ideal electrohydrodynamic equations

The fluid equations in the liquid region remain unchanged from Sec. 2.3 so are still given by

$$\nabla \cdot \underline{v} = 0, \tag{4.1}$$

$$\rho \frac{\partial \underline{v}}{\partial t} + \rho \left(\underline{v} \cdot \nabla \right) \underline{v} = -\nabla p + \eta \nabla^2 \underline{v} + \rho \underline{g} \tag{4.2}$$

when no magnetic fields are present. The electric field in the vacuum region is given by Laplace's equation

$$\nabla^2 \phi = 0 \tag{4.3}$$

which is coupled to the liquid pressure at the vacuum-liquid interface by the jump condition, from Eq. 2.62,

$$\left[\frac{\epsilon_0 E^2}{2} + p\right]_{z=\xi} + \gamma\kappa = 0. \tag{4.4}$$

The boundary condition on the electric field adjacent to the liquid surface remains as

$$\underline{\hat{n}} \times \underline{E}_{z=\xi^+} = \underline{0} \tag{4.5}$$

and the surface convection equation, according to Eq. 2.52, is

$$\frac{\partial \xi}{\partial t} = \left(v_z - v_x \frac{\partial \xi}{\partial x} - v_y \frac{\partial \xi}{\partial y}\right)_{z=\xi}. \tag{4.6}$$

This set of equations and boundary conditions is considerably simpler than the full system of plasma-liquid fluid equations and is suitable for modelling short-scale plasma-liquid interactions on lengthscales shorter than a Debye length. The fact that the plasma does not appear explicitly in these equations does not mean that the plasma has completely disappeared; it is still responsible for the accumulated charge on the liquid surface and hence is the original source of the electric field.

4.1.2 Taylor cones

The first studies of the stability of liquid surfaces under electrostatic forces can be traced back to before 1600 when Gilbert described [221, p. 89] "the case of a spherical drop of water standing on a dry surface; for a piece of amber applied to it at a suitable distance pulls the nearest parts out of their position and draws it up into a cone." Remarkably the mathematical description of these static cones dates back to only 50 years ago [122] and their dynamic behaviour remains an active area of research [222]. These cones are named after Taylor, despite the longstanding experimental observations, for his discovery of a static solution to the ideal electrohydrodynamic equations for a liquid cone in an electric field [122]. Taylor cones have already been integrated into a range of plasma-liquid technologies such as field-emission electric propulsion devices, illustrated in Fig. 1.9, which operate by producing ions and droplets from the tip of a Taylor cone to act as the propellant for the thruster. Taylor cones can also provide a source of droplets for plasma spraying applications [223]. Taylor's original theory is clearly an important prerequisite for theoretical studies of plasma-liquid interfaces.

The configuration of a cone of conducting liquid in a vacuum electric field is illustrated in Fig. 4.1. Spherical coordinates are utilised with the apex of the cone given by $r = 0$ and the surface of the cone located at $\theta = \pi - \alpha$ where the opening angle of the cone is 2α. The unit normal to the surface of the cone is in the negative θ direction so its curvature is given by

$$\kappa = -\left.\nabla \cdot \underline{\hat{n}}\right|_{\theta=\pi-\alpha} = \frac{1}{r\sin\theta}\left.\frac{\partial(\sin\theta)}{\partial\theta}\right|_{\theta=\pi-\alpha} = -\frac{\cot(\alpha)}{r}. \tag{4.7}$$

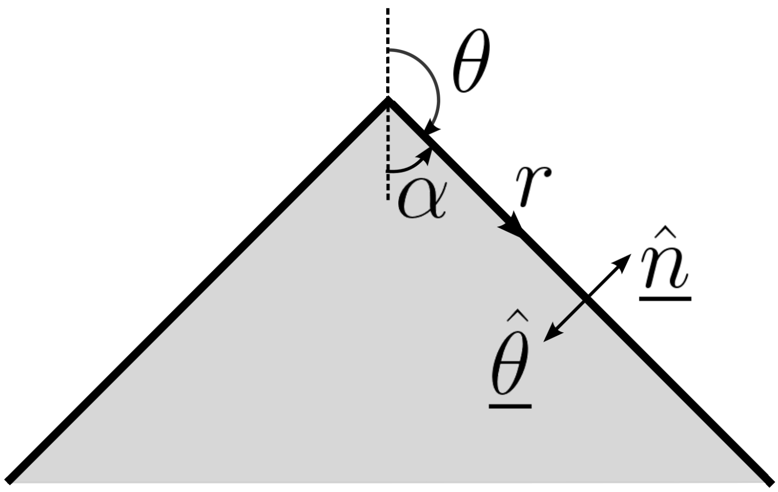

Figure 4.1: Sketch of the spherical coordinate system used to calculate the properties of a static Taylor cone.

The cone is only static when the liquid has no pressure gradients. If the internal pressure of the fluid were to balance the surface tension then it would have to vary spatially like $1/r$ which would induce a flow in the liquid region. Therefore the internal pressure of a static cone must be zero and the stress balance condition is

$$\frac{\epsilon_0}{2} E^2_{\theta,\theta=\pi-\alpha} = -\gamma\kappa = \frac{\gamma\cot(\alpha)}{r}. \tag{4.8}$$

This condition demands that the electric field varies with $r^{-1/2}$ and hence the electrostatic potential must depend on $r^{1/2}$. The corresponding solution of Laplace's equation gives the potential as

$$\phi = Ar^{1/2} P_{1/2}(\cos\theta) \tag{4.9}$$

where $P_{1/2}$ indicates the Legendre function of order 1/2. The potential cannot depend on r along the equipotential surface of the liquid and therefore $P_{1/2}[\cos(\pi-\alpha)] = 0$. The only value of α in the range $0° < \alpha < 180°$ which satisfies this condition is $\alpha = 49.3°$. The opening angles of experimentally-observed cones show incredible agreement with this result [122]. The constant A can be determined, for the sake of completeness, by solving the stress balance condition

$$\frac{1}{r}\frac{\partial}{\partial\theta}\left[Ar^{1/2}P_{1/2}(\cos\theta)\right]_{\theta=\pi-\alpha} = \left(\frac{2\gamma\cot(\alpha)}{\epsilon_0 r}\right)^{1/2} \tag{4.10}$$

to give $A = -452322\gamma^{1/2}$ V N$^{-1/2}$.

4.1.3 Linear stability of a surface in a perpendicular field

The Taylor cone is a static solution to the electrohydrodynamic equations; perhaps the simplest dynamic solution is the linear stability of an initially-flat conducting liquid surface in a perpendicular electric field as first studied by Melcher [224, 225] and

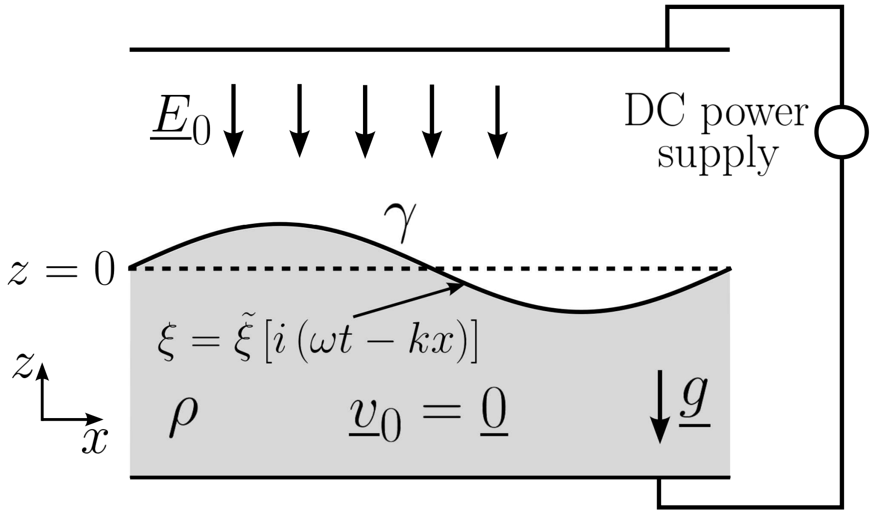

Figure 4.2: Illustration of the setup and parameters involved in determining the linear stability of a liquid surface in a perpendicular electric field.

subsequently by Taylor and McEwan [226]. The original stability theory of Melcher is worth considering in some detail here as a foundation for the stability analysis of a full plasma-sheath-liquid system in Sec. 4.2.1. The initial fluid configuration is illustrated in Fig. 4.2 where the liquid is taken to be below the vacuum region so that gravity acts to stabilise the interface. The surface is subjected to a wave-like perturbation

$$\xi = \tilde{\xi} \exp\left[i\left(\omega t - kx\right)\right] \tag{4.11}$$

where the real part is understood. The objective of a stability analysis is to find an expression for ω in terms of k which is known as the dispersion relation. The dispersion relation determines whether ω is real, in which case the wave travels along the interface and the surface is stable, or imaginary such that the amplitude of the wave grows exponentially and the surface is unstable.

The problem can be linearised by writing all quantities as a sum of terms of different orders of magnitude, for example

$$\xi = \xi_0 + \delta\xi_1 + \delta^2\xi_2 + \cdots, \tag{4.12}$$

$$\underline{v} = \underline{v}_0 + \delta\underline{v}_1 + \delta^2\underline{v}_2 + \cdots \tag{4.13}$$

and so on. Terms which are of the same order of δ can be collected and the resulting equations solved individually. If the perturbation is small enough then the analysis can be restricted to terms of zeroth and first order in δ. The linearised Laplace equation is

$$\nabla^2\phi_0 + \delta\nabla^2\phi_1 + \cdots = 0. \tag{4.14}$$

while the liquid region equations are

$$\nabla \cdot \underline{v}_0 + \delta\left(\nabla \cdot \underline{v}_1\right) + \cdots = 0 \tag{4.15}$$

and

$$\rho\frac{\partial \underline{v}_0}{\partial t} + \rho(\underline{v}_0 \cdot \nabla)\underline{v}_0 + \nabla p_0 + \rho g\hat{\underline{z}} \\ + \delta\left[\rho\frac{\partial \underline{v}_1}{\partial t} + \rho(\underline{v}_0 \cdot \nabla)\underline{v}_1 + \rho(\underline{v}_1 \cdot \nabla)\underline{v}_0 + \nabla p_1\right] + \cdots = 0. \tag{4.16}$$

The boundary conditions at $z = \xi$ can be written similarly in terms of δ. The ordering parameter δ is simply a tool for identifying terms of the same order and can be removed by absorbing it into the first order parameters; stability analyses in the remainder of this thesis will jump straight to the linearised equations. The zeroth and first order terms of ξ are immediately identified as

$$\xi_0 = 0 \qquad \xi_1 = \tilde{\xi}\exp\left[i\left(\omega t - kx\right)\right] \tag{4.17}$$

while the unit normal vector, given by Eq. 2.51, is composed of the terms

$$\underline{\hat{n}}_0 = (0, 0, 1) \qquad \underline{\hat{n}}_1 = \left(-\frac{\partial \xi_1}{\partial x}, 0, 0\right) = \left(ik\xi_1, 0, 0\right). \tag{4.18}$$

The curvature of the interface then follows as

$$\kappa_0 = -\nabla \cdot \hat{n}_0 = 0 \qquad \kappa_1 = -\nabla \cdot \hat{n}_1 = -k^2\xi_1. \tag{4.19}$$

The zeroth order liquid solution is given by the hydrostatic equilibrium configuration of the system as

$$\underline{v}_0 = \underline{0} \qquad p_0 = -g\rho z - \frac{\epsilon_0 E_0^2}{2} + \Pi, \tag{4.20}$$

where Π is an undetermined positive constant with no bearing on the dynamics of the system, while the unperturbed vacuum potential is simply given by $\phi_0 = -E_0 z$ so that $\underline{E}_0 = E_0\hat{\underline{z}}$.

Terms which are of first order in δ are now isolated in order to give the equations describing small perturbations from equilibrium in both regions as

$$\nabla \cdot \underline{v}_1 = 0 \tag{4.21}$$

$$\rho\frac{\partial \underline{v}_1}{\partial t} + \nabla p_1 = 0 \tag{4.22}$$

$$\nabla^2\phi_1 = 0 \tag{4.23}$$

where the result $\underline{v}_0 = \underline{0}$ means that the convective derivative terms have vanished. The wave-like solution of the Laplace equation for the electric potential in the upper region is

$$\phi_1 = C_A\exp\left[-kz + i\left(\omega t - kx\right)\right] \tag{4.24}$$

where the vacuum region has been taken to be extremely wide so that the condition $\phi_1(z \to \infty) = 0$ applies. Taking the divergence of Eq. 4.22, and inserting Eq. 4.21, also gives a Laplace equation $\nabla^2 p_1 = 0$ with the wave-like solution

$$p_1 = C_B \exp\left[kz + i\left(\omega t - kx\right)\right] \tag{4.25}$$

and substitution of this solution into Eq. 4.22 yields

$$\underline{v}_1 = C_B \left(\frac{k}{\omega\rho}\underline{\hat{x}} + \frac{ik}{\omega\rho}\underline{\hat{z}}\right) \exp\left[kz + i\left(\omega t - kx\right)\right]. \tag{4.26}$$

Another deep-fluid condition, $\underline{v}(z \to -\infty) = \underline{0}$, has been made in these solutions; a finite fluid depth would yield a linear combination of $\exp(\pm z)$ terms.

The interfacial conditions apply at $z = \xi$ but they are easiest to apply by using the values of each variable at $z = 0$ so that $\exp(\pm kz) = 1$. This requires a Taylor expansion of each variable. Isolating terms of first order for pressure gives

$$p_{1,z=\xi} = p_{1,z=0} + \xi_1 \left.\frac{\partial p_0}{\partial z}\right|_{z=0} + \xi_0 \left.\frac{\partial p_1}{\partial z}\right|_{z=0} \tag{4.27}$$

and, since $\partial p_0/\partial z = -\rho g$ and $\xi_0 = 0$, this gives

$$p_{1,z=\xi} = p_{1,z=0} - \rho g \xi_1 \tag{4.28}$$

for p_1 in the liquid. The zeroth-order electric field is spatially-invariant so its Taylor expansion is

$$E_{x1,z=\xi} = E_{x1,z=0} + \xi_1 \left.\cancelto{0}{\frac{\partial E_{x0}}{\partial z}}\right|_{z=0} + \mathcal{O}(\xi_1^2). \tag{4.29}$$

This equation is combined with the first-order y-component of the normal field condition in Eq. 4.5,

$$\left[n_{z0}E_{x1} + n_{z1}E_{x0} - n_{x0}E_{z1} - n_{x1}E_{z0}\right]_{z=\xi} = 0, \tag{4.30}$$

which is simplified using $n_{x0} = 0$, $n_{x1} = ik\xi_1$, $n_{z0} = 1$ and $n_{z1} = 0$ from Eq. 4.18 to give

$$E_{x1,z=0} = E_{x1,z=\xi} = ikE_0\xi_1 \tag{4.31}$$

to first-order accuracy. This equation is compared with the electrostatic gradient condition $E_{x1} = -\partial\phi_1/\partial x = ik\phi_1$ to find the constant in Eq. 4.24 as $C_A = E_0\tilde{\xi}$. The first-order electric field in the z direction follows as

$$E_{z1} = -\frac{\partial \phi_1}{\partial z} = E_0 k \xi_1. \tag{4.32}$$

The zeroth-order velocity is also spatially invariant so $\underline{v}_1(z = \xi) = \underline{v}_1(z = 0)$. Linearisation of Eq. 4.6 therefore yields

$$\frac{\partial \xi_1}{\partial t} = v_{z1}(z = 0) \tag{4.33}$$

which sets the constant in the expression for $\underline{v}_1$, Eq. 4.26, as $C_B = \omega^2\rho\tilde{\xi}/k$ with the corresponding pressure

$$p_1 = \frac{\omega^2\rho\xi_1}{k}\exp(kz). \tag{4.34}$$

The stability analysis is concluded by linearising the pressure jump condition to give

$$[\epsilon_0 E_0 E_{z1} + p_1]_{z=\xi} + \gamma\kappa_1 = 0, \tag{4.35}$$

and inserting Eqs. 4.19, 4.28, 4.32 and 4.34 in order to obtain

$$\epsilon_0 E_0^2 k\xi_1 + \frac{\omega^2\rho\xi_1}{k} - \rho g\xi_1 - \gamma k^2\xi_1 = 0. \tag{4.36}$$

This expression rearranges to give the dispersion relation for an ideal electrohydrodynamic wave-like perturbation as

$$\omega^2 = \frac{g\rho k + \gamma k^3 - \epsilon_0 E_0^2 k^2}{\rho}. \tag{4.37}$$

The perturbations are unstable when $\omega^2 < 0$ and the resulting marginal condition for instability,

$$E_0 > \frac{1}{\sqrt{\epsilon_0}}\left(\gamma k + \frac{g\rho}{k}\right)^{1/2}, \tag{4.38}$$

is the same as that found by Taylor and McEwan [226]. Taylor and McEwan's derivation uses a surface stress balance to find the point where the equilibrium configuration first becomes nonplanar and this point is taken as his stability criterion. This analysis can also produce the stability criterion for the standard Rayleigh-Taylor instability described in Sec. 1.3.1; setting $E_0 = 0$ and reversing the sign of g gives the marginal condition for a Rayleigh-Taylor instability of a liquid layer, with density ρ and surface tension γ, placed above a field-free vacuum region as $\rho g > \gamma k^2$.

4.1.4 Effect of cylindrical geometry

If the initial plane-wave perturbation is periodic then it can be decomposed into a sum of waves which each have a specific value of k and the marginal stability condition, Eq. 4.38, applies to each individual plane-wave component. However the initial perturbation might not be planar; consider, instead, an axisymmetric perturbation of the form

$$\xi = \tilde{\xi}\exp(i\omega t)\, J_0(kr) \tag{4.39}$$

where $J_0(kr)$ is the Bessel function of order zero. This function is chosen because it provides eigenvalues of the Laplace equations for ϕ_1 and p_1 of the form

$$\phi_1 = C_A \exp(-kz + i\omega t)\, J_0(kr), \tag{4.40}$$

$$p_1 = C_B \exp(kz + i\omega t)\, J_0(kr). \tag{4.41}$$

The evaluation of v_{z1} from p_1 requires derivatives with respect to z and t only; the constant C_B follows from the surface advection condition, Eq. 4.33, as $C_B = \omega^2 \rho \tilde{\xi}/k$ in exactly the same way as for the plane wave perturbation.

The evaluation of the normal vector, curvature and electric field requires the following differential properties of Bessel functions:

$$\frac{\partial J_0(kr)}{\partial r} = -kJ_1(kr), \qquad \frac{\partial}{\partial r}\left[rJ_1(kr)\right] = krJ_0(kr). \tag{4.42}$$

The first order surface normal and radial electric field are

$$\underline{\hat{n}}_1 = -\frac{\partial \xi_1}{\partial r}\underline{\hat{r}} = k\tilde{\xi}\exp(i\omega t)\,J_1(kr), \tag{4.43}$$

$$E_{r1} = -\frac{\partial \phi_1}{\partial r} = C_A k \exp(-kz + i\omega t)\,J_1(kr) \tag{4.44}$$

so the first-order azimuthal component of the surface normal condition, given by Eq. 4.5 as $\hat{n}_{0z}E_{r1} = \hat{n}_{1r}E_{z0}$, determines the constant as $C_A = E_0\tilde{\xi}$. This constant is the same as for the plane-wave case and E_{z1} remains unchanged from Eq. 4.32. The curvature is

$$\kappa_1 = -\nabla\cdot\hat{n}_1 = -\frac{1}{r}\frac{\partial}{\partial r}\left[rJ_1(kr)\right]\tilde{\xi}\exp(i\omega t) = -k^2\tilde{\xi}\exp(i\omega t)\,J_0(kr) = -k^2\xi_1 \tag{4.45}$$

which, once again, is the same as the corresponding quantity for the planar case given by Eq. 4.19. Putting all of these terms into the linearised pressure jump condition, Eq. 4.35, yields exactly the same dispersion relation as for the plane-wave perturbation. This handy result is particularly relevant to the formation of cylindrically-symmetric Taylor cones.

4.1.5 Axisymmetric simulations of an unstable surface

Two analytic ideal electrohydrodynamic theories have been considered so far: the static equilibrium shape given by a Taylor cone and the linear stability of a perturbed surface in a perpendicular electric field. However most situations do not have such simple solutions and the complete non-linear electrohydrodynamics of a surface can only be resolved by numerically solving Eqs. 4.1–4.6. These simulations are performed in cylindrical (r, z) coordinates in order to make comparisons with both the linear stability analysis and the Taylor cone theory. These coordinates also allow a straightforward extension of the simulations to axisymmetric droplets in Chapter 5.

4.1.5.1 Finite-difference, level-set (FDLS) simulation method

The finite-difference, level-set method (FDLS) has emerged as a popular scheme for simulating electrohydrodynamic flows over the past decade [227]. The popularity of these methods is attributable to their simple implementation and natural handling of complex configurations and merging or breakup of the interface. The position and motion of the plasma-liquid interface is captured by defining an additional scalar field

ψ, known as the level-set function [228], which is positive inside the conducting fluid and negative outside it; the interface between the two regions is then given by the contour $\psi = 0$. A popular choice for ψ is the signed distance function, as used here to specify the initial surface configuration, which gives the closest distance from the interface at any point and which changes sign across the interface. The level-set function is convected with the velocity field according to

$$\frac{\partial \psi}{\partial t} + (\underline{v} \cdot \nabla)\psi = 0 \tag{4.46}$$

and the surface of the fluid moves with it. This equation replaces Eq. 4.6 for describing the motion of the liquid surface. The level-set function allows straightforward calculation of the normal vector and curvature of the free surface using the formulae $\underline{\hat{n}} = -\nabla\psi/|\nabla\psi|$ and $\kappa = -\nabla\cdot\underline{\hat{n}}$. The disadvantage of the level-set method, compared to alternatives such as the volume-of-fluid method, is that the volume of the fluid tends not to be conserved; however, for the cases tested so far, the code described here conserves more than 99.9% of its initial volume. This better-than-expected volume conservation is most likely to be due to the choice of a divergence-free fictional velocity and the avoidance of any reinitialisation algorithms.

A simulation method using a finite-difference discretisation of the ideal electrohydrodynamic equations, with level-set interface tracking, is fully described in Ref. [227]. This code uses a uniform staggered grid configuration, as introduced for the plasma simulations in Sec. 3.1.2, with ρ, ϕ and ψ specified at the centres of cells and the components of $\underline{v}$ given at the edges of cells. The method for solving the Navier-Stokes equation, Eq. 4.2, is essentially given by the Chorin projection method as outlined in Ref. [178]. Provisional values of the liquid velocity at the next time step are calculated using the forward Euler method but with the ∇p terms excluded. These provisional velocities are then substituted into the incompressibility condition to produce a Poisson equation for the pressure at the next step. The boundary conditions on this Poisson equation are given by the pressure jump condition at the liquid surface, Eq. 4.4, which itself depends on the solution of $\nabla^2\phi = 0$ for the electric potential in the vacuum. Both the Laplace equation for ϕ and the Poisson equation for p are solved using overrelaxation; the provisional velocities are then updated according to the calculated pressure values at the next step. This method is described as semi-implicit since the velocities are updated explicitly while the pressures are updated implicitly.

4.1.5.2 Simulation results

The method described above is used to simulate the motion of a liquid surface in an electric field and the results compared with the perturbation theory in Sec. 4.1.3 in order to verify that the code is producing physically-realistic results. The simulation domain is a cylinder of radius 10 μm and height 20 μm which is half-filled by a conducting liquid with the same viscosity, density and surface tension as tungsten as given in Tab. 1.1. The Debye length in tokamak plasmas is slightly larger than 10 μm so the dimensions

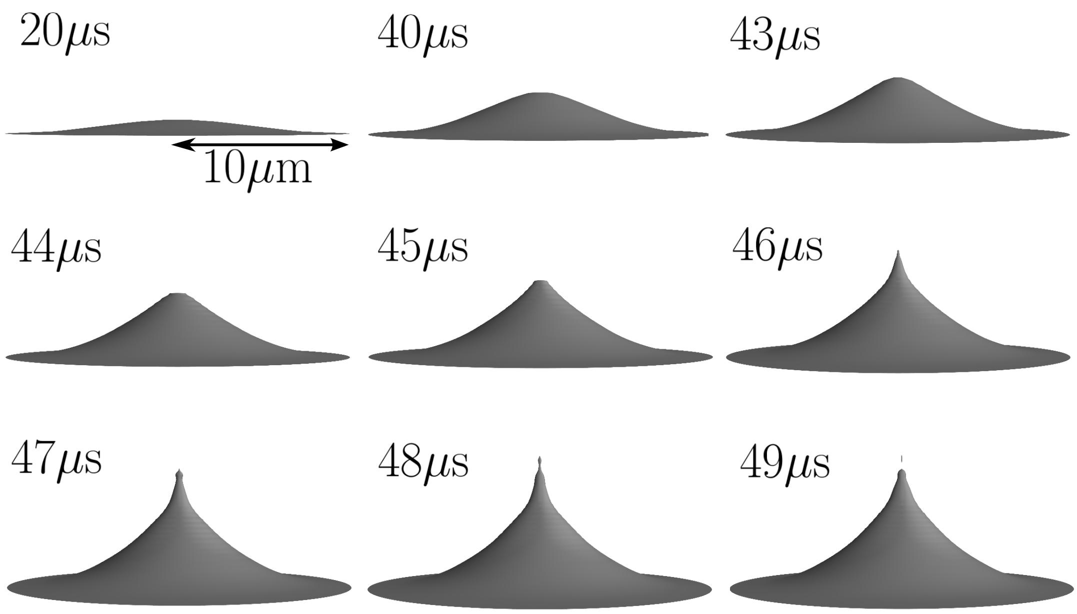

Figure 4.3: Axisymmetic simulation of the growth of a Taylor cone and ejection of droplets from an unstable tungsten surface of radius 10 μm in an electric field given by $\epsilon_0 E_0^2/\gamma k = 1.1$.

of the simulation correspond to the ideal electrohydrodynamic regime described at the start of this chapter. A fixed potential difference is applied between the top of the cylinder and the liquid surface which has an initial height perturbation given by a zeroth-order Bessel function with peak-to-trough amplitude 0.5 μm. The radial wavenumber is $k = 3.8217 \times 10^5$ m^{-1} which corresponds to the first minimum of the Bessel function occurring at $r = 10$ μm. The linear perturbation theory predicts, from the dispersion relation in Eq. 4.37, that this perturbation grows exponentially at a rate of

$$i\omega = \left(\frac{\gamma k^3}{\rho}\right)^{1/2} \left(\frac{\epsilon_0 E_0^2}{\gamma k} - 1\right)^{1/2} \tag{4.47}$$

where gravity is neglected. Growth rates can be extracted from the simulations and compared with this prediction in order to make a quantitative comparison between theory and simulation.

The growth of a Taylor cone from this initial setup is shown in Fig. 4.3 for an electric field given by $\epsilon_0 E_0^2/\gamma k = 1.1$. The apex of the cone is then drawn out into a jet which pinches off into a fine jet of droplets. This process appears to be in good qualitative agreement with experimental observations [229] although the exact mechanism of droplet pinch-off is likely to be adversely affected by the grid spacing used in the simulation as the apex of the cone approaches the size of the numerical grid. As such the size of the ejected droplets tends to be determined by the grid resolution, which places a lower limit on the size of the simulated droplets, rather than by any physical effects.

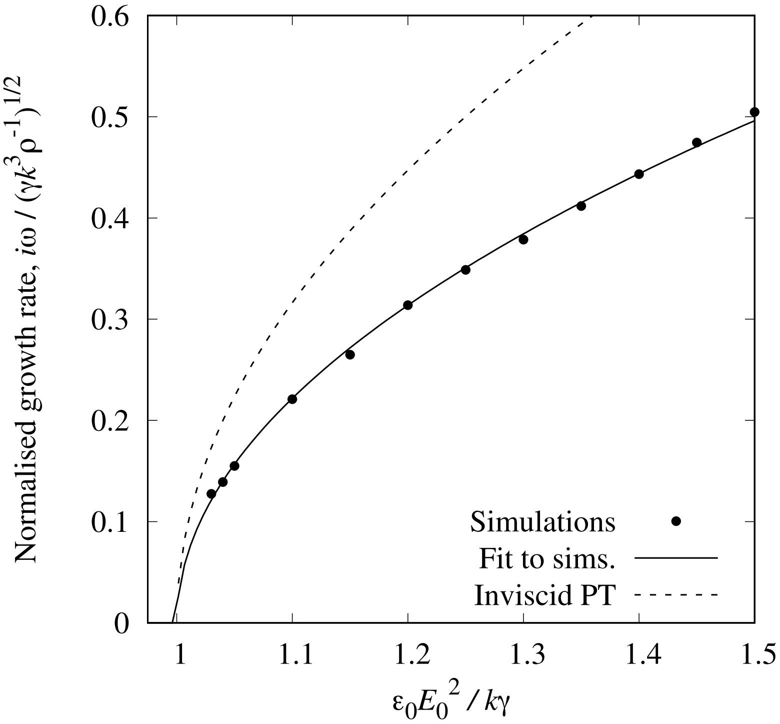

Figure 4.4: Comparison of the growth rates of ideal electrohydrodynamic instabilities as estimated from simulations of a 10 μm radius tungsten surface in an electric field and the linear perturbation theory (PT) according to Eq. 4.47.

The simulation is run for various electric field strengths as characterised by the factor $\epsilon_0 E_0^2/\gamma k$. The amplitude of the surface perturbation increases exponentially during the early stages of each simulation, as predicted by the linear perturbation theory, so growth rates can be extracted by least-squares fitting exponential curves to these growing amplitudes. The results are shown in Fig. 4.4 along with the growth rates predicted by Eq. 4.47. The simulation results lie on a line with the formula $0.702(\epsilon_0 E_0^2/\gamma k - 1)^{1/2}$ whereas the linear perturbation theory predicts that the factor before the square root should be exactly one. Therefore the growth rates observed in the simulation are 30% lower than predicted the linear perturbation theory; this discrepancy is tentatively assigned to the inclusion of viscosity in the simulations. However the marginal stability limit, $\epsilon_0 E_0^2 = \gamma k$, is accurately reproduced by the code which gives a strong indication that the simulations are producing physically-realistic results.

4.1.5.3 Ideal electrohydrodynamic instabilities in practice

At this point it is natural to wonder whether the electrohydrodynamic instability described by these simulations is responsible for the ejection of droplets from plasma-facing liquid metal surfaces in tokamaks. The answer is likely to be no. The critical electric field required to make a tungsten surface become unstable, determined according to Eq. 4.47 as $\epsilon_0 E_0^2 = \gamma k$, is over 100 MV m^{-1} for the 10 μm radius perturbation shown in

Fig. 4.3. The electric field at a surface in a planar floating-potential hydrogen sheath, with $\Phi_{Z=0} = -2.839$ according to Eq. 3.14, is

$$E_{z=0} = \frac{k_B T_e}{e\lambda_D} F_{z=0} = \frac{k_B T_e}{e\lambda_D} \left[2\left(1-2\Phi\right)^{1/2} + 2\exp\left(\Phi\right) - 4 \right]_{z=0}^{1/2} = 3.32 \text{ MV m}^{-1} \quad (4.48)$$

where F is defined in Tab. 2.1 and determined by the stress continuity equation in the sheath as given in Eq. 3.15. This electric field is clearly insufficient to initiate a short-wavelength electrohydrodynamic instability of the surface. If the initial perturbation has a larger wavelength than these simulations, and hence a smaller value of k, then the marginal stability criterion predicts a smaller critical electric field strength which could be experienced in a standard sheath. However such a perturbation would require surface deformations on a lengthscale larger than the Debye radius and the ideal electrohydrodynamic equations would no longer apply. The full plasma-liquid theory and simulation of these large scale instabilities is considered in Sec. 4.2.

On the other hand some applications of plasma-liquid interactions involve the application of a large electrical voltage, which far exceeds the floating value, to a liquid cathode. Vyalykh provided the first experimental study of electrically-driven oscillations and instabilities of liquid cathode surfaces in low-pressure glow discharges [230]. Bruggeman later applied the electrohydrodynamic marginal stability condition, Eq. 4.38, to argue that water cathodes are always electrically-unstable for typical plasma glow discharge parameters and that this instability is manifest in observations of the plasma splitting into a filamentary structure [231]. The importance of charge accumulation on plasma-facing liquid surfaces is also demonstrated by the recent experiments of Dubinov who observed unusual deformations of a liquid surface in a capillary tube and between thinly-spaced capillary plates when a spark discharge was applied to the surface of an ionic solution [232].

4.1.6 Bubble bursting in an electric field

The linear stability theory and simulations considered so far make the assumption that the surface of the liquid is almost flat before the instability begins. This idealised initial configuration is not always accurate; for example the bubble bursting mechanism for droplet formation from a liquid surface, as introduced in Sec. 1.3.4, begins with the air cavity left at the surface of the liquid after its covering thin film has burst. Previous work has identified this mechanism as a leading contender for droplet ejection from molten surfaces in tokamaks but have not yet accounted for the role of the electric field in the sheath. The significance of this omission is indicated by the experiments of de Temmerman *et al.* where the ejection of droplets from melted aluminium and tungsten targets in the Magnum-PSI device was attributed to bubble bursting [31]. The ejection rate of aluminium droplets increased by a factor of 10 when the surface was at floating potential, rather than being grounded, and further increased by another factor of 10 when the target was biased at -40 V. The axisymmetric simulation described in the

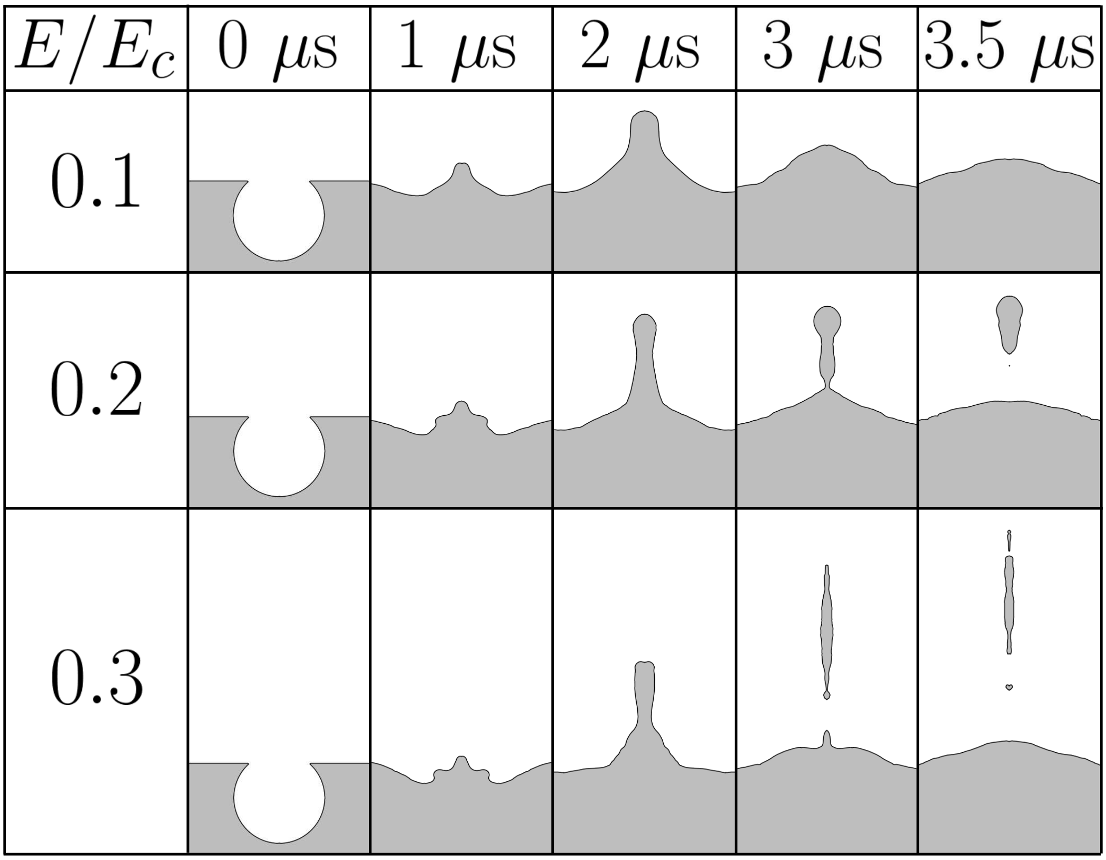

Figure 4.5: Axisymmetric simulations of droplet formation by a bursting bubble at a molten aluminium surface in an electric field. The simulation domain extends beyond the regions shown. The application of an electric field to the surface, such as the field generated by a plasma sheath, enhances the ejection rate of droplets even when the field alone would be insufficient to cause an electrohydrodynamic instability.

previous section can be used to investigate the role of electric fields in enhancing the bubble bursting mechanism and to explain the findings of these experiments.

The evolution of an aluminium surface with a spherical cavity, of radius 10 μm and with its centre positioned 7.5 μm below the liquid surface, is shown in the top row of Fig. 4.5. The liquid region is 4 bubble radii (40 μm) deep and 4 bubble radii from its centre to its outer radial edge. A small potential difference is applied between the liquid and the top of the simulation domain which is located 8 bubble radii (80 μm) above the liquid surface. Gravity is ignored in this simulation. The electric field at the start of the simulation has some enhancement at the corners where the bubble meets the surface while the electric field inside the bubble is almost zero due to the shielding effect of the bubble cap. The bubble collapses rapidly after the simulation is initiated which causes a jet of liquid to shoot upwards but, before it can pinch off into a droplet, surface tension pulls this jet back down. This contradicts the findings of Shi, Miloshevsky and Hassanein who did observe pinching-off of the liquid aluminium column [155]. This difference could well be due to their smaller simulation domain, which is 3 bubble radii in depth and 2 bubble radii in radius, which concentrates energy into the upwards motion of the jet.

The second and third rows of Fig. 4.5 show the development of the bubble-bursting process with the same initial conditions as before but with a larger potential difference applied between the liquid and the top of the simulation domain. If the surface was perfectly-flat then the electric field generated by this potential difference would still be insufficient to initiate an electrohydrodynamic instability with a wavelength equal to the bubble radius; the ratio of the applied field to the critical field required for this electrohydrodynamic instability is indicated for each simulation. The electric field strength is significantly enhanced once the liquid jets begin to form as evidenced by the small nodules which are pulled out of the liquid surfaces in the 1 μm frames. The second row shows the electric field removing a single large droplet from the rising jet of liquid whereas the jet is elongated before being pinched-off in the third row. The resulting column of liquid in the bottom-right frame then appears to become unstable to the Rayleigh-Plateau instability discussed in Sec. 1.3.3. The ejection of liquid droplets from the bubble-bursting mechanism is clearly facilitated and enhanced by sub-critical electric fields in accordance with de Temmerman's experimental observations [31]. The highly-curved surfaces created by the bubble bursting mechanism lead to significant enhancements in the electric field strength over that of a planar surface; such geometric effects can be just as important in determining the stability of a plasma-facing surface as the raw strength of the electric field.

4.2 Full plasma-sheath-liquid interface

The results of the previous section are valid when deformations to the plasma-liquid interface occur on lengthscales smaller than a Debye length but the effects of the ions and electrons, on both the modification to the electric field and their thermal and ram pressures on the liquid, must be included for larger scale surface deformations. This section considers the theory and simulations of plasma-liquid interfaces with these effects included.

4.2.1 Linear stability theory

The linear stability theory for a liquid surface in a perpendicular electric field can be extended by replacing the vacuum region with a plasma. The basic model is one of a liquid surface adjacent to a standard Bohm sheath described in Sec. 3.1 as illustrated in Fig. 4.6. The height of the liquid surface has a plane-wave perturbation and gravity is neglected. Much of the preliminary donkey work has already been performed in Sec. 4.1.3. The equations in the liquid region remain unchanged, as does the surface convection condition, so the pressure in the liquid is still given by Eq. 4.34 as

$$p_1 = \frac{\omega^2 \rho \xi_1}{k} \exp(kz). \tag{4.49}$$

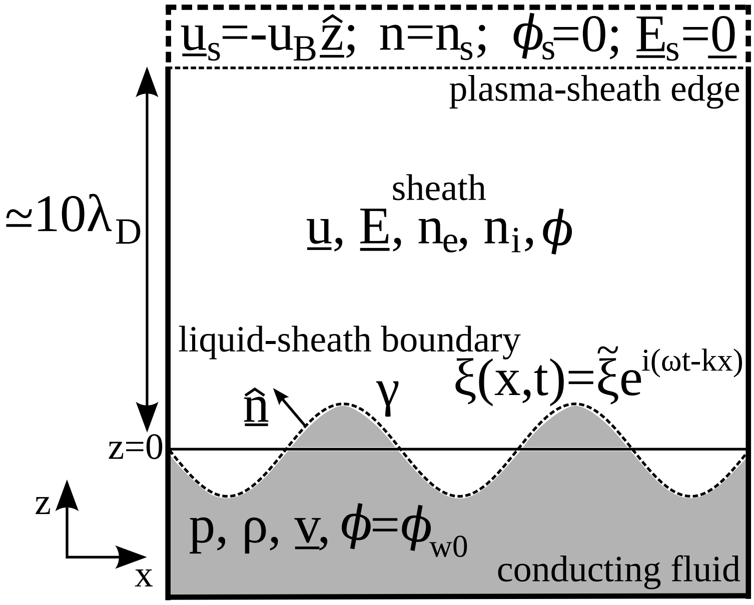

Figure 4.6: Illustration of the plasma-sheath-liquid transition with a plane-wave surface perturbation (from Ref. [233]). The liquid surface is biased by a fixed wall potential ϕ_{w0}.

Likewise the normal and curvature of the surface are unmodified from Eqs. 4.18 and 4.19. However the equations in the plasma region and the pressure jump condition must now account for the presence of the electrons and ions.

The cold-ion, Boltzmann-electron plasma equations are

$$\frac{\partial N_i}{\partial \tau} + \nabla \cdot (N_i \underline{U}_i) = 0, \tag{4.50}$$

$$\frac{\partial \underline{U}_i}{\partial \tau} + (\underline{U}_i \cdot \nabla)\underline{U}_i = -\nabla \Phi, \tag{4.51}$$

$$\nabla^2 \Phi = \exp(\Phi) - N_i \tag{4.52}$$

as previously stated in Eqs. 3.21-3.23. The boundary conditions for these equations are given by the equality form of the Bohm condition far from the surface as

$$N_i (Z \to \infty) = 1, \qquad \underline{U}_i (Z \to \infty) = -\hat{\underline{z}}, \qquad \Phi (Z \to \infty) = 0 \tag{4.53}$$

and at the surface by

$$\hat{\underline{n}} \times [\underline{F}]_{z=\xi} = \underline{0}. \tag{4.54}$$

Note that N_i and $\underline{U}_i$ require only one boundary condition each, as only their first derivatives appear in the sheath equations, while Φ requires two boundary conditions. The plasma is coupled to the liquid by the pressure jump condition, Eq. 2.63, which is

$$p_{z=\xi} = n_s k_B T_e \left[-\hat{\underline{n}} \cdot \underline{\underline{\Sigma}} \cdot \hat{\underline{n}} - \frac{1}{Bo_P} \frac{\kappa}{\lambda_D} \right]_{z=\xi} \tag{4.55}$$

Table 4.1: Typical values of the plasma Bond number for some common plasma-liquid interfaces involving the liquids and plasmas specified in Tabs. 1.1 and 1.2.

Plasma	Liquid	Bo_P
MAST	Lithium	4×10^{-4}
ITER	Beryllium	2×10^{-3}
ITER	Tungsten	7×10^{-4}
Arc torch	Aluminium	1×10^{-3}
DC air	Water	5×10^{-5}
RF argon	Methanol	6×10^{-5}

where $\underline{\underline{\Sigma}}$ is the dimensionless plasma stress tensor, defined by Eq. 2.39, and

$$Bo_P = \frac{n_s k_B T_e \lambda_D}{\gamma} \tag{4.56}$$

is named as the plasma Bond number. The plasma Bond number can be identified as the ratio of the plasma pressure at the sheath edge to the capillary pressure at the liquid surface; this name is motivated by comparison with the electric Bond number which is the ratio of electrostatic Maxwell stress to capillary pressure [234]. Typical values of Bo_P for common plasma-liquid interfaces are around 10^{-3} or 10^{-4} as indicated by Tab. 4.1. The pressure jump condition allows ω and k to be related and hence provides the dispersion relation; however the ultimate purpose of this perturbation analysis is to determine the marginal stability condition of the surface perturbations which is the point where ω transitions from real to imaginary values *i.e.* at $\omega^2 = 0$. With this aim in mind, the cold-ion, Boltzmann-electron equations are simplified by removing the ω terms. Furthermore the liquid pressure perturbation, in Eq. 4.49, is zero at this point so the transition from a stable to unstable surface is determined by the linearised marginal stability condition

$$\left[\left(\underline{\hat{n}} \cdot \underline{\underline{\Sigma}} \cdot \underline{\hat{n}}\right)_1\right]_{z=\xi} - \frac{1}{Bo_p}\frac{\kappa_1}{\lambda_D} = 0. \tag{4.57}$$

The zeroth-order solution in the plasma region is determined by the numerical integration of Eq. 3.15 starting from the wall; the wall potential is taken here to be fixed by an externally-applied voltage, as is common for industrial low-pressure plasma-liquid applications, rather than given by the floating condition. Although the spatial sheath profiles require a numerical integration they have an implicit solution in terms of Φ_0 as

$$U_{iz0} = -\left(1 - 2\Phi_0\right)^{1/2}, \tag{4.58}$$

$$N_{i0} = \left(1 - 2\Phi_0\right)^{-1/2}, \tag{4.59}$$

$$F_{z0} = -\left[2\left(1 - 2\Phi\right)^{1/2} + 2\exp\left(\Phi\right) - 4\right]^{1/2} \tag{4.60}$$

where the expression for the field follows from the continuity of stress, $\nabla \cdot \underline{\underline{\Sigma}}$, which gives $\Sigma_{zz0} = -2$ where the constant is determined by the equality Bohm condition at $Z \to \infty$. Note, as a brief aside, that the equation for F_{z0} can be used to determine the critical potential of the liquid surface, Φ_c, at which it becomes susceptible to ideal electrohydrodynamic instabilities. The ideal electrohydrodynamic marginal stability condition is given by Eq. 4.38 as $\epsilon_0 E_0^2 > \gamma k$ in the absence of gravity. E_0 can be expressed in terms of F_0 according to $E_0 = k_B T_e F_0 / e\lambda_D$, as defined in Tab. 2.1, and the surface tension γ is expressed in terms of Bo_P from Eq. 4.56 to give

$$\epsilon_0 \frac{k_B^2 T_e^2 F_0^2}{e^2 \lambda_D^2} > \frac{n_s k_B T_e \lambda_D}{Bo_P} k. \tag{4.61}$$

Inserting Eq. 4.60 for F_0 and making the assumption $\Phi \ll -1$, so that $\exp(\Phi) \approx 0$, gives an expression for the ideal electrohydrodynamic marginal stability transition in terms of a critical liquid surface potential Φ_c as

$$\Phi_c = \frac{1}{2}\left[1 - \left(2 + \frac{k\lambda_D}{2Bo_P}\right)^2\right]. \tag{4.62}$$

The first-order sheath equations, after ω has been set to zero, are given by

$$\frac{\partial \Phi_1}{\partial Z} = -F_{z1}, \tag{4.63}$$
$$\frac{\partial \left(N_i U_{iz}\right)_1}{\partial Z} = ik\lambda_D N_{i0} U_{ix1}, \tag{4.64}$$
$$\frac{\partial U_{ix1}}{\partial Z} = \frac{ik\lambda_D \Phi_1}{U_{i0}}, \tag{4.65}$$
$$\frac{\partial (U_{iz0} U_{iz1})}{\partial Z} = F_{z1}, \tag{4.66}$$
$$\frac{\partial F_{z1}}{\partial Z} = N_{i1} - \Phi_1 \exp\left(\Phi_0\right) - \left(k\lambda_D\right)^2 \Phi_1, \tag{4.67}$$

and the linearised surface condition, from Eq. 4.54, gives

$$\Phi_{1,z=\xi} = F_{z0,z=0} \frac{\xi_1}{\lambda_D} \tag{4.68}$$

which is simply Eq. 4.32 expressed in terms of dimensionless variables. These perturbed equations require numerical evaluation, even with the $\omega = 0$ simplification made, and the numerical method is briefly outlined as follows. Firstly Eq. 4.66 can be immediately integrated to give $U_{iz1} = -\Phi_1 / U_{iz0}$. Application of the chain rule $\partial/\partial Z = -F_{z0} \partial/\partial \Phi_0$ then allows the integration to be performed over a finite domain of Φ_0 values rather than the infinite domain of Z values; this also allows direct use of the implicit zeroth-order solutions in Eqs. 4.58-4.60. However using Φ_0 as the integration variable introduces an irregular point at the sheath edge where $\Phi_0 = 0$. A Taylor series expansion of Eqs. 4.63-4.67 at this point proved itself to be extremely difficult to find so an alternative shoot-and-correct method has been developed. This method essentially guesses the values of the perturbed sheath quantities after the first step of the integration and calculates the subsequent steps using the shooting RK4 method until the liquid surface at $\Phi_0 = \Phi_{0w}$ is reached. The perturbation to the electric potential is then compared

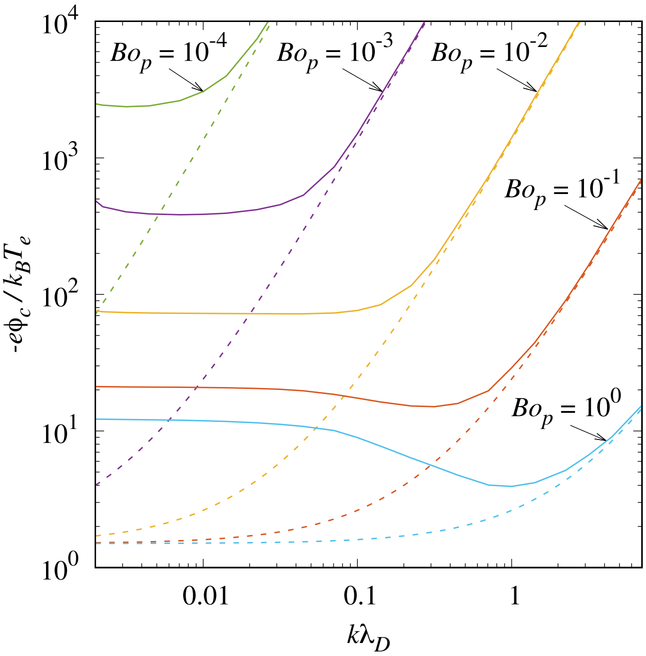

Figure 4.7: The critical value of the potential of the liquid surface at which the liquid becomes unstable as a function of wavenumber k and for a range of plasma Bond numbers Bo_P (from Ref. [233]). The ideal electrohydrodynamic behaviour, from Eq. 4.62, is indicated by the dashed lines and is replicated by the plasma-liquid interface when, roughly, $k\lambda_D > 1$.

to the boundary condition $\Phi_{1,z=0} = F_{z0,z=0}\xi_1/\lambda_D$ and the initial guessed values are updated accordingly. This cycle of shooting and correcting is continued until the Φ_1 boundary condition is satisfied to within a given error tolerance which was taken to be at least 1 part in 10^5.

The solution of the linearised sheath equations gives the zz-component of the first-order stress tensor at the liquid surface in its normalised form according to

$$\Sigma_{zz1,z=0} = \left[F_{z0}F_{z1} + U_{iz0} - U_{iz0}\left(N_iU_{iz}\right)_1 - \Phi_1\right]_{z=0} \tag{4.69}$$

which is, of course, a linear function of the surface height perturbation ξ_1/λ_D. The fact that Σ_{zz0} is constant throughout the sheath means that no Taylor expansion needs to be considered in order to extrapolate the stress from $z = 0$ to $z = \xi$. This stress perturbation is inserted into the linearised marginal stability condition

$$\Sigma_{zz1,z=0}\frac{\lambda_D}{\xi_1} = \frac{k^2\lambda_D^2}{Bo_P}. \tag{4.70}$$

which follows from Eq. 4.57. The term on the left is computed for various values of surface potential and wavenumber and Eq. 4.70 is subsequently solved for different values of Bo_P in order to find the critical surface potential Φ_c at which the surface becomes unstable. The results are displayed as solid lines in Fig. 4.7.

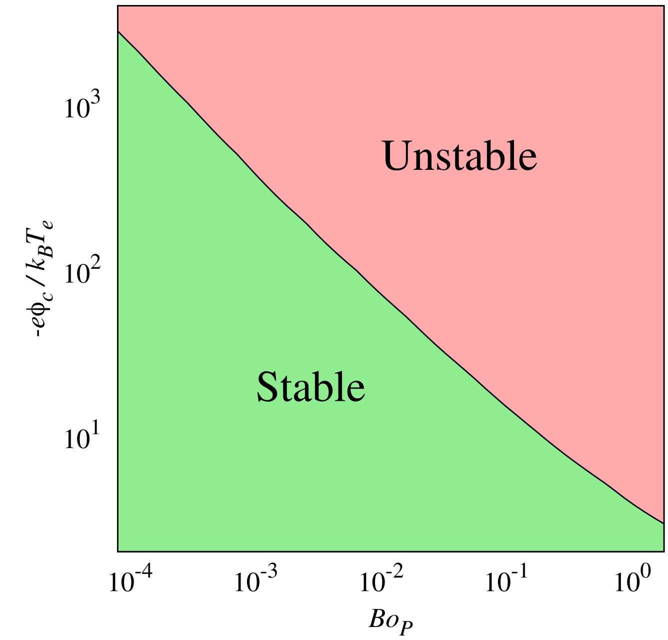

Figure 4.8: Plot of the minimum surface potential required to cause the liquid surface to become unstable for each value of Bo_P (from Ref. [233]). These values are determined by the minimum points of the solid curves shown in Fig. 4.7.

Two main regimes are observed in Fig. 4.7. The sloping region towards the right of the plot corresponds exactly to the critical field strength for the EHD instability given earlier by Eq. 4.62 and displayed as dashed lines. However this behaviour ceases when, roughly, $k\lambda_D \lesssim 1$ *i.e.* for plane-wave perturbations with wavelengths longer than a few Debye lengths. This departure from the ideal electrohydrodynamic theory indicates that the electric field no longer provides the dominant force on the liquid surface and ion bombardment of the surface can suppress the onset of the electrohydrodynamic instability. The transition between the two regimes is relatively sharp for $Bo_P \ll 1$ but becomes broader and exhibits a slight dip in the critical surface potential as Bo_P approaches unity.

The stability criterion can be investigated further by finding the minimum potential which must be applied to the liquid surface in order to make any plane-wave surface perturbation become unstable. These are extracted as the minima of curves such as those in Fig. 4.7 and are plotted against the plasma Bond number in Fig. 4.8. The results tend to $\Phi_c = -1/2$ for large values of Bo_P in accordance with the ideal electrohydrodynamic limit given by Eq. 4.62.

The last part of Sec. 4.1.5.3 speculated that large wavelength perturbations in tokamaks might be susceptible to electrohydrodynamic instabilities. The full plasma-liquid theory developed in the present section refutes this suggestion. Typical values of Bo_P for tokamaks, as given in Tab. 4.1, tend to be no greater than 10^{-3} while their floating surface potentials are around $e\phi_0/k_BT_e \approx -3$. These values mean that liquid surfaces in tokamaks operate well inside the stable region indicated on Fig. 4.8. However, although the sheath alone is insufficient to cause droplet emission, it remains highly plausible that the electric field plays some role in enhancing the size and rate of droplet ejection by the bubble-bursting mechanism considered in Sec. 4.1.6.

4.2.2 Simulations of sheath-liquid interfaces

The linear perturbation theory can predict the onset of an instability but can only describe the dynamics of a plasma-liquid interface when $\xi \ll \lambda_D$. The non-linear dynamics beyond these small perturbations must be resolved with numerical simulations. These are performed by coupling the axisymmetric cold-ion, Boltzmann-electron equation solver, which is described in Sec. 3.1.2, with the axisymmetric ideal electrohydrodynamic simulator detailed in Sec. 4.1.5 using the plasma-liquid interface pressure jump condition in Eq. 4.55. This combined simulation therefore solves the Navier-Stokes equations in the liquid region under the pressure gradients generated by surface tension, electric fields, ion ram pressure and electron thermal pressure at the liquid surface. The surface of the liquid evolves on a long timescale compared to the time taken for rapidly-moving electrons and ions to adjust to the new surface shape. These different temporal scales are accounted for by taking numerous steps of the plasma simulation to find a steady sheath profile at each time step of the liquid simulation. The amalgamation of the two codes into one simulation is relatively straightforward as they both utilise a staggered grid arrangement which remains unchanged throughout the simulation domain. The level-set method is still used to determine surface tension forces and to distinguish the plasma and liquid regions; positive values of the level-set function indicate the liquid region while negative values demarcate the plasma region.

The simulations presented in this section are initially configured with a liquid occupying the bottom of a cylindrical domain with a depth of $10\lambda_D$. A small zeroth-order Bessel function perturbation is applied to its surface with its maximum at $r = 0$ and its first minimum at the outer radius of the simulation domain. Varying the outer radius of the domain therefore determines the value of $k\lambda_D$ for the initial perturbations. The liquid is taken to have the viscosity and surface tension of water specified by Tab. 1.1.

The plasma (sheath) region has a height of $30\lambda_D$ above the liquid surface and the asymptotic boundary conditions of Sec. 3.1.2 are applied at its upper edge. A fixed potential drop is applied across this sheath region. Increasing the width of the sheath region beyond $30\lambda_D$ leads to prohibitively long runtimes; this limit on the sheath width means that attention is restricted to potential drops of $\Phi_w < 1000$ and hence plasma Bond numbers of $Bo_P > 0.01$. These values of Bo_P are outside the typical range for plasma-liquid interfaces given in Tab. 4.1 but the dynamics of stable or unstable surfaces, *i.e.* cone and jet formation, are expected be similar for all plasma-liquid interfaces.

Simulations are run, for specified values of $k\lambda_D$ and Bo_P, with a range of wall potentials in order to determine the transition from stable to unstable surfaces. A typical stable surface is displayed in Fig. 4.9 which has $k\lambda_D = 1$, $Bo_P = 0.1$ and $\Phi_w = -30$.

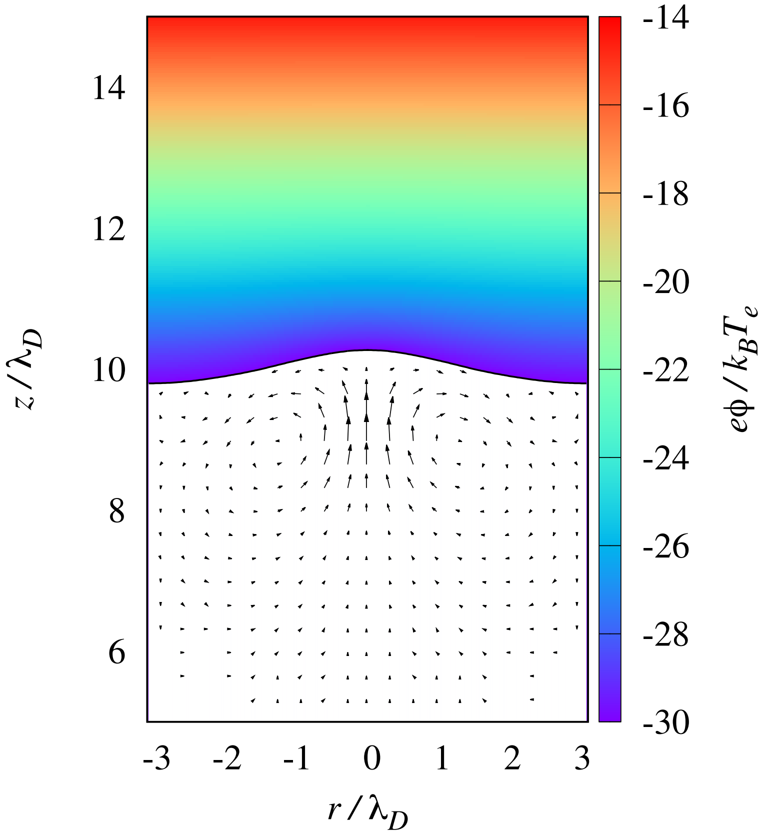

Figure 4.9: Simulation of a stable plasma-facing liquid interface, with $Bo_P = 0.1$ and $\Phi_w = -30$, showing the formation of a shallow cone. The liquid is not stationary but circulates steadily under the pressure gradients generated by the plasma stresses at the liquid surface.

The surface rapidly assumes a cone-like shape but with a rounded top and a much shallower opening angle than the $\alpha = 49.3°$ predicted by Taylor's theory in Sec. 4.1.2. Furthermore the liquid is not stationary but circulates steadily in response to the pressure gradients generated by the plasma stresses at the liquid surface.

The stable cone shown in Fig. 4.9 is on the cusp of becoming unstable; a slight increase in the potential of the liquid surface to $\Phi_w = -32$ leads to the formation of a jet of droplets as shown in Fig. 4.10. The simulation method imposes that these droplets are at the same potential as the liquid surface which is certainly true at the instant of their formation but which might change as they interact with the plasma and attain their floating potential. Once these droplets are ejected they appear to shield the tip of the cone from the electric field in the sheath which leads to the collapse of the cone. The duration of the entire process is around 10 μs for the water-like liquid parameters used in this simulation.

The critical wall potential, which causes a transition from stable cones to unstable droplet formation, is identified for a range of initial perturbation wavelengths and plasma Bond numbers of 0.01, 0.1 and 1. The results are plotted in Fig. 4.11 and compared with the linear stability calculation from Sec. 4.2.1. The simulations are in good agreement with the linear theory for short-wavelength perturbations in the sloping region where

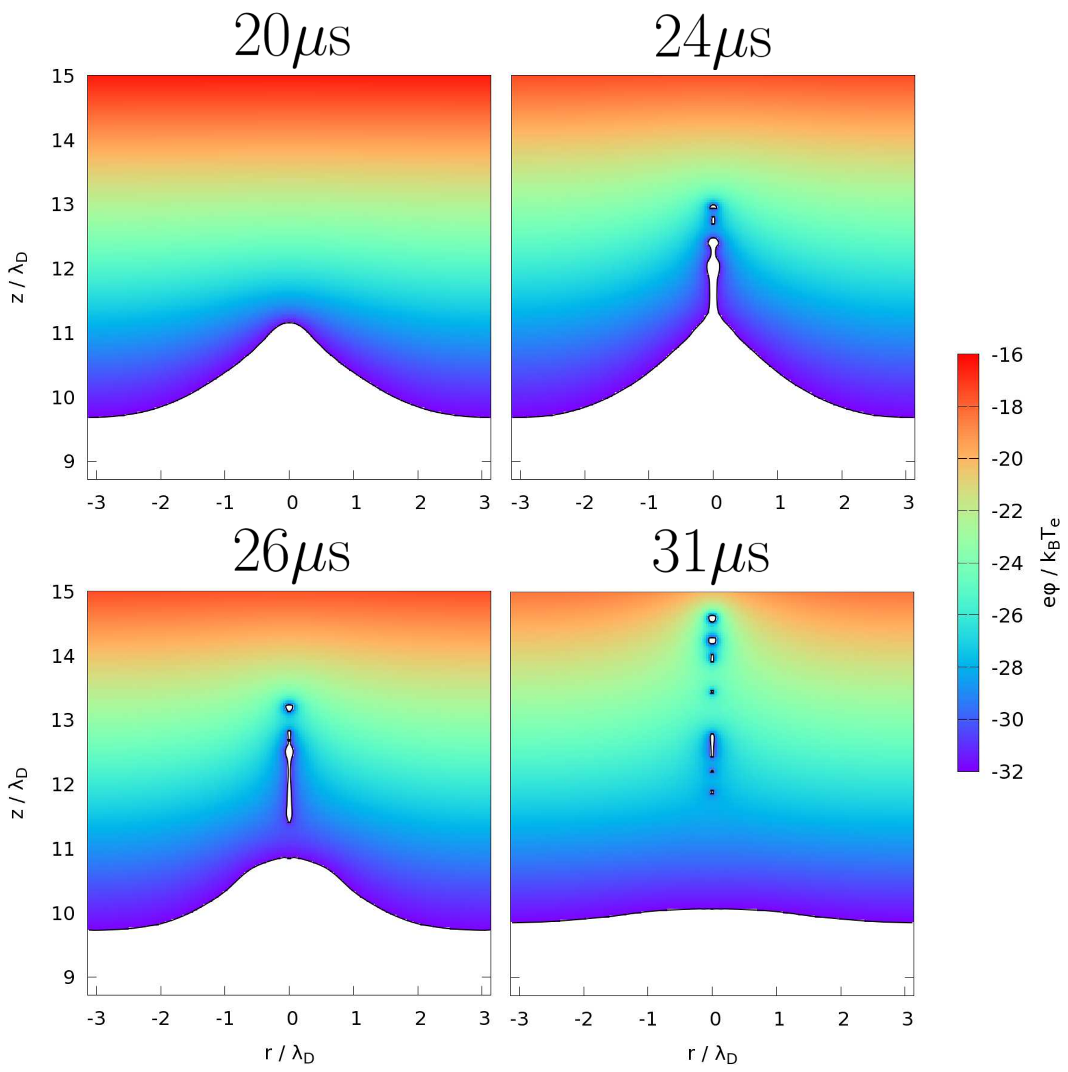

Figure 4.10: Simulation of an unstable plasma-liquid interface, with $Bo_P = 0.1$ and $\Phi_w = -32$, showing the formation of a Taylor cone, ejection of a burst of droplets, and subsequent collapse of the cone. The duration of the entire process is around 10 μs for the water-like liquid parameters used in this simulation.

the ideal electrohydrodynamic equations are valid. Both sets of results then flatten-out for wavelengths longer than the Debye length but the corresponding values of Φ_w differ between the linear theory and simulations: the linear theory flattens at normalised potentials of 12, 21 and 72, for plasma Bond numbers of 1, 0.1 and 0.01 respectively, whereas the equivalent values for the simulations are 2, 8 and 50. However the presence of the electrons and ions in the plasma still stabilises the surface compared to having the electric field alone.

There are several possible causes of the quantitative discrepancy between theory and simulation. For example the linear theory in Sec. 4.2.1 is developed for plane-wave perturbations whereas the simulations use axisymmetric cylindrical geometry. The marginal stability condition is identical for plane-wave and cylindrical perturbations

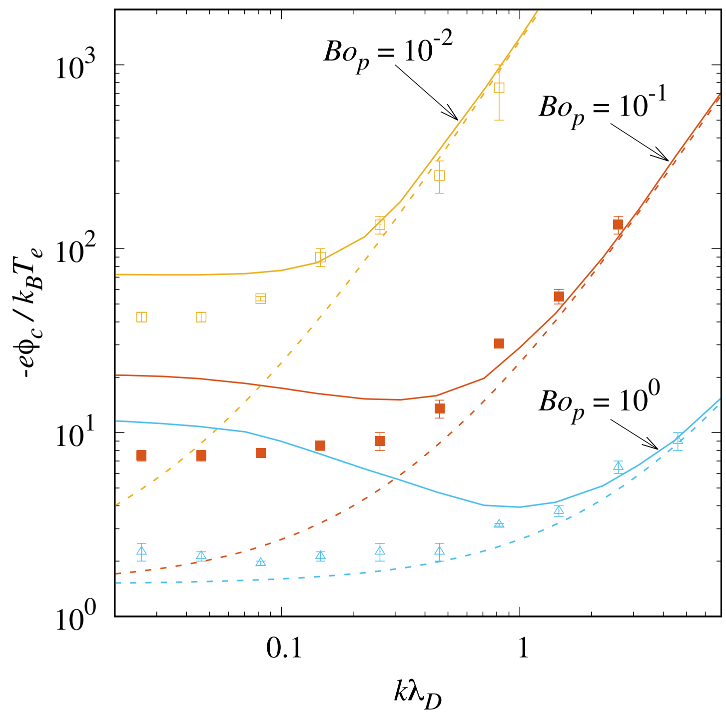

Figure 4.11: Comparison of the critical wall potential, which causes a transition from stable to unstable surfaces, given by the plane-wave perturbation theory in Fig. 4.7 and numerical simulations of a plasma-liquid interface in cylindrical coordinates. The suppression of electrohydrodynamic instabilities by ion impact, while still present, has less effect on axisymmetric perturbations than plane-wave perturbations.

of the ideal electrohydrodynamic liquid-vacuum interface, as shown in Sec. 4.1.4, but this does not appear to be true when the electron and ion effects are included. The simulations also require a finite-sized perturbation to initiate the instability, rather than the infinitesimal surface displacement of the linear theory, which could remove the system from a local equilibrium configuration. Most significant, however, is probably the difference in equilibrium shape. The linear theory took a perfectly-flat surface as the unperturbed equilibrium while the simulations can also handle conical equilibrium shapes. The electric field at the tip of a cone is enhanced compared to a flat surface so, for the same applied potential, the conical surface experiences a higher electric field and is expected to be less stable. A similar geometric field-enhancement effect has already been seen in the earlier example of bursting bubbles where the electric field can initiate droplet ejection below the planar ideal electrohydrodynamic stability limit.

4.2.3 Experimental comparison

The recent experiments of Shirai *et al.* have imaged the formation of corona discharges on the surface of a Taylor cones which are accompanied by the ejection of fine droplets from the cone tip [235, 236]. The formation of droplet plumes is also reported by Schwartz

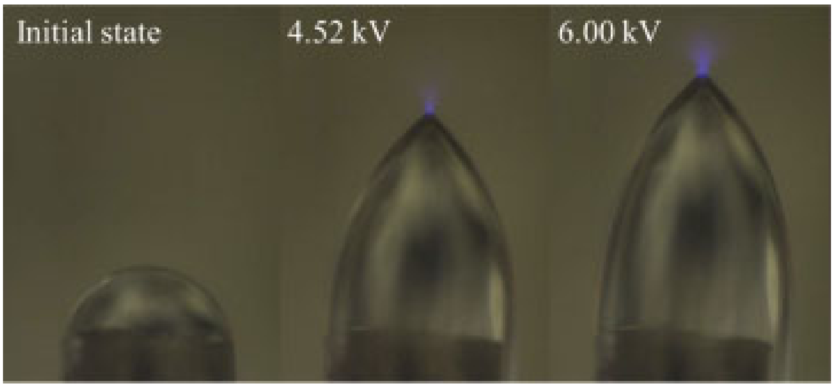

Figure 4.12: The formation of a Taylor cone in an experimental DC air-water discharge (from Ref. [235], copyright 2014 The Japan Society of Applied Physics). The onset of cone formation and droplet ejection is consistent with the marginal stability condition calculated by the linear theory of plasma-liquid interfaces.

et al. [237]. It is difficult to make exact comparisons between Shirai's experiments and the simulations reported on here but some important similarities can be identified.

Shirai's most recent experiment used a nozzle of diameter 1.5 mm filled with an ionic solution as a negative electrode and placed it beneath an upper plate electrode. A DC potential difference of up to 15 kV was applied between these two electrodes in order to initiate a plasma in the atmospheric air above the liquid cathode. Various compounds were dissolved in the water: sodium dodecyl sulfate to lower its surface tension and sodium chloride to increase its conductivity. When the applied voltage reached 4.52 kV the liquid surface deformed into a Taylor cone, as shown in Fig. 4.12, and produced a fine jet of droplets. It is difficult to determine exactly how much of the potential difference is dropped across the sheath and the presheath but assuming an electron temperature of 1 eV, as indicated for a typical DC air discharge in Tab. 1.2, gives a normalised sheath potential drop of $\Phi_w \approx -4500$. Furthermore the Bond number of the plasma-liquid interface is roughly $Bo_P \approx 10^{-4}$ when the lowering of surface tension due to the surfactant is accounted for. These values correspond well to the theoretical stable-to-unstable transition encountered in the upper-left corner of Fig. 4.8.

The cones formed in Shirai's experiments also lead to the formation of droplets and detection of current pulses at the upper plate electrode. These current pulses, which are displayed in Fig. 4.13, are accompanied by a sharp increase in the light intensity from the discharge. The numerical studies of droplet formation from Taylor cones at a plasma-liquid interface provide one possible explanation for these current pulses. The simulation shown in Fig. 4.10 illustrates the ejection of a burst of droplets followed by the collapse of the Taylor cone over a timescale of around 10 μs which roughly matches the duration of the current bursts in Fig. 4.12. A slow recovery of the tip of the cone over the following 100 μs would then account for the gaps between the current pulses. It would be unwise to place too much weight on this circumstantial comparison between simulation and experiment but it confirms the importance of including electrohydrodynamic effects in theoretical studies of the plasma-liquid interface.

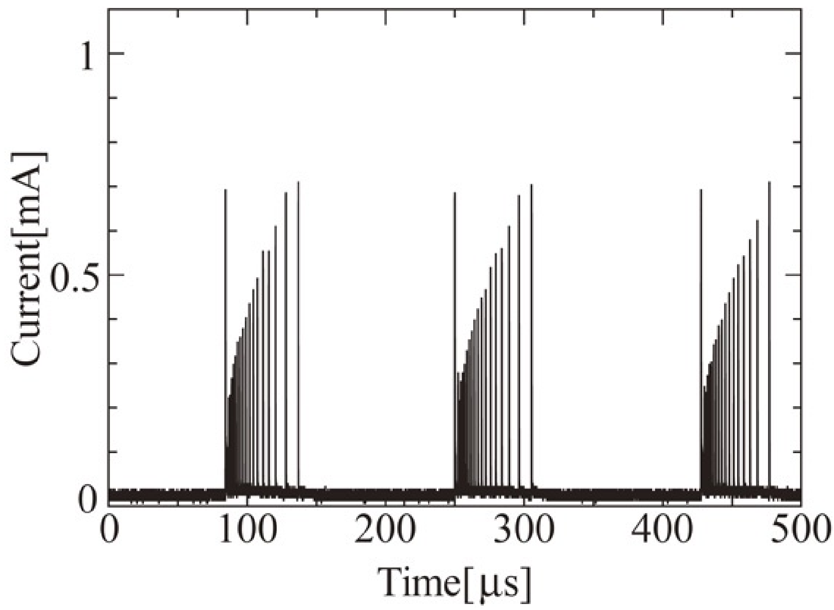

Figure 4.13: Experimental observations of current pulses at an electrode above a droplet-forming Taylor cone (from Ref. [238], copyright 2016 The Japan Society of Applied Physics). The timescales of these pulses indicates that they could be caused by the collection of bursts of charged droplets on the electrode.

4.3 Overview of plasma-facing liquid surfaces

This chapter has detailed some theoretical and computational investigations into the shapes and stability of liquid surfaces under the influence of an adjacent plasma. The role of the plasma in depositing charge on the liquid surface, and thereby exposing it to strong electric fields, is particularly crucial in determining the dynamics of the surface. The simulations of Sec. 4.2.2 show that electric fields in the plasma can deform the surface into a Taylor cone which ejects bursts of droplets from its apex in accordance with experimental observations. The ions from the plasma, which are accelerated through the electric field of the sheath, provide a countering force on the liquid surface which can suppress the onset of electrohydrodynamic instabilities; this mitigating effect is stronger for plane-wave perturbations than the axisymmetric perturbations which lead to Taylor cone formation. Ion bombardment of the liquid surface prevents electrohydrodynamic instabilities from occuring under typical tokamak edge conditions. However the field strength alone does not entirely determine the stability of a plasma-facing surface; the initial shape of the surface, and any geometric enhancement of the electric field, is vital in determining its behaviour. The example of field-enhanced droplet ejection from the bubble-bursting mechanism, considered in Sec. 4.1.6, demonstrates the importance of these geometric effects and explains the anomalous increase in droplet emission in experiments where the surface has a slight potential bias [31]. The electric field configuration must be fully accounted for when considering the stability of a plasma-facing liquid surface.

5 Plasma-immersed droplets

The shape and stability of a plasma-facing liquid surface has now been examined in detail. However Chapter 1 introduced a second major class of plasma-liquid interactions: droplets immersed in plasmas. Such droplets exist in plasma spraying processes, the exhaust from liquid-based plasma thrusters, and due to erosion of metal particles from tokamak walls or in plasmas cutting and welding devices. The interactions between these droplets and plasmas, as considered in Chapter 3, can cause the droplets to become charged or begin to spin rapidly. The present chapter investigates the implications of these effects on the shape and stability of droplets in plasmas.

5.1 Breakup of charged drops

5.1.1 The Rayleigh charge limit

A charged droplet experiences an outwards electrostatic force which tends to pull it apart; if this force exceeds the surface tension which holds the droplet together then it will disintegrate. Rayleigh first considered the electrohydrodynamic stability limit of charged droplets in 1882 [239] although his description is rather sparse and amounts to little more than writing down the result, now known as the Rayleigh criterion, that droplets which carry a charge

$$Q > 8\pi \left(\epsilon_0 \gamma a^3\right)^{1/2} \tag{5.1}$$

are unstable. The lack of detail in Rayleigh's derivation has prompted a number of revisitations of his linear theory, notably that of Hendricks and Schneider which boldly proclaims "to present the derivation of the stability theory, leaving out only the most obvious steps" before proceeding to omit intermediate results at the crucial moments [240]. A more thorough approach is taken in the 23-page derivation of Somboonkittichai [241]. Fortunately the Rayleigh limit can be obtained by the simpler means of an energy analysis of spheroidal droplets.

The surface area of a spheroid is given by the elongation α, defined in Fig. 3.10, as

$$S(\alpha) = \begin{cases} 2\pi a^2 \left[\alpha^{-1} + \dfrac{\alpha^2}{\left(1-\alpha^3\right)^{1/2}} \operatorname{sech}^{-1}\left(\alpha^{3/2}\right)\right] & \text{for} \quad \alpha < 1 \\ 4\pi a^2 & \text{for} \quad \alpha = 1 \\ 2\pi a^2 \left[\alpha^{-1} + \dfrac{\alpha^2}{\left(\alpha^3-1\right)^{1/2}} \sec^{-1}\left(\alpha^{3/2}\right)\right] & \text{for} \quad \alpha > 1 \end{cases} \tag{5.2}$$

which allows the energy associated with the surface tension of a liquid surface to be calculated as $U_S = \gamma S$. The electrostatic energy of a conducting spheroid which carries charge Q is given by $U_Q = Q^2/2C$ where the capacitance of the spheroid has already been given in Eq. 3.51. If the charge is quantified by the dimensionless parameter

$$x = \frac{Q^2}{64\pi^2\epsilon_0\gamma a^3}, \tag{5.3}$$

known as the fissility of the droplet, then the total energy of the spheroid, $U = U_S + U_Q$, can be expressed as

$$\frac{U(\alpha)}{2\pi a^2\gamma} = \begin{cases} \alpha^{-1} + \dfrac{\alpha^2}{(1-\alpha^3)^{1/2}}\,\mathrm{sech}^{-1}\left(\alpha^{3/2}\right) + \dfrac{4\alpha^{1/2}x}{(1-\alpha^3)^{1/2}}\cos^{-1}\left(\alpha^{3/2}\right) & \text{for} \quad \alpha < 1 \\ 2 + 2x & \text{for} \quad \alpha = 1 \\ \alpha^{-1} + \dfrac{\alpha^2}{(\alpha^3-1)^{1/2}}\sec^{-1}\left(\alpha^{3/2}\right) + \dfrac{4\alpha^{1/2}x}{(\alpha^3-1)^{1/2}}\cosh^{-1}\left(\alpha^{3/2}\right) & \text{for} \quad \alpha > 1. \end{cases} \tag{5.4}$$

where a normalising factor of $2\pi a^2\gamma$ has been utilised. This energy function is plotted in Fig. 5.1 for a range of oblate and prolate shapes. Stable spheroidal droplet shapes are identified using an energy minimisation procedure: equilibrium shapes correspond to stationary points of the energy function and these equilibria are stable if the stationary point is a minimum. The equations to be solved for stable spheroidal drops follow as

$$\frac{\partial U}{\partial \alpha} = 0 \qquad\qquad \frac{\partial^2 U}{\partial \alpha^2} > 0. \tag{5.5}$$

It is straightforward to extract the locations of the stationary points from Fig. 5.1 and plot them in terms of x and α to produce the bifurcation diagram shown in Fig. 5.2. Two bifurcation points are immediately evident with the transcritical bifurcation at $x = 1$ corresponding exactly to Rayleigh's stability limit. The other bifurcation point, for significantly elongated spheroids with $\alpha = 1.75$, is of little relevance to real liquid drops which will become highly nonspheroidal and unstable at such large deformations. The transcritical nature of the Rayleigh-limit bifurcation has been identified previously by Tsamopoulos, Akylas and Brown [242] and, subsequently, the family of oblate spheroid shapes at $x > 1$ were shown to be unstable to nonaxisymmetic perturbations by Natarajan and Brown [243]. Tsamopoulos notes that the existence of the unstable prolate spheroid shape family means that spherical drops charged below the Rayleigh limit are unstable to finite-amplitude perturbations which helps to explain the difficulties encountered in the experimental verification of the Rayleigh limit [244, 245].

The nonlinear dynamics of the disruption of charged, nonrotating drops can be resolved by numerical simulations using the finite-difference, level-set (FDLS) method described in Sec. 4.1.5 to solve the full set of ideal electrohydrodynamic equations. However the boundary conditions on these simulations must be adapted to account for the new configuration of the liquid surface. The electric potential takes a constant value at the surface of the conducting drop and, at the outer edge of the simulation, is

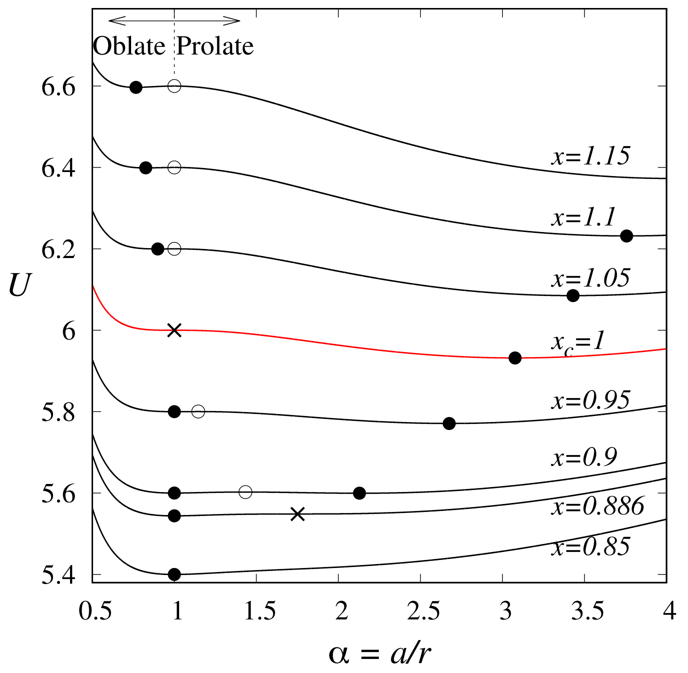

Figure 5.1: The potential energies of charged spheroidal liquid drops as a function of elongation α and charge fissility x. Closed circles indicate minima, *i.e.* stable equilibrium shapes, while the maxima shown by open circles give unstable equilibrium shapes. Reproduced from Ref. [227].

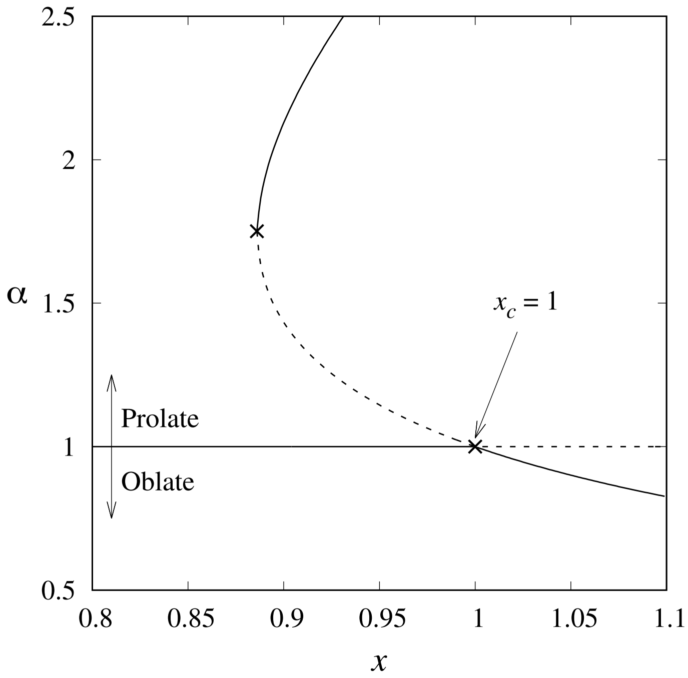

Figure 5.2: Bifurcation diagram for charged and non-rotating spheroidal liquid drops with the Rayleigh limit, $x = 1$, clearly displayed. The solid and dashed lines indicate stable and unstable axisymmetric equilibria respectively. The oblate spheroids for $x > 1$ are unstable to non-axisymmetric perturbations. Reproduced from Ref. [227].

determined by a truncated multipole expansion,

$$\phi(r,z) = \frac{Q}{4\pi\epsilon_0 R} + \frac{r^2 P_{rr} + z^2 P_{zz}}{4\pi\epsilon_0 R^5} + \mathcal{O}\left(\frac{1}{R^5}\right) \tag{5.6}$$

where Q is the charge on the drop, $R = (r^2 + z^2)^{1/2}$ is the radial distance in spherical coordinates and the quadrupole moments are estimated by those of a spheroid with the same charge and polar-to-equatorial axis ratio as the drop (Ref. [202, p. 28]):

$$P_{rr} = \frac{Q}{3}\left(l_2^2 - l_1^2\right), \tag{5.7}$$

$$P_{zz} = \frac{2Q}{3}\left(l_1^2 - l_2^2\right). \tag{5.8}$$

The symbols l_1 and l_2 indicate the major and minor axes, respectively, of the spheroid which approximates the shape of the drop in accordance with Fig. 3.10. The axisymmetric drops simulated in this paper have no dipole ($\phi \sim 1/R^2$) or hexapole ($\phi \sim 1/R^4$) moments so the leading-order omitted term is the the octupole ($\phi \sim 1/R^5$) term. Taking the gradient of Eq. 5.6 gives the electric field

$$E_z = \frac{Qz}{4\pi\epsilon_0 R^3} + \frac{5r^2 z P_{rr} + \left(3z^3 - 2r^2 z\right) P_{zz}}{4\pi\epsilon_0 R^7} + \mathcal{O}\left(\frac{1}{R^6}\right) \tag{5.9}$$

which is enforced as a Neumann boundary condition at the upper and lower edges of the cylindrical domain and a similar condition, with $r \leftrightarrow z$, at the outer radial surface. The shortest distance from these boundaries to the surface of the drop is three times the radius of the drop. The greatest inaccuracy in these boundary conditions arises from assuming spheroid-like quadrupole moments. This assumption is valid for moderately-deformed drops during the early development of the Rayleigh breakup process and, accordingly, it was found that extending the simulation domain did not modify the stability of the drops.

The deformation and eventual disruption of a drop, which is charged to just above the Rayleigh limit with $x = 1.02$, is displayed in Fig. 5.3. The simulation parameters correspond to a water drop of diameter 1 cm. The droplet is initialised with a slight prolate elongation of $\alpha = 1.02$ in order to trigger the instability which causes the droplet to slowly elongate, over several seconds, and form two symmetrical Taylor cones. Jets of highly-charged droplets are then rapidly emitted, on a sub-second timescale, from the tips of these cones which carry away the excess charge on the drop. This simulated breakup process is exactly the same as in experimental observations of overcharged drops [244, 245].

The charge accumulated on droplets in plasmas can, in some circumstances, be sufficient to initiate their electrostatic disruption as first noted by Coppins [246]. Combining the Rayleigh criterion, Eq. 5.1, with the vacuum capacitance of a sphere from Eq. 3.51

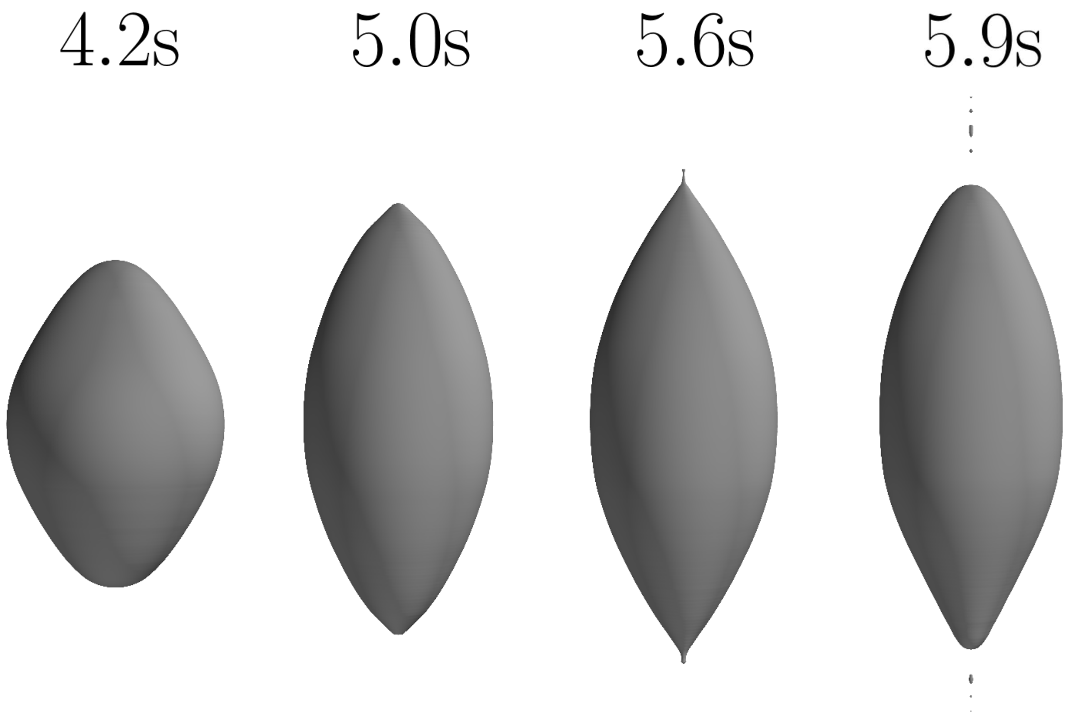

Figure 5.3: Simulation results for the evolution and disruption of an overcharged axisymmetric water drop of diameter 1 cm and fissility $x = 1.02$ via the formation of two Taylor cones. Adapted from Ref. [227].

gives an expression for the minimum electrostatically-stable droplet radius as

$$a_{min} = \frac{\epsilon_0 \phi_a^2}{4\gamma}. \tag{5.10}$$

Droplets which are larger than this value are stable while those which are smaller are disrupted into jets of smaller subdroplets through the Rayleigh mechanism. These subdroplets carry away most of the original charge on the droplet so the leftover main droplet becomes stable if the total droplet charge is conserved. However droplets in plasmas are rapidly recharged to above the Rayleigh limit by the electrons in the plasma; the initial triggering of electrostatic breakup in a plasma therefore causes the complete annihilation of the droplet [246].

5.1.2 Electrostatic breakup of small droplets in plasmas

The charge accumulated by a particular plasma-immersed droplet must be known in order to determine whether it is stable or unstable. Fortunately two droplet charging theories have already been considered in Secs. 3.2.1 and 3.2.3: the orbit-motion limited (OML) theory applies to small droplets, with $a \ll \lambda_D$, in plasmas with arbitrary T_i while the Allen-Boyd-Reynolds (ABR) theory applies to arbitrarily-sized droplets in cold-ion plasmas. The OML case is considered first.

The minimum droplet size for given plasma conditions can be estimated by comparing Eq. 5.10 with the maximum OML charge values in Eq. 3.49 which results in the expression

$$a_{min} = \frac{\epsilon_0}{4\gamma}\left[\frac{k_B T_e}{2e} W_0\left(\frac{m_i}{2m_e}\right)\right]^2. \tag{5.11}$$

The ion temperature is assumed to take the value which maximises ϕ_a, and therefore minimises a_{min}, so T_i does not appear explicitly in this expression. Inserting the typical plasma-liquid parameters in Sec. 1.4 yields a_{min} values of 12 nm, 27 nm or 74 nm for tungsten, beryllium or lithium droplets, respectively, in the edge plasma of JET. Typical droplets in tokamaks are over a micron in size but the Rayleigh breakup mechanism could play a role in the final stages of a droplet's lifetime. Water droplets in an DC air discharges have a smaller minimum radius of $a_{min} = 1$ nm, while methanol droplets in RF argon plasmas have $a_{min} = 16$ nm, which suggests that droplets in both cases are mostly immune from electrostatic breakup but, as in the tokamak case, the eventual annihilation of the droplets is electrically-driven. Note that the condition $a_{min} \ll \lambda_D$ is satisfied in all of these cases so the small-sphere OML limit is appropriate. Two factors could increase these values of a_{min} in real-world applications: sub-Rayleigh limit breakup is possible, perhaps even probable, for finite-sized perturbations of the droplet shape as noted above; and the presence of impurities or elevated temperatures can significantly reduce the surface tension of the liquids.

Bennet *et al.* have recently proposed a technique to deliver precise quantities of charge onto droplets by passing them through a plasma and initiating their electrostatic disruption [247]. However they intend to apply this method to micron-sized drops which are significantly larger than the typical values of a_{min}. No experimental observations of electrostatically-disrupting droplets in plasmas have been obtained yet but Bennet *et al.* have promised to make efforts in this direction [247].

5.1.3 Electrostatic breakup of large droplets in cold-ion plasmas

The OML theory is restricted to small droplets, with $a \ll \lambda_D$, where the electric field is well-described by a Coulomb potential but the presence of high numbers of electrons and ions in the vicinity of a large droplet can enhance its surface electric field. These large droplets might be susceptible to electrostatic breakup. The ABR theory provides a complete account of the radial motion of electrons and ions and allows the pressure at the surface of a spherical droplet to be evaluated, according to the pressure jump condition Eq. 2.63, as

$$p_{r=a} = n_0 k_B T_e \left[N_i U_{ir}^2 + N_e - \frac{F^2}{2}\right]_{r=a} - \gamma\kappa. \tag{5.12}$$

The term in the square brackets is simply the negative of the Σ_{rr} stress component and the surface curvature of the sphere is $\kappa = -2/a$. The surface pressure can be written in terms of the plasma Bond number, defined in Eq. 4.56 as $Bo_P = n_0 k_B T_e \lambda_D/\gamma$, as

$$\frac{p_{r=a}}{n_0 k_B T_e} = \left[N_i U_{ir}^2 + N_e - \frac{F^2}{2}\right]_{r=a} + \frac{2}{Bo_P}\frac{\lambda_D}{a} = -\left[\Sigma_{rr}\right]_{r=a} + \frac{2}{Bo_P}\frac{\lambda_D}{a}. \tag{5.13}$$

The droplet can only be in an equilibrium spherical configuration if this pressure is positive although this condition gives no information on whether the equilibrium is stable or unstable. Nevertheless a crude method for determining the disruption limit for the droplet is to find the point where the liquid pressure becomes negative. Note that this method yields the exact Rayleigh criterion for a charged droplet in a vacuum but this is no longer the case when the droplet is in an external gas of finite pressure.

The rr-component of the plasma stress tensor is required to determine the pressure inside the drop. Two limiting values of the radial plasma stress, for large and small spheres, are relatively straightforward to evaluate. The plasma near the surface of a large sphere, with $a \gg \lambda_D$, forms a standard planar sheath. The normal component of stress is uniform throughout this plasma, in accordance with the planar stress continuity equation Eq. 3.4, and can be evaluated far away from the surface as $\Sigma_{rr}(a \gg \lambda_D) = -1$. The pressure in Eq. 5.13 is always positive in this limit so the surface can be in equilibrium; however this equilibrium is not necessarily stable and its stability limit is determined by the perturbation theory in Sec. 4.2.1.

The opposite, small sphere, limit of the radial stress is dominated by the electric field generated by the highly-curved surface. Assuming a Coulomb-like electric field and utilising the small-sphere limit of the ABR sphere potential, provided by Eq. 3.32, gives the surface stress as

$$\Sigma_{rr,r=a}\,(a \ll \lambda_D) = \frac{F_A^2}{2} = \frac{\Phi_A^2}{2}\left(\frac{\lambda_D}{a}\right)^2 = \frac{(0.98)^2}{2}\frac{m_i}{2\pi m_e} = 0.0764\frac{m_i}{m_e}. \tag{5.14}$$

The small-sphere limit of the surface stress is always positive so, if it is sufficiently large, the pressure in Eq. 5.13 can become negative. In this case no spherical equilibrium droplets can exist and such droplets would always disrupt.

The radial stress component at the surfaces of spheres of varying radius and in different species of plasma are calculated using the ABR theory and displayed in Fig. 5.4. The small-sphere limit, shown by the dashed lines, is clearly evident. The use of a logarithmic scale means that the large-sphere limit cannot be displayed but, as already discussed, the pressure inside such large spherical droplets is always positive. The radial stress components from Fig. 5.4 are then compared to the strength of the surface tension of the droplet as quantified by Bo_P. The condition for the liquid pressure to be negative, and hence for no equilibrium to exist, is given by Eq. 5.13 as

$$[\Sigma_{rr}]_{r=a} > \frac{2}{Bo_P}\frac{\lambda_D}{a}. \tag{5.15}$$

This region of non-equilibrium spherical droplets is given by the area above the solid curves in Fig. 5.5. The small-sphere limit, given by Eq. 5.14, is displayed by the dashed lines. The typical values of Bo_P given in Tab. 4.1 are all well inside the "equilibrium exists" region of this plot although it must be remembered that these curves represent upper bounds for the stability limit and droplets with Bo_P values below the curves could still be unstable.

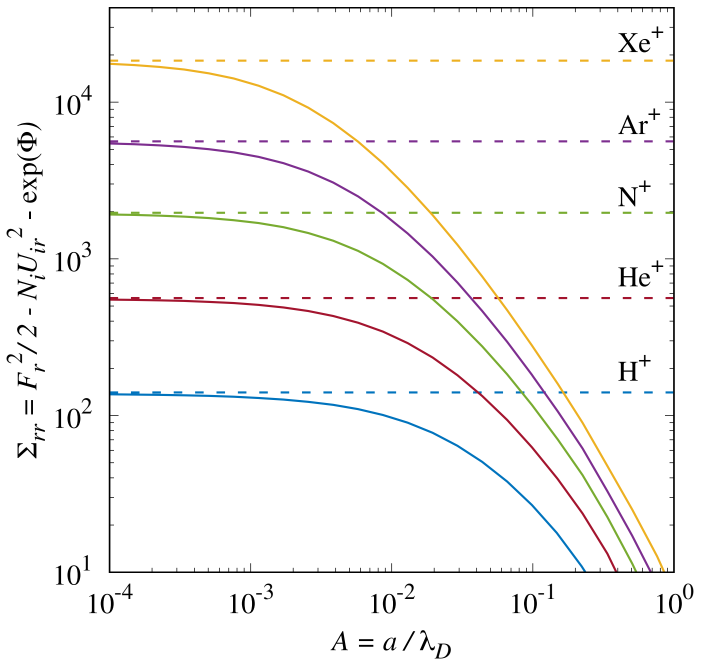

Figure 5.4: The rr-component of the plasma stress tensor at the surface of a spherical object in various cold-ion plasmas as calculated using the ABR theory. The small-sphere values, from Eq. 5.14, are indicated by the dashed lines.

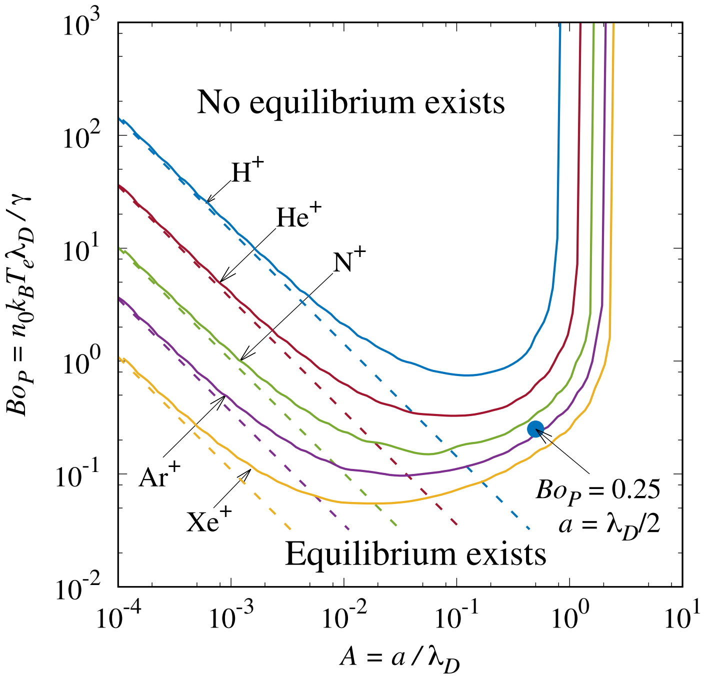

Figure 5.5: Upper bounds for the stability limits of droplets in cold-ion plasmas as determined by Eq. 5.15. Droplets described by the region above the curve have negative pressure so cannot exist in a spherical equilibrium shape. The stability limit $Bo_P = 0.25$ for a droplet with radius $a = \lambda_D/2$ in a cold-ion hydrogen plasma is indicated by the circle. This value of Bo_P is significantly higher than those encountered in typical plasma-droplet interactions.

5.2 Droplet breakup in flowing cold-ion plasmas

The calculation described in the previous section, where the loss of equilibrium of a droplet is determined from the point where its internal pressure becomes negative, provides an upper bound for the stability limit of droplets in cold-ion plasmas. A calculation of the exact stability limit for these droplets could proceed by two options: a linear perturbation theory or numerical solution of the full nonlinear equations describing the droplets. This section takes the second option for its extensibility to flowing plasmas.

The axisymmetric simulation method described in Sec. 4.2.2, which calculates the evolution and stability of a plasma-facing liquid surface, can be adapted to study a conducting liquid drop surrounded by a cold-ion, Boltzmann-electron plasma. Simulations of cold-ion plasma flow past an object, which have already been presented in Sec. 3.2.2, provide boundary conditions at the outer edge of the simulation domain. The plasma and liquid regions are coupled using the pressure jump condition and the simulation is run for various ratios of plasma pressure to surface tension, as quantified by Bo_P, in order to determine the shape and stability of these droplets. The results for droplets of radius $a = \lambda_D/2$ in flowing hydrogen plasmas are shown in Fig. 5.6.

The first thing to notice about Fig. 5.6 is that the value of Bo_P which is required to disrupt the droplet appears to be independent of the plasma flow speed; droplets with $Bo_P \leq 0.2$ are all stable while those with $Bo_P \geq 0.3$ are all unstable. The stability limit for a droplet in a cold-ion hydrogen plasma is tentatively placed at $Bo_P = 0.25$ irrespective of the flow speed. This point is indicated by the circle on Fig. 5.5 and found to be inside the region where equilibrium configurations for droplets in hydrogen plasmas exist. This agrees with the earlier assertion that the curves in Fig. 5.5 provide upper bounds on the stability limits. Conditions encountered by real-world plasma-immersed droplets, as characterised by Bo_P values in the range 10^{-3}–10^{-4} according to Tab. 4.1, are clearly insufficient for electrostatic or flow-induced breakup to occur.

The shapes of stable droplets, and the breakup dynamics of unstable droplets, are strongly affected by the speed of the plasma flow. Stable droplets with flow speeds of $u_f \leq 2c_s$ are deformed into teardrop shapes with the pointed ends aligned downstream. These pointed ends resemble the smoothed cones encountered in simulations of plasma-facing liquid surfaces, such as the one displayed in Fig. 4.9, and appear to be related to the formation of Taylor cones by electrical stresses. Fast flow speeds of $u_f \geq 4c_s$ cause the droplet to become slightly squashed shape in the direction of the flow. These squashed shapes closely match those of falling raindrops [248] and, as such, are probably attributable to the ram pressure of ions on the leading face of the drop. The timescale for deformation of the droplets is determined by the liquid parameters of the droplet; for example molten aluminium droplets of radius 10 μm take around 10 μs to assume a stable, static shape which is much slower than a typical plasma oscillation.

The shapes of unstable droplets immediately before their disruption follow a similar pattern. Moderate plasma flows of $u_f \leq 2c_s$ create teardrop shapes which eject subdroplets from their pointed downstream end while fast flows of $u_f \geq 4c_s$ cause the

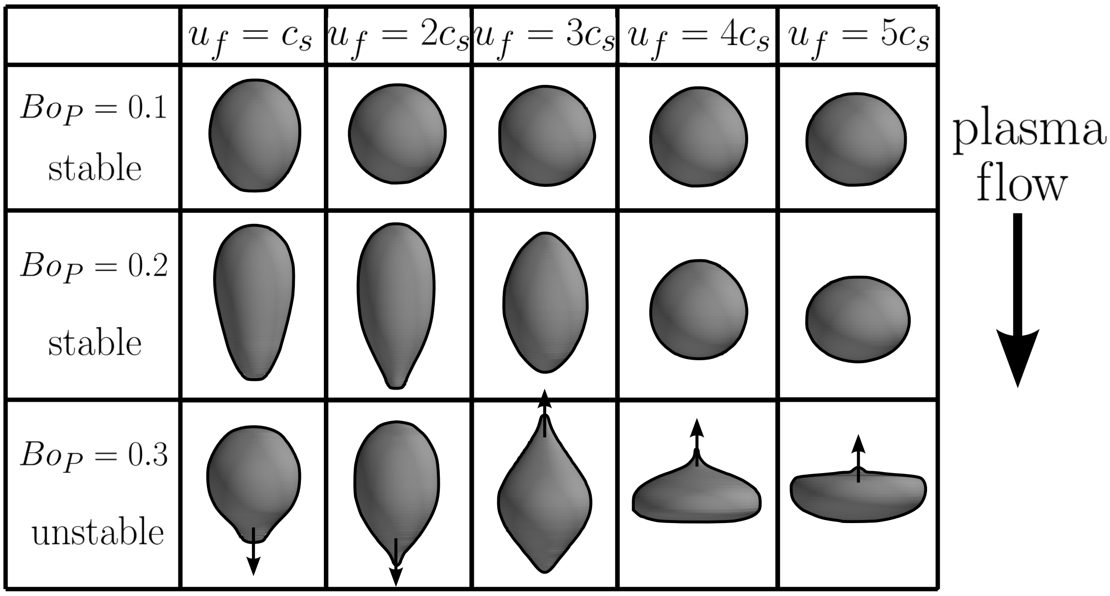

Figure 5.6: The shapes of stable droplets with $Bo_P \leq 0.2$ and unstable droplets with $Bo_P = 0.3$, shown immediately before their disruption, in cold-ion hydrogen plasmas. Slow flows cause the droplets to assume teardrop shapes while fast flows squash the droplets along the direction of the flow. Unstable droplets disrupt by ejecting subdroplets in the directions indicated by the arrows.

droplets to become flattened and eject subdroplets in the upstream direction. Droplets with intermediate flow speeds, of $u_f = 3c_s$, become elongated and release a jet of subdroplets in the upstream direction. These breakup mechanisms for droplets in flowing cold-ion plasmas all involve the ejection of charged jets of subdroplets in similarity with the electrostatic breakup process shown in Fig. 5.3.

5.3 Breakup of charged and spinning drops

The electrostatic breakup mechanism discussed Sec. 5.1.2 might explain the disruption of very small liquid droplets in warm-ion plasmas but it appears to be unable to explain the forked trajectories observed in images such as those from JET, as illustrated in Fig. 1.8, and DIII-D [37, Fig. 10]. These droplets split into two equally-sized subdroplets, which then split into another pair of subdroplets, and so on until the smallest droplets become invisible to the cameras; this is certainly inconsistent with the jet-forming electrostatic disruption mechanism shown in Fig. 5.2. Fortunately there is a second potential breakup mechanism for droplets in magnetised plasmas: rotational breakup.

The rotational breakup of simulated droplets is shown in Fig. 5.7 and is discussed in detail in Sec. 5.3.1. For now it is sufficient to observe that the breakup occurs through the formation of a two-lobed dumbbell shape and a subsequent split into a pair of equally-sized subdroplets. This two-lobed breakup mechanism is in good qualitative agreement with the camera images from tokamaks but a quantitative assessment requires knowledge of the stability limits of rotating droplets.

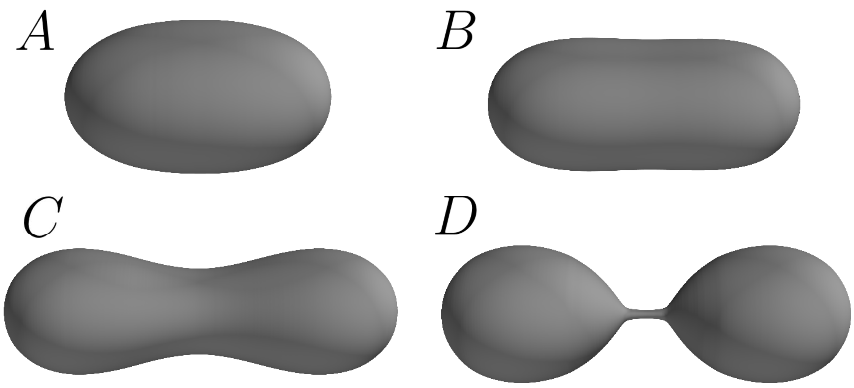

Figure 5.7: Simulated shapes of an uncharged, rotating drop with slowly increasing angular momentum as reproduced from Ref. [227]. The final drop (D) is shown immediately before a symmetrical fission and has $L = 1.146$; the corresponding experimental value is $L^{\max} = 1.15$ [249].

5.3.1 Stability limits of uncharged rotating droplets

The introduction of dimensionless parameters facilitates a straightforward comparison between existing theories and experiments and between drops on different lengthscales. The conventional definition of the dimensionless angular velocity, as introduced by Chandrasekhar [250], is

$$\Omega = \left(\frac{\rho_d a^3}{8\gamma}\right)^{1/2} \omega_d \tag{5.16}$$

where ω_d is the dimensional angular velocity of the droplet. The radius a is defined as that of a sphere with the same volume as the drop. The dimensionless angular momentum is defined in terms of the dimensional angular momentum $\mathcal{L}$ and the volume of the drop V as

$$L = \frac{\mathcal{L}}{(V^{7/3}\rho\gamma)^{1/2}} \tag{5.17}$$

using the convention of García-Garrido, Fontelos and Kindelán [251] and Liao and Hill [249]. Note that this differs from the definition used by others such as Brown and Scriven [252, 253].

The first comprehensive study of the breakup of uncharged rotating drops is the finite element analysis of Brown and Scriven [252, 253] which has since been extended by Heine [254]. These calculations show that slowly-spinning drops assume an axisymmetric flattened shape which is aligned with the axis of rotation. Such shapes are evident in, for example, the slight equatorial bulge of the Earth and can be well-approximated by oblate spheroids. When the angular velocity of the drop exceeds a critical value Ω^*, or equivalently the angular momentum exceeds L^*, the drop begins to elongate in a direction perpendicular to the axis of rotation. The values of Ω^* and L^* have been determined analytically and numerically as 0.559 and 0.628 respectively [250, 253] and confirmed by experiments [249, 255]. The drop transitions through triaxial ellipsoidal

Table 5.1: Summary of literature values of dimensionless angular velocity and momentum for the spheroid-to-capsule transition point of uncharged rotating droplets, Ω^* and L^*, and for the angular momentum which causes two-lobed fissioning of the droplet, L^{max}. †Chandrasekhar's exact Ω^* does not appear in his original paper but Brown & Scriven deciphered it as being 1.1% larger than their value.

Authors	Method	Ω^*	L^*	L^{max}
Chandrasekhar† [250, 253]	Theory	0.565	-	-
Brown & Scriven [253]	Simulation	0.559	0.628	1.08
Wang *et al.* (1986) [256]	Experiment	0.47	-	-
Biswas, Leung & Trinh [257]	Experiment	0.44	-	-
Wang *et al.* (1994) [255]	Experiment	0.563	-	-
García-Garrido, Fontelos & Kindelán [251]	Simulation	-	0.640	-
Liao & Hill [249]	Experiment	0.57	0.65	1.15
Holgate & Coppins [227]	Theory	0.53	0.626	-
Holgate & Coppins [227]	Simulation	0.48	0.618	1.148

shapes when Ω^* is reached before assuming an elongated capsule-like shape. The moment of inertia of the drop is increased in this capsule configuration and the angular velocity decreases as the angular momentum is increased. As such the angular velocities of stable drops do not exceed Ω^*. If additional angular momentum continues to be supplied to the drop then it assumes a two-lobed dumbbell shape which eventually splits into two large drops; this process has already been illustrated in Fig. 5.7. Often these are joined by a thin thread of liquid which subsequently bursts into several smaller drops. This breakup process occurs at L^{max} which has been determined experimentally as 1.15 [249] and numerically as 1.148 [227]. The full range of literature values of Ω^*, L^* and L^{max}, as determined by various methods, are summarised in Tab. 5.1.

The spheroid-to-capsule transition point can be investigated by means of a spheroidal energy minimisation approximation in the same way as for charged droplets. The moment of inertia of a spheroid is expressed in terms of the elongation α so that the rotational kinetic energy can be written as

$$\frac{T_0(\alpha)}{2\pi a^2\gamma} = \begin{cases} \dfrac{16\Omega^2}{15\alpha} & \text{for} \quad \alpha \leq 1 \\ \dfrac{8}{15}\left(\alpha^2 + \dfrac{1}{\alpha}\right)\Omega^2 & \text{for} \quad \alpha > 1. \end{cases} \tag{5.18}$$

with the dimensionless angular velocity Ω defined in Eq. 5.16. The total energy of the spheroid which is spinning with constant angular velocity is given by the slightly unusual-looking expression $U - T_0$ where U is the surface energy given by Eq. 5.4. The origin of the minus sign is the constraint of fixed angular velocity, rather than fixed angular momentum, which is analogous to switching the sign in the energy of a charged conductor in electrostatics. The change in energy of a charged conductor is $Q^2/2C$ when it has fixed charge but $-C\phi^2/2$ when it has fixed potential. Landau and Lifshitz explain the physical origin of the sign change by including the energy change of an external reservoir of charge; if the conductor gains some charge such that ϕ remains constant then the reservoir loses electrical energy with the overall energy change totalling $-C\phi^2/2$ [202, p. 32]. They also provide a more rigorous proof using the differential identity

$$dU = \phi dQ - F dx \tag{5.19}$$

where $U \equiv U(Q, x) = Q^2/2C$ has natural variables Q and x. Taking the partial derivative of $Q^2/2C$ with respect to Q gives Q/C which, by the definition of capacitance as $C = Q/\phi$, gives

$$\phi = \left.\frac{\partial U}{\partial Q}\right|_{\phi=const} \tag{5.20}$$

in accordance with the differential identity for dU. The force on this collection of charges is

$$F = -\left.\frac{\partial U}{\partial x}\right|_{\phi=const} \tag{5.21}$$

as usual. An exact differential with the natural variable ϕ can be constructed using $\tilde{U} = U - \phi Q = -U$ to give

$$d\tilde{U} = -Q d\phi - F dx \tag{5.22}$$

where $\tilde{U} \equiv \tilde{U}(\phi, x)$. This differential identity states that

$$Q = -\left.\frac{\partial \tilde{U}}{\partial \phi}\right|_{Q=const} = \left.\frac{\partial U}{\partial \phi}\right|_{Q=const} \tag{5.23}$$

which is once again evident by differentiating $U = C\phi^2/2$ and inserting $\phi = Q/C$. However the force on a conductor of fixed electrical potential is now given by

$$F = -\left.\frac{\partial \tilde{U}}{\partial x}\right|_{Q=const} = -\left.\frac{\partial (-U)}{\partial x}\right|_{Q=const}. \tag{5.24}$$

Similar arguments can be applied to the kinetic energy of a rotating body as given by $T_0 = I\omega_d^2/2 = \mathcal{L}^2/2I$ where I is the moment of inertia. The differential identity for a rotating body with fixed angular momentum is $dT_0(\mathcal{L}, x) = \omega_d d\mathcal{L} - F dx$ such that

$$F = -\left.\frac{\partial T_0}{\partial x}\right|_{\mathcal{L}=const} \tag{5.25}$$

while, for fixed angular velocity, it is $d\tilde{T_0}(\omega_d, x) = -\mathcal{L} d\omega_d - F dx$ and hence

$$F = -\left.\frac{\partial \tilde{T_0}}{\partial x}\right|_{\omega_d=const} = -\left.\frac{\partial (-T_0)}{\partial x}\right|_{\omega_d=const}. \tag{5.26}$$

The rotational energy contribution for a droplet spinning at fixed angular velocity is, therefore, $\tilde{T_0} = T_0 - \omega_d \mathcal{L} = -T_0$.

The spheroid energy, $U - T_0$, is calculated using Eq. 5.4, with $x = 0$, and Eq. 5.18.

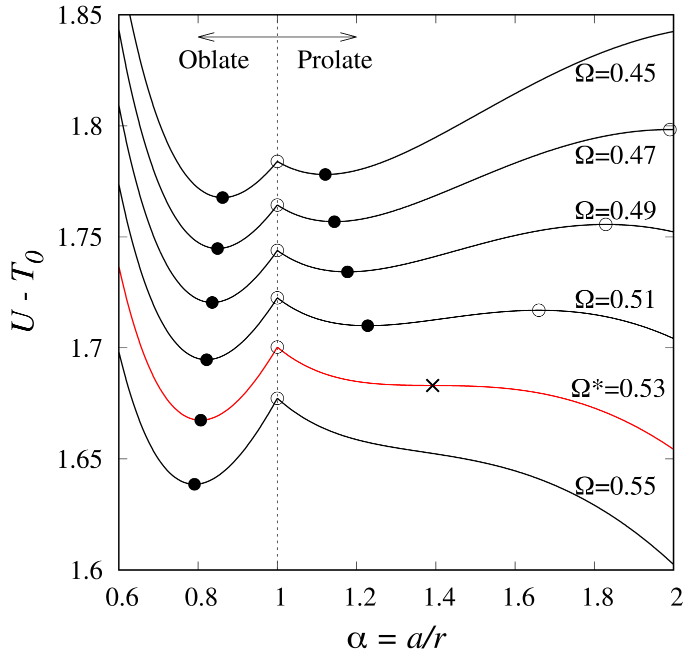

Figure 5.8: The potential energy of rotating and uncharged spheroidal liquid drops as functions of elongation and dimensionless angular velocity as reproduced from Ref. [227]. The oblate spheroid rotates around its unique axis of length l_1 while the prolate spheroid rotates around a degenerate axis of length l_2; this flipping of the rotation axis leads non-smooth solutions at $\alpha = 1$. The prolate shape family loses stability at the saddle-node bifurcation indicated by the cross for $\Omega^* = 0.53$.

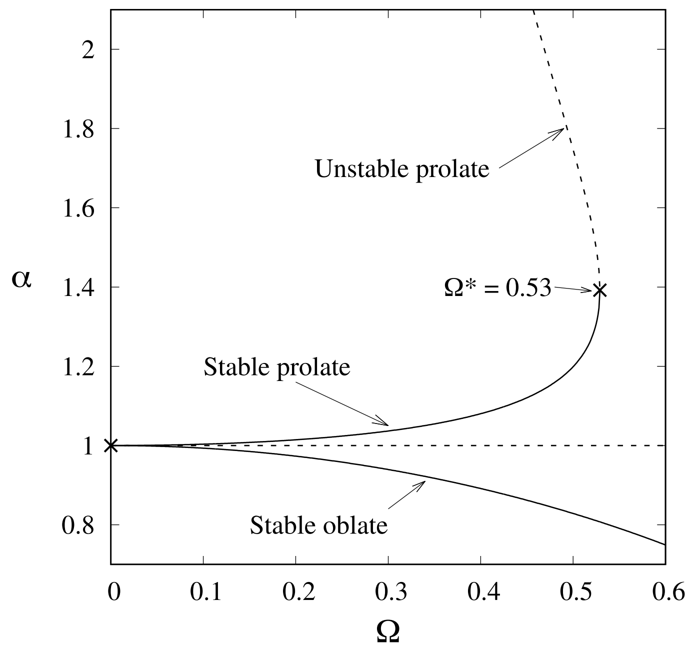

Figure 5.9: Bifurcation diagram for rotating and uncharged spheroidal liquid drops as reproduced from Ref. [227]. The prolate shape family transitions from stable to unstable equilibria, indicated by solid and dashed lines respectively, at the saddle-node bifurcation point at Ω^* with $\alpha = 1.4$. The oblate shape family remains stable for $\Omega > \Omega^*$.

These energies are plotted in Fig. 5.8 for spheroids with a range of angular velocities and elongations. The transition between prolate and oblate shapes at $\alpha = 1$ is not smooth because the axis of rotation flips from the unique axis of length l_1 for the oblate spheroids to one of the degenerate axes of length l_2 in the prolate case. The stable equilibria are, once again, determined by the locations of the minima while the maxima are identified as unstable equilibria which allows the bifurcation diagram in Fig. 5.9 to be constructed. A single saddle-node bifurcation is observed at $\Omega = 0.53$ which is close to the accepted value of the spheroid-to-capsule transition point $\Omega^* = 0.559$. Stable prolate spheroid shapes cannot exist for values of Ω above this transition point. However the stable oblate shape family extends to values of Ω beyond this transition point; this is in contradiction to Brown and Scriven's assertion that "all axisymmetric shapes that spin more rapidly than Ω_{II} [this paper's Ω] prove to be unstable to a two-lobed perturbation" [253, p. 345]. Drops which are having their angular momentum gradually increased can therefore remain in an oblate configuration above the Ω^* transition point; conversely drops which are having their angular momentum steadily decreased can assume stable prolate shapes below Ω^*. The coexistence of stable oblate and prolate shape families means that the shape of a droplet is dependent on its history. Such behaviour is termed hysteresis and is observed in droplet-spinning experiments [249, 255, 256]. The spheroid energy minimisation approximation can account for these previously-unexplained observations of shape hysteresis.

The prolate spheroid shape family with $\alpha > 1.4$ is unstable according to energy minimisation arguments. However real liquid drops do not immediately become unstable at large elongations and instead transition into two-lobed capsule and dumbbell shapes which cannot be captured by the spheroid approximation. These shapes can be resolved using numerical simulations instead. These simulations use the same numerical method as the finite-difference, level-set method introduced in Sec. 4.1.5 but with no electric field in the vacuum region. The disruptive force on the drop arises from its rotation instead. If the drop rotates like a rigid body, *i.e.* all fluid elements within the drop have the same angular velocity ω_d, then it can be studied in a frame of reference co-rotating with the drop with the momentum equation

$$\rho\frac{\partial \underline{v}}{\partial t} + \rho(\underline{v}\cdot\nabla)\underline{v} = -\nabla p + \eta\nabla^2\underline{v} + \rho r\omega_d^2. \tag{5.27}$$

The simulations are still performed on a staggered grid in cylidrical (r, z) coordinates which restricts the droplets to be axisymmetric; however if the axis of symmetry is chosen to be perpendicular to the axis of rotation then capsule and dumbbell shapes can be resolved. The simulation begins with a non-rotating drop which is subjected to a small, time-invariant torque. The angular velocity therefore varies slowly, *i.e.* adiabatically, on the timescale of deformation of the drop. This procedure replicates commonly-used experimental methods where levitated drops are slowly spun up and down by the application of small torques [249, 255, 256].

The change in elongation and angular velocity for a drop which is simulated by this

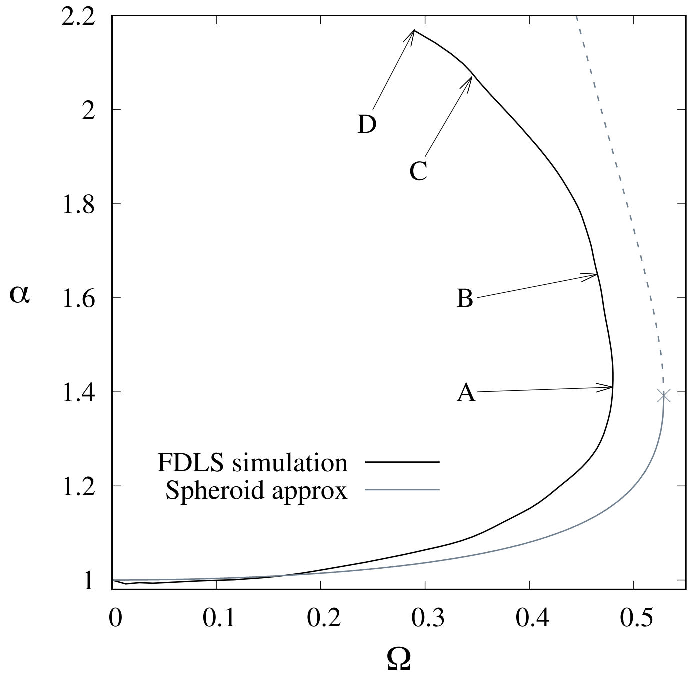

Figure 5.10: The elongation and dimensionless angular velocity of an uncharged simulated drop which is spun up by the application of a small, time-invariant torque as reproduced from Ref. [227]. The transition from prolate to capsule and dumbbell shapes is illustrated by the drop shapes at points A-D which are displayed in Fig. 5.7. The transition to these capsule and dumbbell shapes corresponds to the loss of stability of prolate spheroids in the spheroid model as indicated by the dashed grey line.

numerical method is displayed in Fig. 5.10. The parameters for a water drop of initial diameter 1 cm are used and the z-axis of the simulation is aligned perpendicularly to the rotation axis so that prolate and dumbbell shapes are captured. Figure 5.10 clearly exhibits the bending-back of the curve but the maximum angular velocity has a slightly lower value, $\Omega^* = 0.48$, than expected from the spheroid model and from previous theoretical and experimental studies. These discrepancies are likely to be caused by the axisymmetric constraint on the model whereas real drops can transition through arbitrary triaxial shapes. However the dimensionless angular momentum of the drop at this point is 0.618 which is in excellent agreement with both the spheroidal energy minimisation method, which predicts $L^* = 0.626$, and Brown and Scriven's value [253] of $L^* = 0.628$.

The angular momentum is steadily increased beyond the bend-back and the resulting drop shapes with angular momenta $L = \{0.6, 0.8, 1.1, 1.146\}$ are shown in Fig. 5.7. These correspond to the points labelled A-D respectively on Fig. 5.10. The drop eventually breaks up when the angular momentum reaches $L = 1.148$ which is slightly larger than Brown and Scriven's numerically-calculated value [253] of $L^{\max} = 1.08$ but in excellent agreement with Liao and Hill's experimentally-determined value [249] of $L^{\max} = 1.15$. However the experimental error in Liao and Hill's value makes it difficult to conclude

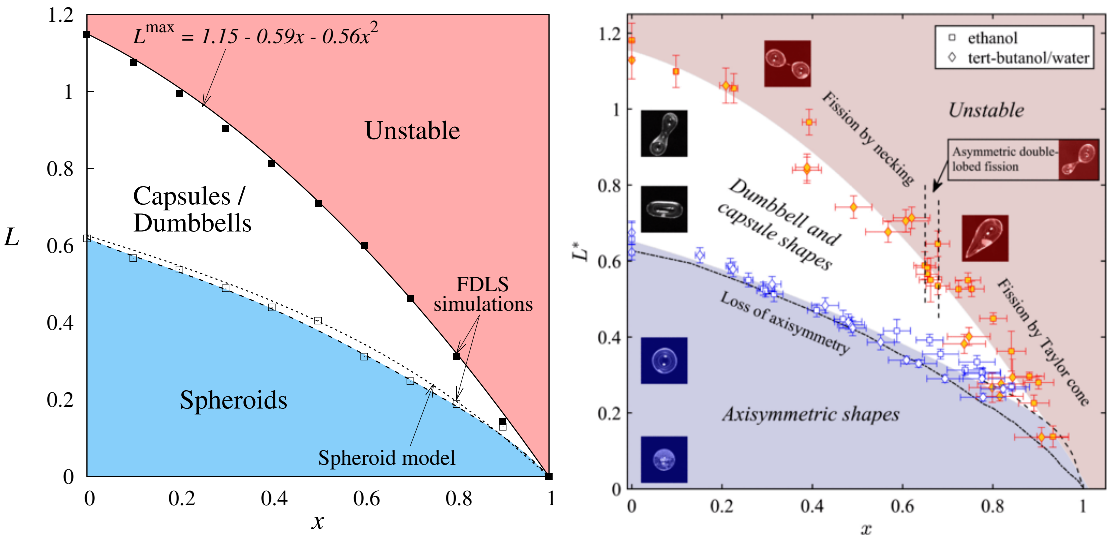

Figure 5.11: Left panel: Stability diagram for the spinning up of charged and rotating drops according to the spheroid model and FDLS simulations as reproduced from Ref. [227]. This diagram is in excellent quantitative agreement with the experimental results of Liao and Hill [249] (right panel). Note that Liao and Hill's variable L^* corresponds to the symbol L used in this thesis.

whether the simulations presented here are particularly more accurate than those of Brown and Scriven.

5.3.2 Stability limits of charged and rotating droplets

Droplets in magnetised plasmas are inevitably both charged and rotating, as discussed in Sec. 3.3, so the coexistence of both charge and rotation should be accounted for. The recent experiments of Liao and Hill [249] have investigated the stability limits of these drops; their results are shown in the right panel of Fig. 5.11. These results can be reproduced using the spheroidal energy minimisation approximation and simulation methods outlined in the previous section. The energy of charged and rotating spheroids is found from $U - T_0$ using Eqs. 5.4 and 5.18 but allowing for nonzero values of x. The simulations are initialised in the same manner as the water drops in the previous subsection but with a given amount of charge placed on the drop at the start of the simulation. The results of both methods are displayed in the left panel of Fig. 5.11. The empirical expression

$$L^{max} = 1.15 - 0.59x - 0.56x^2 \tag{5.28}$$

provides a good working formula for the stability limits of these charged and rotating drops. However caution is advised in the use of this formula for highly-charged drops with x approaching 1 which are unstable against non-linear perturbations which remove the drop from its local energy minimum as discussed in Sec. 5.1.1.

The unstable charged and rotating droplets can break up either through the formation of Taylor cones or by necking. Experimental observations show that charged drops

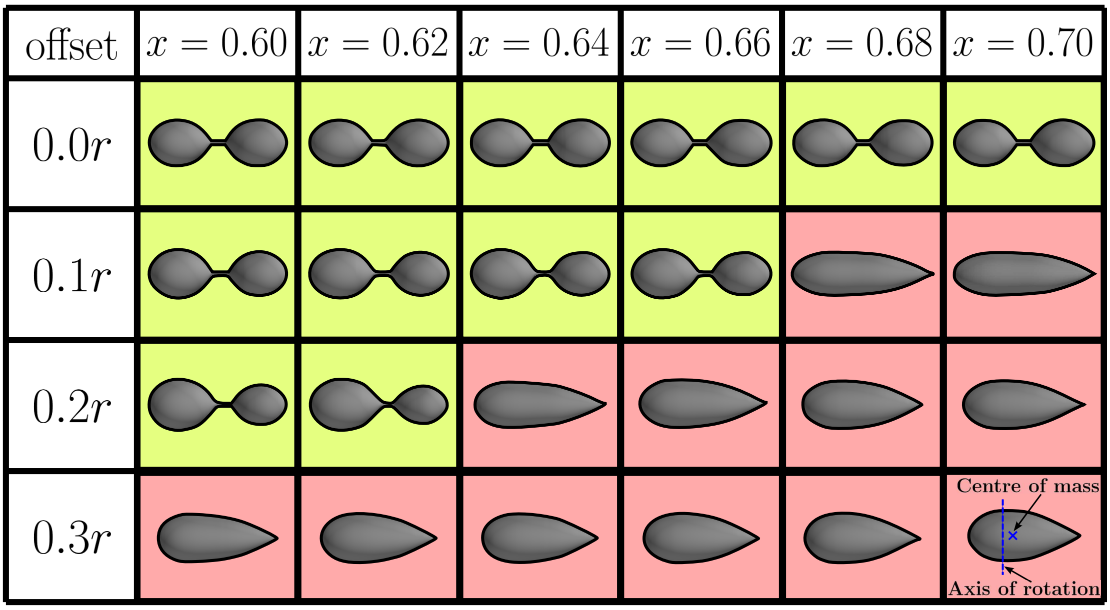

Figure 5.12: The shapes of various droplets immediately before they disrupt; the charge on the drops increases from left to right and the degree of offset between the rotation axis and the centre of mass, as illustrated in the bottom-right corner, increases from top to bottom. The transition from necking to coning breakup processes, indicated by the green and pink background colours respectively, is highly sensitive to initial perturbations of each droplet's position and shape.

tend to form only a single Taylor cone while rotating drops, particularly those which are also charged, can fission into unequally-sized drops [249, 258]. Liao and Hill placed the transition between coning and necking in the range $0.65 < x < 0.68$; droplets within these bounds may disrupt unpredictably by hybrid coning and necking mechanisms. The simulations considered so far have assumed an unrealistic degree of symmetry in the initial shape and position of the droplet. Small imperfections, such as shape perturbations or wobbling of the droplet about is rotation axis, are inherent in experimental and industrial environments and clearly have a significant effect on the subsequent breakup of the drop.

Figure 5.12 shows the shapes of several drops with $0.6 \leq x \leq 0.7$ immediately before disruption. The axis of rotation of each drop is offset from its centre of mass, by an increasing amount going down the table, which breaks the reflectional symmetry between the two lobes of the drops. Non-offset drops exhibit symmetric necking fission while small offsets lead to slightly asymmetric fission. The degree of asymmetry increases as the charge on the drops is increased, going from left to right in the table, until the breakup mechanism transitions into the formation of a single Taylor cone. This point is in the experimental hybrid transition region of $0.65 < x < 0.68$ [249] for an offset of only one-tenth of the spherical radius and illustrates the sensitivity of the breakup mechanism to slight initial imperfections which are, of course, always present in real liquid drops.

5.3.3 Rotational breakup of droplets in tokamaks

The preceding sections have investigated the stability limits of charged and rotating droplets in considerable detail. The rotational velocity required for the breakup of droplets in tokamaks can be estimated from the maximum value of Ω as given by $\Omega^* = 0.56$ for uncharged droplets. Combining the definition of Ω in Eq. 5.16 with the estimated rotational velocity after time t due to the $\underline{J} \times \underline{B}$ mechanism, from Eq. 3.58, gives the typical time taken for an uncharged droplet to break up as

$$t^* \sim \frac{0.56}{eBn_0c_s}\left(\frac{8\gamma\rho_d}{a}\right)^{1/2}. \tag{5.29}$$

This breakup timescale is plotted in Fig. 5.13 for tungsten and beryllium droplets in the edge plasmas of JET and ITER, with magnetic fields of 3 T and 5 T respectively, using the typical liquid and plasma parameters from Tabs. 1.1 and 1.2. This plot indicates that beryllium droplets with sizes 10–100 μm survive for around 0.01–0.1 s before they split into a pair of subdroplets due to rotational disruption. These timescales match up remarkably well with those of the forked trajectories seen in JET as shown in the left panel of Fig. 5.14, despite the rather unrefined estimations used to obtain Eq. 3.58, which suggests that these forked trajectories are likely to be due to rotational breakup. As such these observations represent the the first experimental evidence for the rapid spinning of droplets in magnetised plasmas. Note that these breakup timescales could not be attributable to electrostatic breakup which occurs on the nanosecond timescale of electron charge collection on the droplet [246]. Furthermore the complete vapourisation of the droplet only occurs once it has entered the core plasma region so these thermal mass losses provide no fixed limit on its survival time [220].

The timescales for rotational breakup could well be considerably less than the estimates shown in Fig. 5.13 due to the increase in plasma density and temperature as the droplets move towards the core plasma region; the plasma temperature increases by a factor of four, causing c_s to double, while the plasma density increases by around a factor of two so that t^* could be a quarter of these crude estimates. Furthermore the surface tensions of the liquid metals are likely to be reduced by the high liquid temperatures and any impurities dissolved in the metals.

The charge on the droplets has been neglected in this discussion of the rotational stability of liquid metals in tokamaks. This is quite a reasonable assumption for the large droplets which are susceptible to rotational breakup. For example the Rayleigh fissility parameter x, as defined in Eq. 5.3, can be estimated for a 10 μm beryllium droplet as follows: making the assumptions of a vacuum potential, so that $Q = 4\pi\epsilon_0 a\phi$, and a typical droplet potential of $\Phi = -3$ gives

$$x = \frac{Q^2}{64\pi^2\epsilon_0\gamma a^3} = \frac{\epsilon_0\phi^2}{4\gamma a} = \frac{\epsilon_0}{4\gamma a}\left(\frac{3k_BT_e}{e}\right)^2 = 2.9 \times 10^{-3} \tag{5.30}$$

for $T_e = 50$ eV. Inserting this value of x into Eq. 5.28 results in an insignificant reduction

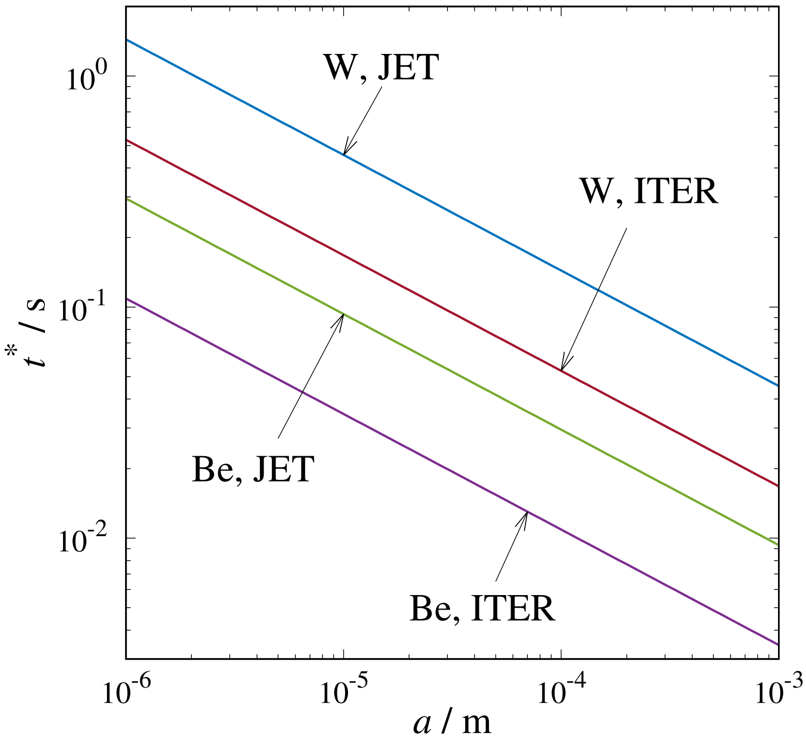

Figure 5.13: Estimates of the lifetime of tungsten and beryllium droplets in JET- and ITER-like tokamak plasmas for differing droplet radii. These lifetimes become up to four times smaller as the droplets encounter elevated plasma densities and temperatures as they approach the core region.

to the rotational stability limit by just 0.15%. Electrohydrodynamic effects are not expected to play any role in the rotational breakup of droplets which are observed in tokamaks.

The effect of rotational breakup on the behaviour of droplets in tokamak plasmas can be investigated further by including this breakup process in existing simulations for dust transport in tokamaks. One such framework is Imperial College's Dust in Tokamaks (DTOKS) code which has recently been rehabilitated by Luke Simons. This code tracks the motion of dust or droplets by self-consistently solving a charging equation, equation of motion and heating equation as the particle moves through a fixed plasma background which is generated by the SOLPS code [259]. A full description of the physical model and its implementation in DTOKS could fill two entire theses [260, 261]. The lifetime of droplets is determined by a boiling-only vapourisation model in the original versions of the code but Simons has now fully incorporated evaporational mass losses, as calculated according to the Hertz-Knudsen equation [262], in addition to the electrostatic and rotational breakup processes described earlier in this chapter. The angular velocity of each droplet is now calculated and compared with the $\Omega^* = 0.56$ condition in order to determine the rotational stability of the droplet. The main contributions to the torque on each droplet are still provided by Eqs. 3.55 and 3.56 but the resulting differential equation for the increase in angular velocity cannot be directly integrated because the

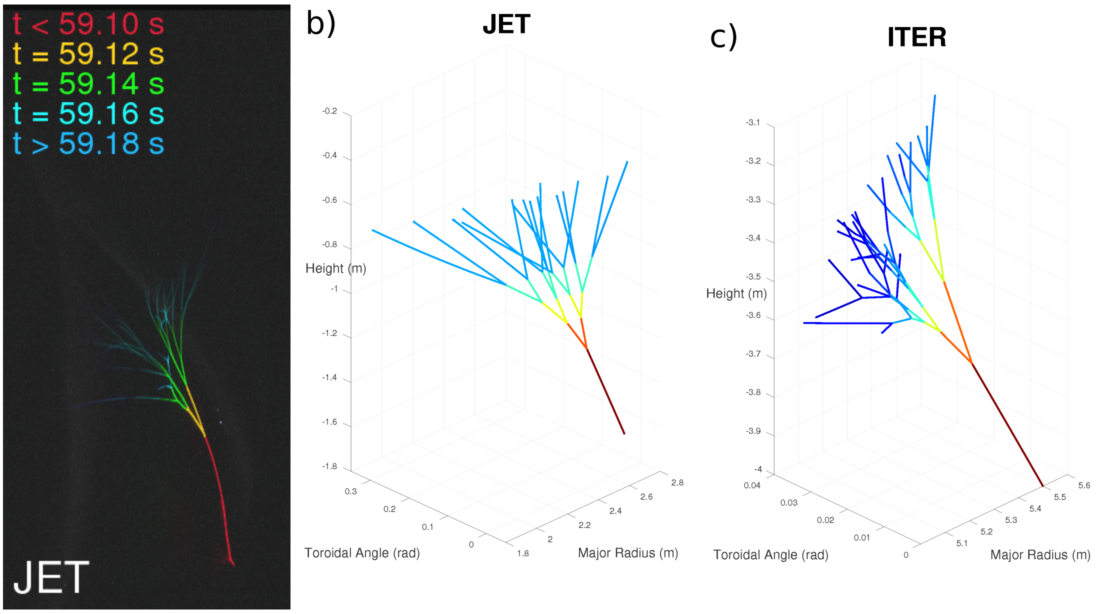

Figure 5.14: Left: reproduction of the forked droplet trajectory from JET pulse number 86124 in Fig. 1.8 with successive 20 ms exposure frames distinguished by different colours. Centre and right: DTOKS simulations of forking trajectories of tungsten droplets, with initial radii of 100 μm, in the JET (b) and ITER (c) tokamaks (credit Luke Simons; adapted from Ref. [62]). The increase in branching in the ITER simulation is highly beneficial for the operation of future tokamaks.

plasma conditions, and droplet size, vary as the droplet moves through the plasma. If the droplet does break up then the resulting pair of equal-mass subdroplets move apart with randomly-orientated opposite velocities of magnitude $a\omega_d$ in their centre-of-mass-frame. The angular momentum of these subdroplets is then reset to zero and their motion is tracked in the same way as for the original droplet.

The upgraded DTOKS code produces tree-like branched trajectories as displayed in the centre and right panels of Fig. 5.14. These simulations take a 100 μm tungsten droplet which is initially at its melting temperature and moving with a vertically-directed velocity from the outer edge of the JET and ITER divertor plates at 10 m s^{-1} and 100 m s^{-1} respectively. The ultimate fate of each droplet, which occurs at the end of each branch, is determined by the electrostatic Rayleigh condition. Droplets completely disintegrate once this limit is reached. The simulated trajectories are in good qualitative agreement with those observed using fast cameras in tokamaks, such as the image from JET shown in the left panel of Fig. 5.14, particularly in the region where the branching rate increases dramatically as the droplets approach the core plasma region. Note that the smaller droplets near the core might be expected to break up less frequently, according to Eq. 5.29, but the increase in plasma density and temperature compensates for this effect.

The rotational breakup mechanism and accompanying branched trajectories should be highly beneficial for future tokamak operations. The main hazard posed by droplets in tokamaks is the localised deposition of impurities in the core plasma as discussed in Sec. 1.2. These impurities, particularly those with high atomic masses such as tungsten, are the leading cause of disruptions in current tokamaks which cannot be tolerated in next-generation devices [12–15]. The risk presented by tungsten droplets is mitigated by their rotational breakup which spreads the impurities over a large region to help ensure that the local tungsten density does not induce a radiative collapse and disruption of the plasma. This mitigation should be improved further by the enhanced magnetic field, plasma density and temperature of next-generation tokamaks which will promote the spinning and disruption of tungsten droplets. This is clearly indicated by the proliferation of branching events for droplets in ITER as shown in Fig. 5.14.

5.4 Overview of droplets in plasmas

The present chapter has reviewed and developed some hydrodynamic stability limits for droplets which are charged and/or rotating. These stability limits are combined with the charging and spinning mechanisms from Chapter 3 in order to determine the survivability of droplets in plasmas. Electrostatic breakup only becomes important for small droplets in plasmas, with radii in the range 10–100 nm, as outlined in Sec. 5.1.2. Rotational breakup is crucial for determining the behaviour of droplets in magnetised plasmas; the $\underline{J} \times \underline{B}$ spinning mechanism, introduced in Sec. 3.3.2, causes the droplets to spin rapidly and split into a pair of subdroplets. The repeated branching of these rapidly-spun droplets is manifest in the tree-like trajectories observed with fast cameras in tokamaks and is reproduced in simulations of droplet transport as shown in Fig. 5.14. These patterns provide the first experimental verification of rapid droplet spinning in magnetised plasmas. The subsequent dispersion of tungsten impurities across a large region of the tokamak is highly beneficial for the operation of future tokamaks due to the reduced disruption risk from localised impurity-induced radiative heat losses.

6 Conclusion

The interactions between ionised gases, known as plasmas, and liquids are currently enabling the development of a diverse range of emerging technologies. This thesis documents recent theoretical and computational investigations into the hydrodynamic behaviour of these plasma-liquid interfaces. The present, and final, chapter draws together the main findings of this work and makes some suggestions for future avenues of study.

6.1 Summary

6.1.1 Overview of thesis

Chapter 1 provides the most inclusive review to date of the pivotal role of plasma-liquid interactions in numerous industrial applications. The insights of visionaries such as Faraday, Langmuir and Empedocles laid the foundation for an extensive survey encompassing molten metal surfaces in magnetic nuclear fusion devices, advanced materials processing techniques, electric propulsion of spacecraft, chemical catalysis, nanoparticle synthesis, plasma medicine and decontamination of food and drinks. The technological possibilities of plasma-liquid interactions are only just beginning to be realised but, so far, have been developed mostly through experimental studies.

Chapter 2 seeks to remedy the scarcity of theoretical and computational studies of plasma-liquid interactions, as previously identified, through the introduction of a complete fluid model of a plasma, a liquid, and an interface which separates them. The electrons and ions in the plasma are treated as separate fluids so that the large electric fields caused by charge separation can be resolved. Particular attention is paid to the formulation of the forces in each region in terms of a stress tensor which allows a simple condition for the pressure jump across a plasma-liquid interface to be derived.

Chapter 3 is concerned with the solution of the fluid equations in the plasma region only. Important results regarding sheath formation and the accumulation of charge on plasma-facing surfaces emerge from the fluid model. A code for solving the plasma fluid model in two dimensions is reviewed, based on Ref. [177], and extended to calculate the currents and drag force on a spherical object in a flowing plasma. A kinetic model of droplet charging in plasmas, the orbit-motion limited (OML) theory, is also considered; this theory had previously been used to study the charging of spheroids in stationary plasmas [203] and is further applied to spheroids in flowing plasmas here. Modifications to plasma behaviour near objects due to the presence of magnetic fields are also described: results for the charging of spheres in magnetised plasmas are presented, as calculated using the treecode in Ref. [210], and a novel mechanism for droplet spinning is discussed.

Chapter 4 gives the first theoretical account of the dynamics of plasma-facing liquid surfaces to fully account for the behaviour of a plasma near a surface. The ideal electrohydrodynamic limit, where the electric field behaves as if it were in a vacuum, applies to short, sub-Debye length deformations of a conducting liquid surface. Ideal electrohydrodynamic simulations show that the rate of droplet ejection from bubbles bursting at the liquid surface is enhanced by the electric field of the plasma sheath, in accordance with experimental observations, and supports previous assertions that this mechanism is responsible for droplet formation from melted surfaces in tokamaks. A plane-wave linear stability analysis of a plasma-liquid interface, which fully accounts for the electrons and ions in the plasma, is then reviewed based on Ref. [233]. The bombardment of the liquid surface with fast-moving ions from the plasma suppresses the onset of large-wavelength electrohydrodynamic surface instabilities. This suppression is confirmed with new simulations of the plasma-liquid interface in axisymmetric coordinates although the magnitude of the suppression is smaller for cylindrical surface perturbations than for plane-wave perturbations. These simulations also resolve the non-linear dynamics of unstable plasma-liquid interfaces; the ejection of bursts of droplets, which can be inferred from current pulses in experiments using high-voltage atmospheric discharges over ionic solutions, are clearly reproduced.

Chapter 5 considers the behaviour of plasma-immersed liquid droplets. Very small liquid droplets, with radii in the range 10–100 nm, are susceptible to electrostatic breakup while simulations show that droplets in flowing plasmas are always stable under typically-encountered plasma conditions. However the intriguing tree-like trajectories of droplets in tokamak plasmas, such as those observed with fast cameras on JET, attests that large plasma-immersed droplets must be vulnerable to some breakup mechanism. This process is identified as rotational breakup by comparing the spin-up mechanism of Sec. 3.3.2 with calculations of the stability limits of charged and spinning droplets. The rotational breakup mechanism is incorporated into the dust transport code DTOKS and produces strikingly-similar forked droplet trajectories to those observed with fast cameras in tokamaks. The dispersion of droplets by rotational breakup helps to reduce the local concentration of impurities which is highly beneficial for the successful operation of magnetic fusion devices.

6.1.2 Outlook and impact

This thesis has provided several new insights into the hydrodynamic behaviour of plasma-liquid interfaces. The electric field in the sheath, which has been neglected in previous studies, has been shown to play a critical role in the enhancement of droplet formation rates from the bubble bursting mechanism and provides an explanation for the experimental observations of de Temmerman *et al.* as reported in Sec. 4.1.6. Field-enhanced bubble bursting is thus identified as a crucial mechanism for droplet generation and injection in tokamaks and techniques for reducing the formation of bubbles and blisters should be explored.

The behaviour of droplets once they enter the plasma has also been examined and an intriguing new rotational breakup process has been identified. Simulations of droplet trajectories which incorporate this mechanism are in excellent quantitative agreement with observations of influx events in the JET tokamak. This mechanism results in the dispersal of impurities in the edge plasma of the tokamak and prevents large droplets from entering the core region of the plasma; as such the operational hazards of droplet influx events, in particular the triggering of disruptions, are significantly reduced. This mitigating effect is predicted to be amplified by the high magnetic fields of next-generation fusion devices, providing a positive outlook for their successful operation.

This thesis also advocates the advance of liquid metal surfaces to handle the high heat loads on plasma-facing surfaces in tokamaks. The main historic issue with these surfaces is the formation of droplets and resulting deposition of impurities in the core plasma. However the rotational breakup of these droplets in the high magnetic fields of future devices should reduce the impact of droplets on the core plasma and alleviate concerns about droplet formation. The hesitancy of fusion researchers to incorporate liquid metal technology into mainstream tokamak devices is understandable, given the large investment and delays in building the next-generation ITER experiment, but encouragement can be found in smaller trials at Princeton's Lithium Tokamak eXperiment (LTX) [263], Italy's Frascati Tokamak Upgrade (FTU) device [264], and in private endeavours such as at Tokamak Energy Ltd.

By contrast, the industrial applications of plasma-liquid interfaces are proliferating quickly in both number and complexity. The small scale and relatively low cost of these devices allows rapid proof-of-concept experiments and deployment of new technologies and, as such, these applications are expected to be the primary driver for innovation in plasma-liquid interactions over the next decade and beyond. Many of these new concepts use atmospheric-pressure plasmas which have some significant differences from the plasmas considered in this thesis; in particular they are highly-collisional and often composed of multiple species of ions and neutral particles which undergo chemical reactions with each other. Simulations of these plasmas require separate fluids for each ion and neutral species and must account for the collisions and reactions between these fluids [265]. However the pressure-jump condition developed in Chapter 2 can be straightforwardly extended to include these additional fluids which will facilitate simulations of plasma-liquid interactions under atmospheric conditions. Furthermore Sec. 4.2.3 describes the qualitative similarity between numerical simulations and the atmospheric-pressure experiments of Shirai *et al.*, which both exhibit the formation of Taylor cones and ejection of droplet bursts, thereby indicating the applicability of the models developed in this thesis to a broad range of plasma-liquid interactions.

6.2 What remains to be done?

This thesis represents just one incremental advance in the study and application of plasma-liquid interactions and offers several possibilities for future extensions. One obvious improvement would be an upgrade to the rather outdated numerical methods which are used in the simulations of plasma-liquid interactions. The current methods were chosen as they can be coded quite quickly and with relative ease; however if the simulations are to be adopted widely then more sophisticated underlying algorithms must be introduced. In particular the use of higher-order finite difference schemes and the conjugate gradient method for solving Poisson's equation would bring the code up to date with the latest codes for simulating free liquid surfaces [266].

The physical model underpinning these simulations should also be enhanced: the addition of magnetic fields, electron emission from the surface, currents in the liquid, multiple ion species, and collisions and ionisation in the plasma would allow the code to simulate a broader range of physically-realistic conditions than it is currently capable of. One potential application of the upgraded code would be to further investigate the spinning mechanisms for droplets in magnetised plasmas. The control surface arguments, as used to find drag forces in Sec. 3.2.2, could be used to calculate the torque on droplets and refine the order-of-magnitude estimates given in Sec. 3.3.2. These improved torques could subsequently be incorporated into DTOKS in order to improve its predictive capabilities for reproducing the forked droplet trajectories shown in Fig. 5.14.

However theory and simulation are not the only frontiers of research into plasma-liquid interactions and must be complemented by experimental observations and practical applications. An extensive study of droplet trajectories in tokamaks is imminently achievable with the current availability of JET camera data. The images shown in this thesis, such as those in Fig. 1.8, were identified by eye while laboriously trawling through around 400 pulses. However this number represents only a small fraction of the more than 20000 plasma pulses which have been run on JET since the installation of the ITER-like wall. The task of detecting and classifying droplet trajectories in these pulses would be ideally suited to automation by a computer program.

Further afield, it would be highly advantageous to make contact with experimentalists studying plasma-liquid interactions in the laboratory in order to share their insights into how the models and simulations in this thesis could be tailored to specific industrial applications. Their expertise and facilities would also allow some of the results presented in this thesis to be tested. For example experiments are routinely performed by the Technological Plasmas Research Group at Liverpool University where solid dust grains are injected into low pressure RF discharges with strong magnetic fields applied; it would be very interesting to replace these solid particles with liquid droplets and directly observe their behaviour in the laboratory. A collaboration between theoretical and experimental approaches will be crucial for realising the full industrial potential of plasma-liquid interactions.

Bibliography

[1] Russell, B. A. W. *History of Western Philosophy.* Routledge Classics, Abingdon, (1996). 17

[2] Boyd, T. J. M. and Sanderson, J. J. *The Physics of Plasmas.* Cambridge University Press, (2003). 17, 39

[3] Jones, B. and Faraday, M. *The life and letters of Faraday*, volume 2nd. Cambridge University Press, (2010). 17

[4] Tonks, L. *American Journal of Physics* **35**, 857–858 (1967). 17

[5] Chen, F. F. *Introduction to Plasma Physics and Controlled Fusion.* Plenum Press, New York, 2nd edition, (1984). 17

[6] Bruggeman, P. J., Kushner, M. J., Locke, B. R., Gardeniers, J. G. E., Graham, W. G., Graves, D. B., Hofman-Caris, R. C. H. M., Maric, D., Reid, J. P., Ceriani, E., et al. *Plasma Sources Science and Technology* **25**(5), 053002 (2016). 18, 29, 37

[7] Tabarés, F. L. *Plasma Physics and Controlled Fusion* **58**(1), 014014 (2016). 18, 24, 36

[8] Eddington, A. S. *Nature* **106**, 14–20 (1920). 18

[9] Llewellyn-Smith, C. and Ward, D. *European Review* **13**(3), 337–359 (2005). 18

[10] Pitts, R. A., Carpentier, S., Escourbiac, F., Hirai, T., Komarov, V., Kukushkin, A., Lisgo, S., Loarte, A., Merola, M., Mitteau, R., et al. *Journal of Nuclear Materials* **415**(1), S957–S964 (2011). 19

[11] Matthews, G. F., Beurskens, M., Brezinsek, S., Groth, M., Joffrin, E., Loving, A., Kear, M., Mayoral, M. L., Neu, R., Prior, P., et al. *Physica Scripta* **T145**, 014001 (2011). 19

[12] Kallenbach, A., Neu, R., Dux, R., Fahrbach, H., Fuchs, J., Giannone, L., Gruber, O., Herrmann, A., Lang, P., Lipschultz, B., et al. *Plasma Physics and Controlled Fusion* **47**(12B), B207–B222 (2005). 19, 128

[13] Hogeweij, G. M. D., Leonov, V., Schweinzer, J., Sips, A. C. C., Angioni, C., Calabrò, G., Dux, R., Kallenbach, A., Lerche, E., Maggi, C., et al. *Nuclear Fusion* **55**(6), 063031 (2015). 19, 128

[14] Neu, R. L., Brezinsek, S., Beurskens, M., Bobkov, V., de Vries, P., Giroud, C., Joffrin, E., Kallenbach, A., Matthews, G. F., Mayoral, M.-L., et al. *IEEE Transactions on Plasma Science* **42**(3), 552–562 (2014). 19, 128

[15] De Vries, P. C., Baruzzo, M., Hogeweij, G. M. D., Jachmich, S., Joffrin, E., Lomas, P. J., Matthews, G. F., Murari, A., Nunes, I., Pütterich, T., et al. *Physics of Plasmas* **21**(5), 056101 (2014). 19, 128

[16] Guillemaut, C., Jardin, A., Horacek, J., Borodkina, I., Autricque, A., Arnoux, G., Boom, J., Brezinsek, S., Coenen, J. W., De La Luna, E., et al. *Physica Scripta* **T167**, 014005 (2016). 19

[17] Matthews, G. F., Bazylev, B., Baron-Wiechec, A., Coenen, J., Heinola, K., Kiptily, V., Maier, H., Reux, C., Riccardo, V., Rimini, F., et al. *Physica Scripta* **T167**, 014070 (2016). 19, 20, 32, 150

[18] Laux, M., Balden, M., and Siemroth, P. *Physica Scripta* **T159**, 014026 (2014). 19

[19] Loewenhoff, T., Linke, J., Pintsuk, G., and Thomser, C. *Fusion Engineering and Design* **87**(7-8), 1201–1205 (2012). 19, 23, 152

[20] Sergienko, G., Arnoux, G., Devaux, S., Matthews, G. F., Nunes, I., Riccardo, V., Sirinelli, A., Huber, A., Brezinsek, S., Coenen, J. W., et al. *Physica Scripta* **T159**, 014041 (2014). 19, 32, 36

[21] Flanagan, J. C., Sertoli, M., Bacharis, M., Matthews, G., de Vries, P. C., Widdowson, A., Coffey, I. H., Arnoux, G., Sieglin, B., Brezinsek, S., et al. *Plasma Physics and Controlled Fusion* **57**(1), 014037 (2015). 20

[22] Lehnen, M., Alonso, A., Arnoux, G., Baumgarten, N., Bozhenkov, S. A., Brezinsek, S., Brix, M., Eich, T., Gerasimov, S. N., Huber, A., et al. *Nuclear Fusion* **51**(12), 123010 (2011). 20

[23] Tolias, P., Ratynskaia, S., De Angeli, M., De Temmerman, G., Ripamonti, D., Riva, G., Bykov, I., Shalpegin, A., Vignitchouk, L., Brochard, F., et al. *Plasma Physics and Controlled Fusion* **58**(2), 025009 (2016). 20

[24] Coenen, J. W., Arnoux, G., Bazylev, B., Matthews, G., Autricque, A., Balboa, I., Clever, M., Dejarnac, R., Coffey, I., Corre, Y., et al. *Nuclear Fusion* **55**(2), 023010 (2015). 21

[25] Chapman, I. T., Holgate, J. T., Ayed, N. B., Cunningham, G., Ham, C. J., Harrison, J. R., Kirk, A., McArdle, G., Patel, A., Scannell, R., et al. *Plasma Physics and Controlled Fusion* **56**(7), 075004 (2014). 21

[26] Hirai, T., Escourbiac, F., Carpentier-Chouchana, S., Fedosov, A., Ferrand, L., Jokinen, T., Komarov, V., Kukushkin, A., Merola, M., Mitteau, R., et al. *Fusion Engineering and Design* **88**(9-10), 1798–1801 (2013). 21

[27] Coenen, J. W., Philipps, V., Brezinsek, S., Bazylev, B., Kreter, A., Hirai, T., Laengner, M., Tanabe, T., Ueda, Y., Samm, U., et al. *Nuclear Fusion* **51**(8), 083008 (2011). 21

[28] Coenen, J. W., Bazylev, B., Brezinsek, S., Philipps, V., Hirai, T., Kreter, A., Linke, J., Sergienko, G., Pospieszczyk, A., Tanabe, T., et al. *Journal of Nuclear Materials* **415**(1), S78–S82 (2011). 21, 152

[29] Krieger, K., Lunt, T., Dux, R., Janzer, A., Müller, H. W., Potzel, S., Pütterich, T., Yang, Z., et al. *Physica Scripta* **T145**, 014067 (2011). 21

[30] Bazylev, B., Landman, I., Loarte, A., Klimov, N. S., Podkovyrov, V. L., and Safronov, V. M. *Physica Scripta* **T138**, 014061 (2009). 21, 33

[31] De Temmerman, G., Daniels, J., Bystrov, K., Van den Berg, M. A., and Zielinski, J. J. *Nuclear Fusion* **53**(2), 023008 (2013). 21, 36, 37, 93, 95, 106, 151

[32] Lipschultz, B., Coenen, J. W., Barnard, H., Howard, N. T., Reinke, M. L., Whyte, D. G., and Wright, G. M. *Nuclear Fusion* **52**(12), 123002 (2012). 21, 22, 151

[33] Arnas, C., Irby, J., Celli, S., De Temmerman, G., Addab, Y., Couëdel, L., Grisolia, C., Lin, Y., Martin, C., Pardanaud, C., et al. *Nuclear Materials and Energy* **11**, 12–19 (2017). 21

[34] Allen, J. E. and Magistrelli, F. *Nature* **194**(4834), 1167 (1962). 22

[35] Kajita, S., Takamura, S., and Ohno, N. *Nuclear Fusion* **49**(3), 032002 (2009). 22

[36] Aussems, D. U. B., Nishijima, D., Brandt, C., Van Der Meiden, H. J., Vilémová, M., Matějíček, J., De Temmerman, G., Doerner, R. P., and Cardozo, N. J. L. *Journal of Nuclear Materials* **463**, 303–307 (2015). 22

[37] Rudakov, D. L., Litnovsky, A., West, W. P., Yu, J. H., Boedo, J. A., Bray, B. D., Brezinsek, S., Brooks, N. H., Fenstermacher, M. E., Groth, M., et al. *Nuclear Fusion* **49**(8), 085022 (2009). 22, 25, 116

[38] Rudakov, D. L., Chrobak, C. P., Doerner, R. P., Krasheninnikov, S. I., Moyer, R. A., Umstadter, K. R., Wampler, W. R., and Wong, C. P. C. *Journal of Nuclear Materials* **438**, S805–S808 (2013). 22

[39] Bykov, I., Chrobak, C. P., Abrams, T., Rudakov, D. L., Unterberg, E. A., Wampler, W. R., Hollmann, E. M., Moyer, R. A., Boedo, J. A., Stahl, B., et al. *Physica Scripta* **T170**, 014034 (2017). 22

[40] Kajita, S., Fukumoto, M., Tokitani, M., Nakano, T., Noiri, Y., Ohno, N., Masuzaki, S., Takamura, S., Yoshida, N., and Ueda, Y. *Nuclear Fusion* **53**(5), 053013 (2013). 22

[41] Rohde, V., Endstrasser, N., Toussaint, U. v., Balden, M., Lunt, T., Neu, R., Hakola, A., Bucalossi, J., and the ASDEX Upgrade Team. *Journal of Nuclear Materials* **415**(1), S46–S50 (2011). 22

[42] Herrmann, A., Balden, M., Laux, M., Krieger, K., Müller, H. W., Pugno, R., Rohde, V., et al. *Journal of Nuclear Materials* **390**, 747–750 (2009). 22

[43] Garcia-Carrasco, A., Petersson, P., Rubel, M., Widdowson, A., Fortuna-Zalesna, E., Jachmich, S., Brix, M., Marot, L., and JET Contributors. *Nuclear Materials and Energy* **12**, 506–512 (2017). 22, 23, 25

[44] Makhlaj, V. A., Garkusha, I. E., Aksenov, N. N., Bazylev, B., Landman, I., Linke, J., Malykhin, S. V., Pugachov, A. T., Sadowski, M. J., Skladnik-Sadowska, E., et al. *Physica Scripta* **T159**, 014024 (2014). 23

[45] Loewenhoff, T., Bardin, S., Greuner, H., Linke, J., Maier, H., Morgan, T. W., Pintsuk, G., Pitts, R. A., Riccardi, B., and De Temmerman, G. *Nuclear Fusion* **55**(12), 123004 (2015). 23

[46] Kovalenko, D. V., Klimov, N. S., Podkovyrov, V. L., Kupriyanov, I. B., Poresanov, N. P., Zabirova, N. E., Bazaleev, E. B., Safronov, V. M., Muzichenko, A. D., Putrik, A. B., et al. *Nuclear Materials and Energy* **12**, 156–163 (2017). 23

[47] Ticoş, C. M., Galaţanu, M., Galaţanu, A., Luculescu, C., Scurtu, A., Udrea, N., Ticoş, D., and Dumitru, M. *Applied Surface Science* **434**, 1122–1128 (2018). 23

[48] van Eden, G. G., Morgan, T. W., Aussems, D. U. B., van den Berg, M. A., Bystrov, K., and van de Sanden, M. C. M. *Physical Review Letters* **116**(13), 135002 (2016). 23

[49] Eden, G. G., Kvon, V., Sanden, M. C. M., and Morgan, T. W. *Nature Communications* **8**(1), 192 (2017). 23

[50] Maingi, R., Kaye, S. M., Skinner, C. H., Boyle, D. P., Canik, J. M., Bell, M. G., Bell, R. E., Gray, T. K., Jaworski, M. A., Kaita, R., et al. *Physical Review Letters* **107**(14), 145004 (2011). 23

[51] Li, J., Guo, H. Y., Wan, B. N., Gong, X. Z., Liang, Y. F., Xu, G. S., Gan, K. F., Hu, J. S., Wang, H. Q., Wang, L., et al. *Nature Physics* **9**(12), 817–821 (2013). 23, 25

[52] Majeski, R., Kaita, R., Boaz, M., Efthimion, P., Gray, T., Jones, B., Hoffman, D., Kugel, H., Menard, J., Munsat, T., et al. *Fusion Engineering and Design* **72**(1-3), 121–132 (2004). 23

[53] Whyte, D. G., Evans, T. E., Wong, C. P. C., West, W. P., Bastasz, R., Allain, J. P., and Brooks, J. N. *Fusion Engineering and Design* **72**(1-3), 133–147 (2004). 23

[54] Ruzic, D. N., Xu, W., Andruczyk, D., and Jaworski, M. A. *Nuclear Fusion* **51**(10), 102002 (2011). 24

[55] Ren, J., Hu, J. S., Zuo, G. Z., Sun, Z., Li, J. G., Ruzic, D. N., and Zakharov, L. E. *Physica Scripta* **T159**, 014033 (2014). 24

[56] Fiflis, P., Morgan, T. W., Brons, S., Van Eden, G. G., Van Den Berg, M. A., Xu, W., Curreli, D., and Ruzic, D. N. *Nuclear Fusion* **55**(11), 113004 (2015). 24, 151

[57] Fortuna-Zaleśna, E., Grzonka, J., Rasinski, M., Balden, M., Rohde, V., Kurzydlowski, K. J., et al. *Physica Scripta* **T159**, 014066 (2014). 24, 25, 153

[58] Fortuna-Zaleśna, E., Grzonka, J., Moon, S., Rubel, M., Petersson, P., Widdowson, A., and JET Contributors. *Physica Scripta* **T170**, 014038 (2017). 24, 26, 153

[59] Fortuna-Zaleśna, E., Weckmann, A., Grzonka, J., Rubel, M., Esser, H. G., Freisinger, M., Kreter, A., Sergienko, G., and Ström, P. *Physica Scripta* **T167**, 014059 (2016). 24

[60] Bacharis, M., Coppins, M., Fundamenski, W., and Allen, J. E. *Plasma Physics and Controlled Fusion* **54**(8), 085010 (2012). 25, 36, 64, 76

[61] Krasheninnikov, S. I., Smirnov, R. D., and Rudakov, D. L. *Plasma Physics and Controlled Fusion* **53**(8), 083001 (2011). 25

[62] Holgate, J. T., Simons, L., Andrew, Y., Stavrou, C. K., and JET Contributors. *Manuscript under review* (2018). 25, 26, 127

[63] Mansfield, D. K., Hill, K. W., Strachan, J. D., Bell, M. G., Scott, S. D., Budny, R., Marmar, E. S., Snipes, J. A., Terry, J. L., Batha, S., et al. *Physics of Plasmas* **3**(5), 1892–1897 (1996). 25

[64] Hu, J. S., Sun, Z., Guo, H. Y., Li, J. G., Wan, B. N., Wang, H. Q., Ding, S. Y., Xu, G. S., Liang, Y. F., Mansfield, D. K., et al. *Physical Review Letters* **114**(5), 055001 (2015). 25

[65] Osborne, T. H., Jackson, G. L., Yan, Z., Maingi, R., Mansfield, D. K., Grierson, B. A., Chrobak, C. P., McLean, A. G., Allen, S. L., Battaglia, D. J., et al. *Nuclear Fusion* **55**(6), 063018 (2015). 25

[66] Nemchinsky, V. A. and Severance, W. S. *Journal of Physics D: Applied Physics* **39**(22), R423–R438 (2006). 27

[67] Krajcarz, D. *Procedia Engineering* **69**, 838–843 (2014). 27

[68] Xu, W. J., Fang, J. C., and Lu, Y. S. *Journal of Materials Processing Technology* **129**(1-3), 152–156 (2002). 27

[69] Bhuvenesh, R., Norizaman, M. H., and Manan, M. S. A. *International Journal of Industrial and Manufacturing Engineering* **6**(2), 459–462 (2012). 27

[70] Maity, K. P. and Bagal, D. K. *The International Journal of Advanced Manufacturing Technology* **78**(1-4), 161–175 (2015). 27

[71] Hakola, A., Likonen, J., Karhunen, J., Korhonen, J. T., Aints, M., Laan, M., Paris, P., Kolehmainen, J., Koskinen, M., and Tervakangas, S. *Fusion Engineering and Design* **96**, 101–106 (2015). 27

[72] Fauchais, P. *Journal of Physics D: Applied Physics* **37**(9), R86–R108 (2004). 27

[73] Vardelle, A., Moreau, C., Themelis, N. J., and Chazelas, C. *Plasma Chemistry and Plasma Processing* **35**(3), 491–509 (2015). 27

[74] Fauchais, P., Vardelle, M., Goutier, S., and Vardelle, A. *Plasma Chemistry and Plasma Processing* **35**(3), 511–525 (2015). 27

[75] Ivchenko, D., Zhang, T., Mariaux, G., Vardelle, A., Goutier, S., and Itina, T. E. *Journal of Thermal Spray Technology* **27**(1-2), 3–13 (2018). 27

[76] Ogawa, D., Saraf, I., Sra, A., Timmons, R., Goeckner, M., and Overzet, L. *Journal of Vacuum Science & Technology A: Vacuum, Surfaces, and Films* **27**(2), 342–351 (2009). 27, 37

[77] Sutton, G. P. and Biblarz, O. *Rocket propulsion elements*. John Wiley & Sons, 9th edition, (2017). 27

[78] Burton, R. L. and Turchi, P. J. *Journal of Propulsion and Power* **14**(5), 716–735 (1998). 28

[79] Kakami, A., Koizumi, H., Komurasaki, K., and Arakawa, Y. *Vacuum* **73**(3-4), 419–425 (2004). 28

[80] Böhrk, H., Lau, M., Herdrich, G., Hald, H., and Röser, H.-P. *CEAS Space Journal* **3**(1-2), 1–6 (2012). 28

[81] Rezaeiha, A. and Schönherr, T. *Journal of Propulsion and Power* **30**(2), 253–264 (2014). 28

[82] Gamero-Castaño, M. and Hruby, V. *Journal of Propulsion and Power* **17**(5), 977–987 (2001). 28

[83] Lozano, P. and Martínez-Sánchez, M. *Journal of colloid and interface science* **282**(2), 415–421 (2005). 28

[84] Krpoun, R. and Shea, H. R. *Journal of Micromechanics and Microengineering* **19**(4), 045019 (2009). 28

[85] Lenguito, G. and Gomez, A. *Journal of Applied Physics* **114**(15), 154901 (2013). 28

[86] Wright, W. P. and Ferrer, P. *Progress in Aerospace Sciences* **74**, 48–61 (2015). 28

[87] Bock, D. and Tajmar, M. *Acta Astronautica* **144**, 422–428 (2018). 28

[88] Antonucci, F., Armano, M., Audley, H., Auger, G., Benedetti, M., Binetruy, P., Boatella, C., Bogenstahl, J., Bortoluzzi, D., Bosetti, P., et al. *Classical and Quantum Gravity* **28**(9), 094001 (2011). 28

[89] Cavendish, H. *Philosophical Transactions of the Royal Society of London* **75**, 372–384 (1785). 29

[90] Siemens, W. v. *Annalen der Physik* **178**(9), 66–122 (1857). 29

[91] Miller, S. L. et al. *Science* **117**(3046), 528–529 (1953). 29, 31

[92] Neyts, E. C., Ostrikov, K., Sunkara, M. K., and Bogaerts, A. *Chemical Reviews* **115**(24), 13408–13446 (2015). 29

[93] Samukawa, S., Hori, M., Rauf, S., Tachibana, K., Bruggeman, P., Kroesen, G., Whitehead, J. C., Murphy, A. B., Gutsol, A. F., Starikovskaia, S., et al. *Journal of Physics D: Applied Physics* **45**(25), 253001 (2012). 29

[94] Lukes, P., Dolezalova, E., Sisrova, I., and Clupek, M. *Plasma Sources Science and Technology* **23**(1), 015019 (2014). 29

[95] Mariotti, D., Patel, J., Švrček, V., and Maguire, P. *Plasma Processes and Polymers* **9**(11-12), 1074–1085 (2012). 29

[96] Rumbach, P., Bartels, D. M., Sankaran, R. M., and Go, D. B. *Nature Communications* **6**, 7248 (2015). 29

[97] Patel, J., Němcová, L., Maguire, P., Graham, W. G., and Mariotti, D. *Nanotechnology* **24**(24), 245604 (2013). 29, 30

[98] Schaper, L., Stalder, K. R., and Graham, W. G. *Plasma Sources Science and Technology* **20**(3), 034004 (2011). 29

[99] Maguire, P. D., Mahony, C. M. O., Kelsey, C. P., Bingham, A. J., Montgomery, E. P., Bennet, E. D., Potts, H. E., Rutherford, D. C. E., McDowell, D. A., Diver, D. A., et al. *Applied Physics Letters* **106**(22), 224101 (2015). 29

[100] Yan, Z. C., Li, C., and Lin, W. H. *International Journal of Hydrogen Energy* **34**(1), 48–55 (2009). 29

[101] Gao, J., Chen, L., He, Y. Y., Yan, Z. C., and Zheng, X. J. *Journal of Hazardous Materials* **265**, 261–270 (2014). 29

[102] Richmonds, C. and Sankaran, R. M. *Applied Physics Letters* **93**(13), 131501 (2008). 30

[103] Graham, W. G. and Stalder, K. R. *Journal of Physics D: Applied Physics* **44**(17), 174037 (2011). 30

[104] Švrček, V., Mariotti, D., and Kondo, M. *Applied Physics Letters* **97**(16), 161502 (2010). 30

[105] Nakano, T., Kubo, H., Higashijima, S., Asakura, N., Takenaga, H., Sugie, T., and Itami, K. *Nuclear Fusion* **42**(6), 689 (2002). 30

[106] Neuwirth, D., Rohde, V., Schwarz-Selinger, T., and the ASDEX Upgrade Team. *Plasma Physics and Controlled Fusion* **54**(8), 085008 (2012). 30

[107] Abrams, T., Jaworski, M. A., Chen, M., Carter, E. A., Kaita, R., Stotler, D. P., De Temmerman, G., Morgan, T. W., van den Berg, M. A., and van der Meiden, H. J. *Nuclear Fusion* **56**(1), 016022 (2016). 30, 36

[108] Surowsky, B., Schlüter, O., and Knorr, D. *Food Engineering Reviews* **7**(2), 82–108 (2015). 30

[109] Magureanu, M., Mandache, N. B., and Parvulescu, V. I. *Water Research* **81**, 124–136 (2015). 30

[110] Yang, Y., Cho, Y. I., and Fridman, A. *Plasma Discharge in Liquid: Water Treatment and Applications*. CRC Press, (2012). 30, 31

[111] Gurol, C., Ekinci, F. Y., Aslan, N., and Korachi, M. *International Journal of Food Microbiology* **157**(1), 1–5 (2012). 30

[112] Surowsky, B., Fröhling, A., Gottschalk, N., Schlüter, O., and Knorr, D. *International Journal of Food Microbiology* **174**, 63–71 (2014). 30

[113] Almeida, F. D. L., Cavalcante, R. S., Cullen, P. J., Frias, J. M., Bourke, P., Fernandes, F. A. N., and Rodrigues, S. *Innovative Food Science & Emerging Technologies* **32**, 127–135 (2015). 30

[114] Fridman, G., Friedman, G., Gutsol, A., Shekhter, A. B., Vasilets, V. N., and Fridman, A. *Plasma Processes and Polymers* **5**(6), 503–533 (2008). 30

[115] Dobrynin, D., Wu, A., Kalghatgi, S., Park, S., Chernets, N., Wasko, K., Dumani, E., Ownbey, R., Joshi, S. G., Sensenig, R., et al. *Plasma Medicine* **1**(1), 93–108 (2011). 30

[116] Miyamoto, K., Ikehara, S., Takei, H., Akimoto, Y., Sakakita, H., Ishikawa, K., Ueda, M., Ikeda, J.-i., Yamagishi, M., Kim, J., et al. *Archives of Biochemistry and Biophysics* **605**, 95–101 (2016). 30

[117] Brehmer, F., Haenssle, H. A., Daeschlein, G., Ahmed, R., Pfeiffer, S., Görlitz, A., Simon, D., Schön, M. P., Wandke, D., and Emmert, S. *Journal of the European Academy of Dermatology and Venereology* **29**(1), 148–155 (2015). 30

[118] Schlegel, J., Köritzer, J., and Boxhammer, V. *Clinical Plasma Medicine* **1**(2), 2–7 (2013). 30

[119] Keidar, M. *Plasma Sources Science and Technology* **24**(3), 033001 (2015). 30

[120] Macky, W. A. *Proceedings of the Royal Society of London A* **133**(822), 565–587 (1931). 31

[121] English, W. N. *Physical Review* **74**(2), 179–189 (1948). 31

[122] Taylor, G. I. *Proceedings of the Royal Society of London A* **280**(1382), 383–397 (1964). 31, 83, 84

[123] Latham, J. *Reports on Progress in Physics* **32**(1), 69–134 (1969). 31

[124] Pack, A., Höweling, A., Hezel, D. C., Stefanak, M. T., Beck, A.-K., Peters, S. T. M., Sengupta, S., Herwartz, D., and Folco, L. *Nature Communications* **8**, 15702 (2017). 31

[125] Lavvas, P., Yelle, R. V., Koskinen, T., Bazin, A., Vuitton, V., Vigren, E., Galand, M., Wellbrock, A., Coates, A. J., Wahlund, J.-E., et al. *Proceedings of the National Academy of Sciences* **110**(8), 2729–2734 (2013). 31

[126] Kurilovich, D., Klein, A. L., Torretti, F., Lassise, A., Hoekstra, R., Ubachs, W., Gelderblom, H., and Versolato, O. O. *Physical Review Applied* **6**(1), 014018 (2016). 31

[127] Price, C. J., Donnelly, T. D., Giltrap, S., Stuart, N. H., Parker, S., Patankar, S., Lowe, H. F., Drew, D., Gumbrell, E. T., and Smith, R. A. *Review of Scientific Instruments* **86**(3), 033502 (2015). 31

[128] Rohwetter, P., Kasparian, J., Stelmaszczyk, K., Hao, Z., Henin, S., Lascoux, N., Nakaema, W. M., Petit, Y., Queißer, M., Salamé, R., et al. *Nature Photonics* **4**(7), 451 (2010). 31

[129] Starikovskiy, A., Yang, Y., Cho, Y. I., and Fridman, A. *Plasma Sources Science and Technology* **20**(2), 024003 (2011). 31

[130] Dai, X. J., Corr, C. S., Ponraj, S. B., Maniruzzaman, M., Ambujakshan, A. T., Chen, Z., Kviz, L., Lovett, R., Rajmohan, G. D., de Celis, D. R., et al. *Plasma Processes and Polymers* **13**(3), 306–310 (2016). 31

[131] Graham, W. G., Hüwel, L., Morgan, T., and Murakami, T. In *44th IOP Plasma Physics Conference, Oxford, 3–6 April 2017*. 31

[132] Chu, H.-Y. and Lee, H.-K. *Physical review letters* **107**(22), 225001 (2011). 31

[133] Barber, B. P. and Putterman, S. J. *Nature* **352**, 318–320 (1991). 32

[134] Suslick, K. S. and Flannigan, D. J. *Annu. Rev. Phys. Chem.* **59**, 659–683 (2008). 32

[135] Reich, E. *Nature News* , 1103 (2009). 32

[136] Taleyarkhan, R. P., West, C. D., Cho, J. S., Lahey, R. T., Nigmatulin, R. I., and Block, R. C. *Science* **295**, 1868–1873 (2002). 32

[137] Jaworski, M. A., Abrams, T., Allain, J. P., Bell, M. G., Bell, R. E., Diallo, A., Gray, T. K., Gerhardt, S. P., Kaita, R., Kugel, H. W., et al. *Nuclear Fusion* **53**(8), 083032 (2013). 32, 33

[138] Jaworski, M. A., Khodak, A., and Kaita, R. *Plasma Physics and Controlled Fusion* **55**(12), 124040 (2013). 32

[139] Lingwood, R. J. and Alboussiere, T. *Physics of Fluids* **11**(8), 2058–2068 (1999). 32

[140] Bazylev, B., Janeschitz, G., Landman, I., Pestchanyi, S., Loarte, A., Federici, G., Merola, M., Linke, J., Zhitlukhin, A., Podkovyrov, V., et al. *Physica Scripta* **T128**, 229–233 (2007). 33

[141] Brailovsky, A. B., Gaponov, S. V., and Luchin, V. I. *Applied Physics A* **61**(1), 81–86 (1995). 33

[142] Miloshevsky, G. V. and Hassanein, A. *Nuclear Fusion* **50**(11), 115005 (2010). 33

[143] Miloshevsky, G. V. and Hassanein, A. *Journal of Nuclear Materials* **438**, S155–S159 (2013). 33

[144] Miloshevsky, G. V. and Hassanein, A. *Nuclear Fusion* **54**(4), 043016 (2014). 33

[145] Fiflis, P., Christenson, M., Szott, M., Kalathiparambil, K., and Ruzic, D. N. *Nuclear Fusion* **56**(10), 106020 (2016). 33, 35

[146] Gomes, R. B., Fernandes, H., Silva, C., Sarakovskis, A., Pereira, T., Figueiredo, J., Carvalho, B., Soares, A., Varandas, C., Lielausis, O., et al. *Fusion Engineering and Design* **83**(1), 102–111 (2008). 34, 154

[147] Gomes, R. B., Fernandes, H., Silva, C., Borba, D., Carvalho, B., Varandas, C., Lielausis, O., Klyukin, A., Platacis, E., Mikelsons, A., et al. *AIP Conference Proceedings* **875**(1), 66–71 (2006). 34

[148] Mesyats, G. A. and Zubarev, N. M. *Journal of Applied Physics* **117**(4), 043302 (2015). 34

[149] Hassanein, A. and Konkashbaev, I. *Supplement to Nuclear Fusion* **5**, 193–224 (1994). 35

[150] Hassanein, A., Belan, V., Konkashbaev, I., Nikandrov, L., Safronov, V., Zhitlukhin, A., and Litunovsky, V. *Journal of Nuclear Materials* **241**, 288–293 (1997). 35, 154

[151] Balden, M., Rohde, V., Lindig, S., Manhard, A., Krieger, K., and the ASDEX Upgrade Team. *Journal of Nuclear Materials* **438**, S220–S223 (2013). 35

[152] Bird, J. C., De Ruiter, R., Courbin, L., and Stone, H. A. *Nature* **465**(7299), 759–762 (2010). 35

[153] Liger-Belair, G., Polidori, G., and Jeandet, P. *Chemical Society Reviews* **37**(11), 2490–2511 (2008). 35

[154] Duchemin, L., Popinet, S., Josserand, C., and Zaleski, S. *Physics of Fluids* **14**(9), 3000–3008 (2002). 35

[155] Shi, Y., Miloshevsky, G., and Hassanein, A. *Fusion Engineering and Design* **86**(2-3), 155–162 (2011). 36, 94

[156] Blairs, S. *International Materials Reviews* **52**(6), 321–344 (2007). 36

[157] Kim, S., Thiessen, P. A., Bolton, E. E., Chen, J., Fu, G., Gindulyte, A., Han, L., He, J., He, S., Shoemaker, B. A., Wang, J., Yu, B., Zhang, J., and Bryant, S. H. *Nucleic Acids Research* **44**(D1), D1202–13, Epub 2015 Sep 22 [PubMed PMID: 26400175] (2016). 36

[158] Militello, F. and Fundamenski, W. *Plasma Physics and Controlled Fusion* **53**(9), 095002 (2011). 36, 37

[159] Freton, P., Gonzalez, J. J., Peyret, F. C., and Gleizes, A. *Journal of Physics D: Applied Physics* **36**(11), 1269–1283 (2003). 37

[160] Calaprice, A. *The Ultimate Quotable Einstein*. Princeton University Press, (2010). 38

[161] Landau, L. D., Lifshitz, E. M., and Pitaevskii, L. P. *Fluid Mechanics*. Elsevier, 2nd edition, (1987). 38, 43, 44, 53

[162] Lamb, H. *Hydrodynamics*. Cambridge University Press, (1932). 38, 51

[163] Faber, T. E. *Fluid Dynamics for Physicists*. Cambridge University Press, (1995). 38

[164] Acheson, D. J. *Elementary fluid dynamics.* Oxford University Press, (1990). 38, 49

[165] Bittencourt, J. A. *Fundamentals of Plasma Physics.* Springer Science & Business Media, 3rd edition, (2004). 39, 40, 41

[166] Bellan, P. M. *Fundamentals of Plasma Physics.* Cambridge University Press, (2006). 39

[167] Woods, L. C. *Journal of Fluid Mechanics* **23**(2), 315–323 (1965). 40

[168] Griffiths, D. J. *Introduction to Electrodynamics.* Prentice Hall, 3rd edition, (1999). 42

[169] Franklin, R. N. *Journal of Plasma Physics* **78**(1), 21–24 (2012). 44

[170] Makkonen, T., Airila, M. I., and Kurki-Suonio, T. *Physica Scripta* **90**(1), 015204 (2015). 46

[171] Brackbill, J. U., Kothe, D. B., and Zemach, C. *Journal of Computational Physics* **100**(2), 335–354 (1992). 52

[172] Langmuir, I. *Science* **58**(1502), 290–291 (1923). 55

[173] Allen, J. In *Plasma Physics,* Keen, B. E., editor, chapter 5. IOP Publishing, Bristol (1974). 56

[174] Bohm, D. In *The Characteristics of Electrical Discharges in Magnetic Fields,* Guthrie, A. and Wakerling, R. K., editors, chapter 3, 90. McGraw-Hill, New York (1949). 56

[175] Riemann, K.-U. *Journal of Physics D: Applied Physics* **24**(4), 493 (1991). 56, 57

[176] Allen, J. E. and Holgate, J. T. *Nuclear Materials and Energy* **12**, 999–1003 (2017). 57

[177] Holgate, J. T. and Coppins, M. *Physics of Plasmas* **25**(4), 043514 (2018). 60, 61, 65, 129

[178] Griebel, M., Dornseifer, T., and Neunhoeffer, T. *Numerical simulation in fluid dynamics: a practical introduction.* SIAM, Philadelphia, (1997). 61, 90

[179] Forbes, R. G., Edgcombe, C. J., and Valdre, U. *Ultramicroscopy* **95**, 57–65 (2003). 61

[180] Holgate, J. T. and Coppins, M. *Physical Review Applied* **7**, 044019 (2017). 61

[181] Allen, J. E., Boyd, R. L. F., and Reynolds, P. *Proceedings of the Physical Society. Section B* **70**(3), 297 (1957). 62

[182] Kennedy, R. V. and Allen, J. E. *Journal of Plasma Physics* **67**(4), 243–250 (2002). 62, 64

[183] Thomas, D. M. *Theory and simulation of the charging of dust in plasmas.* PhD thesis, Imperial College London, (2016). 62, 63, 64, 70, 72, 78

[184] Dubinov, A. E. and Dubinova, I. D. *Journal of Plasma Physics* **71**(5), 715–728 (2005). 63

[185] Arinaminpathy, N., Allen, J. E., and Ockendon, J. R. *Journal of Plasma Physics* **73**(5), 793–810 (2007). 64

[186] Thomas, D. M. Personal communication by email, (August 1, 2017). 64

[187] Kang, M., Fedkiw, R. P., and Liu, X.-D. *Journal of Scientific Computing* **15**(3), 323–360 (2000). 64

[188] Altobelli, N., Postberg, F., Fiege, K., Trieloff, M., Kimura, H., Sterken, V., Hsu, H.-W., Hillier, J., Khawaja, N., Moragas-Klostermeyer, G., Blum, J., Burton, M., Srama, R., Kempf, S., and Gruen, E. *Science* **352**(6283), 312–318 (2016). 64

[189] Miloch, W. J., Kroll, M., and Block, D. *Physics of Plasmas* **17**(10), 103703 (2010). 65

[190] Hutchinson, I. H. *Physical Review Letters* **107**(9), 095001 (2011). 65

[191] Allen, J. E. *Journal of Plasma Physics* **73**(5), 773–783 (2007). 65, 67

[192] Nitter, T. *Plasma Sources Science and Technology* **5**(1), 93 (1996). 68

[193] Allen, J. E., Annaratone, B. M., and De Angelis, U. *Journal of Plasma Physics* **63**(4), 299–309 (2000). 68, 72

[194] Kennedy, R. V. and Allen, J. E. *Journal of Plasma Physics* **69**(6), 485–506 (2003). 70, 72, 73

[195] Allen, J. E. *Physica Scripta* **45**(5), 497–503 (1992). 70

[196] Lampe, M. *Journal of Plasma Physics* **65**(3), 171–180 (2001). 72

[197] Annaratone, B. M., Allen, M. W., and Allen, J. E. *Journal of Physics D: Applied Physics* **25**(3), 417–424 (1992). 73

[198] Díaz-Cabrera, J. M., Ballesteros, J., Palop, J. I. F., and Tejero-del Caz, A. *Plasma Sources Science and Technology* **24**(2), 025026 (2015). 73

[199] Chen, F. F. *Plasma Sources Science and Technology* **18**(3), 035012 (2009). 73

[200] Laframboise, J. G. and Parker, L. W. *The Physics of Fluids* **16**(5), 629–636 (1973). 73

[201] Zahed, H., Mahmoodi, J., and Sobhanian, S. *Physics of Plasmas* **13**(5), 053505 (2006). 74

[202] Landau, L. D. and Lifshitz, E. M. *Electrodynamics of Continuous Media*. Pergamon Press, Oxford, (1960). 74, 110, 119

[203] Holgate, J. T. and Coppins, M. *Physical Review E* **93**(3), 033208 (2016). 74, 129

[204] *Journal of Physics: Conference Series* **958**, 011001 (2018). 76

[205] Jones, R. V. and Spitzer Jr, L. *The Astrophysical Journal* **147**, 943–964 (1967). 76

[206] Milnes, J., Ayed, N. B., Dhalla, F., Fishpool, G., Hill, J., Katramados, I., Martin, R., Naylor, G., OGorman, T., Scannell, R., et al. *Fusion Engineering and Design* **96**, 42–47 (2015). 76

[207] Sonmor, L. J. and Laframboise, J. G. *Physics of Fluids B: Plasma Physics* **3**(9), 2472–2490 (1991). 76, 77, 79

[208] Patacchini, L., Hutchinson, I. H., and Lapenta, G. *Physics of plasmas* **14**(6), 062111 (2007). 77

[209] Lange, D. *Journal of Plasma Physics* **82**, 1–16 (2016). 78

[210] Thomas, D. M. and Holgate, J. T. *Plasma Physics and Controlled Fusion* **59**(2), 025002 (2017). 78, 130

[211] Barnes, J. and Hut, P. *Nature* **324**(6096), 446–449 (1986). 78

[212] Hutchinson, I. H. *Plasma Physics and Controlled Fusion* **45**(8), 1477–1500 (2003). 78

[213] Ishihara, O. and Sato, N. *IEEE Transactions on Plasma Science* **29**(2), 179–181 (2001). 78

[214] Draine, B. T. and Weingartner, J. C. *The Astrophysical Journal* **470**, 551–565 (1996). 78

[215] Krasheninnikov, S. I., Tomita, Y., Smirnov, R. D., and Janev, R. K. *Physics of Plasmas* **11**(6), 3141–3150 (2004). 78

[216] Hutchinson, I. H. *New Journal of Physics* **6**(1), 43 (2004). 78, 79

[217] Krasheninnikov, S. I., Shevchenko, V. I., and Shukla, P. K. *Physics Letters A* **361**(1-2), 133–135 (2007). 79

[218] Krasheninnikov, S. I. *Physics of Plasmas* **13**(11), 114502 (2006). 79, 80, 81

[219] Smirnov, R. D., Soboleva, T. K., Krasheninnikov, S. I., and Esquivel, A. In *34th EPS Conference on Plasma Phys. Warsaw, 2–6 July 2007 ECA*, volume 31F, P–2.091, (2007). 79, 81

[220] Martin, J. D., Coppins, M., and Counsell, G. F. *Journal of Nuclear Materials* **337**, 114–118 (2005). 81, 125

[221] Gilbert, W. *De Magnete*. Petrus Short, London, (1600). Translation by Mottelay, P. F. 1958 (Dover, New York). 83

[222] Collins, R. T., Jones, J. J., Harris, M. T., and Basaran, O. A. *Nature Physics* **4**(2), 149 (2008). 83

[223] Pongrác, B., Kim, H. H., Janda, M., Martišovitš, V., and Machala, Z. *Journal of Physics D: Applied Physics* **47**, 315202 (2014). 83

[224] Melcher, J. R. *The Physics of Fluids* **4**(11), 1348–1354 (1961). 84

[225] Melcher, J. R. *Field-coupled surface waves*. MIT Press, (1963). 84

[226] Taylor, G. I. and McEwan, A. D. *Journal of Fluid Mechanics* **22**(1), 1–15 (1965). 85, 88

[227] Holgate, J. T. and Coppins, M. *Physics of Fluids* **30**, 064107 (2018). 89, 90, 109, 111, 117, 118, 120, 122, 123

[228] Sethian, J. A. and Smereka, P. *Annual Review of Fluid Mechanics* **35**(1), 341–372 (2003). 90

[229] Morad, M. R., Rajabi, A., Razavi, M., and Sereshkeh, S. R. P. *Scientific Reports* **6**, 38509 (2016). 91

[230] Vyalykh, D. V., Dubinov, A. E., Mikheev, K. E., Lashmanov, Y. N., Lvov, I. L., Sadovoi, S. A., and Selemir, V. D. *Technical Physics* **50**(10), 1374–1375 (2005). 93

[231] Bruggeman, P., Liu, J., Degroote, J., Kong, M. G., Vierendeels, J., and Leys, C. *Journal of Physics D: Applied Physics* **41**, 215201 (2008). 93

[232] Dubinov, A. E., Kozhayeva, J. P., Lyubimtseva, V. A., and Selemir, V. D. *IEEE Transactions on Plasma Science* **45**(12), 3094–3099 (2017). 93

[233] Holgate, J. T., Coppins, M., and Allen, J. E. *Applied Physics Letters* **112**(2), 024101 (2018). 96, 99, 100, 130

[234] IEEE-DEIS-EHD Technical Committee. *IEEE Transactions on Dielectrics and Electrical Insulation* **10**(1), 3–6 (2003). 97

[235] Shirai, N., Sekine, R., Uchida, S., and Tochikubo, F. *Japanese Journal of Applied Physics* **53**(2), 026001 (2014). 104, 105, 155

[236] Shirai, N., Matsui, K., Ibuka, S., and Ishii, S. *IEEE Transactions on Plasma Science* **39**(11), 2210–2211 (2011). 104

[237] Schwartz, A. J., Ray, S. J., Elish, E., Storey, A. P., Rubinshtein, A. A., Chan, G. C.-Y., Pfeuffer, K. P., and Hieftje, G. M. *Talanta* **102**, 26–33 (2012). 105

[238] Shirai, N., Sekine, R., Uchida, S., and Tochikubo, F. *Japanese Journal of Applied Physics* **55**(1), 019202 (2016). 106, 155

[239] Rayleigh, L. *The London, Edinburgh, and Dublin Philosophical Magazine and Journal of Science* **14**(87), 184–186 (1882). 107

[240] Hendricks, C. D. and Schneider, J. M. *American Journal of Physics* **31**(6), 450–453 (1963). 107

[241] Somboonkittichai, N. *Computational and theoretical studies of metallic dust transport in Tokamaks*. PhD thesis, Imperial College London, (2015). 107

[242] Tsamopoulos, J. A., Aklas, T. R., and Brown, R. A. *Proceedings of the Royal Society of London A* **401**(1820), 67–88 (1985). 108

[243] Natarajan, R. and Brown, R. A. *Proceedings of the Royal Society of London A* **410**(1838), 209–227 (1987). 108

[244] Duft, D., Lebius, H., Huber, B. A., Guet, C., and Leisner, T. *Physical Review Letters* **89**(8), 084503 (2002). 108, 110

[245] Duft, D., Achtzehn, T., Müller, R., Huber, B. A., and Leisner, T. *Nature* **421**(6919), 128 (2003). 108, 110

[246] Coppins, M. *Physical Review Letters* **104**(6), 065003 (2010). 110, 111, 125

[247] Bennet, E. D., Mahony, C. M. O., Potts, H. E., Everest, P., Rutherford, D., Askari, S., McDowell, D. A., Mariotti, D., Kelsey, C., Perez-Martin, F., et al. *Journal of Aerosol Science* **100**, 53–60 (2016). 112

[248] Beard, K. V., Bringi, V. N., and Thurai, M. *Atmospheric Research* **97**(4), 396–415 (2010). 115

[249] Liao, L. and Hill, R. J. A. *Physical Review Letters* **119**(11), 114501 (2017). 117, 118, 121, 122, 123, 124

[250] Chandrasekhar, S. *Proceedings of the Royal Society of London A* **286**, 1–26 (1965). 117, 118

[251] García-Garrido, V. J., Fontelos, M. A., and Kindelán, U. *The Quarterly Journal of Mechanics and Applied Mathematics* **66**(4), 489–516 (2013). 117, 118

[252] Brown, R. A. and Scriven, L. E. *Physical Review Letters* **45**(3), 180–183 (1980). 117

[253] Brown, R. A. and Scriven, L. E. *Proceedings of the Royal Society of London A* **371**(1746), 331–357 (1980). 117, 118, 121, 122

[254] Heine, C.-J. *IMA Journal of Numerical Analysis* **26**(4), 723–751 (2006). 117

[255] Wang, T. G., Anilkumar, A. V., Lee, C. P., and Lin, K. C. *Journal of Fluid Mechanics* **276**, 389–403 (1994). 117, 118, 121

[256] Wang, T. G., Trinh, E. H., Croonquist, A. P., and Elleman, D. D. *Physical Review Letters* **56**(5), 452–455 (1986). 118, 121

[257] Biswas, A., Leung, E. W., and Trinh, E. H. *The Journal of the Acoustical Society of America* **90**(3), 1502–1507 (1991). 118

[258] Rhim, W.-K., Chung, S. K., and Elleman, D. D. In *AIP Conference Proceedings*, volume 197, 91–105. AIP, (1990). 124

[259] Coster, D. P., Bonnin, X., and Warrier, M. *Physica Scripta* **T124**, 9–12 (2006). 126

[260] Martin, J. D. *Theory and simulation of dust in tokamak plasmas.* PhD thesis, Imperial College London, (2006). 126

[261] Bacharis, M. *Theoretical study of dust in RF discharges and tokamak plasmas.* PhD thesis, Imperial College London, (2009). 126

[262] Koffman, L. D., Plesset, M. S., and Lees, L. *Physics of Fluids* **27**(4), 876–880 (1984). 126

[263] Schmitt, J. C., Bell, R. E., P, B. D., Esposti, B., Kaita, R., Kozub, T., LeBlanc, B. P., Lucia, M., Maingi, R., Majeski, R., et al. *Physics of Plasmas* **22**, 056112 (2015). 131

[264] Iafrati, M., Apicella, M. L., Boncagni, L., Lyublinski, I., Mazzitelli, G., and Vertkov, A. *Fusion Engineering and Design* **117**, 157–162 (2017). 131

[265] Hasan, M. I. and Bradley, J. W. *Journal of Physics D: Applied Physics* **48**, 435201 (2015). 131

[266] Gibou, F., Fedkiw, R., and Osher, S. *Journal of Computational Physics* **353**, 82–109 (2018). 132

Permissions

This Appendix contains the permission documents for any third party copyrighted figures used in this thesis. Any figures which are reprinted in this thesis and which do not appear in this Appendix were originally published under a Creative Commons Attribution (CC BY or CC BY-NC-ND) license and can be freely reproduced without seeking permission.

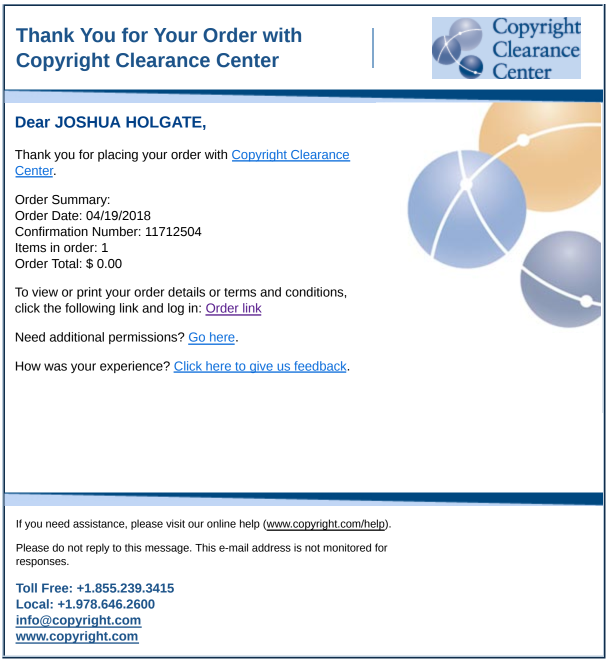

Thank You for Your Order with Copyright Clearance Center

Copyright Clearance Center

Dear JOSHUA HOLGATE,

Thank you for placing your order with Copyright Clearance Center.

Order Summary:
Order Date: 04/19/2018
Confirmation Number: 11712504
Items in order: 1
Order Total: $ 0.00

To view or print your order details or terms and conditions, click the following link and log in: Order link

Need additional permissions? Go here.

How was your experience? Click here to give us feedback.

If you need assistance, please visit our online help (www.copyright.com/help).

Please do not reply to this message. This e-mail address is not monitored for responses.

Toll Free: +1.855.239.3415
Local: +1.978.646.2600
info@copyright.com
www.copyright.com

Figure A.1: Permission to reprint Fig. 1.1, originally in Ref. [17].

Subject: Permission request to reprint figures
From: "EDVARDSEN, Miriam" <M.Edvardsen@iaea.org>
Date: 27/04/18 11:02
To: "j.holgate14@imperial.ac.uk" <j.holgate14@imperial.ac.uk>

Dear Mr Holgate,

Following your request for permission to reuse material:

Figure 7, from "Divertor tungsten tile melting and its effect on core plasma performance", Nucl. Fusion 52, No. 12, 123002 (2012), by B. Lipschultz et al.

Figure 7, from "Performance of the lithium metal infused trenches in the magnum PSI linear plasma simulator", Nucl. Fusion 55, No. 11, 113004 (2015), by P. Fiflis et al.

The IAEA is pleased to grant permission for the figures listed above to be reproduced to the extent and for the purposes detailed in your email. Please could you also notify the corresponding authors

Figure 6, from "Melt-layer motion and droplet ejection under divertor-relevant plasma conditions", Nucl. Fusion 53, No. 2, 023008 (2013), by G. De Temmerman et al.

The IAEA is pleased to grant permission for the figure listed above to be reproduced to the extent and for the purposes detailed in your email. Please note that you also have to inform EURATOM prior to such use and also notify the corresponding author.

Concerning your request to reproduce Figure 10, from Analysis of tungsten melt-layer motion and splashing under tokamak conditions at TEXTOR", Nucl. Fusion 51, No. 8, 083008 (2011), by J.W. Coenen et al. please note the reference [12] in the figure caption. We kindly ask you to contact the copyright owners directly to get their permission.

Best regards,

Ms Miriam EDVARDSEN | Publications Assistant (Marketing and Sales)|
Publishing section| Division of Conference and Document Services| Department of Management|
International Atomic Energy Agency | Vienna International Centre, PO Box 100, 1400 Vienna, Austria|
Email: **M.Edvardsen@iaea.org**| T: (+43-1) 2600-22530 |F : (+43-1) 2600-29302

Follow us on www.iaea.org

ATOMS FOR PEACE AND DEVELOPMENT

The IAEA Publishing Section operates an environmental management system certified to ISO 14001:2015

Figure A.2: Permission to reprint Figs. 1.2b, 1.3 and 1.5, originally in Refs. [31], [32] and [56] respectively.

Thank you for your order!

Dear Mr. JOSHUA HOLGATE,

Thank you for placing your order through Copyright Clearance Center's RightsLink® service.

Order Summary

Licensee:	Imperial College London
Order Date:	Apr 27, 2018
Order Number:	4337030677014
Publication:	Journal of Nuclear Materials
Title:	Tungsten melt layer motion and splashing on castellated tungsten surfaces at the tokamak TEXTOR
Type of Use:	reuse in a thesis/dissertation
Order Total:	0.00 USD

View or print complete details of your order and the publisher's terms and conditions.

Sincerely,

Copyright Clearance Center

Figure A.3: Permission to reprint Fig. 1.2a, originally in Ref. [28].

Thank you for your order!

Dear Mr. JOSHUA HOLGATE,

Thank you for placing your order through Copyright Clearance Center's RightsLink® service.

Order Summary

Licensee:	Imperial College London
Order Date:	Apr 19, 2018
Order Number:	4332561255625
Publication:	Fusion Engineering and Design
Title:	Tungsten and CFC degradation under combined high cycle transient and steady state heat loads
Type of Use:	reuse in a thesis/dissertation
Order Total:	0.00 GBP

View or print complete details of your order and the publisher's terms and conditions.

Sincerely,

Copyright Clearance Center

Figure A.4: Permission to reprint Fig. 1.4b, originally in Ref. [19].

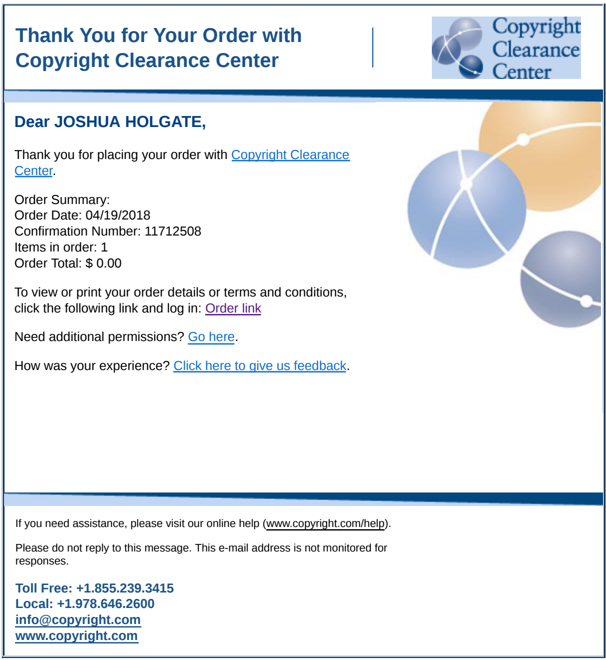

Thank You for Your Order with Copyright Clearance Center

Copyright Clearance Center

Dear JOSHUA HOLGATE,

Thank you for placing your order with Copyright Clearance Center.

Order Summary:
Order Date: 04/19/2018
Confirmation Number: 11712508
Items in order: 1
Order Total: $ 0.00

To view or print your order details or terms and conditions, click the following link and log in: Order link

Need additional permissions? Go here.

How was your experience? Click here to give us feedback.

If you need assistance, please visit our online help (www.copyright.com/help).

Please do not reply to this message. This e-mail address is not monitored for responses.

Toll Free: +1.855.239.3415
Local: +1.978.646.2600
info@copyright.com
www.copyright.com

Figure A.5: Permission to reprint Fig. 1.6, originally in Ref. [57].

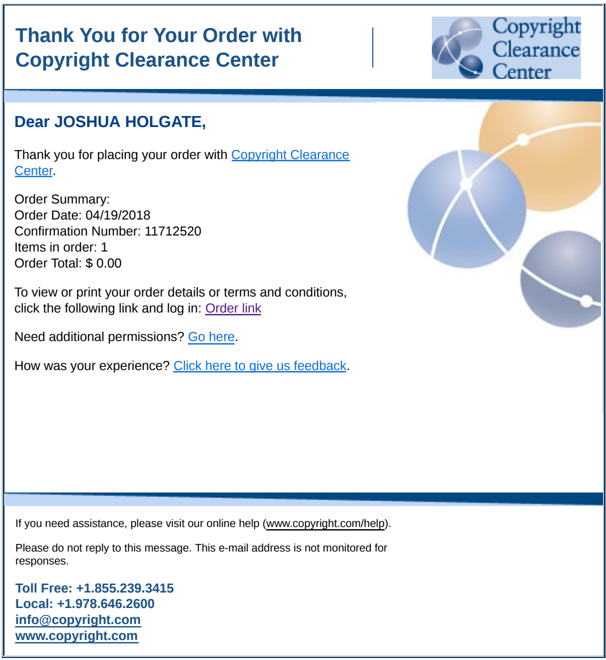

Thank You for Your Order with Copyright Clearance Center

Copyright Clearance Center

Dear JOSHUA HOLGATE,

Thank you for placing your order with Copyright Clearance Center.

Order Summary:
Order Date: 04/19/2018
Confirmation Number: 11712520
Items in order: 1
Order Total: $ 0.00

To view or print your order details or terms and conditions, click the following link and log in: Order link

Need additional permissions? Go here.

How was your experience? Click here to give us feedback.

If you need assistance, please visit our online help (www.copyright.com/help).

Please do not reply to this message. This e-mail address is not monitored for responses.

Toll Free: +1.855.239.3415
Local: +1.978.646.2600
info@copyright.com
www.copyright.com

Figure A.6: Permission to reprint Fig. 1.7, originally in Ref. [58].

Thank you for your order!

Dear Mr. JOSHUA HOLGATE,

Thank you for placing your order through Copyright Clearance Center's RightsLink® service.

Order Summary

Licensee:	Imperial College London
Order Date:	Apr 19, 2018
Order Number:	4332561070786
Publication:	Fusion Engineering and Design
Title:	Interaction of a liquid gallium jet with the tokamak ISTTOK edge plasma
Type of Use:	reuse in a thesis/dissertation
Order Total:	0.00 GBP

View or print complete details of your order and the publisher's terms and conditions.

Sincerely,

Copyright Clearance Center

Figure A.7: Permission to reprint Fig. 1.11, originally in Ref. [146].

Thank you for your order!

Dear Mr. JOSHUA HOLGATE,

Thank you for placing your order through Copyright Clearance Center's RightsLink® service.

Order Summary

Licensee:	Imperial College London
Order Date:	Apr 19, 2018
Order Number:	4332570059870
Publication:	Journal of Nuclear Materials
Title:	Modeling and simulation of melt-layer erosion during plasma disruption
Type of Use:	reuse in a thesis/dissertation
Order Total:	0.00 GBP

View or print complete details of your order and the publisher's terms and conditions.

Sincerely,

Copyright Clearance Center

Figure A.8: Permission to reprint Fig. 1.12, originally in Ref. [150].

[Notice]

If you are the one of the authors of the paper, you don't have to apply for a permission with the following conditions.

1. Follow the Copyright Policy of the Japan Society of Applied Physics
2. A credit line of "Copyright (published year) The Japan Society of Applied Physics" should be added to the end of the figure caption in the Content.
3. The Content must be cited as a reference in the Publication.

20 / 04 / 2018
Day Month Year

To: President of the Japan Society of Applied Physics

Submit to:
The Japan Society of Applied Physics
1st Floor, 1-21-5 Nezu, Bunkyo-ku, Tokyo 113-0031, Japan
TEL: +81-3-3828-7727 FAX: +81-3-3823-1811 E-mail address: permission@jsap.or.jp

Application for Permission to Reproduce Material

I request permission to reproduce the following material, copyrighted by the Japan Society of Applied Physics.

Publication where material is reproduced (the Publication)

Name of the Publication (e.g., journal title, book title): PhD Thesis
Publisher (e.g., publishing company): Imperial College London
Planned date of publication: July 2018
Number of copies: N/A (online publication only)

Content of reproduction (the Content)

Journal title: Japanese Journal of Applied Physics
Volume/Year/ID(starting page): 53/2014/026001
Article title: Atmospheric corona discharge using Taylor cone as a liquid cathode
Author(s): N. Shirai, R. Sekine, S. Uchida, F. Tochikubo
Content to be reproduced (please specify): Figure 3, Figure 4a

Applicant (only to be completed by the author of the Publication)

Name: Joshua Holgate
Affiliation (e.g., university, company, organization):
Imperial College London
E-mail address: j.holgate14@imperial.ac.uk

I will abide by the following conditions of reproduction.

1. A credit line "Copyright *publication year* The Japan Society of Applied Physics" must be added to the Content (in the figure caption(s)). The material containing the Content, copyrighted by the Japan Society of Applied Physics, must be cited in the references of the Publication.
2. The Content will not be modified.
3. The Content will not be reproduced in other materials.

Signature of applicant: J Holgate.

* The purpose of reproduction will be considered before permission is granted.

ENDORSEMENT

Dr. Joshua Holgate

I permit the reproduction of the Content in the Publication.

23/04/2018
Day Month Year

Shigeaki Zaima
President, The Japan Society of Applied Physics

The Japan Society of Applied Physics, 1st Floor, 1-21-5 Nezu, Bunkyo-ku, Tokyo 113-0031, Japan
TEL: +81-3-3828-7727/FAX: +81-3-3823-1811/E-mail address: permission@jsap.or.jp

Released March 2014, Revised June 2017

Figure A.9: Permission to reprint Figs. 4.12 and 4.13, originally in Ref. [235]. Fig. 4.13 uses the corrected figure according to the erratum in Ref. [238].